

DISSERTATION

submitted to the
Combined Faculties for the Natural Sciences and for Mathematics
of the Ruperto-Carola University of Heidelberg, Germany
for the degree of
Doctor of Natural Sciences

Put forward by
Asier Piñeiro Orioli

Born in: San Sebastián, Spain

Oral examination: 20.12.2017

Quantum dynamics and universality far from equilibrium

Referees: Prof. Dr. Jürgen Berges
Priv. Doz. Tilman Enss

*Quantum dynamics and universality
far from equilibrium*

Abstract

The aim of the present thesis is to contribute to a better understanding of the nonequilibrium dynamics of isolated many-body quantum systems, and to develop new theoretical methods for their description. Important questions that will be addressed here concern the emergence of universal behavior far from equilibrium as well as the role of genuine quantum effects on the dynamics.

In the first part, we study the far-from-equilibrium universal dynamics of relativistic and nonrelativistic quantum field theories close to a nonthermal fixed point. In this regime, the dynamics is characterized by self-similar scaling and transport of conserved quantities. Using classical-statistical simulations we compute the scaling functions and scaling exponents of different equal-time and unequal-time correlation functions, including statistical as well as spectral components. This analysis is complemented by analytical estimates using a resummed kinetic theory based on a nonperturbative $1/N$ expansion of the two-particle irreducible (2PI) effective action. Our results shed light on the process of condensate formation, the transport of particles at low momenta, as well as the spectrum of excitations.

In the second part, we theoretically and experimentally investigate the relaxation dynamics of an XY dipolar-interacting quantum spin model in an external field, which is realized with ultracold Rydberg atoms. Starting from a fully magnetized initial state, we suddenly switch on the external field and study the subsequent demagnetization dynamics. To disentangle the processes responsible for the relaxation in a closed system, we employ a well-defined hierarchy of theoretical approximations. Our analysis reveals the role of disorder and quantum fluctuations in the dynamics.

In the last part, we investigate possible extensions of the classical-statistical or truncated Wigner approximation (TWA) to include quantum effects. Corrections to TWA are added by applying the sampling over initial conditions to a larger set of variables and equations of motion to solve. We consider two different approaches. In the first one, we benchmark a scheme based on BBGKY-type equations by comparing to exact solutions of a spin-boson model relevant for trapped-ion experiments. In the second one, we use 2PI equations instead and compare to exact numerical results of an anharmonic oscillator. Furthermore, we test the potential of the method to capture essential aspects needed for quantum thermalization in a relativistic scalar field theory. Our findings indicate that these methods may be capable of describing thermalization in quantum systems in which both classical fluctuations and genuine quantum effects are important.

*Quantendynamik und Universalität
fern des Gleichgewichts*

Zusammenfassung

Das Ziel dieser Arbeit ist es, zum Verständnis der Nichtgleichgewichtsdynamik isolierter Vielteilchenquantensysteme beizutragen, und neue theoretische Methoden für deren Beschreibung zu entwickeln. Im Vordergrund stehen dabei Fragen rund um Universalität fern des Gleichgewichts und die Rolle genuiner Quanteneffekte in der Dynamik.

Im ersten Teil untersuchen wir universelle Dynamik fern des Gleichgewichts in relativistischen und nichtrelativistischen Skalartheorien nah eines nichtthermischen Fixpunktes. Während dieser Phase zeichnet sich die Dynamik durch selbstähnliches Skalierungsverhalten und Transport von Erhaltungsgrößen aus. Unter Benutzung klassisch-statistischer Simulationen berechnen wir die Skalenfunktionen und Skalenexponenten verschiedener Korrelationsfunktionen. Dafür betrachten wir gleichzeitige und ungleichzeitige Größen, sowie statistische und spektrale Komponenten der Korrelationsfunktionen. Ergänzt wird die Analyse durch analytische Rechnungen mit einer resummierten kinetischen Theorie, die auf einer nichtperturbativen $1/N$ Entwicklung der zwei-Teilchen-irreduziblen (2PI) effektiven Wirkung basiert ist. Unsere Ergebnisse geben Einblicke in den Kondensationsprozess, den Teilchentransport bei kleinen Impulsen, und das Spektrum der elementaren Anregungen.

Im zweiten Teil untersuchen wir die Relaxationsdynamik eines dipolar wechselwirkenden XY Quantenspinmodells, welches von Rydbergatomen realisiert wird, von einer theoretischen und experimentellen Perspektive. Wir betrachten dazu die Demagnetisierungsdynamik eines anfänglich voll magnetisierten Zustands, welcher nach schneller Änderung eines externen Parameters aus dem Gleichgewicht gerät. Wir benutzen eine wohldefinierte Hierarchie theoretischer Näherungen, um die Natur der Prozesse, die für die Relaxation dieses geschlossenen Systems verantwortlich sind, zu enthüllen. Unsere Analyse offenbart die Rolle der Unordnung und der Quantenfluktuationen in der Dynamik.

Im letzten Teil befassen wir uns mit möglichen Erweiterungen der klassisch-statistischen oder trunkierten Wigner Näherung (TWA) mit dem Ziel, Quanteneffekte miteinzubeziehen. Um Korrekturen zur TWA hinzuzufügen, wenden wir das Mitteln über Anfangsbedingungen auf eine größere Anzahl von Variablen und Bewegungsgleichungen an. Wir betrachten zwei Ansätze. Beim Ersten benutzen wir BBGKY-artige Gleichungen und überprüfen die Genauigkeit der Vorhersagen dieser Methode, indem wir sie mit exakten Lösungen eines Spin-Boson Modells vergleichen, welches zur Beschreibung gefangener Ionen relevant ist. Beim Zweiten benutzen wir stattdessen 2PI Gleichungen, deren Vorhersagen wir mit der numerisch exakten Lösung eines anharmonischen Oszillators vergleichen. Außerdem untersuchen wir das Potenzial dieser Methode, wesentliche Aspekte der Quantenthalisierung einer relativistischen Quantenfeldtheorie wiederzugeben. Unsere Resultate suggerieren, dass diese Methoden Thermalisierung von Quantensystemen beschreiben könnten, in welchen sowohl klassische Fluktuationen als auch genuine Quanteneffekte von Bedeutung sind.

List of Publications

The results presented in this thesis have led to the following pre-prints and peer-reviewed publications, which have been written and published during the course of my doctoral studies:

- **A. Piñeiro Orioli, K. Boguslavski, J. Berges**, “*Universal self-similar dynamics of relativistic and nonrelativistic field theories near nonthermal fixed points*”, *Phys. Rev. D* **92**, 025041 (2015).
- **A. Schachner, A. Piñeiro Orioli, J. Berges**, “*Universal scaling of unequal-time correlation functions in ultracold Bose gases far from equilibrium*”, *Phys. Rev. A* **95**, 053605 (2017).
- **A. Piñeiro Orioli, A. Safavi-Naini, M. L. Wall, A. M. Rey**, “*Nonequilibrium dynamics of spin-boson models from phase space methods*”, *Phys. Rev. A* **96**, 033607 (2017).
- **A. Piñeiro Orioli, A. Signoles, H. Wildhagen, G. Günter, J. Berges, S. Whitlock, M. Weidemüller**, “*Relaxation of an isolated dipolar-interacting Rydberg quantum spin system*”, [arXiv:1703.05957](https://arxiv.org/abs/1703.05957) (2017). (submitted to *Physical Review Letters*)

Contents

Abstract, Zusammenfassung	i
List of Publications	iii
1 Introduction	1
1.1 Outline of the thesis	6
2 Nonequilibrium Quantum Field Theory	9
2.1 Scalar field theories	9
2.1.1 Relativistic	10
2.1.2 Nonrelativistic	10
2.2 Functional Integral Description	11
2.2.1 Generating functional on a closed time contour	11
2.2.2 Nonequilibrium Green's Functions	12
2.3 2PI effective action	13
2.3.1 2PI evolution equations	15
2.3.2 Perturbative coupling expansion	15
2.3.3 Nonperturbative $1/N$ expansion	17
2.4 Transport equations	18
2.5 Classical Statistical or Truncated Wigner Approximation	20
2.5.1 Path integral for classical-statistical theory	20
2.5.2 Classality condition	22
2.5.3 Wigner representation of quantum dynamics	23
I Nonthermal Fixed Points	27
3 Universal Self-similar Dynamics in Relativistic and Nonrelativistic Theories	29
3.1 Introduction	30
3.1.1 Nonthermal fixed points	30
3.1.2 Outline of results	33
3.2 Nonrelativistic Bose gas	35
3.2.1 Overoccupied initial conditions	36
3.2.2 Self-similarity from classical statistical simulations	37
3.2.3 Condensate formation	39
3.3 Relativistic quantum field theory	41
3.3.1 Overoccupied initial conditions	41
3.3.2 Self-similarity from classical statistical simulations	42

3.3.3	Generation of a mass gap	45
3.3.4	Condensate formation	48
3.4	Vertex-resummed kinetic theory	48
3.4.1	Self-similarity from kinetic theory	49
3.4.2	Perturbative scaling	50
3.4.3	Nonperturbative scaling	52
3.5	Anomalous scaling	56
3.5.1	Nonrelativistic field theory	56
3.5.2	Relativistic field theory	59
3.6	Conclusions	60
4	Unequal-time correlators and Dynamical Exponent	63
4.1	Scaling of unequal-time correlators	64
4.2	Nonequilibrium evolution	65
4.3	Finite size scaling	67
4.4	Conclusions	72
5	Spectral Function and Anomalous Dimension	73
5.1	Spectral function from linear response	74
5.1.1	Uniform perturbation field	74
5.1.2	Random perturbation field	76
5.2	Classical-statistical spectral function	76
5.2.1	Numerical implementation	77
5.2.2	Equation of motion	77
5.3	Nonequilibrium evolution	78
5.4	Quasiparticle spectrum	79
5.4.1	Frequency spectrum	81
5.4.2	Quasiparticles and dispersion relation	82
5.5	Self-similar scaling of the spectral function	87
5.6	Breaking of fluctuation-dissipation relation	89
5.7	A challenge for kinetic theory	92
5.8	Conclusions	93
	II Rydberg Spin Dynamics	95
6	Relaxation Dynamics in a Dipolar Spin System	97
6.1	Realization of a dipolar XY model	98
6.2	Theoretical description of spin systems	100
6.2.1	Moving Average Cluster Expansion	100
6.2.2	Discrete TWA for spins	101
6.3	Relaxation dynamics of a Rydberg spin system	102
6.4	Role of quantum fluctuations	106
6.5	Conclusions	111

III	Quantum Corrections beyond TWA	113
7	BBGKY Extension: Spin-Boson Dynamics	115
7.1	Introduction	116
7.2	Spin boson model	117
7.3	Nonequilibrium dynamics from phase-space methods	119
7.3.1	TWA for spins and bosons	120
7.3.2	BBGKY extension	121
7.4	Benchmark of TWA and BBGKY	123
7.4.1	Single mode	123
7.4.2	Many modes	126
7.4.3	Role of sampling in BBGKY	127
7.4.4	Large system sizes	128
7.5	Conclusions	130
8	2PI Extension: Anharmonic Oscillator and φ^4-theory	133
8.1	Anharmonic Oscillator	134
8.2	Sampled 2PI	136
8.3	Quantum corrections to TWA	138
8.4	Scalar field theory	142
8.5	On thermalization and the quantum 1/2	144
8.6	Conclusions	147
9	Conclusions and Outlook	149
	Acknowledgements	155
A	Numerical Methods	157
A.1	Space and Time Discretization	157
A.2	2PI equations	158
A.3	Crank-Nicolson	159
A.4	Anharmonic Oscillator	160
B	Self-similarity fit procedure	161
C	BBGKY Equations	165
D	Discrete sampling	169
	Bibliography	173

Chapter 1

Introduction

Isolated quantum systems out of equilibrium are ubiquitous in physics, and their study often connects vastly different fields such as ultracold quantum gases, collision experiments with heavy nuclei, or early-universe cosmology. While these systems differ immensely in energy scales and the models used for their description, the fundamental questions of interest are often similar. How do isolated quantum systems evolve in time and eventually reach an equilibrium state? Are there any interesting states or new phenomena taking place out of equilibrium? These questions are at the core of the present thesis. As we will show, certain aspects of them can even establish links between these different systems on a quantitative level.

Before proceeding, it is essential to specify what is meant by equilibrium. Real physical systems are never in true equilibrium.¹ Nevertheless, many systems hardly ‘change’ in time and can be regarded as being approximately in a stationary state characterized by time-translation invariance. In a simple and elegant way, quantum statistical mechanics [1] describes the properties of such systems via thermal equilibrium ensembles, which are determined by the values of only few conserved quantities such as, e.g., energy or particle number (or the corresponding densities). The latter is an important feature of equilibrium systems. They contain no *memory* of the past, except for the few thermodynamic quantities defining it.

Isolated systems evolving under unitary evolution cannot reach such an equilibrium state *globally*. Unitarity implies perfectly reversible dynamics and hence all the memory about the initial state is to all times encoded in the state of the system. Remarkably though, isolated quantum systems can undergo an *effective* loss of details about the initial state and approach equilibrium in the sense that relevant observables become indistinguishable from their thermal equilibrium values at long enough times [2–7]. Loosely speaking, the system can act as its own reservoir for subsystems of itself. By now, it is widely believed that typical interacting quantum systems equilibrate in this sense, with some possible famous counterexamples including integrable systems² [10] and many-body localization [11].

Having said this, the present thesis is devoted to the study of how isolated many-body quantum systems initially prepared in a far-from-equilibrium state evolve in time and eventually approach equilibrium (Fig. 1.1 depicts a possible scenario that will be discussed below). The

¹This is meant from a fundamental point of view, since equilibrium requires time-translation invariance and can only be reached asymptotically.

²Using the notion of generalized Gibbs ensembles [8], even integrable systems can approach equilibrium [9].

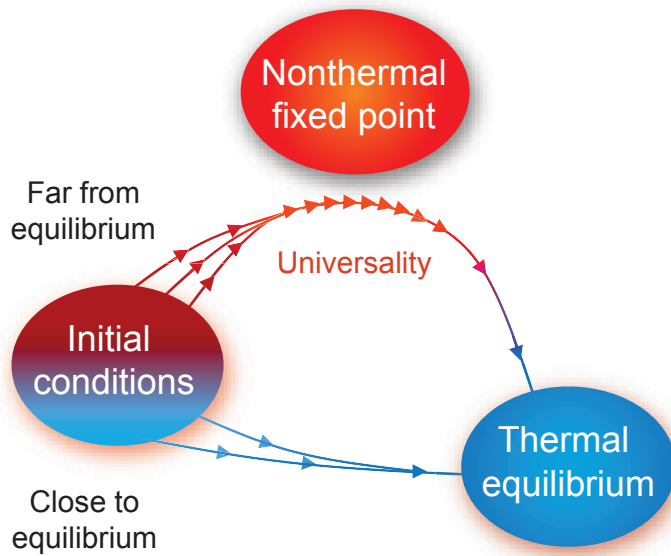


FIGURE 1.1: Conceptual picture of a nonthermal fixed point. For a subset of far-from-equilibrium initial conditions, the system approaches, on the way to equilibrium, a nonthermal fixed point, where the dynamics becomes universal and is characterized by self-similar scaling and transport of conserved quantities. For other initial conditions, the dynamics is not attracted to the nonthermal fixed point and may instead be driven by different processes. This picture was used in the online version of [12].

emphasis lies here on understanding and characterizing the dynamical evolution out of equilibrium. In particular, are there any general mechanisms or even universal aspects applicable to different types of systems? What is the role of the quantum nature of the system? And which theoretical methods are needed to describe the nonequilibrium dynamics of such systems?

Far from being a purely fundamental question, understanding the nonequilibrium dynamics of isolated many-body quantum systems has broad-ranging applications. Research on these topics has been particularly boosted in the last years by recent advances in the field of atomic, molecular and optical physics (AMO). Since the experimental realization of a Bose-Einstein condensate [13–15], a series of experimental breakthroughs has allowed this field to gain an unprecedented degree of control over quantum systems composed of many particles - some people call this era ‘the third quantum revolution’ [16]. This has led to an explosive rise of proposals to use ultracold gases for quantum technologies, including applications in quantum metrology and quantum information [17–19].

Systems of ultracold gases are ideally suited for investigating the dynamics of closed quantum systems for at least two reasons: the timescales involved are much slower than, e.g., typical condensed matter experiments and the systems can be almost perfectly isolated from the environment. Using ultracold atoms, ions or molecules, it is possible to engineer a large variety of artificial quantum systems with highly tunable features such as dimensionality, strength (and sometimes type) of interactions or symmetry (for recent reviews see [20, 21]). The malleability of these systems allows to even implement and study models with potential applications in other branches such as condensed matter or high energy physics. This makes them potential candidates to realize so-called quantum simulators [22, 23]. Thus, experiments

with ultracold quantum gases constitute excellent platforms to learn about the nonequilibrium dynamics of a myriad of physical models.

High-energy systems where the dynamics of isolated quantum systems plays an important role include heavy-ion collisions and early-universe cosmology. Collision experiments with heavy nuclei are currently being carried out at the Large Hadron Collider (LHC) at CERN and at the Relativistic Heavy Ion Collider (RHIC) at Brookhaven National Lab. One of their aims is to probe features of the strong interaction, described by Quantum Chromodynamics (QCD), under extreme conditions, e.g. the confinement-deconfinement transition [24, 25]. Strong evidence supports that after the collision a quark-gluon plasma (QGP) is formed [26–28]. Initially in a far-from-equilibrium state, this plasma rapidly expands and evolves in the surrounding vacuum. The specific space-time evolution of the plasma can have a large impact on the observables measured in the experiment. Hence, a proper description of the nonequilibrium dynamics of non-Abelian plasmas is essential to understand the physics of heavy-ion collisions [29].

A similar scenario is encountered in the early-time evolution of the universe, specifically shortly after the inflationary era. The theory of inflation was introduced to solve among others the horizon and flatness problems [30, 31] resulting from observations of the Cosmic Microwave Background (CMB) [32, 33]. During inflation, the universe expands exponentially fast such that the whole energy and matter of the universe gets diluted. This is often described in terms of a slowly-rolling scalar field named the inflaton. Once inflation is over, the whole energy density of the universe is stored in a huge macroscopic inflaton field, which constitutes a far-from-equilibrium state. The subsequent evolution, named ‘reheating’ dynamics [34], involves the decay of the inflaton field into the elementary particles that form the matter we know today. Understanding the mechanisms governing the nonequilibrium particle production after inflation can hence provide intriguing insights into key aspects of the history of our universe.

Universality

Do ultracold quantum gases, heavy-ion collisions and early-universe cosmology have something in common, in particular are there any universal aspects in their dynamical evolution?

In equilibrium, the concept of universality is essential in the description of the behavior of many-body (quantum and classical) systems. Universality emerges naturally within the framework of the renormalization group [35–38], which allows for a classification of theories according to their behavior close to (thermal) fixed points of the renormalization group flow. As a consequence of universality, certain numbers (e.g. scaling exponents or amplitude ratios) can be quantitatively the same regardless of details of the underlying system. One of the most well-known examples is found in the physics of second order phase transitions. At the critical point of the transition, a correlation length diverges and the system becomes scale invariant. Because of this, various quantities such as the order parameter or correlation functions show scaling behavior in the vicinity of the critical point. The values of the associated scaling exponents can be classified into different universality classes and are solely determined by few system parameters such as symmetry and dimensionality.

In recent years, new universality classes in systems far from equilibrium [39–67] have been discovered. In this case, the universality is based on the existence of nonthermal fixed

points [41, 68, 69], which represent attractor solutions with self-similar scaling dynamics (see Fig. 1.1). For a large class of initial conditions, the system on the way to equilibrium is first attracted to a nonthermal fixed point where the dynamics becomes extremely slow. During this regime, correlation functions show self-similar scaling in time, characterized by a set of scaling exponents and scaling functions. For instance, for an occupation number distribution $f(t, \mathbf{p})$ (t is time, \mathbf{p} is momentum), self-similar evolution is given by $f(t, \mathbf{p}) = t^\alpha f_S(t^\beta \mathbf{p})$ with scaling exponents α and β and scaling function f_S . The dynamics close to the nonthermal fixed point is universal in two senses. On the one hand, the values of the exponents (e.g., α and β) and the shape of the scaling function (e.g., f_S) are to a large extent independent of details on the initial conditions. Most importantly though, these quantities can be the same for different theories. While the defining properties of far-from-equilibrium universality classes are still unclear, there are striking indications that they can even encompass systems with different symmetry, such as gauge and scalar $O(N)$ theories [12], relativistic and nonrelativistic theories [66], or models with different number of field components [67].

A class of initial conditions that leads to such a behavior involves very highly occupied or ‘overoccupied’ modes up to a certain momentum scale Q . In terms of the distribution function introduced above, one typically considers $f(0, Q) \sim 1/\lambda$, where $\lambda \ll 1$ is a small interaction or ‘diluteness’ parameter [12, 66, 70]. Such initial conditions can in principle be prepared using ultracold quantum gases via quenches or nonequilibrium instabilities [71–73]. However, they are essentially motivated by the high-energy systems introduced above. In some chaotic inflationary models, the decay of the inflaton occurs via nonequilibrium instabilities, which lead to a large occupation of modes at resonant momenta [74]. Similarly, in heavy-ion experiments the state of the plasma created shortly after the collision is expected to be described in terms of highly occupied gluon fields [75].

Because of the nature of such initial conditions, the physics close to the nonthermal fixed point is dominated by transport of conserved quantities, such as energy or particle number. This leads to the formation of cascades, similar to the phenomenon of wave turbulence [76, 77], but without external sources or sinks. In scalar theories, for instance, an energy cascade forms at high momenta which transfers energy to higher modes, while an inverse particle cascade at low momenta transports particles to the infrared [40, 41, 55, 66, 69]. The latter leads eventually to the formation of a Bose-Einstein condensate out of equilibrium [57, 59]. This process is reminiscent of the physics of coarsening or phase-ordering kinetics [78], which is determined by the dynamics of topological defects. Indeed, such defects have been found as well in the dynamics close to nonthermal fixed points [49, 56, 60, 64].

Quantum dynamics

Since the universal regime close to the nonthermal fixed points discussed above involves large occupancies, $f \gg 1$, the dynamics is essentially classical (statistical). Quantum effects play, however, a crucial role in the evolution after the nonthermal fixed point, especially at large momenta where the occupation numbers become of order one, $f \sim 1$. In this regime, purely classical evolution would lead to classical equipartition, which has a well-known Rayleigh-Jeans divergence at large momenta and violates important quantum bounds related to zero-energy

fluctuations³ [51, 79, 80]. To describe the equilibration of the system to the correct quantum distribution expected from quantum statistical mechanics, e.g. the Bose-Einstein distribution in the case of bosons, and to respect the corresponding quantum bounds, it is hence necessary to take quantum effects into account.

The quantum nature of the system can also play an essential role in the nonequilibrium dynamics of other systems, such as in fermionic or spin systems, where the corresponding occupancies are usually low. Quantum spin models are often used to describe quantum magnetism [81] and can be effectively realized in AMO setups using, e.g. ultracold molecules [82–84], ions [85–89], or Rydberg atoms [90–92]. While the general mechanisms responsible for relaxation in these systems are hard to disentangle, identifying them can have important implications, e.g., for quantum technologies [17, 18, 93] and may motivate better theoretical approximations. An intriguing aspect in the dynamics of these systems concerns the creation and role of classical and quantum correlations. In particular, while the dynamics of these systems may be expected to be strongly influenced by the peculiarities of quantum theory, it is vital to figure out in which way they differ from corresponding semiclassical models.

Of course, profound understanding of the nonequilibrium dynamics of many-body quantum systems requires the existence of theoretical methods capable of describing them. Methods based on the density matrix renormalization group (DMRG) [94] have proven extremely useful in the description of a myriad of quantum systems, especially in low dimensions. However, for most of the problems considered in this thesis, their use is limited, as they quickly become inefficient in higher dimensions or for long times.

As suggested above, the physics of nonthermal fixed points, which will be investigated here, can be well described using a mapping to classical-statistical field theory [95–99] due to the high occupancies involved. This method is also known as the truncated Wigner approximation (TWA) [100, 101]. Recent developments [102, 103] suggest that TWA can even be useful in the description of some quantum spin systems. Nonetheless, these methods have clear limitations as well. In particular, regimes of low occupancies are not well described by them, and their range of validity for spin systems with small spin quantum number is unclear. For weak interactions, such low-occupied regimes may be described using functional integral techniques based on two-particle irreducible (2PI) effective actions [5, 70, 104] or using effective kinetic theories [40, 54, 105, 106]. However, they fail as soon as the occupancies become of the order $f \gtrsim 1/\lambda$ ($\lambda \ll 1$), as can be the case in the low-momentum region of nonthermal fixed points. These methods can be extended to describe such highly-occupied nonperturbative regimes by using appropriate resummation schemes, such as nonperturbative $1/N$ expansions in the number of field components N [65, 70, 107, 108]. Unfortunately though, such resummations are in general hard to develop, in particular for non-Abelian gauge theories [109]. Thus, the development of methods that can both capture the classical regime as well as genuine quantum effects is essential to make progress in our understanding of isolated many-body quantum systems out of equilibrium.

.....

³In quantum theory, the occupation of energy modes is given by $f(t, \mathbf{p}) + 1/2$, which can not fall below the ‘quantum 1/2’. However, classical theory does not respect this bound.

In this thesis, we investigate universal dynamics and other relaxation mechanisms in isolated quantum systems as well as theoretical methods for their description. A large part of the thesis is dedicated to a thorough study and characterization of nonthermal fixed points in bosonic field theories. However, we will also study spin-1/2 systems and explore the relevant mechanisms responsible for relaxation in this case. Inspired by these phenomena, we further analyze and develop extensions of TWA based on a combination with functional methods, which may allow access to currently unavailable regimes. While we will focus our investigation on systems of ultracold quantum gases, we will also consider relativistic theories with possible applications in inflationary cosmology. A more detailed outline of the thesis is presented in the following.

1.1 Outline of the thesis

This thesis is divided into three parts. The first part is devoted to the study of the universal self-similar dynamics emerging in nonrelativistic (Gross-Pitaevskii) Bose gases and relativistic scalar field theories. One of the main objectives is to achieve a better understanding of the physics behind the phenomenon as well as to thoroughly characterize the corresponding nonthermal fixed point by computing the universal exponents associated to the dynamics of different correlation functions. The second part deals with the nonequilibrium dynamics of a spin-1/2 model realized with Rydberg atoms. Here, the main interest will be to understand and disentangle the relevant mechanisms behind the relaxation process observed. The third and last part explores possible ways to add quantum corrections to the classical-statistical approximation or TWA.

We begin in Chap. 2 with an introduction to nonequilibrium quantum field theory along with the main tools and approximations that will be used in the main text. A central role in the treatment is played by the two-particle-irreducible (2PI) effective action. We derive self-consistent evolution equations for correlation functions, discuss the emergence of kinetic theory and present both perturbative and nonperturbative approximation schemes for the effective action. At the end, we exhaustively discuss the classical-statistical approximation or TWA both from the path integral and from the Wigner representation perspective.

Chapter 3 is the first of three chapters dedicated to the study of nonthermal fixed points in scalar field theories. In this chapter, we study the universal self-similar dynamics of both nonrelativistic and relativistic scalar field theories close to a nonthermal fixed point. Starting from an overoccupied initial condition, we examine the universal properties of the (particle) distribution function $f(t, \mathbf{p})$ (t is time, \mathbf{p} is momentum) in the infrared. In this way, this chapter generalizes previous work [41, 43, 55, 69] that had concentrated on stationary aspects related to power-law behavior in momentum space. We compute the universal exponents and scaling functions characterizing the self-similar evolution during the universal regime using two nonperturbative approaches: classical statistical simulations as well as analytical estimates based on an expansion of the 2PI effective action in the number of the field components to next-to-leading order (NLO) [108]. Remarkably, both relativistic and nonrelativistic theories turn out to be described by the same set of exponents and scaling functions. Furthermore, our findings conclusively demonstrate the existence of an inverse particle cascade at low momenta and shed light on the formation of a Bose condensate during the universal regime.

In Chap. 4 we concentrate on the nonrelativistic Bose gas, and extend the previous analysis to unequal-time correlation functions $F(t, t', \mathbf{p})$, which are related to the expectation value of the anticommutator of the fields. Using a finite-size scaling analysis we numerically compute the self-similar dynamics of this quantity close to the nonthermal fixed point. This gives access to the dynamical exponent z , which relates scaling in frequency to momentum and further characterizes the universality class. Moreover, our analysis contributes towards characterizing the features of the growing condensate.

We close the first part with Chap. 5, where we compute the spectral function $\rho(t, t', \mathbf{p})$, which is related to the expectation value of the commutator of the fields. For this we use a method based on linear response to external perturbations, applied to classical statistical simulations. A scaling analysis of the spectral function gives us access to the anomalous dimension η of the system close to the nonthermal fixed point. Furthermore, this quantity contains information about the low-energy excitations of the system. Our analysis reveals a surprisingly simple quasiparticle structure with well-defined dispersion relation and demonstrates the breaking of the fluctuation-dissipation relation at low momenta.

In Chap. 6 (part two), we theoretically and experimentally investigate the relaxation dynamics of a dipolar XY spin model realized with ultracold Rydberg atoms. Specifically, we study the demagnetization dynamics of an initially fully magnetized state after a quench of an external parameter. We demonstrate that the observed dynamics is consistent with fully unitary evolution. Using a well-defined hierarchy of theoretical approximations we further disentangle the mechanisms responsible for the relaxation and shed light on the role of disorder and quantum fluctuations during the dynamics. This demonstrates the potential of Rydberg atoms to address relevant questions related to the dynamics of isolated spin systems.

Chapter 7 inaugurates the third part, where extensions of TWA are investigated. In this chapter, we consider a system with both spin and bosonic degrees of freedom and generalize a recent proposal [110] to add corrections to TWA by enlarging the set of variables and equations of motion to solve, in a manner similar to a BBGKY hierarchy. We further make use of recently developed discrete sampling schemes for the spins [102]. To test the accuracy of the method, we compare to exact results of a spin-boson model relevant for the description of trapped-ion systems.

In Chap. 8 we employ a similar concept and propose a method to add quantum corrections to TWA by using 2PI equations of motion instead. Using a perturbative expansion of the self-energies, we demonstrate the applicability of the method on an anharmonic oscillator and compare to exact numerical results. After that we apply it to the nonequilibrium dynamics of a relativistic scalar field theory in two dimensions. In this context, we explore the potential of the method to capture essential aspects needed for quantum thermalization.

Finally, Chap. 9 summarizes the main results of the thesis and gives some outlook onto possible ramifications of this work.

Chapter 2

Nonequilibrium Quantum Field Theory

In this chapter, we present the main tools and approximations that will be used to describe the nonequilibrium dynamics of many-body quantum systems. What follows is largely based on Ref. [70], where a more detailed discussion can be found. Further details on some of the topics can also be found in Refs. [70, 100, 111–114].

We start with the functional integral representation of nonequilibrium quantum field theory and introduce then the two-particle irreducible (2PI) effective action. From it we derive exact evolution equations for Green's functions, which constitute our main observables of interest. Following that we present a number of approximation schemes with different regimes of validity. At the level of the effective action we consider both perturbative loop expansions and nonperturbative $1/N$ approximations. After that we show how effective kinetic equations can be derived from the resulting dynamic equations. We close the chapter with an extensive discussion of the classical statistical approximation, both from the path integral and the operator perspective.

The following presentation focuses mainly on scalar field theories, which will play a major role throughout this thesis. However, we emphasize that some of the presented tools will later be used to treat other many-body quantum systems as well. Details on this will be given in the corresponding chapters.

2.1 Scalar field theories

We consider both relativistic and nonrelativistic N -component scalar field theories [115]. To keep the discussion general we use φ_a to denote the components of a real scalar field and let the index a encode what type of theory is being considered. Most of the expressions that depend on the form of the action will be given for the relativistic case. However, the corresponding nonrelativistic expressions can be straightforwardly obtained by simple substitutions which will be specified further below. Throughout this thesis we use natural units with $\hbar = 1$.

2.1.1 Relativistic

On the relativistic side, we consider an $O(N)$ -symmetric theory for an N -component real scalar field $\varphi_a(x) \equiv \varphi_a(x_0, \mathbf{x})$, where $a \in \{1, \dots, N\}$, in d spatial dimensions and with classical action given by

$$S[\varphi] = \int_{x, \mathcal{C}} \left[\frac{1}{2} \partial^\mu \varphi_a(x) \partial_\mu \varphi_a(x) - \frac{m^2}{2} \varphi_a(x) \varphi_a(x) - \frac{\lambda}{4!N} (\varphi_a(x) \varphi_a(x))^2 \right]. \quad (2.1)$$

Here, $\int_{x, \mathcal{C}} \equiv \int_{-\infty}^{\infty} d^d \mathbf{x} \int_{\mathcal{C}} dx_0$ and the time contour \mathcal{C} will be introduced in the next section (see Fig. (2.1)). Minimizing the action as $\delta S / \delta \varphi = 0$, one obtains the classical equation of motion

$$\left(\partial^\mu \partial_\mu + m^2 + \frac{\lambda}{6N} \varphi_c(x) \varphi_c(x) \right) \varphi_a(x) = 0. \quad (2.2)$$

In quantum field theory one upgrades the classical field $\varphi_a(x)$ to an operator $\hat{\varphi}_a(x)$. The latter fulfils the equal-time commutation relations

$$[\hat{\varphi}_a(t, \mathbf{x}), \hat{\pi}_b(t, \mathbf{y})] = i \delta_{ab} \delta(\mathbf{x} - \mathbf{y}), \quad (2.3)$$

where we introduced the conjugate momentum operator $\hat{\pi}_a(x)$, which is the operator corresponding to the momentum field $\pi_a(x) = \partial_{x_0} \varphi_a(x)$.

2.1.2 Nonrelativistic

The fundamental field in the nonrelativistic theory is complex and we denote it by $\psi_\alpha(x)$ where $\alpha \in \{1, \dots, N\}$. We separate it into its real and imaginary parts as $\psi_\alpha = (\varphi_{1,\alpha} + i \varphi_{2,\alpha}) / \sqrt{2}$ and write the two indices compactly as $a = (i_a, \alpha)$ with $i_a \in \{1, 2\}$. This notation helps connecting the relativistic and nonrelativistic expressions. We consider a $U(N)$ -symmetric theory with classical action given by

$$S[\varphi] = \int_{x, \mathcal{C}} \left\{ \frac{1}{2} \varphi_a(x) \left[-i \sigma_{ab}^2 \partial_{x_0} + \delta_{ab} \frac{\nabla^2}{2m} \right] \varphi_b(x) - \frac{g}{8N} (\varphi_a(x) \varphi_a(x))^2 \right\}, \quad (2.4)$$

where $\sigma_{ab}^2 = \delta_{\alpha\beta} \sigma_{i_a i_b}^y$ and $\sigma^y = \begin{pmatrix} 0 & -i \\ i & 0 \end{pmatrix}$ is the second Pauli matrix. Note that summation over a indices implies summation over both i_a and α . The classical equation of motion for this action reads

$$i \sigma_{ab}^2 \partial_{x_0} \varphi_b(x) = \left[\frac{\nabla^2}{2m} - \frac{g}{2N} \varphi_b(x) \varphi_b(x) \right] \varphi_a(x), \quad (2.5)$$

which for $N = 1$ becomes the well-known Gross-Pitaevskii equation (GPE)

$$i \partial_{x_0} \psi(x) = \left[-\frac{\nabla^2}{2m} + g |\psi(x)|^2 \right] \psi(x). \quad (2.6)$$

In order to promote the field variable $\psi_\alpha(x)$ to the operator $\hat{\psi}_\alpha(x)$, one imposes the equal-time commutation relations $[\hat{\psi}_\alpha(t, \mathbf{x}), \hat{\psi}_\beta^\dagger(t, \mathbf{y})] = \delta_{\alpha\beta} \delta(\mathbf{x} - \mathbf{y})$. In terms of the real and imaginary

parts this becomes

$$[\hat{\varphi}_a(t, \mathbf{x}), \hat{\varphi}_b(t, \mathbf{y})] = -\sigma_{ab}^2 \delta(\mathbf{x} - \mathbf{y}). \quad (2.7)$$

2.2 Functional Integral Description

The main difference in the treatment of nonequilibrium quantum field theory with path integral methods as compared to vacuum or thermal field theory is the fact that the time variable t lives on a closed time contour \mathcal{C} called the *Schwinger-Keldysh* contour [116, 117]. The contour $\mathcal{C} = \mathcal{C}^+ \cup \mathcal{C}^-$ is divided into a forward branch (\mathcal{C}^+) running from the initial time t_0 all the way up to $t \rightarrow +\infty$ and a backward branch (\mathcal{C}^-) doing the inverse path from $+\infty$ to t_0 , as depicted in Fig. 2.1.

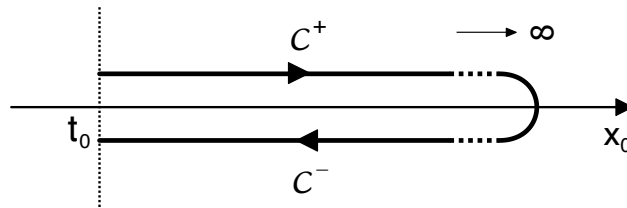


FIGURE 2.1: Closed time contour \mathcal{C} .

To understand the origin of such a closed time contour it is useful to consider for a moment a quantum system with density matrix ρ_0 at time $t = t_0$ and Hamiltonian H [111]. The time evolution of such a system is determined by the time evolution operator $U(t, t_0)$, which for a time-independent Hamiltonian is given by $e^{-iH(t-t_0)}$. In the Heisenberg picture and assuming $\text{Tr} \rho_0 = 1$, the expectation value of an observable $O(t)$ is given by

$$\langle O(t) \rangle = \text{Tr} \{ \rho_0 U(t_0, t) O U(t, t_0) \}. \quad (2.8)$$

Reading from the right to the left, one first evolves from t_0 to t , acts with O , and then evolves back from t to t_0 to project onto ρ_0 before taking the trace. In other words, we see here that dynamical evolution in a quantum system generally involves going forward and backwards in time.

2.2.1 Generating functional on a closed time contour

The main objective of this chapter is to derive equations of motion for correlation functions. For this it is useful to start with a generating functional for correlation functions, analogous to statistical as well as vacuum and thermal field theory. The first step is to rewrite the identity $Z \equiv \text{Tr} \{ \rho_0 U(t_0, t) U(t, t_0) \} = 1$ as a path integral. This is best accomplished using coherent states $|\varphi\rangle$, which are eigenstates of the Heisenberg operator $\hat{\varphi}(x)$, i.e. $\hat{\varphi}(x)|\varphi\rangle = \varphi(x)|\varphi\rangle$. The standard procedure involves dividing the time interval in infinitesimally small slices and inserting a complete set of coherent states inbetween each two slices. However, as anticipated above, a forward and a backward branch appear due to $U(t, t_0)$ and $U(t_0, t)$. To distinguish

which branch a given coherent state belongs to we write $\varphi(x) = \varphi^\pm(x)$ if $x_0 \in \mathcal{C}^\pm$. Letting $t \rightarrow \infty$ this leads to [70, 111, 114]

$$Z = \int \mathcal{D}\varphi_0^+ \mathcal{D}\varphi_0^- \langle \varphi_0^+ | \rho_0 | \varphi_0^- \rangle \int_{\varphi_0^-}^{\varphi_0^+} \mathcal{D}'\varphi e^{iS[\varphi]}, \quad (2.9)$$

where the integral measure $\mathcal{D}'\varphi$ includes all field configurations with $x_0 > t_0$ and has the boundary condition $\varphi^\pm(x_0 = t_0, \mathbf{x}) = \varphi_0^\pm(\mathbf{x})$.

Although the above expression seems at first like a cumbersome rewriting of the identity, adding sources to it allows us to generalize it to a generating functional of correlation functions. Specifically, we introduce linear $J_a(x)$ and quadratic sources $R_{ab}(x, y)$, where $x_0, y_0 \in \mathcal{C}$, and define the generating functional as [70]

$$Z[J, R; \rho_0] = \int \mathcal{D}\varphi_0^+ \mathcal{D}\varphi_0^- \langle \varphi_0^+ | \rho_0 | \varphi_0^- \rangle \int_{\varphi_0^-}^{\varphi_0^+} \mathcal{D}'\varphi e^{i\left(S[\varphi] + \int_{x, \mathcal{C}} J_a(x) \varphi_a(x) + \frac{1}{2} \int_{x, y, \mathcal{C}} \varphi_a(x) R_{ab}(x, y) \varphi_b(y)\right)}. \quad (2.10)$$

Taking derivatives with respect to the sources generates correlation functions as

$$\left. \frac{\delta^n Z}{\delta J_{a_1}(x_1) \dots \delta J_{a_n}(x_n)} \right|_{J, R=0} = \langle \mathcal{T}_{\mathcal{C}} \hat{\varphi}_{a_1}(x_1) \dots \hat{\varphi}_{a_n}(x_n) \rangle, \quad (2.11)$$

where the contour time ordering operator $\mathcal{T}_{\mathcal{C}}$ orders the field operators from right to left in increasing order of appearance of the time variables along the contour \mathcal{C} (see Fig. 2.1).

In the following we will focus on Gaussian initial states $\rho_0^{(\text{Gauss})}$. These are states that are fully determined by one- and two-point correlation functions. Because of this, the term $\langle \varphi_0^+ | \rho_0 | \varphi_0^- \rangle$ appearing in the generating functional can be absorbed into a redefinition of the sources J and R , i.e.

$$Z \left[J, R, \rho_0^{(\text{Gauss})} \right] \longrightarrow Z[J, R]. \quad (2.12)$$

2.2.2 Nonequilibrium Green's Functions

The whole information about the quantum many-body theory is contained in the correlation functions. In particular, low-order correlation functions are usually connected to common observables which can be experimentally accessed. For our purposes, we define the one-point function and the two-point connected Greens function as

$$\phi_a(x) \equiv \langle \hat{\varphi}_a(x) \rangle, \quad (2.13)$$

$$\begin{aligned} G_{ab}(x, y) &\equiv \langle \mathcal{T}_{\mathcal{C}} \hat{\varphi}_a(x) \hat{\varphi}_b(y) \rangle - \phi_a(x) \phi_b(y) \\ &\equiv \langle \mathcal{T}_{\mathcal{C}} \hat{\varphi}_a(x) \hat{\varphi}_b(y) \rangle_c. \end{aligned} \quad (2.14)$$

These quantities are also known as the *macroscopic field* and the (connected) *propagator*, respectively. In the context of nonequilibrium quantum field theory, it is useful to define as

well

$$F_{ab}(x, y) = \frac{1}{2} \langle \{\hat{\varphi}_a(x), \hat{\varphi}_b(y)\} \rangle_c, \quad (2.15)$$

$$\rho_{ab}(x, y) = i \langle [\hat{\varphi}_a(x), \hat{\varphi}_b(y)] \rangle. \quad (2.16)$$

The function $F_{ab}(x, y)$ is called the *statistical two-point function* and contains information about the average occupancy of energy modes, whereas $\rho_{ab}(x, y)$ is known as the *spectral function* and is related to the availability of energy modes and the dispersion relation. These two functions are related to the propagator G via

$$G_{ab}(x, y) = F_{ab}(x, y) - \frac{i}{2} \rho_{ab}(x, y) \operatorname{sgn}_{\mathcal{C}}(x_0 - y_0), \quad (2.17)$$

where $\operatorname{sgn}_{\mathcal{C}}(x_0 - y_0)$ is $+1$ (-1) if x_0 comes later (earlier) than y_0 along the contour \mathcal{C} .

Insight into the physics contained in the spectral and statistical functions is gained when considering them in thermal equilibrium. Assuming spatial homogeneity, F and ρ depend in this case only on the difference $x - y$ and are related to each other via the *fluctuation-dissipation theorem* [118]

$$F_{ab}^{(\text{eq})}(\omega, \mathbf{p}) = -i \left(\frac{1}{2} + f_{\text{BE}}(\omega) \right) \rho_{ab}^{(\text{eq})}(\omega, \mathbf{p}), \quad (2.18)$$

where $f_{\text{BE}}(\omega) = (e^{\beta\omega} - 1)^{-1}$ is the Bose-Einstein distribution. Here, the frequency ω and momentum \mathbf{p} are the Fourier conjugate variables to $x_0 - y_0$ and $\mathbf{x} - \mathbf{y}$, respectively. While out of equilibrium the fluctuation-dissipation theorem generally does not hold, its form will later be useful to define appropriate nonequilibrium particle distribution functions.

2.3 2PI effective action

Given the generating functional $Z[J, R]$ one may seek to make approximations by expanding the exponential around the free Gaussian solution in powers of the coupling. This is, however, notoriously inefficient due to the large number of Feynman diagrams needed to obtain reasonable results. Furthermore, such perturbative approaches usually lead to secular behavior in time. A more efficient way of doing this is by recasting and reorganizing the series expansion into more compact expressions that avoid a considerable amount of redundancies.

The use of *two-particle-irreducible* (2PI) effective actions [119–121] simplifies this procedure considerably and allows for a self-consistent treatment of initial-value problems. For this one defines first the *generating functional of connected correlation functions* $W[J, R]$ via

$$\begin{aligned} Z[J, R] &\equiv \exp(iW[J, R]) \\ &= \int \mathcal{D}\varphi \exp \left\{ i \left[S[\varphi] + \int_{x, \mathcal{C}} J_a(x) \varphi_a(x) + \frac{1}{2} \int_{xy, \mathcal{C}} \varphi_a(x) R_{ab}(x, y) \varphi_b(y) \right] \right\}. \end{aligned} \quad (2.19)$$

Taking derivatives with respect to the sources yields

$$\frac{\delta W[J, R]}{\delta J_a(x)} \equiv \phi_a(x), \quad (2.20)$$

$$\frac{\delta W[J, R]}{\delta R_{ab}(x, y)} \equiv \frac{1}{2} (\phi_a(x)\phi_b(y) + G_{ab}(x, y)), \quad (2.21)$$

where ϕ and G depend in principle on J and R unless the sources are explicitly set to zero. The 2PI effective action is the double Legendre transform of $W[J, R]$ with respect to the source fields:

$$\begin{aligned} \Gamma[\phi, G] &= \Gamma[\phi] - \frac{1}{2} \int_{xy, \mathcal{C}} [\phi_a(x)\phi_b(y) + G_{ab}(x, y)] R_{ab}(x, y) \\ &= W[J, R] - \int_{x, \mathcal{C}} \phi_a(x) J_a(x) - \frac{1}{2} \int_{xy, \mathcal{C}} [\phi_a(x)\phi_b(y) + G_{ab}(x, y)] R_{ab}(x, y). \end{aligned} \quad (2.22)$$

Here, $\Gamma[\phi]$ denotes the usual *one-particle-irreducible* (1PI) effective action [115], which is a Legendre transform of $W[J, R=0]$ with respect to J only. Taking derivatives of $\Gamma[\phi, G]$ yields the following equations of motion for the one- and two-point functions

$$\frac{\delta \Gamma[\phi, G]}{\delta \phi_a(x)} = -J_a(x) - \int_{y, \mathcal{C}} R_{ab}(x, y) \phi_b(y), \quad (2.23)$$

$$\frac{\delta \Gamma[\phi, G]}{\delta G_{ab}(x, y)} = -\frac{1}{2} R_{ab}(x, y), \quad (2.24)$$

also known as stationarity conditions. Higher order derivatives with respect to ϕ and G yield higher-order correlation functions, which will not be considered in this work. A very useful decomposition of the 2PI effective action is to separate the contributions coming from the classical action and the one-loop correction from the rest as [121]

$$\Gamma[\phi, G] = S[\phi] + \frac{i}{2} \text{Tr}_{\mathcal{C}} \ln G^{-1} + \frac{i}{2} \text{Tr}_{\mathcal{C}} G_0^{-1}(\phi) G + \Gamma_2[\phi, G] + \text{const}, \quad (2.25)$$

where $iG_{0,ab}^{-1}(x, y; \phi) = \delta S[\phi] / \delta \phi_a(x) \delta \phi_b(y)$ is the classical inverse propagator. The rest functional $\Gamma_2[\phi, G]$ contains the sum over all 2PI diagrams, where each line represents a full propagator G and the remaining rules for computing these diagrams will be given in Sec. 2.3.2. The nature of Γ_2 reveals the power of the 2PI effective action: it allows to make self-consistent approximations in terms of the full ϕ and G and one only needs to consider diagrams that are two-particle irreducible.

Inserting the above decomposition into the stationarity condition (2.24) one obtains

$$G_{ab}^{-1}(x, y) = G_{0,ab}^{-1}(x, y; \phi) - iR_{ab}(x, y) - \Sigma_{ab}(x, y; \phi, G), \quad (2.26)$$

where the self-energy Σ is defined as

$$\Sigma_{ab}(x, y; \phi, G) \equiv 2i \frac{\delta \Gamma_2[\phi, G]}{\delta G_{ab}(x, y)}. \quad (2.27)$$

This definition implies that the self-energy Σ is given by the sum of all 1PI diagrams with two external legs. This together with Eq. (2.26) further shows that the full propagator G

and hence each single diagram in the expansion of the 2PI effective action contains an infinite resummation of diagrams with lines associated to the free propagator G_0 .

2.3.1 2PI evolution equations

The equations of motion (2.26) and (2.23) for the propagator and macroscopic field can be rearranged into an equation of motion for F , ρ and ϕ using the decomposition (2.17). For this purpose, it is convenient to decompose the self-energy in a similar fashion as the propagator via

$$\Sigma_{ab}(x, y) = -i\Sigma_{ab}^{(0)}(x)\delta(x - y) + \Sigma_{ab}^F(x, y) - \frac{i}{2}\Sigma_{ab}^\rho(x, y) \operatorname{sgn}_c(x_0 - y_0), \quad (2.28)$$

where $\Sigma^{(0)}$ is a local contribution that leads to a shift of the effective mass. After some algebra one arrives at the 2PI equations of motion [70, 113]

$$\left[\mathcal{D}_{ab}(x) + M_{ab}^\phi(x) \right] \phi_b(x) = \frac{\delta\Gamma_2}{\delta\phi_a(x)}, \quad (2.29)$$

$$\left[\mathcal{D}_{ac}(x) + M_{ac}(x) \right] F_{cb}(x, y) = - \int_{t_0}^{x_0} dz \Sigma_{ac}^\rho(x, z) F_{cb}(z, y) + \int_{t_0}^{y_0} dz \Sigma_{ac}^F(x, z) \rho_{cb}(z, y), \quad (2.30)$$

$$\left[\mathcal{D}_{ac}(x) + M_{ac}(x) \right] \rho_{cb}(x, y) = - \int_{y_0}^{x_0} dz \Sigma_{ac}^\rho(x, z) \rho_{cb}(z, y), \quad (2.31)$$

where the differential operator matrix $\mathcal{D}_{ab}(x)$ and ‘mass’ functions $M_{ab}^\phi(x)$ and $M_{ab}(x)$ depend on the theory being considered. For the relativistic action of Eq. (2.1) these functions are given by

$$\begin{aligned} \mathcal{D}_{ab}^{(\text{rel})}(x) &= \square_x \delta_{ac}, \\ M_{ab}^{(\text{rel})}(x) &= \left(m^2 + \frac{\lambda}{6N} \phi_c(x) \phi_c(x) \right) \delta_{ab} + \frac{\lambda}{3N} \phi_a(x) \phi_b(x) + \Sigma_{ab}^{(0)}(x), \\ M_{ab}^{\phi(\text{rel})}(x) &= \left(m^2 + \frac{\lambda}{6N} [\phi_c(x) \phi_c(x) + F_{cc}(x, x)] \right) \delta_{ab} + \frac{\lambda}{3N} F_{ab}(x, x). \end{aligned} \quad (2.32)$$

For the nonrelativistic action of Eq. (2.4) they are

$$\begin{aligned} \mathcal{D}_{ab}^{(\text{nr})}(x) &= i\sigma_{ab}^2 \partial_{x_0} - \delta_{ab} \frac{\nabla^2}{2m}, \\ M_{ab}^{(\text{nr})}(x) &= \frac{g}{2N} \phi_c(x) \phi_c(x) \delta_{ab} + \frac{g}{N} \phi_a(x) \phi_b(x) + \Sigma_{ab}^{(0)}(x), \\ M_{ab}^{\phi(\text{nr})}(x) &= \frac{g}{2N} [\phi_c(x) \phi_c(x) + F_{cc}(x, x)] \delta_{ab} + \frac{g}{N} F_{ab}(x, x). \end{aligned} \quad (2.33)$$

2.3.2 Perturbative coupling expansion

The evolution equations for F , ρ and ϕ of the previous section have been derived without any approximations. In order to be useful though, approximations need to be made for the self-energy Σ or, in other words, for Γ_2 . The latter is the sum of all topologically distinct 2PI diagrams that can be constructed according to the following rules [70, 112]:

1. Vertices are obtained by shifting the classical action $S[\varphi] \rightarrow S[\varphi + \phi]$ and collecting all terms with more than 2 powers of the field φ . In this way, one obtains for the relativistic action (2.1)

$$S_{\text{int}}[\varphi, \phi] = -\frac{\lambda}{6N} \int_{x,\mathcal{C}} \phi_a(x) \varphi_a(x) \varphi_b(x) \varphi_b(x) - \frac{\lambda}{4!N} \int_{x,\mathcal{C}} (\varphi_a(x) \varphi_a(x))^2. \quad (2.34)$$

Diagrammatically we represent these vertices as

$$-i \frac{\lambda}{4!N} \int_{x,\mathcal{C}} \sim \begin{array}{c} \diagup \\ \diagdown \end{array} \begin{array}{c} x \\ x \end{array}, \quad (2.35)$$

$$-i \frac{\lambda}{6N} \int_{x,\mathcal{C}} \phi_a(x) \sim \begin{array}{c} \diagup \\ \diagdown \end{array} \begin{array}{c} \otimes \\ x, a \end{array}. \quad (2.36)$$

The corresponding nonrelativistic expressions are obtained by substituting $\lambda \rightarrow 3g$, as can be seen by comparing (2.1) to (2.4).

2. Given a number of vertices one connects them with lines in all possible different ways, making sure that that each diagram remains 2PI. Each line is then associated to a full propagator G .
3. An overall multiplicative factor of $-i/n!$, where n is the number of vertices, needs to be included for each diagram due to the expansion of the exponential and the definition of Γ_2 .

Depending on the system parameters and the initial conditions that are being considered, the physics will be dominated by the contribution of different diagrams. Assuming a small coupling, $\lambda \ll 1$ ($g \ll 1$), one may argue that diagrams with a large number of vertices will be suppressed by increasing powers of λ . Hence, the most important contributions will come from the diagrams with the lowest order in λ . Up to order $O(\lambda^2)$ these are given by

$$\Gamma_2^{O(\lambda)} = \begin{array}{c} \bigcirc \quad \bigcirc \end{array}, \quad (2.37)$$

$$\Gamma_2^{O(\lambda^2)} = \begin{array}{c} \bigcirc \\ \bigcirc \end{array} + \begin{array}{c} \otimes \\ \text{---} \end{array} \begin{array}{c} \bigcirc \\ \text{---} \end{array} \begin{array}{c} \otimes \end{array}. \quad (2.38)$$

Following the rules presented above, the contribution to linear order in the coupling can be written for the relativistic theory as

$$\Gamma_2^{O(\lambda)} = -i \left(\frac{-i\lambda}{4!N} \right) \int_{x,\mathcal{C}} [2 G_{ab}(x, x) G_{ab}(x, x) + G_{aa}(x, x) G_{bb}(x, x)] \quad (2.39)$$

This term contributes to the local part of the self-energy as

$$\Sigma_{ab}^{(0)}(x) = \frac{\lambda}{6N} [2 F_{ab}(x, x) + \delta_{ab} F_{aa}(x, x)]. \quad (2.40)$$

which leads to a shift of the ‘mass’ functions M and M^ϕ in the 2PI equations. The terms quadratic in the coupling contribute on the other hand to Σ^F and Σ^ρ .

Note that this coupling expansion is only valid if ϕ and G are of the order 1. This is, however, not the case in a number of relevant physical scenarios such as parametric resonance [122] or close to nonthermal fixed points [41], which will be studied in Chap. 3. In this case, the particle occupancies may become of the order of the inverse coupling and hence a proper power counting in λ requires to take this into account.

2.3.3 Nonperturbative $1/N$ expansion

The $1/N$ expansion uses the number of field components N as an expansion parameter instead of the coupling [107, 108]. At any given order in N , different orders in the coupling contribute and hence this constitutes a nonperturbative expansion. For the power counting each vertex contributes a factor of $1/N$, whereas each trace over field indices, such as $\text{Tr}(\phi\phi)$, $\text{Tr}(G^n)$ or $\text{Tr}(\phi\phi G^n)$, is proportional to N . The leading order (LO) term scales with N and each subsequent order scales with one power of N less. Assuming $\phi = 0$, the diagrams contributing up to next-to-leading order (NLO) are given by

$$\Gamma_2^{\text{LO}} = \begin{array}{c} \text{---} a \text{---} \\ \text{---} a \text{---} \end{array} \begin{array}{c} \text{---} b \text{---} \\ \text{---} b \text{---} \end{array}, \quad (2.41)$$

$$\Gamma_2^{\text{NLO}} = \begin{array}{c} \text{---} a \text{---} \\ \text{---} b \text{---} \end{array} \begin{array}{c} \text{---} b \text{---} \\ \text{---} a \text{---} \end{array} + \begin{array}{c} \text{---} \text{---} \\ \text{---} \text{---} \end{array} + \begin{array}{c} \text{---} \text{---} \\ \text{---} \text{---} \end{array} + \begin{array}{c} \text{---} \text{---} \\ \text{---} \text{---} \end{array} + \dots, \quad (2.42)$$

where the indices of the NLO diagrams without labels need to be combined such that each diagram scales as N^0 . Remarkably, the infinite series of diagrams contributing to NLO can be resummed into a compact form. The contribution to the local self-energy $\Sigma^{(0)}$ is the same as in Eq. (2.40), while the rest of the self-energy to NLO in the $1/N$ expansion is given by

$$\Sigma_{ab}^F(x) = -\frac{\lambda}{3N} \left(F_{ab}(x, y) I^F(x, y) - \frac{1}{4} \rho_{ab}(x, y) I^\rho(x, y) \right), \quad (2.43)$$

$$\Sigma_{ab}^\rho(x) = -\frac{\lambda}{3N} \left(F_{ab}(x, y) I^\rho(x, y) + \rho_{ab}(x, y) I^F(x, y) \right), \quad (2.44)$$

where

$$I^F(x, y) = \Pi^F(x, y) - \int_{t_0}^{x_0} dz I^\rho(x, z) \Pi^F(z, y) + \int_{t_0}^{y_0} dz I^F(x, z) \Pi^\rho(z, y), \quad (2.45)$$

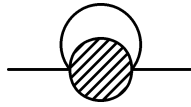
$$I^\rho(x, y) = \Pi^\rho(x, y) - \int_{y_0}^{x_0} dz I^\rho(x, z) \Pi^\rho(z, y) \quad (2.46)$$

and

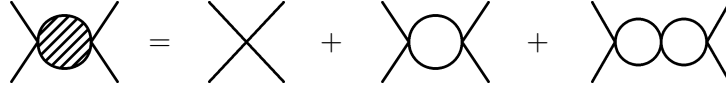
$$\Pi^F(x, y) = \frac{\lambda}{6N} \left(F_{ab}(x, y) F_{ab}(x, y) - \frac{1}{4} \rho_{ab}(x, y) \rho_{ab}(x, y) \right), \quad (2.47)$$

$$\Pi^\rho(x, y) = \frac{\lambda}{3N} F_{ab}(x, y) \rho_{ab}(x, y). \quad (2.48)$$

Again, substituting $\lambda \rightarrow 3g$ yields the nonrelativistic expressions. Diagrammatically, the resummation of diagrams at NLO can be rewritten as

$$\Sigma_{NLO}^{(\phi=0)} \sim \text{diagram} \quad , \quad (2.49)$$


where the shaded circle is defined as

$$\text{diagram} = \text{diagram} + \text{diagram} + \text{diagram} + \dots \quad (2.50)$$


In Chap. 3 we will see that this resummed vertex can indeed be interpreted as an effective 4-point interaction modified by nonlinear effects present at NLO. For nonvanishing macroscopic field ϕ an analogous resummation can be carried out. This case is, however, beyond the scope of this work.

2.4 Transport equations

The nonequilibrium dynamics of a quantum system starting from a given initial state is often characterized by rapid changes in the early stages and a slower time evolution at intermediate and long times. Due to the slow dynamics in the later phases of the evolution, approximations based on a low-order expansion in spatial-time derivatives can be used to derive effective dynamic equations for slowly varying observables. We will in particular be later interested in describing the dynamics of particle distribution functions, which are related to *equal-time* correlators. Using a gradient expansion we derive in the following a set of equations [113, 123] that will set the basis for a kinetic description of such distribution functions and their transport properties.

We start by introducing the Wigner coordinates

$$X^\mu \equiv \frac{x^\mu + y^\mu}{2}, \quad (2.51)$$

$$s^\mu \equiv x^\mu - y^\mu, \quad (2.52)$$

known as the center and relative coordinates, respectively. We further define Fourier transforms with respect to the relative variable as

$$F_{ab}(X, p) = \int_{-2X_0}^{2X_0} ds_0 e^{ip_0 s_0} \int_{-\infty}^{\infty} d^d s e^{-i\mathbf{p}\mathbf{s}} F_{ab} \left(X + \frac{\mathbf{s}}{2}, X - \frac{\mathbf{s}}{2} \right), \quad (2.53)$$

$$\tilde{\rho}_{ab}(X, p) = -i \int_{-2X_0}^{2X_0} ds_0 e^{ip_0 s_0} \int_{-\infty}^{\infty} d^d s e^{-i\mathbf{p}\mathbf{s}} \rho_{ab} \left(X + \frac{\mathbf{s}}{2}, X - \frac{\mathbf{s}}{2} \right), \quad (2.54)$$

and equivalently for the self-energies Σ^F and $\tilde{\Sigma}^\rho = -i\Sigma^\rho$. In the following, we set $\phi = 0$ and assume spatial homogeneity, i.e. functions will be independent of the variable \mathbf{X} . Furthermore, we assume to be in a late stage of the evolution such that we can approximate $t_0 \rightarrow -\infty$ and extend the integration boundaries of the Fourier integrals above to infinity ($X_0 \rightarrow \infty$).

To derive an effective equation for the statistical function F , we first subtract Eq. (2.30) from the same equation with the substitution $x \leftrightarrow y$. Following that we take the trace over the field indices and Fourier transform both sides. Expanding the resulting expressions in powers

of derivatives and neglecting $O(\partial_{X^\mu}\partial_{p_\mu})$ we obtain

$$2p_0 \frac{\partial}{\partial t} \text{Tr}[F(t, p)] = \text{Tr} \left[\tilde{\Sigma}_\rho(t, p) F(t, p) - \Sigma_F(t, p) \tilde{\rho}(t, p) \right] \quad (\text{relativistic}), \quad (2.55)$$

$$\frac{\partial}{\partial t} \text{Tr}[\sigma^2 F(t, p)] = - \text{Tr} \left[\tilde{\Sigma}_\rho(t, p) F(t, p) - \Sigma_F(t, p) \tilde{\rho}(t, p) \right] \quad (\text{nonrelativistic}), \quad (2.56)$$

where we relabelled $X_0 \equiv t$. This expansion is justified assuming the evolution is sufficiently slow. The right hand sides of these equations have already the gain minus loss structure of a kinetic equation. In Chap. 3 we will indeed transform them into kinetic equations with the help of a suitable definition for a particle number distribution and some additional manipulations. Following the same procedure with the equation for the spectral function, Eq. (2.31), yields

$$2p_0 \frac{\partial}{\partial t} \text{Tr}[\tilde{\rho}(t, p)] = 0 \quad (\text{relativistic}), \quad (2.57)$$

$$\frac{\partial}{\partial t} \text{Tr}[\sigma^2 \tilde{\rho}(t, p)] = 0 \quad (\text{nonrelativistic}). \quad (2.58)$$

Remarkably, the spectral function turns out to be time-independent to this order of approximation.

The gradient expansion can also be used to invert the implicit equations for the resummation functions I^F and I^ρ of the $1/N$ expansion of Sec. 2.3.3. For this we first Fourier transform Eq. (2.46) and employ a gradient expansion to lowest order yielding

$$I^R(t, p) = \frac{\Pi^R(t, p)}{1 + \Pi^R(t, p)}, \quad (2.59)$$

where we introduced retarded and advanced quantities as $I^R(x, y) = \Theta(x^0 - y^0)I^\rho(x, y)$, $I^A = -\Theta(y^0 - x^0)I^\rho(x, y)$ and similar for Π^R and Π^A . Using $I^\rho = I^R - I^A$ and proceeding in the same way with (2.45), one obtains

$$I^F(t, p) = v_{\text{eff}}(t, p) \Pi^F(t, p), \quad (2.60)$$

$$I^\rho(t, p) = v_{\text{eff}}(t, p) \Pi^\rho(t, p), \quad (2.61)$$

with the vertex-resummed coupling

$$v_{\text{eff}}(t, p) = \frac{1}{|1 + \Pi^R(t, p)|^2}, \quad (2.62)$$

and the one-loop self-energy¹

$$\Pi^R(t, p) = \frac{\lambda}{3N} \int_q F_{ab}(t, q - p) G_{ba}^R(t, q). \quad (2.63)$$

These expressions will be useful in the derivation of a kinetic equation in Chap. 3.

¹These expressions are also valid for the nonrelativistic theory with the substitution $\lambda \rightarrow 3g$.

2.5 Classical Statistical or Truncated Wigner Approximation

Quantum theory is generally expected to be well-described by a corresponding classical (statistical) theory whenever the macroscopic field becomes large and coherent or energy modes are highly occupied. In such cases, the full quantum dynamics captured by the generating functional (2.19) and the evolution equations (2.29)-(2.31) can be mapped onto a classical statistical field theory. In this framework, the classical field evolves according to the classical equation of motion and observables are obtained by averaging functions of this field over an ensemble of initial conditions. This approximation constitutes an immense reduction in complexity as compared to the full many-body quantum problem and has been applied and investigated in a wide range of fields from cosmology [95, 96], quantum field theory [97, 99] and heavy-ion collisions [124–127] to quantum optics and ultracold quantum gases [100, 101].

We present here first a derivation of the classical statistical approximation starting from the full generating functional introduced above and discuss its range of validity [70]. Following that we give an alternative derivation based on the so-called Wigner representation of quantum dynamics [100, 128–130], where the classical statistical approximation is known instead as the Truncated Wigner Approximation (TWA). This language will allow us to study next-order quantum corrections to this approximation in a systematic way in Chs. 7 and 8. For clarity, we consider throughout this section the relativistic action (2.1) and refer to the literature for the nonrelativistic case [95], whose derivation follows along similar lines.

The classical statistical or Truncated Wigner approximation occupies a central position in this work, both as a tool for the description of various quantum systems and as a basis for the study of improved approximation methods.

2.5.1 Path integral for classical-statistical theory

The time integral $\int_{x,\mathcal{C}}$ over the closed contour \mathcal{C} appearing in (2.1) can be split into two integrals $\int_x \equiv \int_{t_0}^{\infty} dt \int_{-\infty}^{\infty} d^d x$ making use of the φ^{\pm} notation as

$$\begin{aligned} S[\varphi] &\equiv \int_{x,\mathcal{C}} \mathcal{L}[\varphi] = \int_x (\mathcal{L}[\varphi^+] - \mathcal{L}[\varphi^-]) \\ &\equiv S[\varphi^+, \varphi^-]. \end{aligned} \tag{2.64}$$

Analogous to the previous section we apply a Wigner rotation to the field variables and define center and relative variables as

$$\begin{pmatrix} \varphi \\ \tilde{\varphi} \end{pmatrix} \equiv \underbrace{\begin{pmatrix} 1/2 & 1/2 \\ 1 & -1 \end{pmatrix}}_{\equiv A} \begin{pmatrix} \varphi^+ \\ \varphi^- \end{pmatrix}. \tag{2.65}$$

Analogously, we define the rotated linear sources

$$\begin{pmatrix} J \\ \tilde{J} \end{pmatrix} \equiv A \begin{pmatrix} J^+ \\ J^- \end{pmatrix}, \tag{2.66}$$

and set in the following the quadratic sources R to zero. In terms of the rotated variables, the generating functional (2.19) becomes

$$Z[J, \tilde{J}; \rho_0] = \int \mathcal{D}\varphi_0 \mathcal{D}\tilde{\varphi}_0 \left\langle \varphi_0 + \frac{\tilde{\varphi}_0}{2} \middle| \rho_0 \middle| \varphi_0 - \frac{\tilde{\varphi}_0}{2} \right\rangle \times \int_{\varphi_0, \tilde{\varphi}_0} \mathcal{D}'\varphi \mathcal{D}'\tilde{\varphi} \exp \left\{ iS[\varphi, \tilde{\varphi}] + i \int_x \left(\varphi_a(x) \tilde{J}_a(x) + \tilde{\varphi}_a(x) J_a(x) \right) \right\}. \quad (2.67)$$

It is instructive to see how the rotated variables as well as derivatives of Z with respect to the rotated sources relate to the correlation functions introduced earlier in this chapter. For instance, the two-point correlators are given by

$$F_{ab}(x, y) = \langle \varphi_a(x) \varphi_b(y) \rangle - \langle \varphi_a(x) \rangle \langle \varphi_b(y) \rangle = \frac{\delta^2 iW}{\delta i \tilde{J}_a(x) \delta i \tilde{J}_b(y)} \quad (2.68)$$

$$-iG_{ab}^R(x, y) = \langle \varphi_a(x) \tilde{\varphi}_b(y) \rangle = \frac{\delta^2 iW}{\delta i \tilde{J}_a(x) \delta i J_b(y)} \quad (2.69)$$

$$-iG_{ab}^A(x, y) = \langle \tilde{\varphi}_a(x) \varphi_b(y) \rangle = \frac{\delta^2 iW}{\delta i J_a(x) \delta i \tilde{J}_b(y)} \quad (2.70)$$

where the retarded and advanced propagators are defined as $G_{ab}^R(x, y) \equiv \theta(x_0 - y_0) \rho_{ab}(x, y)$ and $G_{ab}^A(x, y) \equiv -\theta(y_0 - x_0) \rho_{ab}(x, y)$, i.e. $\rho = G^R - G^A$. Note that the correlator $\langle \tilde{\varphi} \tilde{\varphi} \rangle$ is zero for vanishing sources.

The action $S[\varphi, \tilde{\varphi}]$ appearing in (2.67) results from inserting the definition (2.65) into $S[\varphi^+, \varphi^-]$. It is useful to split it into

$$S[\varphi, \tilde{\varphi}] = S_{\text{cl}}[\varphi, \tilde{\varphi}] + S_{\text{q}}[\varphi, \tilde{\varphi}] - \int d^d x \pi_{0,a}(\mathbf{x}) \tilde{\varphi}_{0,a}(\mathbf{x}), \quad (2.71)$$

where $\pi_{0,a}(\mathbf{x}) \equiv \pi_a(t_0, \mathbf{x})$, $\tilde{\varphi}_{0,a}(\mathbf{x}) \equiv \tilde{\varphi}_a(t_0, \mathbf{x})$,

$$S_{\text{cl}}[\varphi, \tilde{\varphi}] = \int_x \tilde{\varphi}_a(x) \left[-(\partial^\mu \partial_\mu + m^2) \varphi_a(x) - \frac{\lambda}{6N} \varphi_a(x) \varphi_b(x) \varphi_b(x) \right], \quad (2.72)$$

$$S_{\text{q}}[\varphi, \tilde{\varphi}] = \int_x \frac{-\lambda}{24N} \tilde{\varphi}_a(x) \tilde{\varphi}_a(x) \tilde{\varphi}_b(x) \varphi_b(x), \quad (2.73)$$

and the boundary term in (2.71) arises from partial integrating the free part of the action. The classical statistical approximation consists in neglecting the contribution from the ‘quantum’ part S_{q} and keeping only the ‘classical’ part S_{cl} , which contains all terms that are linear in the field $\tilde{\varphi}$. Defining the (Wigner) distribution functional via

$$\left\langle \varphi_0 + \frac{\tilde{\varphi}_0}{2} \middle| \rho_0 \middle| \varphi_0 - \frac{\tilde{\varphi}_0}{2} \right\rangle = \int \mathcal{D}\pi_0 W[\varphi_0, \pi_0] e^{i \int d^d x \pi_{0,a}(\mathbf{x}) \tilde{\varphi}_{0,a}(\mathbf{x})} \quad (2.74)$$

and putting all pieces together, the generating functional Z_{cl} for the classical-statistical field theory reads

$$Z_{\text{cl}}[J, \tilde{J}; \rho_0] = \int \mathcal{D}\varphi_0 \mathcal{D}\pi_0 W[\varphi_0, \pi_0] \int_{\varphi_0, \pi_0} \mathcal{D}'\varphi \mathcal{D}'\tilde{\varphi} e^{iS_{\text{cl}}[\varphi, \tilde{\varphi}] + i \int_x (\varphi_a(x) \tilde{J}_a(x) + \tilde{\varphi}_a(x) J_a(x))}. \quad (2.75)$$

This expression can be further simplified by noting that the classical action S_{cl} is linear in $\tilde{\varphi}$ and can be written as $S_{\text{cl}}[\varphi, \tilde{\varphi}] = \int_x \tilde{\varphi}_a(x) \frac{\delta S_{\text{cl}}[\varphi, \tilde{\varphi}]}{\delta \tilde{\varphi}_a(x)}$. The integration over $\tilde{\varphi}$ hence yields a δ -function of the form

$$\int \mathcal{D}\tilde{\varphi} e^{iS_{\text{cl}}[\varphi, \tilde{\varphi}]} = \delta \left[\frac{S_{\text{cl}}[\varphi, \tilde{\varphi}]}{\delta \tilde{\varphi}_a(x)} \right] = \delta [\varphi - \varphi^{\text{cl}}] \underbrace{\mathcal{J}^{-1}[\varphi]}_{=1}, \quad (2.76)$$

where the Jacobi determinant is 1 due to the normalization of the generating functional and φ^{cl} is defined as the solution to the classical equation of motion $\delta S[\varphi, \tilde{\varphi}]/\delta \tilde{\varphi}_a(x) = 0$, i.e. Eq. (2.2), with initial conditions given by φ_0 and π_0 . Using this the classical-statistical expectation value $\langle \cdot \rangle_{\text{cl}}$ of a given function $O[\varphi, \pi]$ of the classical field can be written as

$$\langle O[\varphi, \pi] \rangle_{\text{cl}} = \int \mathcal{D}\varphi_0 \mathcal{D}\pi_0 W[\varphi_0, \pi_0] O \left[\varphi^{\text{cl}}(\varphi_0, \pi_0), \pi^{\text{cl}}(\varphi_0, \pi_0) \right]. \quad (2.77)$$

For Gaussian initial states such as those considered here the Wigner distribution W is positive definite. Hence, the classical average of O can be computed by first sampling initial conditions from the Wigner distribution, evolving each one with the classical equation of motion and finally averaging O over all realizations. Care needs to be taken with the correspondence between expectation values of classical observables and quantum operators. As we will again see in Sec. 2.5.3, products of the field variables φ and π correspond to symmetrically ordered operators such as the statistical function F in Eq. (2.68). The computation of non-symmetrically ordered operators such as the spectral function ρ is, however, more involved and will be further discussed in Chap. 5.

2.5.2 Classicity condition

It was foreshadowed at the beginning of this section that the classical statistical approximation should be valid in the presence of large mode occupancies or for large field amplitudes. To make this statement more precise we return to the action (2.71) written in terms of the Wigner rotated fields φ and $\tilde{\varphi}$. Introducing the diagrammatic notation

$$\varphi_a(x) : x, a \text{ ———— } , \quad \tilde{\varphi}_a(x) : x, a \text{ - - - - } . \quad (2.78)$$

the propagators of Eqs. (2.68)-(2.70) can be written as

$$F_{ab}(x, y) : x, a \text{ ———— } y, b \quad , \quad (2.79)$$

$$G_{ab}^R(x, y) : x, a \text{ — - - - } y, b \quad , \quad (2.80)$$

$$G_{ab}^A(x, y) : x, a \text{ - - - - } y, b \quad . \quad (2.81)$$

The action (2.71) contains a classical vertex $\sim \tilde{\varphi}\varphi^3$ and a quantum vertex $\sim \tilde{\varphi}^3\varphi$. Considering for simplicity the case with vanishing macroscopic field $\phi = 0$, these two vertices give rise in a 2PI action framework to

$$\text{classical: } \begin{array}{c} \diagup \\ \diagdown \\ \diagdown \\ \diagup \end{array} \begin{array}{c} x \\ x \end{array} , \quad \text{quantum: } \begin{array}{c} \diagdown \\ \diagup \\ \diagup \\ \diagdown \end{array} \begin{array}{c} x \\ x \end{array} . \quad (2.82)$$

Of all the diagrams produced by these two vertices, the classical statistical approximation only keeps those where all vertices are classical. Including quantum corrections to this approximation hence implies including diagrams where one or more of the classical vertices have been replaced by quantum ones. Since the quantum vertices contain more dashed $\tilde{\varphi}$ legs than the classical one, such diagrams will have comparably less F propagators, Eq. (2.79), and more ρ functions, Eqs. (2.80) and (2.81). This reasoning leads to a sufficient condition for the validity of the classical-statistical approximation given by [70]

$$F_{ab}(x, y) \gg \rho_{ab}(x, y), \quad \forall x, y. \quad (2.83)$$

In practice, however, this condition is not necessarily satisfied for all points, but for a range of times and momenta. In terms of a particle distribution function $f(t, \mathbf{p})$ this condition becomes

$$f(t, \mathbf{p}) \gg 1, \quad (2.84)$$

for the relevant time and momentum range. In the next chapter, we will see how such a quantity can be defined out of equilibrium using the form of the fluctuation-dissipation relation (2.18).

2.5.3 Wigner representation of quantum dynamics

The Wigner representation is an exact reformulation of quantum theory in terms of classical variables [100, 128–130]. To introduce it, it is convenient to switch to a Hamiltonian description in terms of field operators. For the relativistic theory, the Hamiltonian corresponding to the action (2.1) is given by

$$\hat{H}[\varphi, \pi] = \int d^d x \left[\frac{1}{2} \hat{\pi}_a(x) \hat{\pi}_a(x) + \frac{1}{2} \nabla \hat{\varphi}_a(x) \nabla \hat{\varphi}_a(x) + \frac{m^2}{2} \hat{\varphi}_a(x) \hat{\varphi}_a(x) + \frac{\lambda}{4!N} (\hat{\varphi}_a(x) \hat{\varphi}_a(x))^2 \right] \quad (2.85)$$

where $\hat{\pi}_a(x)$ is the momentum conjugate to $\hat{\varphi}_a(x)$. For later purposes, we work in the Heisenberg picture where the time dependence is in the operators (see [100] for a derivation based on the Schrödinger picture).

The mapping to classical fields takes place using a complete set of eigenstates, similarly to what is done in the derivation of path integrals. Let $|\varphi\rangle$ denote the eigenstate of the operator $\hat{\varphi}_a(t = t_0, \mathbf{x})$ with eigenvalue $\varphi_a(\mathbf{x})$. Each operator $\hat{O}(\hat{\varphi}, \hat{\pi})$ is then mapped onto a function of classical variables called *Weyl symbol* via

$$O_W(\varphi, \pi) = \int d\tilde{\varphi} \left\langle \varphi - \frac{\tilde{\varphi}}{2} \left| \hat{O}(\hat{\varphi}, \hat{\pi}) \right| \varphi + \frac{\tilde{\varphi}}{2} \right\rangle e^{i \int d^d x \pi_a(\mathbf{x}) \tilde{\varphi}_a(\mathbf{x})}, \quad (2.86)$$

where we use the shorthand notation $d\tilde{\varphi} \equiv \prod_{x,a} d\tilde{\varphi}_a(x)$. The Weyl symbol of the density matrix $\hat{\rho}$ is the *Wigner function*

$$W(\varphi, \pi) = \int d\tilde{\varphi} \left\langle \varphi - \frac{\tilde{\varphi}}{2} \left| \hat{\rho} \right| \varphi + \frac{\tilde{\varphi}}{2} \right\rangle e^{i \int d^d x \pi_a(\mathbf{x}) \tilde{\varphi}_a(\mathbf{x})}. \quad (2.87)$$

Comparison to Eq. (2.74) reveals that both definitions of W are equivalent and are connected by an inverse Fourier transform. The normalization of the density matrix, $\text{Tr} \hat{\rho} = 1$, implies

that

$$\int d\varphi d\pi W(\varphi, \pi) = 1, \quad (2.88)$$

where $d\pi \equiv \prod_{x,a} (d\pi_a(x)/2\pi)$. This means that whenever the Wigner function is positive definite, it can be viewed as a probability distribution, as is the case for gaussian initial states. In this framework, expectation values are obtained as

$$\langle \hat{O}(\hat{\varphi}, \hat{\pi}) \rangle = \int d\varphi d\pi W(\varphi, \pi) O_W(\varphi, \pi). \quad (2.89)$$

Although this expression already looks similar to the classical statistical approximation of Eq. (2.77), we emphasize that in (2.89) no approximation has been made yet. In fact, the mapping between operators and classical functions is one-to-one and can be reversed, i.e. no information about the quantum system has been lost.

An important property of the Wigner representation is that the Weyl symbol of totally symmetric products of operators taken at time $t = t_0$ can be obtained by simple substitution as $\hat{\varphi}_a(t_0, \mathbf{x}) \rightarrow \varphi_a(t_0, \mathbf{x})$, $\hat{\pi}_a(t_0, \mathbf{x}) \rightarrow \pi_a(t_0, \mathbf{x})$, i.e.

$$\left(\hat{O}_{\text{sym}}(\hat{\varphi}, \hat{\pi}) \right)_W = O_{\text{sym}}(\varphi, \pi). \quad (2.90)$$

For instance, one finds

$$\varphi_1 \pi_2 = \frac{1}{2} (\hat{\varphi}_1 \hat{\pi}_2 + \hat{\pi}_2 \hat{\varphi}_1)_W(\varphi, \pi), \quad (2.91)$$

$$\varphi_1 \pi_2 \pi_3 = \frac{1}{6} (2 \hat{\varphi}_1 \hat{\pi}_2 \hat{\pi}_3 + \hat{\pi}_2 \hat{\varphi}_1 \hat{\pi}_3 + \hat{\pi}_3 \hat{\varphi}_1 \hat{\pi}_2 + 2 \hat{\pi}_2 \hat{\pi}_3 \hat{\varphi}_1)_W(\varphi, \pi), \quad (2.92)$$

where we use the compact notation $\varphi_i \equiv \varphi_{a_i}(t_0, \mathbf{x}_i)$. Hence, according to Eq. (2.89), the statistical moments of the Wigner function give the expectation values of symmetrically ordered operators at initial time $t = t_0$.

The *Truncated Wigner Approximation* (TWA), or equivalently the classical statistical approximation, is made at the level of the dynamics. In order to obtain the time evolution of a given observable one needs to derive equations of motion for the Weyl symbols. This can be accomplished by first computing the Heisenberg equation of motion, $\partial_t \hat{O} = i[\hat{H}, \hat{O}]$, for the given operator and then taking the Weyl symbol $(\cdot)_W$ of both sides. This yields for the one-point Weyl symbol equations

$$\begin{aligned} \partial_t (\hat{\varphi}_a(x))_W &= (\hat{\pi}_a(x))_W, \\ \partial_t (\hat{\pi}_a(x))_W &= [\nabla^2 - m^2] (\hat{\varphi}_a(x))_W - \frac{\lambda}{6} (\hat{\varphi}_b(x) \hat{\varphi}_b(x) \hat{\varphi}_a(x))_W, \end{aligned} \quad (2.93)$$

which couple due to the interactions to the three-point Weyl symbol. The equation for the latter will couple the three-point symbol to yet higher orders and so forth. TWA consists in truncating this hierarchy by splitting all Weyl symbols of (symmetrically ordered) products of operators into products of the one-point Weyl symbols $(\hat{\varphi}_a(x))_W \equiv \varphi_a(x)$ and $(\hat{\pi}_a(x))_W \equiv \pi_a(x)$, e.g.

$$(\hat{\varphi}_b(x) \hat{\varphi}_b(x) \hat{\varphi}_a(x))_W \approx \varphi_b(x) \varphi_b(x) \varphi_a(x). \quad (2.94)$$

Inserting this into (2.93), the evolution of the *classical* fields $\varphi_a(x)$ and $\pi_a(x)$ is hence given by the classical equations of motion. The above splitting together with Eq. (2.90) further implies

that within TWA products of classical fields averaged over the Wigner function as in Eq. (2.89) correspond to expectation values of symmetrically ordered operators. This conclusively shows that

$$\langle \hat{O}_{\text{sym}}(\hat{\varphi}, \hat{\pi}) \rangle \stackrel{TWA}{\approx} \langle O_{\text{sym}}(\varphi, \pi) \rangle_{\text{cl}}, \quad (2.95)$$

where $\langle \cdot \rangle_{\text{cl}}$ is the classical-statistical approximation defined in Eq. (2.77).

Part I

Nonthermal Fixed Points

Chapter 3

Universal Self-similar Dynamics in Relativistic and Nonrelativistic Theories

This chapter is based on “*Universal self-similar dynamics of relativistic and nonrelativistic field theories near nonthermal fixed points*”, A. Piñeiro Orioli, K. Boguslavski and J. Berges, published in Phys. Rev. D **92**, 025041 (2015) [66]. Figures and parts of the text are taken from that reference. Part of the work is a continuation of the studies started in my Master Thesis “*Turbulence and self-similarity in strongly correlated scalar field theories*” (2014). In order to compare the results presented for nonrelativistic theories to their relativistic counterparts, we also give the relativistic simulation results obtained by Kirill Boguslavski [66], which are discussed in his PhD thesis “*Universality classes far from equilibrium: From heavy-ion collisions to superfluid Bose systems*” (2016).

The aim of the following three chapters (Chaps. 3, 4 and 5) is to study the far-from-equilibrium universal dynamics of isolated many-body quantum systems described by scalar field theories. The universality is related to the existence of nonthermal fixed points [41, 68, 69], which represent attractor solutions characterized by self-similar scaling behavior and transport of conserved quantities. Close to the nonthermal fixed point the dynamics is fully determined by a set of scaling functions and scaling exponents, whose values define new universality classes far from equilibrium.

The motivation for the study of universal behavior far from equilibrium comes from different fields, as mentioned in Chap. 1. For relativistic theories the interest is triggered by recent advances in our understanding of the dynamics in the early universe as well as in relativistic collision experiments with heavy ions. Experimentally, the investigation of quantum systems far from equilibrium is also boosted by the nonrelativistic physics of ultracold quantum gases. Using trapped atoms, molecules or ions, they provide a flexible testbed with tunable interactions, symmetries and dimensionality, to study the nonequilibrium dynamics of a variety of many-body quantum systems. In recent years, important new universality classes have been discovered in both isolated relativistic systems far from equilibrium [39–54] as well as for nonrelativistic Bose gases [55–62, 69].

In this chapter we explore the universal dynamics close to a nonthermal fixed point in the infrared regime of both relativistic and nonrelativistic scalar theories. Compared to previous studies [41, 55] which focused on stationary scaling properties of distribution functions, we study here self-similar dynamics of isolated systems, which involves a rescaling of time. We employ two nonperturbative methods. First, we use classical-statistical simulations to compute the scaling functions and exponents characterizing the self-similar dynamics and we demonstrate that both relativistic and nonrelativistic theories lie in the same universality class. Secondly, we derive a vertex-resummed kinetic theory based on a 2PI $1/N$ expansion to NLO and employ it to obtain analytical estimates for the scaling exponents. Furthermore, we demonstrate that the dynamics close to the nonthermal fixed point is deeply connected to the process of Bose condensation far from equilibrium.

3.1 Introduction

We begin with a detailed description of nonthermal fixed points and discuss its relation to other dynamical scaling phenomena. After that we present an overview of the results of this chapter.

3.1.1 Nonthermal fixed points

Nonequilibrium scaling phenomena are ubiquitous in physics. In the following, we try to understand the particular properties of nonthermal fixed points and their relation to similar scaling phenomena. For this we treat the nonthermal fixed point of the scalar field theories considered in this chapter as a paradigmatic example.

We consider the evolution of a *distribution function* $f(t, \mathbf{p})$ of particles with momentum \mathbf{p} at time t . In a free theory this quantity would be given by $f(t, \mathbf{p}) = \langle a_{\mathbf{p}}^\dagger(t) a_{\mathbf{p}}(t) \rangle$, where \hat{a} and \hat{a}^\dagger are the corresponding creation and annihilation operators. Using the same definition for an interacting theory, especially out of equilibrium, does not guarantee a straightforward interpretation in terms of (quasi)particles. In these cases, one may view $f(t, \mathbf{p})$ as a particular correlation function. However, the particle interpretation helps elucidate the relevant physics in terms of transport and we will ultimately show in Chap. 5 that this view can be correct even in a highly-occupied nonperturbative regime.

In order to observe dynamical scaling behavior related to the nonthermal fixed point, one generally needs to prepare a state with an extreme ‘overoccupation’ of certain modes at initial time. This will be further detailed in upcoming sections. For such extreme initial conditions, the system undergoes a quick redistribution of modes at early times, followed by slower scaling dynamics related to a nonthermal fixed point. The evolution of $f(t, \mathbf{p})$ near the nonthermal fixed point is strongly influenced by conserved quantities such as energy or particle number. Fig. 3.1 illustrates a typical distribution function $f(t, \mathbf{p})$ near a nonthermal fixed point as a function of momentum \mathbf{p} for two subsequent times $t = t_1$ and $t_2 > t_1$. One can distinguish different momentum ranges by their occupancies $f(t, \mathbf{p})$ in terms of a small (interaction or ‘diluteness’) parameter $\lambda \ll 1$ as will be explained below. In the highly-occupied low-momentum regime, where $f(t, \mathbf{p}) \gtrsim 1/\lambda$ [41], one finds an inverse particle cascade transporting particles

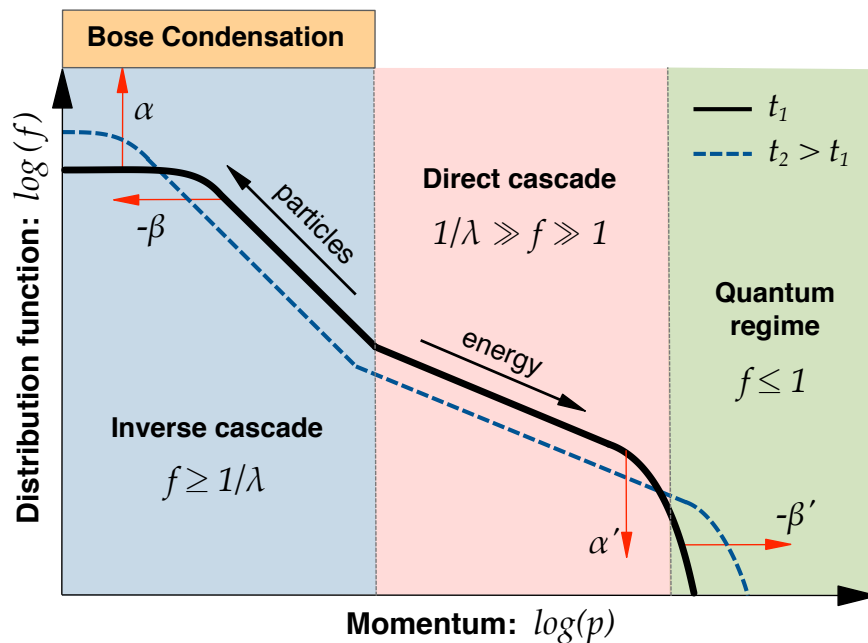


FIGURE 3.1: Schematic illustration of the occupation number distribution near a nonthermal fixed point, shown as a function of momentum p for two subsequent times t_1 and $t_2 > t_1$. The scaling exponents α and β characterize the self-similar evolution according to equation (3.1).

towards low momenta, which eventually leads to the formation of a Bose condensate out of equilibrium. This is part of a dual cascade, in which energy is also transferred by a direct energy cascade towards higher momenta ($1/\lambda \gg f(t, \mathbf{p}) \gg 1$). The latter evolves until a high-momentum scale is reached, where the characteristic mode occupancy becomes comparable to the ‘quantum-half’ ($f(t, \mathbf{p}) \leq 1$) [39].

The different cascades exhibit approximate power-law behavior for mode occupancies $f(t, \mathbf{p})$ in characteristic inertial ranges of momenta. However, in general, isolated systems out of equilibrium cannot realize stationary transport solutions in the absence of external driving forces. Instead, the transport in isolated systems is described in terms of the more general notion of a *self-similar* evolution, where the distribution function obeys for isotropic systems

$$f(t, \mathbf{p}) = t^\alpha f_S(\xi \equiv t^\beta |\mathbf{p}|) \quad (3.1)$$

in a given scaling regime. Here, all quantities are considered to be dimensionless by use of some suitable momentum scale, which is specified below. The values of the scaling exponents α and β , as well as the form of the nonthermal fixed point distribution $f_S(\xi)$ are universal. We emphasize, however, that the universal properties can be different for different inertial ranges. This is indicated in Fig. 3.1, where in the direct cascade regime other scaling exponents α' , β' and a different scaling function f'_S than in the infrared are found.

As we will see in Chaps. 4 and 5, the self-similar scaling behavior also extends to more general correlation functions, such as functions which depend on two times, e.g. the statistical function $F(t, t', \mathbf{p})$ and the spectral function $\rho(t, t', \mathbf{p})$. In this case, self-similarity implies rescaling of the time difference $\Delta t = t - t'$ and the center time $\tau = (t + t')/2$ with potentially different scaling

exponents. This introduces the *dynamical exponent* z and also the *anomalous dimension* η , whose values further specify the universality class.

According to the above exposition, nonthermal fixed points are hence primarily characterized by self-similar scaling in time, such as Eq. (3.1), and transport of conserved quantities. It is important to also note that the systems considered are isolated and far from equilibrium. Having this in mind, we compare now nonthermal fixed points to other well-known dynamical scaling phenomena.¹

An important example concerns the dynamical scaling behavior of systems close to second-order thermal phase transitions, which is captured by the theory of dynamical critical phenomena [133]. The corresponding scaling exponents and scaling functions can be grouped into universality classes based on the existence of renormalization-group thermal fixed points. Importantly though, this describes the behavior of systems *close* to equilibrium. Contrary to our case, this entails time-translation invariance and the validity of the fluctuation-dissipation relation (see Sec. 2.2.2).

While quenches to phase transitions can indeed still be characterized by the corresponding thermal universality classes, quenches across transitions usually can not. The latter are typically described in terms of the phenomenon of coarsening or phase-ordering kinetics [78, 132, 134]. It describes the growth of an order parameter after such a quench in terms of the kinematics of domains and topological defects, which grow, merge or decrease with time. The evolution of correlation functions is characterized by dynamical scaling and power laws. The corresponding scaling exponents and functions are determined by the structure of the order parameter and the topological defects. The formation of a Bose condensate (via the inverse particle cascade) in the nonthermal fixed point described above is reminiscent of this type of physics. Indeed, topological defects have also been found to provide, in some cases, an accurate picture of the dynamics close to the nonthermal fixed point [55, 56, 58]. However, further work has shown that the infrared scaling behavior close to the nonthermal fixed point is remarkably insensitive to the number of field components N and hence to the nature of the different topological obstructions associated with N [67].

Another closely related scaling phenomenon out of equilibrium is wave turbulence [76, 77]. One of its hallmarks is the transport of conserved quantities through momentum space via weakly interacting waves. The transport is triggered in this case by the presence of a source injecting, e.g., energy into the system and a sink dissipating it at a vastly different scale. The cascades emerging are usually characterized by stationary power laws within a range of momenta, similar to the approximate (non-stationary) ones exhibited in nonthermal fixed points. Although rarely discussed, the phenomenon can be generalized to the case without external sources or sinks², where the evolution is then described by the more general notion of self-similarity as in Eq. (3.1). Wave turbulence is usually described in terms of kinetic equations derived for weak nonlinearities. While in the regime of strong nonlinearities³ such descriptions are generally invalid, similar transport phenomena can occur and are termed strong turbulence.

¹Some important scaling phenomena out of equilibrium are consciously left out of the discussion. This includes absorbing phase transitions [131], and ageing [132], which shares an important number of features with coarsening.

²The transport occurs in this case because of a finite but large accumulation of energy at certain scales, which needs to be redistributed.

³That is, when kinetic and potential energy become of the same order.

In this case, however, the physics often involves other types of objects apart from waves, such as eddies, which are common in hydrodynamic turbulence [135]. Similarly, in the highly-occupied infrared scaling regime of the nonthermal fixed point of Fig. 3.1, nonlinearities are strong. Remarkably though, a kinetic description based on propagating quasiparticles seems to be possible in this regime by taking relevant vertex corrections into account (see Secs. 3.4 and 3.5, and Chap. 5).

Having said this, what makes nonthermal fixed points generally different from other dynamical scaling phenomena? A preliminary conclusion of the previous discussion is that the infrared scaling dynamics of the nonthermal fixed point considered here differs from other phenomena in at least two relevant ways. First, the universality class associated with it seems to encompass theories with different underlying topological structures [67] (different number of components N).⁴ This insensitivity renders descriptions based on coarsening of topological defects in some cases inaccurate. Secondly, there exists a description of the strongly nonlinear infrared regime in terms of vertex-resummed kinetic theory together with a quasiparticle interpretation. This is rather uncommon in wave-turbulence physics.

However, using these differences as a defining property of the term ‘nonthermal fixed point’ may restrict its future use to only those systems that have the special properties mentioned above. A possible solution to this could be to extend its meaning to refer to all kinds of universal dynamical scaling phenomena far from equilibrium in isolated system.⁵ In such a unified framework, specific physical processes such as turbulence and coarsening may be seen as (approximate) properties of particular systems or specific fixed points. Nonthermal fixed points would then be defined by the scaling behavior of correlation functions together with the existence of dynamically conserved quantities.

3.1.2 Outline of results

In the following sections we compute the exponents α , β and the scaling function f_S of the self-similar distribution (3.1) in the infrared regime. We present results for nonrelativistic (Gross-Pitaevskii) as well as (massless) relativistic scalar field theory with quartic self-interactions. While the relativistic theory captures important aspects of the Higgs sector of particle physics or of inflationary models for early universe dynamics, the Gross-Pitaevskii field theory is often used to describe dilute Bose gases.

A central conclusion of this chapter is that the infrared scaling exponents and scaling functions of these theories belong to the same universality class, i.e. the results for α , β and the universal form of the scaling function f_S in (3.1) agree. This is nontrivial, in particular, since the nonrelativistic system conserves total particle number whereas in the relativistic theory number-changing processes are possible. The agreement found in the infrared is also remarkable in view of the fact that in the inertial range of the direct energy cascade towards higher momenta the exponents α' , β' and the scaling function f'_S from the different theories do not agree [39, 40].

⁴Such a remarkable insensitivity to details of the underlying theory is also found for scalar and gauge theories in expanding geometries [12].

⁵Whether and in what sense the universality classes defined in this way change when the system is not closed is an intriguing open question.

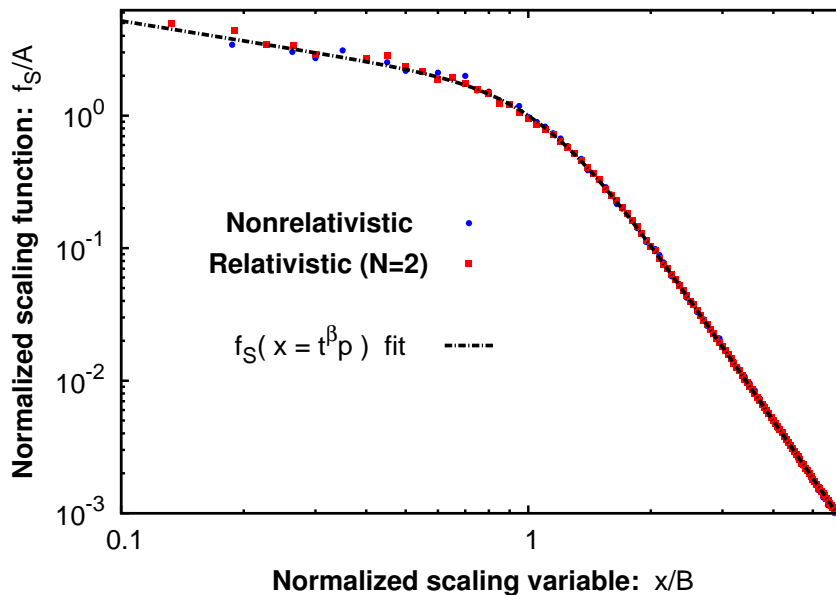


FIGURE 3.2: The scaling function $f_S(\xi \equiv t^\beta |\mathbf{p}|) = t^{-\alpha} f(t, \mathbf{p})$, normalized to the amplitudes A and B , exhibits accurate agreement between the nonrelativistic (circles) and relativistic (squares) simulation results.

Since the large occupancies at low momenta lead to strongly nonlinear dynamics, one cannot apply standard perturbative kinetic theory in the infrared. (Perturbative approaches [39, 40, 76] are often used to describe the direct energy cascade at higher momenta.⁶) We perform two independent nonperturbative calculations. The first approach employs classical-statistical lattice simulation techniques in Secs. 3.2 and 3.3 [43, 95]. The second, analytical method applies a vertex-resummed kinetic theory in Secs. 3.4 and 3.5, which is based on an expansion in the number of field components N to next-to-leading order [107, 108]. The approach extends well-established kinetic descriptions [40, 76, 77] to the nonperturbative regime of overoccupied modes.

This is used to obtain the analytic estimate for the scaling exponents of the

$$\text{particle transport: } \alpha = \beta d, \quad \beta = \frac{1}{2}, \quad (3.2)$$

towards low momenta, with spatial dimension d . This is a central analytic result of this work. In contrast to the previously known negative values for α and β from perturbative estimates [39, 40], the positive values obtained from the vertex-resummed kinetic theory describe an *inverse* particle transport with growing occupation number in the infrared. The fixed relation between α and β reflects the conservation of particle number density $n = \int d^d p / (2\pi)^d f(t, \mathbf{p}) \sim t^{\alpha-d\beta}$ in this (nonrelativistic) inertial range by using the self-similarity (3.1). Most notably, the emergence of an effectively conserved particle number plays a crucial role for the nonequilibrium evolution of the relativistic theory.

⁶Perturbative kinetic theory has also been employed in the infrared to describe Bose condensation at low momenta [136, 137]. However, it is known to neglect important vertex corrections in this case [41, 57] as is explained in Sec. 3.4.

The quantitative agreement of the NLO estimates of $\alpha = 3/2$ and $\beta = 1/2$ for $d = 3$ with the classical-statistical simulation results for the relativistic (Sec. 3.3.2) and for the nonrelativistic (section 3.2.2) theory is remarkable. Though we extend the analytic estimates to include a possible anomalous scaling in section 3.5, we find no strong indications for a nonvanishing anomalous dimension. Furthermore, we analyze the phenomenon of nonthermal Bose condensation from the inverse particle transport towards the zero mode. Most importantly, the dynamical generation of a mass gap m for the (massless) relativistic theory from an intriguing interplay of condensation and medium effects explains why the relativistic theory exhibits nonrelativistic physics at low momenta $|\mathbf{p}| \lesssim m$, as is shown in Sec. 3.3.

All models in the same universality class can be related by a multiplicative rescaling of t and \mathbf{p} . Quantities which are invariant under this rescaling are universal. Accordingly, all system-dependent aspects of the distribution are contained in two nonuniversal amplitudes, which we denote as A and B . It is convenient to define them according to $f_S(\xi = B) = A$ with $df_S(\xi = B)/d\xi = -2A/B$ such that A characterizes the amplitude of the scaling function at $\xi = B$, where the occupation number receives its dominant contribution.

The numerically computed fixed point distribution f_S of equation (3.1) is given in Fig. 3.2. Shown is the normalized distribution f_S/A as a function of the rescaled variable ξ/B , using the model specific amplitudes A and B as defined by $f_S(\xi = B) = A$ and $df_S(\xi = B)/d\xi = -2A/B$. For the relativistic theory, we show results for $N = 2$ field components in Fig. 3.2 but we consider also other values of N in Sec. 3.3. The lattice data for both nonrelativistic and relativistic theories turns out to be well described by the fit (dashed line)

$$f_S(\xi) \simeq \frac{A(\kappa_{>} - \kappa_{<})}{(\kappa_{>} - 2)(\xi/B)^{\kappa_{<}} + (2 - \kappa_{<})(\xi/B)^{\kappa_{>}}} \quad (3.3)$$

for $\xi > 0$ with approximately $\kappa_{<} \simeq 0.5$ and $\kappa_{>} \simeq 4.5$ for the available range of momenta and times. We note that the value for $\kappa_{>}$ is rather close to those obtained for stationary turbulence in nonrelativistic systems [69].⁷

3.2 Nonrelativistic Bose gas

We begin by studying the far from equilibrium dynamics of a one-component nonrelativistic Bose gas in three spatial dimensions. In the dilute regime, such a system can be described by the action given in Eq. (2.4) for $N = 1$. At the classical level, it is described by the Gross-Pitaevskii equation (c.f. Eq. (2.5))

$$i\partial_t\psi(t, \mathbf{x}) = \left(-\frac{\nabla^2}{2m} + g|\psi(t, \mathbf{x})|^2 \right) \psi(t, \mathbf{x}), \quad (3.4)$$

where ψ represents a complex field⁸. An important property of this equation is that the total number of particles, given by $N_{\text{total}} = \int d^3x |\psi(t, \mathbf{x})|^2$, is conserved. The coupling $g = 4\pi a/m$ is not dimensionless and is related to the mass m and the s-wave scattering length a . Using that

⁷We note that other works [67] have obtained a slightly different value for $\kappa_{<}$ closer to zero.

⁸Throughout this section we will employ the complex-field notation for the nonrelativistic theory, instead of the real-field notation used in Chap. 2. They are related by $\psi = \varphi_1 + i\varphi_2$.

for a gas of density n , the average interatomic distance is $n^{-1/3}$, one can define a dimensionless ‘diluteness parameter’

$$\zeta = \sqrt{na^3}. \quad (3.5)$$

For a typical scattering length of, e.g., $a \simeq 5 \text{ nm}$ and a bulk density of $n \simeq 10^{14} \text{ cm}^{-3}$ this diluteness parameter $\zeta \simeq 10^{-3}$ is rather small. Therefore, we will assume in the following that $\zeta \ll 1$. The density and scattering length can also be used to define a characteristic ‘coherence length’, whose inverse is described by the momentum scale

$$Q = \sqrt{16\pi an}. \quad (3.6)$$

3.2.1 Overoccupied initial conditions

To observe the dynamics near nonthermal fixed points for the interacting Bose gas, one needs to prepare an unusually large occupancy of modes at the momentum scale Q . Such nonequilibrium extreme conditions may be obtained, for instance, from a quench or nonequilibrium instabilities [55–61, 69]. Specifically, for a weakly coupled gas of average density $n = \int d^3p/(2\pi)^3 f(|\mathbf{p}|)$ this requires a large characteristic mode occupancy

$$f(Q) \sim \frac{1}{\zeta} \gg 1. \quad (3.7)$$

This represents an extreme nonequilibrium distribution of modes. Conserved quantities such as energy and particle number need to be largely redistributed across the modes for the system to reach equilibrium. As we will see, this will lead to slow self-similar dynamics.

Despite the smallness of the diluteness parameter ζ , the distribution of particles (3.7) leads to strongly correlated dynamics. This can be understood from a mean-field or Hartree-Fock approximation. The effect of the interaction term in this approximation is essentially captured by the local self-energy $\Sigma^{(0)}$ given in Eq. (2.40). This results in a constant energy shift for each particle,

$$\Delta E = 2g\langle|\psi|^2\rangle = 2gn = 2g \int \frac{d^3p}{(2\pi)^3} f(|\mathbf{p}|), \quad (3.8)$$

which can be absorbed in a redefinition of the chemical potential. For the typical momentum Q the shift in energy is, however, not small compared to the relevant kinetic energy, i.e. $2gn \sim Q^2/2m$. Parametrically, this can be directly verified using (3.7):

$$g \int d^3p f(|\mathbf{p}|) \sim g Q^3 f(Q) \sim g \frac{Q^3}{\zeta} \sim g \frac{Q^3}{mgQ} \sim \frac{Q^2}{m}. \quad (3.9)$$

Here we have used that with $a = mg/(4\pi)$ equation (3.6) implies $Q = 2\sqrt{mgn}$ and (3.5) gives $\zeta = mgQ/(16\pi^{3/2})$. Most importantly, the energy shift $2gn$ is of the order of the kinetic energy $Q^2/2m$ irrespective of the coupling strength g . This already hints at a strongly correlated system, where the dependence on the details of the underlying model parameters is lost.

3.2.2 Self-similarity from classical statistical simulations

To simulate the dynamics of the Bose system we use the fact that the nonequilibrium quantum dynamics of the highly occupied system can be mapped onto classical-statistical field theory evolution [95–99]. As argued in Sec. 2.5, this mapping is valid as long as $f \gg 1$ for typical momenta, which is fulfilled for (3.7) and a small diluteness parameter ζ . We recall that in classical-statistical simulations, one samples over initial conditions and evolves each realization according to the classical equation of motion (3.4). This equation is solved on a three-dimensional grid using a split-step method [56, 57]. Then, observables are obtained by averaging over classical trajectories.

We study the scaling behavior of a time-dependent occupation number distribution $f(t, \mathbf{p})$, which we define in the following. In the classical-statistical field theory, we consider the two-point correlation function

$$F(t, t', \mathbf{x} - \mathbf{x}') = \langle \psi(t, \mathbf{x}) \psi^*(t', \mathbf{x}') \rangle \quad (3.10)$$

evaluated at equal times $t = t'$ for spatially homogeneous ensembles. Brackets $\langle \dots \rangle$ indicate sample averages when applied to classical fields. In the quantum theory, this quantity corresponds to the statistical function defined in (2.15) but written in the complex basis. To define a suitable particle number distribution we recall that in the free nonrelativistic theory $f(\mathbf{p}) \sim \langle \hat{a}_{\mathbf{p}}^\dagger \hat{a}_{\mathbf{p}} \rangle$, where the Hamiltonian is diagonalized by the annihilation and creation operators $\hat{a}_{\mathbf{p}} = \int d^d x e^{-i\mathbf{p}\mathbf{x}} \hat{\psi}(\mathbf{x})$ and $\hat{a}_{\mathbf{p}}^\dagger$. Based on this we define [99]

$$f(t, \mathbf{p}) + (2\pi)^3 \delta^{(3)}(\mathbf{p}) |\psi_0|^2(t) \equiv \int d^3 x e^{-i\mathbf{p}\mathbf{x}} F(t, t, \mathbf{x}) = \frac{1}{V} \langle |\psi(t, \mathbf{p})|^2 \rangle, \quad (3.11)$$

where the last equality applies to a finite volume. Because of spatial isotropy, the distribution function depends on the modulus of the momentum, i.e. $f(t, \mathbf{p}) = f(t, |\mathbf{p}|)$. The term $\sim |\psi_0|^2(t)$ multiplying the Dirac δ -function represents the condensate part of the correlator at zero momentum. Using these definitions the condensate fraction at zero momentum is then given by

$$\frac{N_0(t)}{N_{\text{total}}} = \frac{|\psi_0|^2(t)}{\int d^3 p / (2\pi)^3 f(t, \mathbf{p}) + |\psi_0|^2(t)}. \quad (3.12)$$

The corresponding expressions for the finite volumes employed will be discussed further below. We note that the term $|\psi_0|^2(t)$ is usually linked to the presence of a nonvanishing average field $\langle \psi \rangle$. For the initial conditions considered, the one-point function is, however, zero. As we will show in Sec. 3.2.3, this does not exclude the possibility of a term in the correlator that scales proportional to volume.⁹

We consider initial conditions with high occupation numbers as motivated in the previous section. Specifically, we start with a distribution function of the form

$$f(0, \mathbf{p}) \sim \frac{1}{\zeta} \Theta(Q - |\mathbf{p}|), \quad (3.13)$$

⁹In the quantum theory the definition of the distribution function is obtained by the substitution $f \rightarrow f + 1/2$ in (3.11). Since our typical occupation numbers are large, we drop here the ‘quantum-half’.

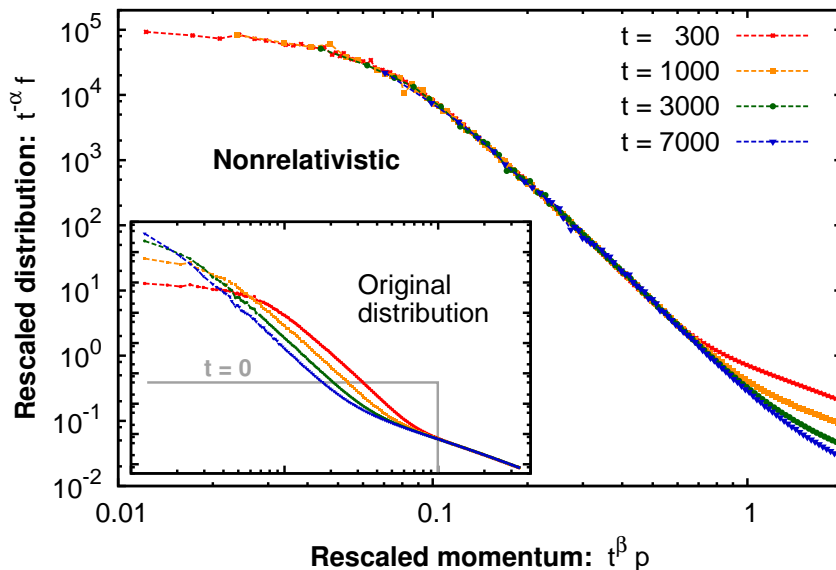


FIGURE 3.3: Rescaled distribution function of the nonrelativistic theory as a function of the rescaled momentum for different times. The inset shows the original distribution without rescaling.

which describes overoccupation up to the characteristic momentum Q . The initial condensate fraction is taken to be zero, i.e. $|\psi_0|^2(t=0) = 0$, with an initial $f(0, \mathbf{p}) = 50/(2mgQ) \Theta(Q - |\mathbf{p}|)$. As mentioned above, we choose the one-point function to be on average zero, i.e. $\langle \psi(t, \mathbf{x}) \rangle = 0$. For the plots we typically average over 10 realizations on a lattice with 512^3 points and a lattice spacing a_s such that $Qa_s = 1$, where we checked insensitivity of our infrared results to cutoff changes (see App. A for details on the discretization of space and time). We always plot dimensionless quantities obtained by the rescalings $f(t, \mathbf{p}) \rightarrow f(t, \mathbf{p}) 2mgQ$, $t \rightarrow t Q^2/(2m)$ and $\mathbf{p} \rightarrow \mathbf{p}/Q$. This reflects the classical-statistical nature of the dynamics in the highly occupied regime, which has the important consequence that if we measure time in units of $2m/Q^2$ and momentum in units of Q then the combination $f(t, \mathbf{p}) 2mgQ$ does not depend on the values of m , g and Q [61].

At the beginning of the evolution, the mode occupancies get quickly redistributed and then a slower behavior sets in. The latter reflects the dynamics near the nonthermal fixed point, where universality can be observed. We concentrate on the low-momentum part of the distribution and analyze its infrared scaling properties. Fig. 3.3 shows the rescaled distribution $(t/t_{\text{ref}})^{-\alpha} f(t, \mathbf{p})$ of the nonrelativistic theory as a function of $(t/t_{\text{ref}})^{\beta} |\mathbf{p}|$, where the reference time $t_{\text{ref}} Q^2/(2m) = 300$ is the earliest time shown. The inset gives the curves at different times together with the initial distribution without rescaling for comparison. With the appropriate choice of the infrared scaling exponents α and β , all the curves at different times lie remarkably well on top of each other after rescaling. This is a striking manifestation of the self-similar dynamics (3.1) near a nonthermal fixed point. The scaling exponents obtained are

$$\alpha = 1.66 \pm 0.12, \quad \beta = 0.55 \pm 0.03, \quad (3.14)$$

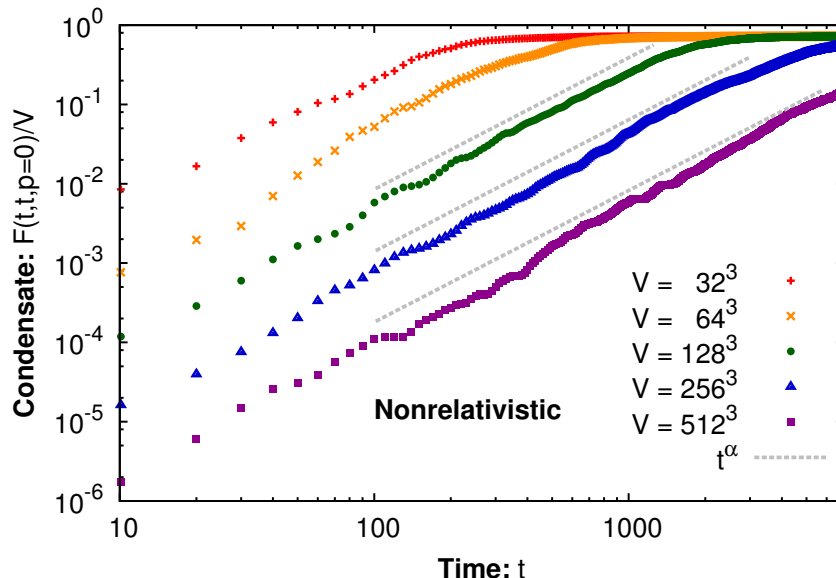


FIGURE 3.4: Evolution of the zero-momentum correlation divided by volume for the nonrelativistic Bose gas. A power-law $\sim t^\alpha$ has been fitted in the time interval with self-similar evolution for the three largest volumes (dashed lines). Subsequently, the results for different volumes converge, signaling the formation of a coherent zero mode spreading over the entire volume.

where the error bars are due to statistical averaging and fitting errors, which is further described in appendix B.

The simulation results confirm that $\alpha = 3\beta$ to very good accuracy as expected from number conservation in the infrared scaling regime (see Sec. 3.1.1). The values for α and β determine the rate and direction of the particle number transport, since according to (3.1) a given characteristic momentum scale $K(t_0) = K_0$ evolves as $K(t) = K_0(t/t_0)^{-\beta}$ with amplitude $f(t, K(t)) \sim t^\alpha$. Therefore, the positive values for the exponents in the infrared scaling regime imply that particle number is being transported towards low momenta, thus confirming an inverse particle cascade.

3.2.3 Condensate formation

At time $t = 0$ there is not condensate present in the system. However, the inverse particle cascade confirmed above continuously populates the zero-mode, thus leading to the formation of a condensate far from equilibrium [57, 59, 61, 138–140]. Near the nonthermal fixed point, the condensation dynamics is expected to exhibit scaling behavior and in the following we determine the relevant scaling exponent.

The condensate was defined in Eq. (3.11) as the term in the Fourier transformed correlator (3.10) that is proportional to $\delta^{(3)}(\mathbf{p})$. Following references [57, 61] we note that for a finite volume V the zero-mode contribution in (3.11) scales with $(2\pi)^3\delta^{(3)}(\mathbf{0}) \rightarrow V$ proportional to volume. This allows us to identify the condensate fraction by its scaling behavior as the volume is varied. Stated differently, if we divide the correlation function (3.11) by the volume,

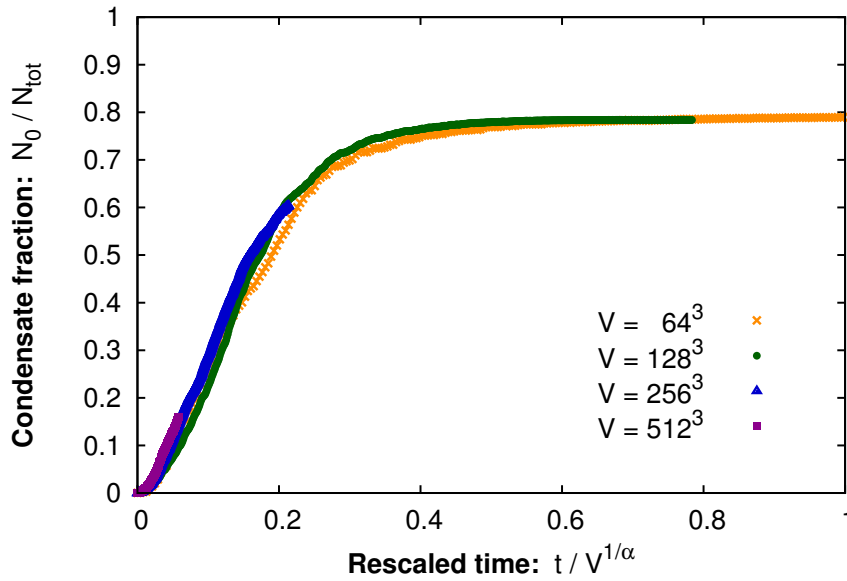


FIGURE 3.5: Evolution of the condensate fraction for the nonrelativistic Bose gas for different volumes V . The different curves become approximately volume independent after rescaling of time by $V^{-1/\alpha}$, in agreement with (3.15).

only correlations which scale with the system size are not suppressed at large volumes and the condensate fraction is related to the volume-independent part.

Fig. 3.4 shows the evolution of the zero-momentum mode $V^{-1}F(t, t, \mathbf{p} = 0)$ for different volumes. These are given in units of Q , ranging from $VQ^3 = 32^3$ to the largest volume $\sim 512^3$. Correspondingly, the plotted dimensionless results are rescaled as $V^{-1}F(t, t, \mathbf{p} = 0) \rightarrow V^{-1}F(t, t, \mathbf{p} = 0) 2mgQ/Q^3$. One observes that at early times the evolution depends strongly on the volume, as expected in the absence of a coherent zero-momentum mode spreading over the entire volume. However, after a transient regime the zero-momentum correlation becomes volume independent. The curves corresponding to different volumes converge towards the same value, thus signaling the formation of a condensate.

The double logarithmic plot of Fig. 3.4 clearly indicates that the growth of the zero-momentum correlation proceeds as a power-law in time. The power-law growth is rather well described by the scaling exponent α found in (3.14) from the self-similar evolution of the distribution function. This can already be understood by noting that according to (3.1) the zero mode of the distribution function grows as $f(t, 0) \sim t^\alpha$. This will be discussed in more detail in Sec. 3.5.

Of course, the time needed to fill the entire volume with a single condensate increases with volume, which is nicely observed from the data. Using that the parametrically slow power-law dynamics dominates until condensation is completed, we can use the scaling exponent α to estimate this condensation time. Taking the value of the zero-momentum correlator $V^{-1}F(t, t, \mathbf{p} = 0)$ at the initial time t_0 of the self-similar regime as $V^{-1}f(t_0, 0)$ and its final value at the time t_f as $|\psi_0|^2(t_f)$, we can estimate from $V^{-1}F(t, t, \mathbf{p} = 0) \sim t^\alpha$ the condensation

time as

$$t_f \simeq t_0 \left(\frac{|\psi_0|^2(t_f)}{f(t_0, 0)} \right)^{1/\alpha} V^{1/\alpha}. \quad (3.15)$$

Correspondingly, we define the condensate fraction (3.12) for the case of finite volumes as $N_0/N_{\text{total}} \rightarrow V^{-1}F(t, t, \mathbf{p} = 0)/F(t, t, \mathbf{x} = 0)$, using that $N_{\text{total}} = F(t, t, \mathbf{x} = 0)$. In Fig. 3.5 we show the evolution of the condensate fraction for different volumes as a function of the rescaled time $t/V^{1/\alpha}$. Indeed, as predicted by (3.15), the different curves are approximately volume independent. One finds that the condensate fraction saturates at $N_0/N_{\text{total}} \simeq 0.8$.

3.3 Relativistic quantum field theory

We study now the far from equilibrium dynamics of an N -component relativistic quantum field theory defined by the action (2.1). We consider the case of a massless theory, $m = 0$, in three spatial dimensions. The classical equation of motion for the massless theory is given by

$$\left(\partial_t^2 - \nabla^2 + \frac{\lambda}{6N} \varphi_a(t, \mathbf{x}) \varphi_a(t, \mathbf{x}) \right) \varphi_b(t, \mathbf{x}) = 0, \quad (3.16)$$

where sum over repeated indices is implied. In the following, we assume the quartic coupling to be small, $\lambda \ll 1$.

3.3.1 Overoccupied initial conditions

To discuss the initial conditions needed in the relativistic theory to observe self-similar dynamics close to the nonthermal fixed point, it is useful to introduce first a suitably defined distribution function $f(t, \mathbf{p})$. The relevant two-point correlation function in the classical-statistical theory we denote as

$$F(t, t', \mathbf{x} - \mathbf{x}') = \frac{1}{N} \langle \varphi_a(t, \mathbf{x}) \varphi_a(t', \mathbf{x}') \rangle. \quad (3.17)$$

Again, this quantity corresponds in the quantum theory to the statistical function (2.15) traced over field indices. At equal times $t = t'$ this can be used to define a distribution function $f(t, \mathbf{p})$ for the relativistic theory:¹⁰

$$\frac{f(t, \mathbf{p})}{\omega(t, \mathbf{p})} + (2\pi)^3 \delta^{(3)}(\mathbf{p}) \phi_0^2(t) \equiv \int d^3x e^{-i\mathbf{p}\mathbf{x}} F(t, t, \mathbf{x}). \quad (3.18)$$

This is in complete analogy to the definition (3.11) for the nonrelativistic system and we will refer to the term $\sim \phi_0^2(t)$ as the condensate part. The only major difference is the appearance of the dispersion $\omega(t, \mathbf{p})$ in the definition for the relativistic case, which is a consequence of the second-order differential equation in time for the fields (3.16). To be more specific, in the free relativistic theory the quasiparticles are defined by the annihilation and creation operators $\hat{a}_{\mathbf{p}} = \sqrt{\frac{\omega_{\mathbf{p}}}{2}} (\hat{\varphi}_{\mathbf{p}} + i\hat{\pi}_{\mathbf{p}}/\omega_{\mathbf{p}})/\sqrt{V}$ and $\hat{a}_{\mathbf{p}}^\dagger$. Inverting this relation yields in the quantum case

¹⁰Similar to the nonrelativistic case, we drop here the ‘quantum-half’ as explained in footnote 9.

$F(t, t, \mathbf{p}) = (f(\mathbf{p}) + \frac{1}{2})/\omega_{\mathbf{p}}$, which explains (3.18). Furthermore, in the free theory we have $\partial_t \partial_{t'} F(t, t, \mathbf{p}) = \omega_{\mathbf{p}}(f(\mathbf{p}) + \frac{1}{2})$, which will be used further below.¹¹

Similar to the above discussion for the nonrelativistic system, we first characterize overoccupied initial conditions for the typical momentum Q by considering a mean-field or large- N approximation to leading order. The evolution of the correlation function (3.17) is then given by (2.30) with the local self-energy (2.40). In spatial Fourier space and setting the macroscopic field to zero this reads (see e.g. [114]):

$$\left(\partial_t^2 + \mathbf{p}^2 + \frac{\lambda}{6} \int \frac{d^3 q}{(2\pi)^3} F(t, t, \mathbf{q}) \right) F(t, t', \mathbf{p}) = 0. \quad (3.19)$$

If there is no condensate initially, we can estimate parametrically the mean-field correction at sufficiently early times as

$$\lambda \int d^3 p F(t, t, \mathbf{p}) \sim \lambda \int \frac{d^3 p}{(2\pi)^3} \frac{f(t, \mathbf{p})}{\omega(\mathbf{p})} \sim \lambda \int^Q dp p^2 \frac{f(t, \mathbf{p})}{|\mathbf{p}|} \sim \lambda f(t, Q) Q^2, \quad (3.20)$$

where we have taken a relativistic dispersion $\omega \sim |\mathbf{p}|$ for massless particles. One observes that this is of the same order as the typical kinetic energy term $\sim Q^2$ in (3.19) if the occupancy is as large as

$$f(t, Q) \sim \frac{1}{\lambda} \gg 1. \quad (3.21)$$

Common scalar inflaton models for early universe dynamics have couplings of order $\lambda \sim 10^{-13}$, such that the typical occupancies are extremely large in that context. Comparing to (3.7), we note that the dimensionless self-coupling λ plays the role of the diluteness parameter ζ in the nonrelativistic theory.

3.3.2 Self-similarity from classical statistical simulations

Similar to the previous section, we perform classical-statistical simulations, which are valid as long as $f(t, \mathbf{p}) \gg 1$ for the relevant times and momenta. For this we solve (3.16) as classical equations of motion on a three dimensional lattice using a leapfrog algorithm [41, 51] and sample over initial conditions. We extract the occupation number distribution according to (3.18) and the subsequent discussion about the free theory by writing for $|\mathbf{p}| > 0$:

$$\frac{f(t, \mathbf{p})}{\omega(t, \mathbf{p})} = F(t, t, \mathbf{p}) = \frac{\sqrt{F(t, t', \mathbf{p}) \partial_t \partial_{t'} F(t, t', \mathbf{p})}}{\sqrt{\partial_t \partial_{t'} F(t, t', \mathbf{p}) / F(t, t', \mathbf{p})}} \Big|_{t=t'}. \quad (3.22)$$

The second equality allows us to identify the dimensionless distribution (see e.g. [114])

$$f(t, \mathbf{p}) = \sqrt{F(t, t', \mathbf{p}) \partial_t \partial_{t'} F(t, t', \mathbf{p})} \Big|_{t=t'}. \quad (3.23)$$

¹¹We employ for our analysis a distribution function f in order to relate it to a resummed kinetic description in Sec. 3.4. However, we emphasize that the observed scaling behavior concerns correlation functions, which are well-defined also in the absence of a suitable choice of an occupation number distribution. This can be, in particular, important for gauge theories, where suitable gauge-invariant definitions of an occupation number in the strongly correlated infrared regime may not be available.

The corresponding dispersion relation is then given by

$$\omega(t, \mathbf{p}) = \sqrt{\frac{\partial_t \partial_{t'} F(t, t', \mathbf{p})}{F(t, t', \mathbf{p})}} \Big|_{t=t'} . \quad (3.24)$$

We emphasize that the notion of particle number is not a uniquely defined concept in a relativistic field theory, where total number changing processes are possible. However, one may always think in terms of the well-defined correlation functions appearing in (3.23). Moreover, this definition turns out to provide an extremely useful quasi-particle interpretation even in the strongly correlated infrared regime [41], which we will exploit further in Sec. (3.4).

Similar to (3.13) for the nonrelativistic theory, we choose overoccupied initial conditions

$$f(0, \mathbf{p}) \sim \frac{1}{\lambda} \Theta(Q - |\mathbf{p}|) \quad (3.25)$$

with $\phi_0^2(t=0) = 0$. All quantities shown will be made dimensionless by appropriate powers of the scale $Q_\epsilon = \sqrt[4]{\lambda\epsilon/N}$, which is obtained from the conserved energy density average

$$\epsilon = \left\langle \frac{1}{2} (\partial_t \varphi_a) (\partial_t \varphi_a) + \frac{1}{2} (\partial_i \varphi_a) (\partial_i \varphi_a) + \frac{\lambda}{4!N} (\varphi_a \varphi_a)^2 \right\rangle , \quad (3.26)$$

where summation over spatial directions i and scalar components a is implied. For the initial condition (3.25), one has $\epsilon \sim NQ^4/\lambda$ such that Q_ϵ becomes independent of the coupling and the number of field components.

For the figures we have chosen the amplitude of (3.25) as $f(0, \mathbf{p}) = 125/\lambda \Theta(Q - |\mathbf{p}|)$ with $Q = 0.8Q_\epsilon$, and we always plot rescaled functions $f(t, \mathbf{p}) \rightarrow \lambda f(t, \mathbf{p})$ and $F(t, t, \mathbf{p}) \rightarrow \lambda F(t, t, \mathbf{p})$ such that these combinations also become independent of the coupling. For the $N = 2$ component theory, computations were made on a 768^3 lattice with lattice spacing $Q_\epsilon a_s = 0.9$ and we averaged over five realizations (see App. A for details on the discretization of space and time). For $N = 4$ we employed a 512^3 lattice with spacing $Q_\epsilon a_s = 1.8$ and averaged over 18 – 50 realizations. We checked that for $N = 2$ all shown results are insensitive to the lattice spacing and the volume. For the relevant infrared quantities this is to good accuracy also the case for the coarser lattices employed for $N = 4$.

In Fig. 3.6 we show the evolution of the occupation number distribution for the relativistic $N = 2$ component theory. As in the nonrelativistic case, we plot $(t/t_{\text{ref}})^{-\alpha} f$ against $(t/t_{\text{ref}})^\beta |\mathbf{p}|$ with $Q_\epsilon t_{\text{ref}} = 600$ to study self-similarity and give the original distribution without rescalings in the inset. With appropriately chosen exponents, in the infrared all curves lie on top of each other after rescaling to remarkable accuracy. The measured exponents are

$$\alpha = 1.51 \pm 0.13, \quad \beta = 0.51 \pm 0.04, \quad (3.27)$$

and we refer to App. B for details on how we estimate the error bars.

In order to check for a possible dependence of the infrared scaling properties on the number of field components, we also perform lattice simulations for $N = 4$. Fig. 3.7 shows $(t/t_{\text{ref}})^{-\alpha} f$ as a function of $(t/t_{\text{ref}})^\beta |\mathbf{p}|$ with $Q_\epsilon t_{\text{ref}} = 800$. The curves corresponding to different times lie

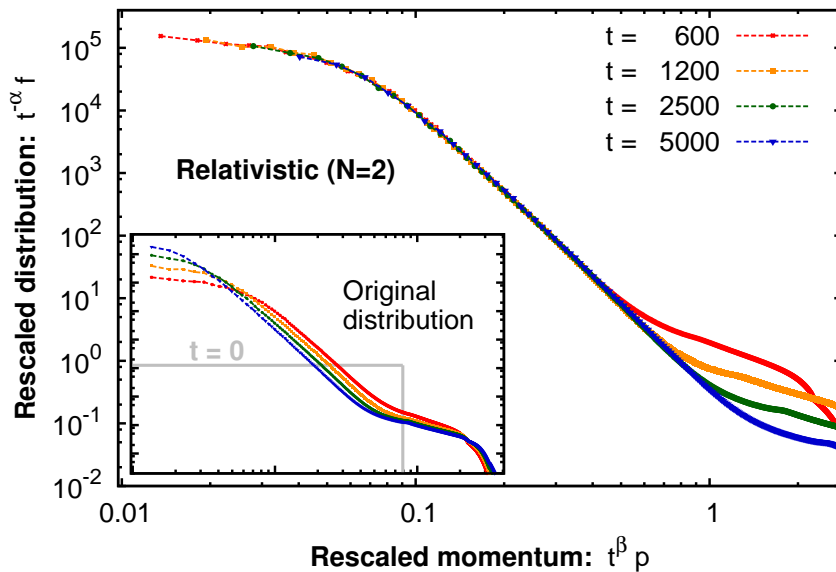


FIGURE 3.6: Rescaled distribution function of the relativistic two-component theory as a function of the rescaled momentum for different times. The inset shows the original distribution without rescaling.

again on top of each other after the rescalings and we extract the exponents

$$\alpha = 1.65 \pm 0.09, \quad \beta = 0.59 \pm 0.03. \quad (3.28)$$

These and the universal scaling form of the distribution function compare rather well to those for the relativistic $N = 2$ component system as well as the nonrelativistic theory. Within the statistical errors we find no indication for a dependence of the corresponding universality class on the number of field components. However, small discrepancies in α , β and f_S are still possible. These could occur in the presence of nonvanishing anomalous dimension η , which is discussed further in Sec. 3.5.

In order to estimate systematic errors, we investigate how the values for the exponents α and β depend on the reference time t_{ref} at which we start our self-similarity analysis. To this end, we perform our analysis for different values of t_{ref} and use the method of App. B with the distribution function evaluated at several times up to $t/t_{\text{ref}} \lesssim 4 - 5$. In Fig. 3.8, we show the extracted values for α and β as a function of the reference time for $N = 4$. One finds that the mean value of α decreases monotonically to about $\alpha \approx 1.5$ while β gets close to a half for the transient times at which self-similarity can be accurately observed. For the relativistic two-component system, the exponents α and β are found to start from comparably larger values at early reference times to the ones given in (3.27). We note that the nonrelativistic system of Sec. 3.2.2 also shows decreasing exponents α and β but our runs last not long enough such that their mean values (3.14) come as close to the expected values $\alpha = 1.5$ and $\beta = 0.5$ as for the relativistic two-component system.

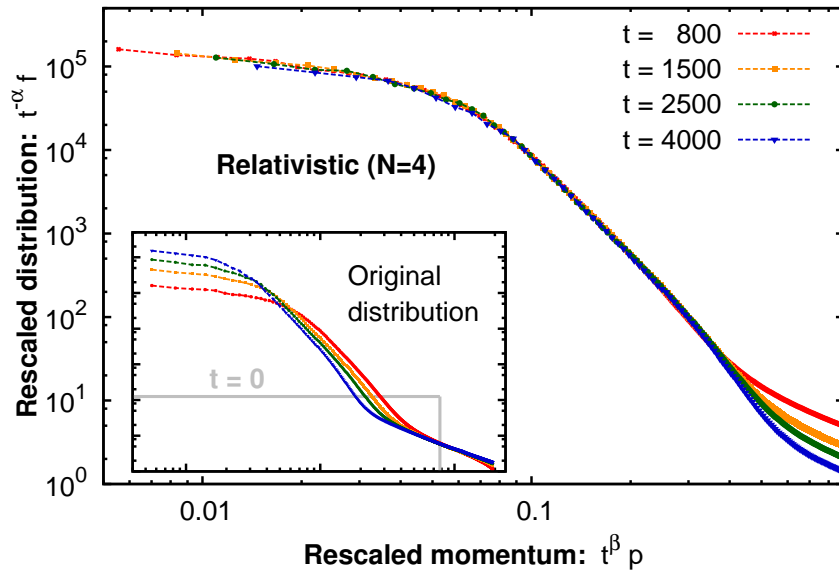


FIGURE 3.7: Rescaled distribution function of the relativistic four-component theory as a function of the rescaled momentum for different times. The inset shows the original distribution without rescaling.

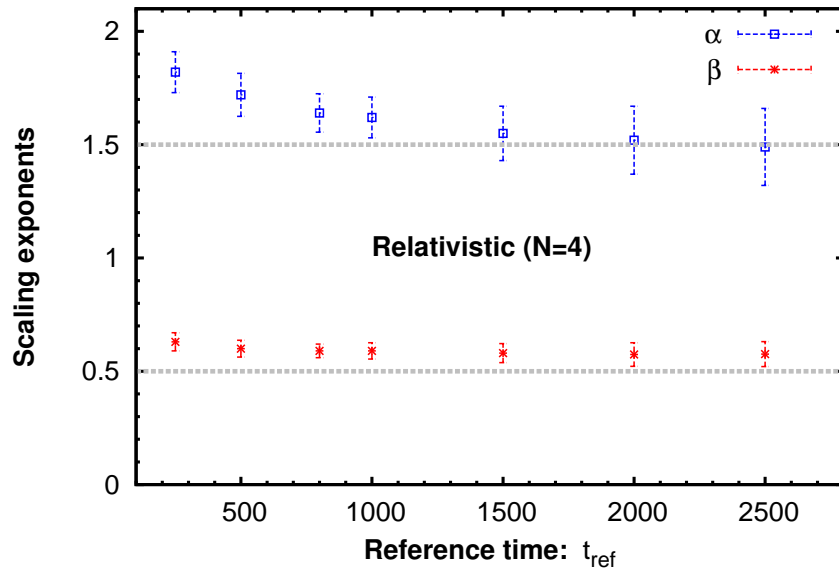


FIGURE 3.8: The exponents α and β with statistical error bars for the relativistic $N = 4$ component field theory extracted at different reference times t_{ref} .

3.3.3 Generation of a mass gap

The values (3.27) or (3.28) for the exponents of the relativistic theories agree within errors with the values (3.14) obtained for the nonrelativistic Bose gas. Moreover, they are rather close to the analytic results (3.2) from the large- N expansion to NLO for the nonrelativistic

theory, while they deviate clearly from the corresponding prediction assuming a relativistic dispersion as will be shown in Sec. 3.4.

Also the universal form of the nonthermal fixed point distribution f_S accurately agrees for relativistic and nonrelativistic theories in the infrared scaling regime. This is shown in Fig. 3.2 by comparing the two-component relativistic and the nonrelativistic theory, where f_S/A is given as a function of $t^\beta |\mathbf{p}|/B$ normalized to the nonuniversal amplitudes A and B as described in Sec. 3.1.2.

To understand the appearance of nonrelativistic dynamics, we analyze the dispersion relation $\omega(t, \mathbf{p})$ according to (3.24), which is shown in Fig. 3.9 at three different times. Although the underlying theory is massless, it can be clearly observed that for low momenta the system generates a mass gap, whereas at large momenta we recover a linear dispersion.

The appearance of an effective mass-like contribution can already be understood qualitatively from the approximate evolution equation (3.19) for the correlator modes $F(t, t', \mathbf{p})$. In the mean-field approximation, the term $\sim (\lambda/6) \int d^3q/(2\pi)^3 F(t, t, \mathbf{q})$ generates a mass-like correction for the overoccupied initial condition (3.25).

To extract the mass gap beyond the mean-field approximation using the lattice simulations, we fit a time-dependent effective mass $m(t)$ from a $\sqrt{m^2(t) + \mathbf{p}^2}$ fit to the $\omega(t, \mathbf{p})$ data. The time evolution of $m(t)$ is shown in the inset of Fig. 3.9. We find that after a quick initial evolution this dispersion relation enters a quasi-stationary regime, which is typical for a prethermalized quantity whose transient evolution is governed by an approximately conserved (particle) number [141].

In addition, we also analyze the oscillation frequency ω_c of the unequal-time correlation function $F(t, 0, \mathbf{p})$ as a function of time t for $|\mathbf{p}| = 0$. Since the zero-momentum mode frequency corresponds to the renormalized mass of the theory, this provides an independent estimate of the mass gap that does not rely on the definition (3.24) of a dispersion. Indeed we find $\omega_c \simeq m$ to very good accuracy as shown in the inset of Fig. 3.9.

In the presence of a mass gap m , low momentum modes with $|\mathbf{p}| \lesssim m$ are expected to behave nonrelativistically. From Fig. 3.9 we can estimate the mass to be $m \simeq 0.55Q_\epsilon \simeq 0.69Q$ for the whole duration of the self-similar evolution. We find that this mass scale separates rather well the inertial ranges for the inverse particle cascade towards low momenta from the direct energy cascade at higher momenta. This can be observed, for instance, from the inset of Fig. 3.6, where the initial scale Q marked by the distribution at $t = 0$ can be used as a reference.

The emergence of a mass gap in the relativistic theory explains why the dynamics in the infrared regime is governed by nonrelativistic physics. Of course, in general the presence of a mass gap does not necessarily imply universal behavior for sufficiently low momentum modes. However, it may be seen as a prerequisite for relativistic theories to belong to the same far-from-equilibrium universality class as the Gross-Pitaevskii field theory.

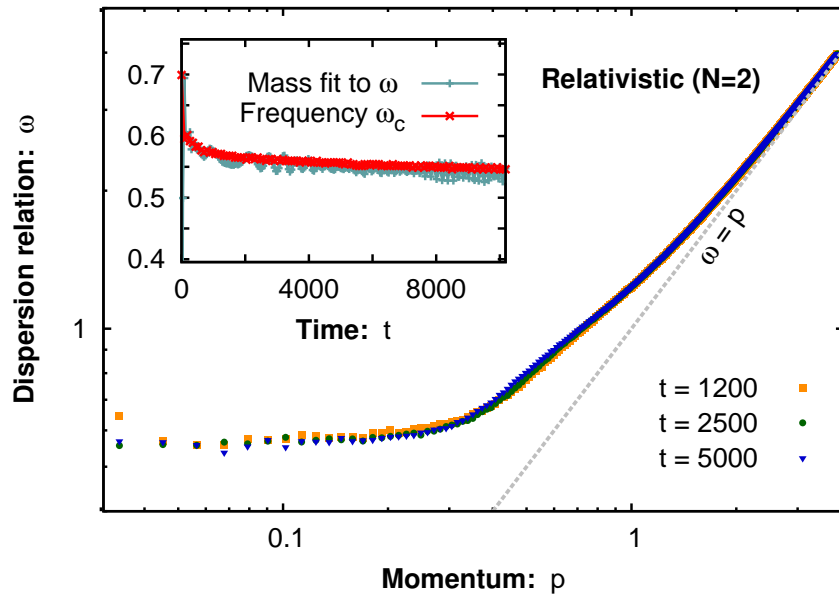


FIGURE 3.9: Dispersion relation for the relativistic $N = 2$ component theory at different times for the same parameters as for Fig. 3.6. In the inset, the time evolution of the mass gap at zero momentum is shown, which is obtained from a $\sqrt{m^2 + \mathbf{p}^2}$ fit to $\omega_{\mathbf{p}}$ at low momenta (+ symbol) and by measuring the oscillation frequency ω_c of the unequal-time correlation function (x symbol).

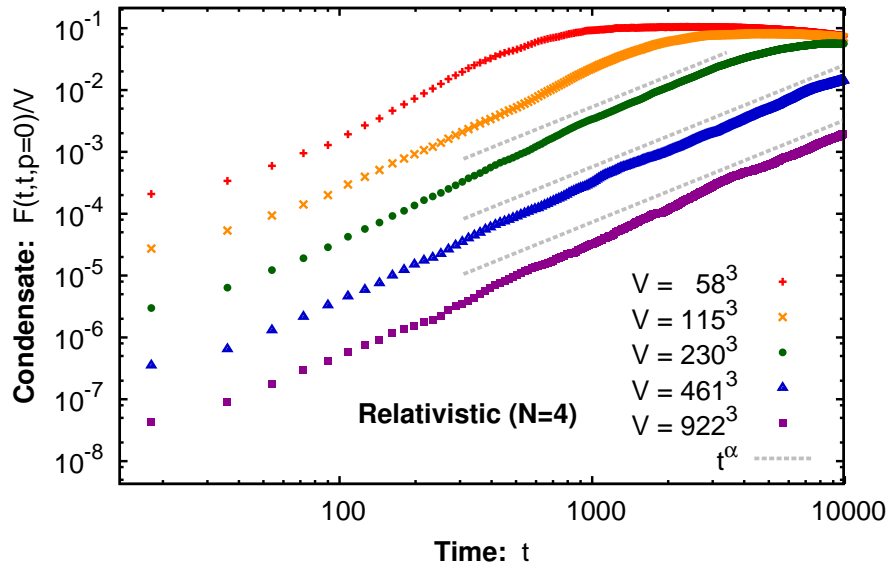


FIGURE 3.10: Evolution of the zero-momentum correlation divided by volume for the relativistic $N = 4$ component theory, similar to FIG. 3.4 for the nonrelativistic case.

3.3.4 Condensate formation

Since we observe for the relativistic scalar field theory the same inverse particle cascade with universal exponents and scaling function as for the nonrelativistic system, one expects condensation to proceed with the same exponent α as found in Sec. 3.2.3. However, this is not entirely trivial since scatterings off the condensate play an important role in the inertial range for the direct energy cascade towards higher momenta, where both theories do not belong to the same universality class [39, 40].

In order to clarify this, we analyze the growth of the condensate during the self-similar regime for the $N = 4$ component theory along the same lines as in Sec. 3.2.3. The results are given in Fig. 3.10 for different volumes, ranging from $VQ_c^3 = 58^3$ to the largest volume $\sim 922^3$. Shown is the time evolution of the zero-mode of the correlation function (3.18) divided by volume. We compare the curves to the expected power-law behavior $\sim t^\alpha$ with the exponent α obtained before from the self-similarity analysis. As in the nonrelativistic case, the dynamics is well described by such a power-law until the results become volume independent, thus signaling the formation of a coherent condensate ϕ_0^2 for the entire volume.

We emphasize that the observed power-law is restricted to the formation of the condensate during the transient self-similar regime, where we find the universal exponent α to govern the dynamics. In particular, we do not discuss here the subsequent late-time approach to thermal equilibrium, where total particle number changing processes in the relativistic theory can make important differences as compared to the number conserving nonrelativistic system [57].

3.4 Vertex-resummed kinetic theory

To gain analytical understanding of the inverse particle cascade and condensation dynamics observed numerically in the previous sections, we study the problem from the perspective of kinetic theory.

In order to derive kinetic equations for the distribution function, a number of assumptions need to be made. For the better flow and readability of the text, a detailed account of the derivation will be postponed to Sec. 3.5 (see also Sec. 2.4). However, a couple of approximations are important to keep in mind in order to correctly interpret the results. First of all, a gradient expansion is used, as explained in Sec. 2.4. To lowest order, this implies that the spectral function ρ [c.f. Eq.(2.16)] is time-independent. Throughout this section we assume the spectral function to be δ -peaked at the dispersion relation $\omega_{\mathbf{p}}$ [see Eqs. (3.64) and (3.80)], which allows a quasiparticle interpretation. The specific forms used for $\omega_{\mathbf{p}}$ will be specified in each case.

To obtain an effective equation for the distribution function $f(t, \mathbf{p})$ alone, we will further relate correlators in frequency space to this frequency-independent quantity. As we will see in Sec. 3.5, this can be done by defining an off-shell distribution function $f(t, \omega, \mathbf{p})$ roughly as $F \sim f\rho$ [see Eq. (3.81)], where F is the statistical function of Eq. (2.15). It should be noted though, that this entails an important assumption on the scaling behavior of the statistical and spectral functions, which will need to be revised in Chap. 5.

We will consider both perturbative and nonperturbative approximations for the self-energy. Perturbative kinetic theory has been successfully applied to the phenomenon of weak wave turbulence [40, 76, 77]. It has also been employed in the literature to describe infrared phenomena such as Bose condensation [136, 137]. However, in this case the approach neglects important vertex corrections since the large occupancies at low momenta lead to strongly nonlinear dynamics [41, 56]. Here we apply a vertex-resummed kinetic theory, which is based on an expansion in the number of field components N to next-to-leading order [69, 107, 108]. While similar nonperturbative descriptions have been employed before for the scaling behavior of stationary transport [41, 68, 69], we consider here instead the more general notion of a self-similar evolution.

3.4.1 Self-similarity from kinetic theory

A self-similar evolution of the distribution function $f(t, \mathbf{p})$ for a spatially homogeneous and isotropic system is characterized as

$$f(t, \mathbf{p}) = s^{\alpha/\beta} f(s^{-1/\beta} t, s\mathbf{p}) \quad (3.29)$$

with the real scaling parameter s and exponents α and β . Again, all quantities are considered to be dimensionless by use of some suitable momentum scale. Choosing $s^{-1/\beta} t = 1$ we recover (3.1), where the time-independent scaling function $f_S(t^\beta \mathbf{p}) \equiv f(1, t^\beta \mathbf{p})$ denotes the *fixed point distribution*. This scaling form represents an enormous reduction of the possible dependence of the dynamics on variations in time and momenta, since $t^{-\alpha} f(t, \mathbf{p})$ depends on the product $t^\beta |\mathbf{p}|$ instead of separately depending on time and momenta. Therefore, an essential part of the time evolution is encoded in the momentum dependence of the fixed point distribution $f_S(\mathbf{p})$.

For the time evolution of the distribution function $f(t, \mathbf{p})$ we write

$$\frac{\partial f(t, \mathbf{p})}{\partial t} = C[f](t, \mathbf{p}) \quad (3.30)$$

with a generic ‘collision integral’ $C[f](t, \mathbf{p})$, which depends on the theory and the approximation employed. For the self-similar distribution (3.29), the scaling behavior of the collision integral is then given by

$$C[f](t, \mathbf{p}) = s^{-\mu} C[f](s^{-1/\beta} t, s\mathbf{p}) = t^{-\beta\mu} C[f_S](1, t^\beta \mathbf{p}), \quad (3.31)$$

where μ is a function of scaling exponents such as α and β . Substituting this scaling form into the kinetic equation leads to the time-independent *fixed point equation* for $f_S(\mathbf{p})$:

$$[\alpha + \beta \mathbf{p} \cdot \nabla_{\mathbf{p}}] f_S(\mathbf{p}) = C[f_S](1, \mathbf{p}), \quad (3.32)$$

and the *scaling relation*:

$$\alpha - 1 = -\beta\mu. \quad (3.33)$$

This follows from comparing the LHS of the kinetic equation,

$$\frac{\partial}{\partial t} \left[t^\alpha f_S(t^\beta \mathbf{p}) \right] = t^{\alpha-1} [\alpha + \beta \mathbf{q} \cdot \nabla_{\mathbf{q}}] f_S(\mathbf{q})|_{\mathbf{q}=t^\beta \mathbf{p}}, \quad (3.34)$$

to its RHS given by (3.31).

Further relations can be obtained by either imposing energy conservation or particle number conservation if applicable. For constant

$$n = \int \frac{d^d p}{(2\pi)^d} f(t, \mathbf{p}) = t^{\alpha-\beta d} \int \frac{d^d q}{(2\pi)^d} f_S(\mathbf{q}), \quad (3.35)$$

$$\epsilon = \int \frac{d^d p}{(2\pi)^d} \omega(\mathbf{p}) f(t, \mathbf{p}) = t^{\alpha-\beta(d+z)} \int \frac{d^d q}{(2\pi)^d} \omega(\mathbf{q}) f_S(\mathbf{q}), \quad (3.36)$$

one obtains, respectively, the relations for

$$\text{particle conservation: } \alpha = \beta d, \quad (3.37)$$

$$\text{energy conservation: } \alpha = \beta(d+z). \quad (3.38)$$

Here the dispersion has been taken to scale with the dynamic exponent z as

$$\omega(\mathbf{p}) = s^{-z} \omega(s\mathbf{p}) \quad (3.39)$$

with $z = 1$ for the gapless relativistic and $z = 2$ for the nonrelativistic free theory. One observes that there is no single scaling solution conserving both energy and particle number. As outlined already above, in this case a dual cascade is expected to emerge such that in a given inertial range of momenta only one conservation law governs the scaling behavior.

3.4.2 Perturbative scaling

We first review some perturbative results for later comparison. The form of the kinetic equations presented in this section follows from a perturbative expansion of the self-energy, as captured by Eq. (2.38). Further details will be given in later sections, especially in Sec. 3.5.

In perturbative kinetic theory, when two particles scatter into two particles, the collision integral is of the form

$$C^{2\leftrightarrow 2}[f](t, \mathbf{p}) = \int d\Omega^{2\leftrightarrow 2}(\mathbf{p}, \mathbf{l}, \mathbf{q}, \mathbf{r}) [(f_{\mathbf{p}} + 1)(f_{\mathbf{l}} + 1)f_{\mathbf{q}}f_{\mathbf{r}} - f_{\mathbf{p}}f_{\mathbf{l}}(f_{\mathbf{q}} + 1)(f_{\mathbf{r}} + 1)], \quad (3.40)$$

where we write $f(t, \mathbf{p}) \equiv f_{\mathbf{p}}$ suppressing the global time dependence to ease the notation. The details of the model enter $\int d\Omega^{2\leftrightarrow 2}(\mathbf{p}, \mathbf{l}, \mathbf{q}, \mathbf{r})$, which for the example of the relativistic N -component scalar field theory with quartic $\lambda/(4!N)$ -interaction of Sec. 3.3 reads

$$\begin{aligned} \int d\Omega^{2\leftrightarrow 2}(\mathbf{p}, \mathbf{l}, \mathbf{q}, \mathbf{r}) &= \lambda^2 \frac{N+2}{6N^2} \int \frac{d^d l}{(2\pi)^d} \frac{d^d q}{(2\pi)^d} \frac{d^d r}{(2\pi)^d} \\ &\times (2\pi)^{d+1} \delta^{(d)}(\mathbf{p} + \mathbf{l} - \mathbf{q} - \mathbf{r}) \frac{\delta(\omega_{\mathbf{p}} + \omega_{\mathbf{l}} - \omega_{\mathbf{q}} - \omega_{\mathbf{r}})}{2\omega_{\mathbf{p}}2\omega_{\mathbf{l}}2\omega_{\mathbf{q}}2\omega_{\mathbf{r}}} \end{aligned} \quad (3.41)$$

where we assumed a dispersion $\omega_{\mathbf{p}} = \sqrt{\mathbf{p}^2 + m^2}$.

The expression represents a standard Boltzmann equation for a gas of relativistic particles, which is not expected to be valid if the occupation numbers per mode become too large. Parametrically, for a weak coupling λ a necessary condition for its validity is $f_{\mathbf{p}} \ll 1/\lambda$

since otherwise strongly nonlinear effects become significant as will be explained in detail in Sec. 3.4.3. On the other hand, scaling is expected for not too small occupation numbers per mode, which we discuss now. For the corresponding regime $1 \ll f_{\mathbf{p}} \ll 1/\lambda$ one may use the above Boltzmann equation, which approximately becomes

$$\frac{\partial}{\partial t} f_{\mathbf{p}} \simeq \int d\Omega^{2\leftrightarrow 2}(\mathbf{p}, \mathbf{l}, \mathbf{q}, \mathbf{r}) [(f_{\mathbf{p}} + f_{\mathbf{l}})f_{\mathbf{q}}f_{\mathbf{r}} - f_{\mathbf{p}}f_{\mathbf{l}}(f_{\mathbf{q}} + f_{\mathbf{r}})]. \quad (3.42)$$

Apart from the energy density ϵ also the total particle number density n is conserved by the collision term.

For the relativistic theory, the scaling assumption (3.29) should be valid for sufficiently high momenta $|\mathbf{p}| \gg m$ such that the dispersion is approximately linear with $\omega_{\mathbf{p}} \sim |\mathbf{p}|$. In this case one obtains for the scaling of the collision integral (3.41) and (3.42) of the theory with quartic self-interaction:

$$C^{2\leftrightarrow 2}[f](t, \mathbf{p}) = s^{-\mu_4} C^{2\leftrightarrow 2}[f](s^{-1/\beta}t, s\mathbf{p}), \quad (3.43)$$

where the scaling is described by

$$\mu_4 = (3d - 4) - (d + 1) - 3\alpha/\beta = 2d - 5 - 3\alpha/\beta. \quad (3.44)$$

The first term in brackets comes from the scaling of the integral measure, the second from energy-momentum conservation for two-to-two scattering and the third from the three factors of the distribution function appearing in (3.42). Apart from the 4-vertex interaction considered, it may be relevant to investigate also scattering in the presence of a coherent field such that an effective 3-vertex appears. To keep the discussion more general, we hence consider a generic collision integral $C^{(l)}[f](t, \mathbf{p}) = s^{-\mu_l} C^{(l)}[f](s^{-1/\beta}t, s\mathbf{p})$ for l -vertex scattering processes. The resulting scaling exponent $\mu_l = (l - 2)d - (l + 1) - (l - 1)\alpha/\beta$ follows from similar arguments as exemplified for the 4-vertex interaction.

Using the scaling relation (3.33) and particle conservation (3.37) gives the perturbative solution for

$$\text{relativistic particle transport: } \alpha = -\frac{d}{l+1}, \beta = -\frac{1}{l+1}. \quad (3.45)$$

Similarly, with (3.38) for relativistic $z = 1$ one finds the perturbative solution for

$$\text{relativistic energy transport: } \alpha = -\frac{d+1}{2l-1}, \beta = -\frac{1}{2l-1}. \quad (3.46)$$

For instance, for quartic self-interactions the perturbative energy transport is characterized by $\alpha = -(d+1)/7$, and $\beta = -1/7$, where the latter is independent of the dimensionality of space d . Likewise, for an effective 3-vertex in the presence of a coherent field one has for the energy transport $\alpha = -(d+1)/5$ and $\beta = -1/5$. Indeed, the latter values for the scaling exponents describe well the energy transport at higher momenta of the relativistic scalar field theory for $d = 3$ of Sec. 3.3 [40]. In particular, their negative values indicate the direction of the transport from lower to higher momenta.

We now turn to the nonrelativistic theory of Sec. 3.2. The perturbative kinetic equation for $2 \leftrightarrow 2$ scattering is given again by (3.42), however, with the nonrelativistic

$$\int d\Omega_{\text{nr}}^{2 \leftrightarrow 2}(\mathbf{p}, \mathbf{l}, \mathbf{q}, \mathbf{r}) = 2g^2 \int \frac{d^d l}{(2\pi)^d} \frac{d^d q}{(2\pi)^d} \frac{d^d r}{(2\pi)^d} \times (2\pi)^{d+1} \delta^{(d)}(\mathbf{p} + \mathbf{l} - \mathbf{q} - \mathbf{r}) \delta(\omega_{\mathbf{p}} + \omega_{\mathbf{l}} - \omega_{\mathbf{q}} - \omega_{\mathbf{r}}) \quad (3.47)$$

where we assumed the dispersion $\omega_{\mathbf{p}} = \mathbf{p}^2/(2m)$, valid in the absence of a condensate. The scaling analysis follows along the same lines as before, but without the inverse-frequency factors from the relativistically invariant measure appearing in (3.41). Accordingly, generalizing again to l -vertex scatterings, one obtains for the scaling relation (3.33) in the nonrelativistic case: $(l-2)\alpha = \beta[(l-2)d-2] - 1$. This leads with (3.37) and (3.38) to the solutions for

$$\text{nonrelativistic particle transport: } \alpha = -\frac{d}{2}, \quad \beta = -\frac{1}{2}, \quad (3.48)$$

and

$$\text{nonrelativistic energy transport: } \alpha = -\frac{d+2}{2(l-1)}, \quad \beta = -\frac{1}{2(l-1)}. \quad (3.49)$$

For instance, for quartic self-interactions the perturbative particle transport would be described by $\alpha = -d/2$, and $\beta = -1/2$.

We emphasize that all the above perturbative estimates with negative values for α and β cannot account for the inverse particle transport observed from the simulations for $d = 3$ in Secs. 3.2.2 and 3.3.2. Of course, perturbation theory is not expected to be applicable to the overoccupied infrared modes and one has to employ an alternative description, which we consider next.

3.4.3 Nonperturbative scaling

Remarkably, the overoccupied regime can still be described in terms of a generalized kinetic theory by taking into account vertex corrections. For the N -component field theory, these corrections can be systematically computed from an expansion in the number of field components N to next-to-leading order [43, 107, 108]. The NLO corrections take scattering events up to infinite order into account. This allows us to describe even strongly correlated regimes, where the typical mode occupancies (3.7) or (3.21) are inversely proportional to the diluteness or coupling parameter, respectively.

Effectively, the change to the perturbative kinetic equations (3.40) or (3.42) is the appearance of a time and momentum dependent matrix element squared:

$$\lambda^2 \quad \rightarrow \quad \lambda_{\text{eff}}^2[f](t, \mathbf{p}, \mathbf{l}, \mathbf{q}, \mathbf{r}). \quad (3.50)$$

Details on the computation will be given in Sec. 3.5. More precisely, one finds at NLO of the expansion in the number of field components for the relativistic theory a kinetic equation

where (3.41) is replaced by:¹²

$$\int d\Omega^{\text{NLO}}[f](t, \mathbf{p}, \mathbf{l}, \mathbf{q}, \mathbf{r}) = \frac{1}{6N} \int \frac{d^d l}{(2\pi)^d} \frac{d^d q}{(2\pi)^d} \frac{d^d r}{(2\pi)^d} \frac{\delta(\omega_{\mathbf{p}} + \omega_{\mathbf{l}} - \omega_{\mathbf{q}} - \omega_{\mathbf{r}})}{2\omega_{\mathbf{p}} 2\omega_{\mathbf{l}} 2\omega_{\mathbf{q}} 2\omega_{\mathbf{r}}} \times (2\pi)^{d+1} \delta^{(d)}(\mathbf{p} + \mathbf{l} - \mathbf{q} - \mathbf{r}) \lambda_{\text{eff}}^2[f](t, \mathbf{p}, \mathbf{l}, \mathbf{q}, \mathbf{r}). \quad (3.51)$$

Here, we assumed a free spectral function with dispersion $\omega_{\mathbf{p}} = \sqrt{\mathbf{p}^2 + m^2}$ and

$$\lambda_{\text{eff}}^2(t, \mathbf{p}, \mathbf{l}, \mathbf{q}, \mathbf{r}) \equiv \frac{\lambda^2}{3} \left[\frac{1}{|1 + \Pi^R(t, \omega_{\mathbf{p}} + \omega_{\mathbf{l}}, \mathbf{p} + \mathbf{l})|^2} + \frac{1}{|1 + \Pi^R(t, \omega_{\mathbf{p}} - \omega_{\mathbf{q}}, \mathbf{p} - \mathbf{q})|^2} + \frac{1}{|1 + \Pi^R(t, \omega_{\mathbf{p}} - \omega_{\mathbf{r}}, \mathbf{p} - \mathbf{r})|^2} \right] \quad (3.52)$$

incorporates the vertex corrections for the different scattering channels. They are depicted in Fig. 3.11 and may be viewed as coming from an effective interaction, which involves the exchange of an intermediate particle whose four-momentum equals $p + l$, $p - q$ and $p - r$, respectively. The appearance of the ‘one-loop’ retarded self-energy,

$$\begin{aligned} \Pi^R(t, \omega, \mathbf{p}) &= \lim_{\epsilon \rightarrow 0} \frac{\lambda}{12} \int \frac{d^d q}{(2\pi)^d} \frac{f(t, \mathbf{p} - \mathbf{q})}{\omega_{\mathbf{q}} \omega_{\mathbf{p} - \mathbf{q}}} \\ &\times \left[\frac{1}{\omega_{\mathbf{q}} + \omega_{\mathbf{p} - \mathbf{q}} - \omega - i\epsilon} + \frac{1}{\omega_{\mathbf{q}} - \omega_{\mathbf{p} - \mathbf{q}} - \omega - i\epsilon} \right. \\ &\left. + \frac{1}{\omega_{\mathbf{q}} - \omega_{\mathbf{p} - \mathbf{q}} + \omega + i\epsilon} + \frac{1}{\omega_{\mathbf{q}} + \omega_{\mathbf{p} - \mathbf{q}} + \omega + i\epsilon} \right], \end{aligned} \quad (3.53)$$

in the denominator is the result of a geometric series summation of the infinite number of NLO processes (see Sec. 2.3.3). It should be emphasized that Π^R , and thus also λ_{eff}^2 , is time-dependent because it is expressed in terms of the evolving distribution function. The above expressions correspond to the on-shell limit of the evolution equations presented in reference [43] and their relation to the underlying field theory is further discussed in Sec. 3.5.

For sufficiently high momenta, the self-energy (3.53) becomes small such that $\Pi^R(t, \omega, \mathbf{p}) \ll 1$ in the squared matrix element (3.52) and we recover the perturbative expression $\lambda_{\text{eff}}^2 \rightarrow \lambda^2$. In this case, the kinetic equation corresponds to (3.41) with the prefactor for large N . Since the scaling solutions of Sec. 3.4.2 do not depend on N , one gets the same results in the high momentum regime.

For low momenta the case $\Pi^R(t, \omega, \mathbf{p}) \gg 1$ can become relevant, which changes the situation dramatically. This becomes even more involved if a mass gap exists, as seen in the simulations of Sec. 3.3.3. An effective mass gap is typically expected because of medium effects even if the mass parameter of the underlying microscopic theory is set to zero. In that case the infrared modes behave effectively nonrelativistically, which allows one to observe the same scaling behavior of the relativistic and the nonrelativistic theory in this regime.

¹²We note that the prefactor $(N + 2)/(6N^2)$ in (3.41) becomes at NLO in the large N expansion $1/(6N)$. A corresponding factor appears in the nonrelativistic case, when going from (3.47) to (3.54).

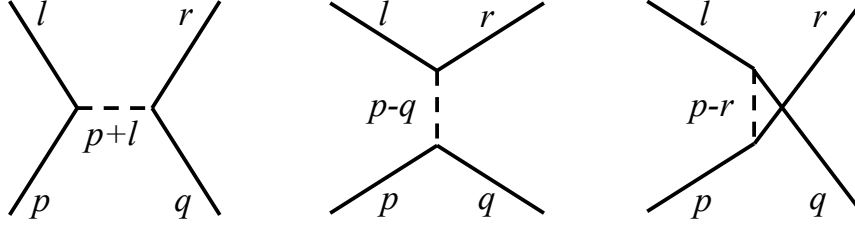


FIGURE 3.11: Illustration of different scattering channels. The vertex correction at NLO may be viewed as an effective interaction, which involves the exchange of an intermediate particle. Left: The incoming particles with momenta p and l join into an intermediate particle that eventually splits. Middle and right: The incoming particle with momentum p emits the intermediate particle and becomes the final particle with momentum q or r , respectively.

For the purpose of scaling, one may obtain the corresponding kinetic equation in the nonrelativistic limit of the relativistic theory (3.51), assuming that the mass appearing in the dispersion relation is much larger than the typical momenta. Expanding $\omega_{\mathbf{p}} = \sqrt{\mathbf{p}^2 + m^2} \simeq m + \mathbf{p}^2/2m$ and inserting this into (3.51), we have $\delta(\omega_{\mathbf{p}} + \omega_{\mathbf{l}} - \omega_{\mathbf{q}} - \omega_{\mathbf{r}}) \rightarrow \delta((\mathbf{p}^2 + \mathbf{l}^2 - \mathbf{q}^2 - \mathbf{r}^2)/(2m))$ and $2\omega_{\mathbf{p}}2\omega_{\mathbf{l}}2\omega_{\mathbf{q}}2\omega_{\mathbf{r}} \rightarrow 16m^4$ to lowest nonvanishing order. Then $g \sim \lambda/m^2$ leads to the nonrelativistic form of the equation. Alternatively, one can obtain the corresponding result from a nonrelativistic N -component complex scalar field theory [69] by performing again the $1/N$ expansion to NLO. This is further described in Sec. 3.5.

Taking into account proper normalizations, we consider for the nonrelativistic case a kinetic equation with

$$\int d\Omega_{\text{nr}}^{\text{NLO}}[f](t, \mathbf{p}, \mathbf{l}, \mathbf{q}, \mathbf{r}) = \int \frac{d^d l}{(2\pi)^d} \frac{d^d q}{(2\pi)^d} \frac{d^d r}{(2\pi)^d} \delta(\omega_{\mathbf{p}} + \omega_{\mathbf{l}} - \omega_{\mathbf{q}} - \omega_{\mathbf{r}}) \times (2\pi)^{d+1} \delta^{(d)}(\mathbf{p} + \mathbf{l} - \mathbf{q} - \mathbf{r}) g_{\text{eff}}^2[f](t, \mathbf{p}, \mathbf{q}) \quad (3.54)$$

where we used a free spectral function with dispersion $\omega_{\mathbf{p}} = \mathbf{p}^2/(2m)$ and

$$g_{\text{eff}}^2(t, \mathbf{p}, \mathbf{q}) \equiv \frac{g^2}{|1 + \Pi_{\text{nr}}^R(t, \omega_{\mathbf{p}} - \omega_{\mathbf{q}}, \mathbf{p} - \mathbf{q})|^2} \quad (3.55)$$

incorporates the vertex corrections. The compact form of (3.55) is achieved by using the symmetries of (3.54) and the nonrelativistic ‘one-loop’ retarded self-energy reads

$$\Pi_{\text{nr}}^R(t, \omega, \mathbf{p}) = \lim_{\epsilon \rightarrow 0} g \int \frac{d^d q}{(2\pi)^d} f(t, \mathbf{p} - \mathbf{q}) \times \left[\frac{1}{\omega_{\mathbf{q}} - \omega_{\mathbf{p}-\mathbf{q}} - \omega - i\epsilon} + \frac{1}{\omega_{\mathbf{q}} - \omega_{\mathbf{p}-\mathbf{q}} + \omega + i\epsilon} \right]. \quad (3.56)$$

By comparison to its relativistic counterpart, this may also be obtained up to normalizations directly from (3.53) if evaluated as in (3.55) by expanding the relativistic dispersion for small momenta and taking the dominant contributions, where the constant mass term cancels in the respective frequency sums.

From the self-similar behavior of the distribution (3.29), we can deduce the scaling property

$$\Pi_{\text{nr}}^R(t, \omega_{\mathbf{p}}, \mathbf{p}) = s^{\alpha/\beta-d+2} \Pi_{\text{nr}}^R(s^{-1/\beta}t, \omega_{s\mathbf{p}}, s\mathbf{p}). \quad (3.57)$$

Since for the relevant cases (3.37) and (3.38) we have $\alpha/\beta \geq d$, we conclude by keeping $s\mathbf{p}$ fixed that Π_{nr}^R can become large in the infrared. In this case, we can use $\Pi_{\text{nr}}^R(t, \omega_{\mathbf{p}}, \mathbf{p}) \gg 1$ to find the scaling behavior of

$$g_{\text{eff}}^2(t, \mathbf{p}, \mathbf{q}, \mathbf{r}) = s^{-2(\alpha/\beta-d+2)} g_{\text{eff}}^2(s^{-1/\beta}t, s\mathbf{p}, s\mathbf{q}, s\mathbf{r}). \quad (3.58)$$

Therefore, we expect the effective matrix element squared to become small in the infrared in accordance with related studies [41]. In turn, we will see in the following that at the same time the distribution function $f(t, \mathbf{p})$ can grow significantly, which results in a ‘Bose enhancement’ of scatterings that counteracts the diminished effective coupling.

We use (3.54) in the corresponding kinetic equation (3.42) and find for the scaling of the collision term

$$\begin{aligned} C_{\text{nr}}^{\text{NLO}}[f](t, \mathbf{p}) &= s^{-(2-\alpha/\beta)} C_{\text{nr}}^{\text{NLO}}[f](s^{-1/\beta}t, s\mathbf{p}) \\ &= t^{\alpha-2\beta} C_{\text{nr}}^{\text{NLO}}[f_S](1, t^\beta \mathbf{p}). \end{aligned} \quad (3.59)$$

Remarkably, with this the exponent β can be obtained solely from the scaling relation (3.33) without using in addition energy or particle conservation, whereas the different solutions for α arise from imposing (3.37) or (3.38), respectively. We thus find in the overoccupied infrared regime for

$$\text{nonrel. transport: } \beta = \frac{1}{2} \text{ of } \begin{cases} \text{particles: } & \alpha = d/2 \\ \text{energy: } & \alpha = (d+2)/2 \end{cases} \quad (3.60)$$

This is a central analytic result of this chapter. In contrast to the previously known negative scaling exponents from perturbative estimates given in Sec. 3.4.2, one observes that the positive values of α and β obtained here describe an *inverse* particle transport with growing occupation number in the infrared. The quantitative agreement of the NLO estimates $\alpha = 3/2$ and $\beta = 1/2$ for $d = 3$ with the full simulation results of Sec. 3.3.2 for the relativistic and Sec. 3.2.2 for the nonrelativistic theory is remarkable. Both the approximate analytic and the full simulation results within their numerical accuracy indicate no strong dependence on N .

For comparison, we finally also analyze the relativistic kinetic equation with (3.51) in the absence of any mass gap. To this end, we use $\omega_{\mathbf{p}} = |\mathbf{p}|$ and proceed as in the nonrelativistic case to find scaling relations for α and β . This leads to

$$C^{\text{NLO}}[f](t, \mathbf{p}) = t^{\alpha-\beta} C^{\text{NLO}}[f_S](1, t^\beta \mathbf{p}) \quad (3.61)$$

and we find for the

$$\text{rel. transport: } \beta = 1 \text{ of } \begin{cases} \text{particles: } & \alpha = d \\ \text{energy: } & \alpha = d + 1 \end{cases}. \quad (3.62)$$

These estimates indicate that the simulation results of Sec. 3.3.2 for the relativistic theory cannot be interpreted in terms of massless scaling in the infrared, which is explained by the presence of a mass gap in Sec. 3.3.3.

3.5 Anomalous scaling

The kinetic description of Sec. 3.4 assumes canonical values for the dynamic exponent z , which describes the scaling of the dispersion (3.39). For the relativistic theory without a mass gap, $\omega_{\mathbf{p}} = |\mathbf{p}|$ is employed. For the Gross-Pitaevskii theory, in the presence of a condensate, the approximate (Bogoliubov) dispersion is given by [142]

$$\omega(\mathbf{p}) = \sqrt{\frac{\mathbf{p}^2}{2m} \left(\frac{\mathbf{p}^2}{2m} + 2g|\psi_0|^2 \right)}. \quad (3.63)$$

At larger momenta, or in the absence of a condensate, one recovers $\omega_{\mathbf{p}} = \mathbf{p}^2/(2m)$, while for low momenta one has $\omega_{\mathbf{p}} = c|\mathbf{p}|$ with $c \equiv \sqrt{g|\psi_0|^2/m}$.

From a field theoretic point of view, these dispersions with integer-valued z are implemented using a canonical spectral function, such as the free-field form

$$\tilde{\rho}_0(p^0, \mathbf{p}) = 2\pi \operatorname{sgn}(p^0) \delta((p^0)^2 - \omega_{\mathbf{p}}^2) \quad (3.64)$$

for the relativistic theory, where $\tilde{\rho} = -i\rho$ and ρ is defined in Eq. (2.16). In principle, nonperturbative scaling phenomena may involve an anomalous scaling exponent for the full spectral function $\tilde{\rho}(p^0, \mathbf{p})$ of the interacting theory. Using spatial isotropy we may write

$$\tilde{\rho}(p^0, \mathbf{p}) = s^{2-\eta} \tilde{\rho}(s^z p^0, s\mathbf{p}), \quad (3.65)$$

with a nonequilibrium ‘anomalous dimension’ η . The dynamic scaling exponent z appears since only spatial momenta are related by rotational symmetry and frequencies may scale differently also in the relativistic theory because of medium effects.

Small discrepancies between the results of our full numerical simulations and the analytic estimates of previous sections could possibly be rooted in the canonical assumption of an integer-valued z and $\eta = 0$. This concerns mainly the infrared regime, where strongly nonlinear behavior occurs. For instance, corresponding infrared scaling phenomena in thermal equilibrium near continuous phase transitions can exhibit non-trivial scaling exponents with a noncanonical z and a nonzero (but typically small) value for η , which is also captured by the NLO approximation employed [143].

Therefore, we consider in this section a field theoretical calculation of the self-similar behavior near nonthermal fixed points taking into account the possibility of anomalous scaling. It is again based on the two-particle irreducible (2PI) generating functional in quantum field theory, which is expanded up to next-to-leading order in the number of field components N [107, 108] (see Sec. 2.3.3). However, without using the additional assumption of a canonical form for the spectral function underlying the kinetic theory of Sec. 3.4.

3.5.1 Nonrelativistic field theory

We consider the nonrelativistic quantum field theory defined by the action (2.4) for $N = 1$ and written in terms of the complex field $\hat{\psi}$. Analog to Eqs. (2.15) and (2.16) we define the

spectral and statistical functions¹³

$$\tilde{\rho}_{ab}(x, y) = \langle [\hat{\psi}_a(x), \hat{\psi}_a^\dagger(y)] \rangle, \quad (3.66)$$

$$F_{ab}(x, y) = \frac{1}{2} \langle \{ \hat{\psi}_a(x), \hat{\psi}_b^\dagger(y) \} \rangle_c. \quad (3.67)$$

Here the index notation for $a, b = 1, 2$ employs

$$\hat{\psi}_1 \equiv \hat{\psi} \quad , \quad \hat{\psi}_2 \equiv \hat{\psi}^\dagger \quad (3.68)$$

in order to have a compact notation for the four different two-point functions that can be built from two complex fields. As mentioned in Sec. 2.2.2, the anticommutator and commutator expectation values are related by the fluctuation-dissipation relation (2.18) in thermal equilibrium. However, they are in general linearly independent for systems out of equilibrium. The absence of a fluctuation-dissipation relation is a crucial property of the scaling behavior near the nonthermal fixed points discussed.

To derive effective (off-shell) kinetic equations we start with the 2PI evolution equations for $F_{ab}(x, y)$ and $\tilde{\rho}_{ab}(x, y)$ given in Eqs. (2.30) and (2.31) for vanishing macroscopic field. After a gradient expansion to lowest order one obtains the transport equations presented in Eqs. (2.56) and (2.58) in Sec. 2.4. It is important to notice that, because of the lowest order gradient expansion, the spectral function is time-independent. We expand the self-energy to NLO in the 2PI $1/N$ expansion as explained in Sec. 2.3.3 and use the gradient expansion to obtain closed expressions for the self-energies (see Sec. 2.4). In this way, one obtains after some manipulations [70] and using $(F_p)_{ab} \equiv F_{ab}(t, p)$ and $(\tilde{\rho}_p)_{ab} \equiv \tilde{\rho}_{ab}(p)$ as a compact matrix notation in (a, b) -index space:¹⁴

$$\begin{aligned} \frac{\partial}{\partial t} \text{Tr}[\sigma^3 F_p] = & - \frac{1}{2(2\pi)^{2d+2}} \int d^{d+1}q d^{d+1}l d^{d+1}r \delta^{(d+1)}(p - q + l - r) g_{\text{eff}}^2[F](t, p - q) \\ & \times \left\{ 2 \text{Tr}[F_p F_q] \text{Tr}[F_l \tilde{\rho}_r] + \text{Tr}[F_p \tilde{\rho}_q] \text{Tr}[F_l F_r] - \text{Tr}[\tilde{\rho}_p F_q] \text{Tr}[F_l F_r] \right\}, \end{aligned} \quad (3.69)$$

where $\text{Tr}[F_p] \equiv F_{aa}(t, p)$ and $\sigma^3 = \text{diag}(1, -1)$ denotes the third Pauli matrix. The time- and momentum-dependent effective coupling squared corresponding to (3.55) reads

$$g_{\text{eff}}^2(t, p) = \frac{g^2}{|1 + \Pi_{\text{nr}}^R(t, p)|^2} \quad (3.70)$$

with the retarded self-energy

$$\Pi^R(t, p) = g \int \frac{d^{d+1}q}{(2\pi)^{d+1}} F_{ab}(t, q - p) G_{ba}^R(q) \quad (3.71)$$

in terms of the retarded propagator $G_{ab}^R(p)$.

¹³The two definitions are related by $F_{\text{complex-basis}} = S F_{\text{real-basis}} S^\dagger$ with $S = \frac{1}{\sqrt{2}} \begin{pmatrix} 1 & i \\ 1 & -i \end{pmatrix}$ and similarly for the spectral function ρ .

¹⁴The corresponding equation (3.69) for N complex fields can be obtained by multiplying the right hand side with $1/N^2$.

To make contact with the definition of the distribution function in (3.11), we write for $\mathbf{p} \neq 0$:

$$f(t, \mathbf{p}) + \frac{1}{2} = \int_0^\infty \frac{dp^0}{2\pi} \text{Tr}[\sigma^3 F(t, p^0, \mathbf{p})], \quad (3.72)$$

where we write the ‘quantum-half’ for completeness though we always consider high typical occupancies such that it can be neglected. With the field theoretical definition of the distribution function at hand, we can obtain a corresponding ‘collision term’ for $\partial f(t, \mathbf{p})/\partial t = C[F](t, \mathbf{p})$ from the p^0 -integral of the RHS of (3.69).

Applying (3.29) to the distribution function with $f(t, \mathbf{p}) \gg 1$ for typical momenta, self-similar behavior for the correlators is described by

$$F_{ab}(t, p^0, \mathbf{p}) = s^{\alpha/\beta+z} F_{ab}(s^{-1/\beta}t, s^z p^0, s\mathbf{p}) \quad (3.73)$$

in addition to the scaling behavior (3.65) for the spectral function $\tilde{\rho}_{ab}(p^0, \mathbf{p})$. We emphasize that this scaling ansatz for F assumes that the exponent z appearing in (3.73) is the same as in (3.65). This assumption will be reconsidered in Chap. 5. This behavior further means $F_{ab}(t, p^0, \mathbf{p}) = t^{\alpha+\beta z} F_{S,ab}(t^{z\beta} p^0, t^\beta \mathbf{p})$ with $F_{S,ab}(p^0, \mathbf{p}) \equiv F_{ab}(1, p^0, \mathbf{p})$. In particular, $f_S(\mathbf{p}) = \int_0^\infty dp^0 / (2\pi) \text{Tr}[\sigma^3 F_S(p^0, \mathbf{p})]$ in this highly occupied scaling regime according to (3.72). With

$$g_{\text{eff}}^2[F](t, p^0, \mathbf{p}) = t^{-2[\alpha+\beta(2-\eta-d)]} g_{\text{eff}}^2[F_S](t^{z\beta} p^0, t^\beta \mathbf{p}) \quad (3.74)$$

one finds

$$C[F](t, \mathbf{p}) = t^{\alpha-\beta(2-\eta)} C[F_S](t^\beta \mathbf{p}). \quad (3.75)$$

We can now proceed in complete analogy to the analysis of Sec. 3.4 from which we find the solution to the scaling relation:

$$\beta = \frac{1}{2-\eta}, \quad (3.76)$$

where the dimensionality d and the exponent α have dropped out. In addition we have the time-independent equation for the nonthermal fixed point function:

$$[\alpha + \beta \mathbf{p} \cdot \nabla_{\mathbf{p}}] f_S(\mathbf{p}) = C[F_S](\mathbf{p}) \quad (3.77)$$

corresponding to (3.32).

To obtain a second scaling relation for the determination of α , it is important to note that the particle number density $n = \int_0^\infty dp^0 \int d^d p / (2\pi)^{d+1} \text{Tr}[\sigma^3 F(t, p)]$ and the energy density $\epsilon = \int_0^\infty dp^0 \int d^d p / (2\pi)^{d+1} p^0 \text{Tr}[\sigma^3 F(t, p)]$ are conserved during the evolution. We find:

$$\alpha = \frac{d}{2-\eta} \quad (\text{particle transport}), \quad (3.78)$$

$$\alpha = \frac{d+z}{2-\eta} \quad (\text{energy transport}). \quad (3.79)$$

Of course, taking $\eta = 0$ and $z = 2$ we recover the results of Sec. 3.4.3. Remarkably, one observes that the scaling exponent for the nonrelativistic particle cascade is independent of the dynamic exponent z . Within the approximations used in this section, this has the important special

consequence that the same scaling behavior for particle transport is found no matter whether the low-momentum dispersion is quadratic, or linear as for the Bogoliubov dispersion (3.63) in the presence of a condensate.

Comparing the expressions for particle transport to our simulation results of Sec. 3.2.2, within the numerical errors we see no strong indication for any deviation from the canonical value $\eta = 0$ employed for the analytical estimates of Sec. 3.4.

We may also consider the growth of the condensate during the self-similar evolution, which we investigated numerically in Secs. 3.2 and 3.3. With $F_{ab}(t, t, \mathbf{p}) \sim \int dp^0 F_{ab}(t, p^0, \mathbf{p})$ and using (3.73) we obtain the scaling of a characteristic mode of the equal-time correlator $\sim t^\alpha$. Since $\alpha > 0$ for not too large η , the condensate zero-mode is expected to grow as a power-law in time. The value $\alpha \simeq 3/2$ for $d = 3$ rather accurately describes our numerical findings.

For completeness, we indicate how to recover the kinetic equation of Sec. 3.4.3 from the evolution equation (3.69) for the anticommutator expectation value. First, one inserts the free-field form of the spectral function [144]

$$\tilde{\rho}(p) = 2\pi \begin{pmatrix} \delta(p^0 - \omega_{\mathbf{p}} & 0 \\ 0 & -\delta(p^0 + \omega_{\mathbf{p}}) \end{pmatrix}, \quad (3.80)$$

where $\omega_{\mathbf{p}} = \mathbf{p}^2/2m$. Second, one can define an off-shell distribution function $f(t, p)$ as

$$F_{ab}(t, p) = \left(f(t, p) + \frac{1}{2} \right) \tilde{\rho}_{ab}(p) \quad (3.81)$$

with $-f(t, -p) = f(t, p) + 1$ in accordance to (3.72). Finally, one uses the identity

$$G_{ba}^R(p) = \lim_{\epsilon \rightarrow 0} \int \frac{d\omega}{2\pi} \frac{-i\rho_{ba}(\omega, \mathbf{p})}{\omega - p^0 - i\epsilon}, \quad (3.82)$$

in order to obtain (3.56) from (3.71). Inserting all this yields for $f(t, \mathbf{p}) \gg 1$ the nonrelativistic kinetic equation employed in Sec. 3.4.3.

3.5.2 Relativistic field theory

We now consider a relativistic quantum field theory for an N -component real scalar field defined by the action (2.1). Following the discussion of Sec. 3.4.3 we will focus here on the case without a mass gap, since otherwise the above nonrelativistic results apply. Along the lines of the previous section, we consider the spectral and statistical functions introduced in Eqs. (2.15) and (2.16) and assume further that $F_{ab} = F \delta_{ab}$ and $\tilde{\rho}_{ab} = \tilde{\rho} \delta_{ab}$. According to (3.18) and taking into account the quantum-half, we get the distribution function for sufficiently high occupancies for $\mathbf{p} \neq 0$ as:

$$f(t, \mathbf{p}) + \frac{1}{2} = \int_0^\infty \frac{dp^0}{2\pi} 2p^0 F(t, p). \quad (3.83)$$

The derivation of the evolution equation for $f(t, \mathbf{p})$ follows along the same lines as for the nonrelativistic theory of the previous section. Using the 2PI $1/N$ expansion to NLO, the

lowest-order gradient expansion leads to

$$\begin{aligned} \frac{\partial f}{\partial t}(t, \mathbf{p}) &= \frac{1}{6N(2\pi)^{2d+3}} \int_0^\infty dp^0 dl^0 dq^0 dr^0 \int d^d l d^d q d^d r \delta^{(d+1)}(p+l-q-r) \\ &\quad \times \lambda_{\text{eff}}^2[F](t, p, l, q, r) \left[(\tilde{\rho}_p F_l + F_p \tilde{\rho}_l) F_q F_r - F_p F_l (\tilde{\rho}_q F_r + F_q \tilde{\rho}_r) \right], \end{aligned} \quad (3.84)$$

where $F_p = F(t, p)$, and λ_{eff}^2 is defined as

$$\lambda_{\text{eff}}^2(t, p, l, q, r) = \frac{\lambda^2}{3} [v_{\text{eff}}(t, p+l) + v_{\text{eff}}(t, p-q) + v_{\text{eff}}(t, p-r)] \quad (3.85)$$

with the vertex function $v_{\text{eff}}(t, p)$ given in (2.62).

With the above kinetic equation we now search for self-similar solutions (3.29). For this we have to write

$$F(t, p^0, \mathbf{p}) = s^{\alpha/\beta+2z} F(s^{-1/\beta}t, s^z p^0, s\mathbf{p}), \quad (3.86)$$

in addition to the scaling behavior (3.65) for the spectral function. We note again that we assume the same z in both (3.86) and (3.65). Inserting the scaling behavior into the evolution equation (3.84) leads to the solution

$$\beta = \frac{1}{2 - \eta - z}, \quad (3.87)$$

and an equation for the universal scaling function corresponding to (3.77). Imposing particle number and energy conservation yields

$$\alpha = \frac{d}{2 - \eta - z} \quad (\text{particle transport}), \quad (3.88)$$

$$\alpha = \frac{d + z}{2 - \eta - z} \quad (\text{energy transport}). \quad (3.89)$$

For $\eta = 0$ and $z = 1$ these values agree with the results in the absence of a mass gap of section 3.4.3. We finally note that the relativistic kinetic equation of that section can be obtained from (3.84) by using the corresponding definition (3.81) with the free spectral function (3.64).

3.6 Conclusions

A consistent picture has emerged for the universal self-similar dynamics of relativistic and nonrelativistic field theories near nonthermal fixed points. The results of classical-statistical numerical simulations are well described by analytic estimates based on the vertex-resummed kinetic theory. The latter extends well-established kinetic descriptions to the nonperturbative regime of overoccupied modes.

The vertex-resummed kinetic theory links the perturbative phenomenon of weak wave turbulence relevant at higher momenta to the nonperturbative physics of strong turbulence and vorticity of the underlying field configurations in the highly nonlinear infrared regime. It is

striking that the range of validity of kinetic descriptions can indeed be extended to capture these very different regimes.

For the examples of nonrelativistic (Gross-Pitaevskii) and relativistic scalar field theory with quartic self-interactions, we have seen that the infrared scaling exponents as well as scaling functions agree. This becomes possible because of the emergence of a mass gap in the relativistic theory. In contrast to the previously known negative values for the scaling exponents α and β from perturbative estimates, we find that their positive values $\alpha = d/(2 - \eta)$ and $\beta = 1/(2 - \eta)$ obtained for small anomalous dimension η describe an inverse particle transport with growing occupation number in the infrared. The growth exponent α is found to describe also the far-from-equilibrium formation of the Bose condensate.

Moreover, the nonrelativistic particle transport solution has the remarkable property to be independent of the dynamic scaling exponent z . As a consequence, this solution applies equally well to a dispersion with quadratic momentum dependence or a possible linear behavior below the characteristic coherence momentum scale in the presence of a Bose gas condensate. However, this result was obtained under the assumption that the statistical and spectral functions scale with the same exponent z . The validity of this will be further investigated in Chap. 5.

The corresponding dynamic universality class turns out to be remarkably large, encompassing both relativistic as well as nonrelativistic quantum and classical systems. As a consequence, the applications can range from table-top experiments with ultracold quantum gases to inflationary dynamics during the very early stages of our universe.

Chapter 4

Unequal-time correlators and Dynamical Exponent

This chapter is based on the paper “*Universal scaling of unequal-time correlation functions in ultracold Bose gases far from equilibrium*”, A. Schachner, A. Piñeiro Orioli and J. Berges, published in Phys. Rev. A **95**, 053605 (2017) [145]. Figures and parts of the text are taken from that reference. Part of the work is a continuation of the studies started in the Bachelor Thesis “*Universality and far from equilibrium dynamics in unequal time correlation functions for non-relativistic scalar field theories*” by Andreas Schachner (2016).

The aim of this chapter is to extend the scaling analysis near the nonthermal fixed point presented in Chap. 3 to unequal-time correlation functions. Since we showed that both relativistic and nonrelativistic theories in the infrared regime belong to the same universality class far from equilibrium, we focus here on the dynamics of the nonrelativistic Bose gas.

The scaling behavior of unequal-time correlators is described by a new scaling exponent, the dynamical exponent z . This exponent relates characteristic frequency and momenta during the scaling regime, and is hence connected to a dispersion relation. Close to equilibrium its value may be inferred from equal-time quantities using scaling relations [133]. However, this is less clear far from equilibrium. For instance, in the scaling regime for energy transport towards short distance scales depicted in Fig. 3.1, z represents an independent exponent [40]. To establish the universality classes of nonthermal fixed points, it is therefore crucial to determine the role and value of z .

In order to extract z for the long-distance scaling behavior of the nonthermal fixed point, i.e., the infrared regime, we consider the zero-momentum mode of the statistical propagator F , defined in Eq. (3.67). In numerical simulations this will introduce a dependence on the finite volume V , which needs to be carefully taken into account in the scaling analysis. As we shall see in Chap. 5, one needs to be cautious as well when interpreting the extracted exponent z .

4.1 Scaling of unequal-time correlators

Similar to Chap. 3, we consider again a one-component nonrelativistic Bose gas described by a complex field $\hat{\psi}(t, \mathbf{x})$ and action (2.4). We investigate here the dynamics of spatially homogeneous systems such that the two-point correlator

$$F(t, t', \mathbf{x} - \mathbf{x}') \equiv \frac{1}{2} \langle \hat{\psi}(t, \mathbf{x}) \hat{\psi}^\dagger(t', \mathbf{x}') + \hat{\psi}^\dagger(t', \mathbf{x}') \hat{\psi}(t, \mathbf{x}) \rangle \quad (4.1)$$

depends only on the spatial difference $\mathbf{x} - \mathbf{x}'$. This definition is the quantum equivalent of (3.10) and identical to the first diagonal element of (3.67). Note that the nonequilibrium evolution entails a breaking of time-translation invariance and a dependence on both t and t' separately.

At equal space-time points ($t = t'$, $\mathbf{x} = \mathbf{x}'$) the quantity (4.1) corresponds to the density n , i.e., the conserved total particle number N_{total} divided by the system's volume V :

$$n \equiv \frac{N_{\text{total}}}{V} = F(t, t, \mathbf{x} - \mathbf{x}). \quad (4.2)$$

For our purposes, it is instructive to consider the absolute value of the spatial integral of (4.1) over the volume $V = L^d$ in a box of length L in d spatial dimensions:

$$F(\tau, \Delta t, V) \equiv \left| \int_V F(t, t', \mathbf{x}) d^d x \right|. \quad (4.3)$$

Here we introduced the central-time coordinate τ and the relative-time coordinate Δt as

$$\tau \equiv \frac{t + t'}{2}, \quad \Delta t \equiv t - t'. \quad (4.4)$$

Taking the absolute value in (4.3) amounts to disregarding a rotating global phase $\sim e^{i\mu\Delta t}$, which could also be absorbed in a redefinition of the fields by $\psi \rightarrow e^{-i\mu\Delta t}\psi$. Furthermore, since the correlation function (4.3) is symmetric under exchange of t and t' , $F(\tau, \Delta t, V) = F(\tau, -\Delta t, V)$, we restrict our presentation to $\Delta t > 0$. Though we keep the dimension d general in our notation, all our numerical results presented in subsequent sections will concern $d = 3$.

Our aim is to investigate scaling solutions of nonequilibrium correlation functions near non-thermal fixed points. The scaling behavior of the correlation function (4.3) may be expressed in terms of real scaling exponents α , β and z as

$$F(\tau, \Delta t, V) = s^{\alpha/\beta} F(s^{-1/\beta}\tau, s^{-z}\Delta t, s^{-d}V) \quad (4.5)$$

under rescaling with the real scaling parameter $s > 0$. The ‘‘occupation number’’ exponent α and the ‘‘central-time’’ exponent β have been computed and discussed in detail for $\Delta t \equiv 0$ in Chap. 3 (Ref. [66]). To determine the ‘‘dynamic’’ scaling exponent z , which is associated to changes in relative times Δt , and the respective unequal-time scaling functions is the main focus of this chapter.¹

¹The scaling ansatz (4.5) is not the only choice to be found in the literature. In studies of ageing and phase-ordering kinetics other scaling forms are sometimes used [78, 132], which may involve splitting the function into

Far from equilibrium, i.e., well beyond the linear response regime, both the central-time exponent β and relative-time exponent z can generally be linearly independent as, for instance, realized in perturbative scaling regimes for energy transport towards short distance scales in related models [40]. Here, we consider the nonperturbative scaling regime (see Fig. 3.1) associated to particle transport towards long-distance scales [66] and determine the role and value of z .

The importance of z stems from the fact that the dynamic scaling exponent for relative times is directly related to the characteristic frequency dependence or dispersion of the model. The dependence on the frequency ω is obtained from Fourier transforming (4.5) with respect to relative times, which gives

$$\begin{aligned} F(\tau, \omega, V) &= 2 \int_0^\infty e^{i\omega\Delta t} F(\tau, \Delta t, V) d(\Delta t) \\ &= s^{z+\alpha/\beta} F(s^{-1/\beta}\tau, s^z\omega, s^{-d}V). \end{aligned} \quad (4.6)$$

We anticipate though that the frequency dependence and thus z may be different for other correlators, as we will see in Chap. 5.

Because the system is considered to have a finite size L^d , the system can already become effectively ordered, when the characteristic correlation length is $\approx L$. Only for shorter times the universal scaling behavior with a full dependence on τ , Δt and V as in (4.5) is expected to hold. Below we determine the corresponding time scale for condensation from equal-time correlation functions and compare this to the characteristic correlation time obtained from unequal-time functions.

4.2 Nonequilibrium evolution

Analog to Chap. 3, we start with an extreme nonequilibrium distribution of modes $f(0, \mathbf{p}) \equiv f_0(\mathbf{p}) \sim 1/\zeta$ with small diluteness parameter $\zeta \ll 1$ in order to observe self-similar dynamics. Because of the large occupancies involved, especially in the infrared regime, we use again the mapping to classical-statistical field theory [99] (c.f. Sec. 2.5 and Chap. 3) to simulate the nonequilibrium dynamics of the Bose system.² In classical-statistical simulations the unequal-time correlation function (4.1) is computed as $\langle \psi(t, \mathbf{x}) \psi(t', \mathbf{x}') \rangle$, where brackets $\langle \dots \rangle$ denote an ensemble average over classical trajectories.

Specifically, we start with a distribution function given by $f_0(\mathbf{p}) = 25/(mgQ)$ for momenta $|\mathbf{p}| < Q$ and zero otherwise. The evolution is described by the Gross-Pitaevskii equation, Eq. (3.4), with parameters chosen as in Chap. 3. To reflect the classical-statistical nature of the dynamics in the highly occupied regime, we measure time in units of $2m/Q^2$ and volumes in units of Q^3 . As a consequence, the combination $F(\tau, \Delta t, V)2mgQ$ for (4.3) does not depend

various parts with different scaling behavior, or rescaling combinations of the times t and t' other than Δt and τ .

²The approximate mapping is usually based on a sufficiently large occupancy of typical modes for equal-time correlation functions. While the validity of this argument is less clear for the computation of general unequal-time correlation functions, it should be valid for power-law behavior in scaling regimes as considered in this work.

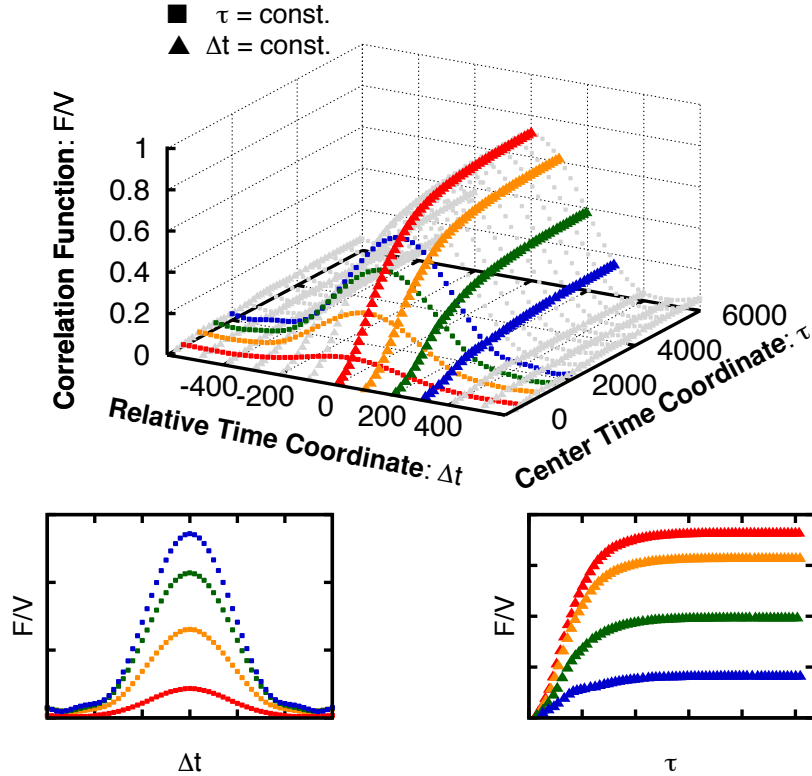


FIGURE 4.1: The upper graph shows the two-times correlation function (4.3) as a function of the central-time coordinate τ and the relative-time coordinate Δt for a volume V with 128^3 lattice points. The colored lines correspond to slices of constant τ (squares) and constant Δt (triangles), which are separately displayed in the lower graphs.

on the values of m , g and Q . Though we will write t , V and F , we always imply the rescalings $t \rightarrow tQ^2/2m$, $\mathbf{p} \rightarrow \mathbf{p}/Q$, $V \rightarrow VQ^3$ and $F(\tau, \Delta t, V) \rightarrow F(\tau, \Delta t, V) 2mgQ$ in the following.

To give an overview, Fig. 4.1 shows the evolution of the correlation function $F(\tau, \Delta t, V)$ as a function of the central-time coordinate τ and the relative time Δt for a volume $V = 128^3$.³ For better visualization, the lower graphs of Fig. 4.1 give slices of constant τ (Δt) as a function of Δt (τ) in the left (right) plot.

Roughly, the correlation function becomes wider and its overall amplitude larger as time passes. The decay of F as a function of Δt establishes a characteristic correlation time $\Delta t_*(V)$, whose scaling with volume is investigated in detail in Sec. 4.3. Likewise, the growth of F as a function of τ is seen to terminate around a time $\tau_*(V)$, which is discussed in the next section. In the previous chapter (Ref. [66]), $\tau_*(V)$ has been associated to the characteristic time scale for condensate formation.

³For all numerical estimates we employ an ultraviolet cutoff at $\sqrt{12}Q$ and verify that our results are insensitive to the value of the cutoff.

4.3 Finite size scaling

In the following we investigate the scaling behavior of the correlation function $F(\tau, \Delta t, V)$ shown in Fig. (4.1), as a function of the finite volume. In a scaling regime described by (4.5), we may choose $s = V^{1/d}$ eliminating the scaling parameter to obtain

$$F(\tau, \Delta t, V) = V^{\alpha/(\beta d)} F_V(V^{-1/(\beta d)}\tau, V^{-z/d}\Delta t), \quad (4.7)$$

where the scaling function F_V is defined in terms of $F_V(V^{-1/(\beta d)}\tau, V^{-z/d}\Delta t) \equiv F(V^{-1/(\beta d)}\tau, V^{-z/d}\Delta t, 1)$. This form makes it explicit that in the scaling regime F_V depends only on two arguments instead of separately on τ , Δt and V . Similarly, it is instructive to consider the choices $s = \tau^\beta$ in (4.5) leading to

$$F(\tau, \Delta t, V) = \tau^\alpha F_\tau(\tau^{-\beta z}\Delta t, \tau^{-\beta d}V), \quad (4.8)$$

or $s = \Delta t^{1/z}$ in (4.5) to get the scaling form

$$F(\tau, \Delta t, V) = \Delta t^{\alpha/\beta z} F_{\Delta t}(\Delta t^{-1/\beta z}\tau, \Delta t^{-d/z}V). \quad (4.9)$$

One may use any of the scaling forms (4.7)–(4.9) to efficiently extract the universal scaling exponents α , β and z from the numerical data. The different shapes of the scaling functions F_V , F_τ and $F_{\Delta t}$ are also universal after fixing their overall amplitudes and the amplitudes of their arguments, similar to the universal scaling function f_S computed in Chap. 3 (see Fig. 3.2) for the equal-time case.

Because the system has a finite size L^d , it can already become effectively ordered at a finite time, as shown for equal-time correlators in Chap. 3 (Ref. [66]). Using the scaling form (4.7), we denote the condensation time

$$\tau_* \sim V^{1/(\beta d)} \quad (4.10)$$

with $\tau_* = \tau_*(V, \Delta t = 0)$ as the time where F_V at equal-times becomes approximately independent of τ for given volume V , i.e., $F_V(V^{-1/(\beta d)}\tau, 0) \simeq \text{const}$ for $\tau \gtrsim \tau_*$. That F_V changes its behavior qualitatively from a power-law $\sim \tau^\alpha$ to become an approximate constant around the time τ_* is indeed seen in numerical solutions as demonstrated in Fig. 4.2.⁴ The figure is discussed in more detail below when we extract the values of the scaling exponents. The interpretation of τ_* as the time for the formation of a Bose condensate was explained in the previous chapter (Ref. [66]).⁵

In addition, we define the correlation time Δt_* from the decay of F_V as a function of relative time, which is exemplified in Fig. 4.3. More precisely, we determine the decay-time from the “width” given by the difference between the inflection points of the curve $F_V(V^{-1/(\beta d)}\tau = \text{const}, V^{-z/d}\Delta t)$ as a function of $V^{-z/d}\Delta t$. This difference is found to grow monotonically with τ until it reaches a maximum at a time $\tau_\Delta(V)$, i.e., the width of the scaling function F_V becomes independent of the central time for $\tau \gtrsim \tau_\Delta$. Though τ_Δ and τ_* turn out to scale in the same way with volume as (4.10), they can be numerically different and we find $\tau_\Delta < \tau_*$. In

⁴This figure is equivalent to Fig. 3.5 except in a double logarithmic plot.

⁵Note that in the previous chapter we wrote $\tau_* \sim V^{1/\alpha}$. Since we have shown that $\alpha = \beta d$ for the inverse particle cascade, this relation is equivalent to Eq. (4.10).

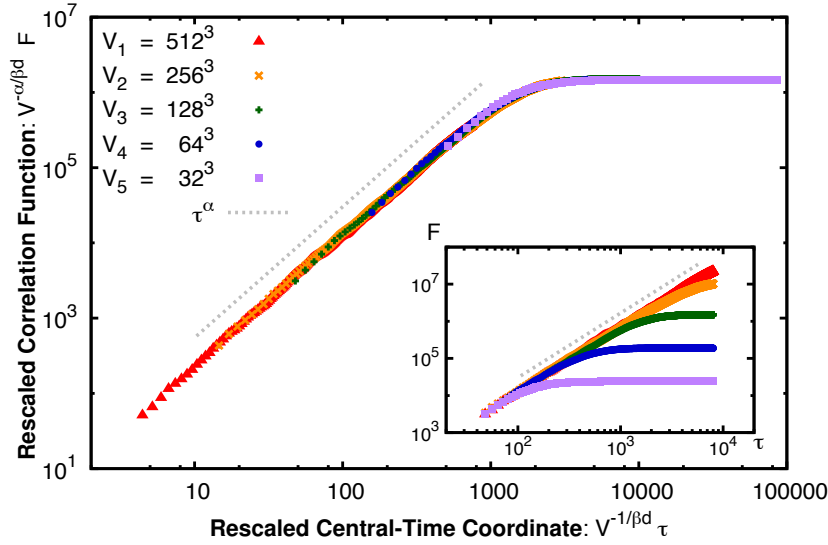


FIGURE 4.2: Rescaled correlation function $F_V = V^{-\alpha/(\beta d)} F$ as a function of the rescaled central time $V^{-1/(\beta d)} \tau$ for $\Delta t = 0$ and a range of volumes V in $d = 3$ spatial dimensions. For the rescalings we employ $\alpha/(\beta d) = 1$ and $1/(\beta d) = 0.57$. The inset shows the function F without rescaling for comparison. The dashed line represents the power law behavior $\sim \tau^\alpha$ with $\alpha = 1.74$. The time where the power-law behavior stops and the curve flattens indicates the characteristic condensation time $\tau_*(V)$.

particular, in this regime (4.7) implies

$$\Delta t_* \sim V^{z/d} \quad (4.11)$$

with $\Delta t_* = \Delta t_*(V, \tau = \tau_\Delta(V))$.

Since $V = L^d$, the condensation time (4.10) and the correlation time (4.11) are related to respective lengths, which scale as

$$L \sim \tau_*^\beta \sim \Delta t_*^{1/z}. \quad (4.12)$$

A special case occurs if $\beta = 1/z$ for which the scalings with central and relative times are the same. We analyze this possibility below.

In the following we extract the values of the universal exponents and determine the universal shape of the scaling functions. Starting from the initial conditions of Sec. 4.2, we follow numerically the relatively short evolution until the system is attracted to the nonthermal fixed point characterized by scaling. We analyze the scaling behavior for times $\tau < \tau_\Delta(V)$ and $\Delta t < \Delta t_*(V, \tau_\Delta)$ for different volumes V . The evolution in this regime is verified to exhibit the scaling behavior (4.5) with suitably chosen exponents.

We start by considering $\Delta t = 0$ and plot the rescaled correlation function $F_V(V^{-1/(\beta d)} \tau, 0)$ as defined in (4.7). In Fig. 4.2 we show results for a set of volumes with $\{32^3, 64^3, 128^3, 256^3, 512^3\}$ lattice points, respectively. For comparison, the inset shows the correlation function $F(\tau, \Delta t = 0, V)$ for the corresponding values of τ without rescaling. With the appropriate choice of values for the combinations of exponents $\alpha/(\beta d)$ and $1/(\beta d)$, the rescaled curves at different V lie

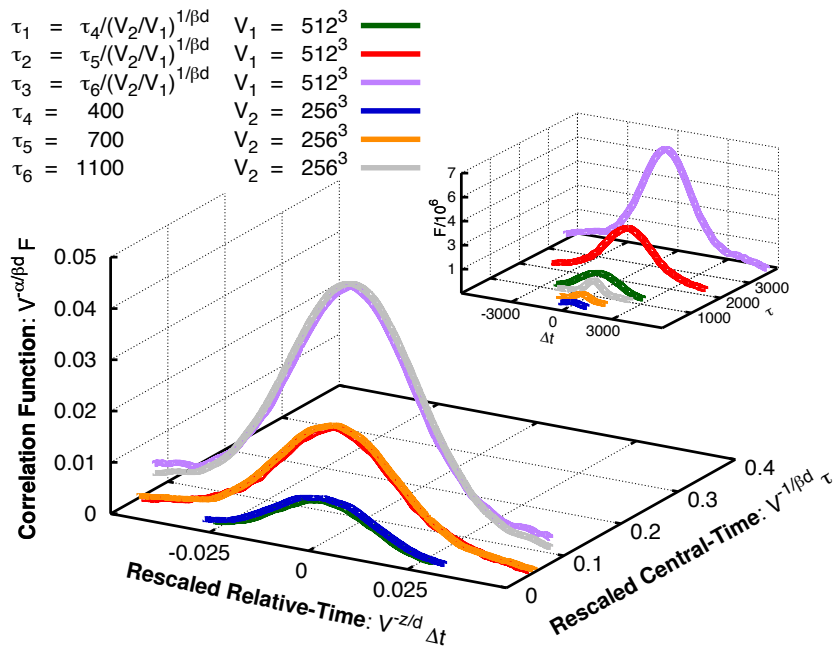


FIGURE 4.3: Rescaled correlation function $F_V = V^{-\alpha/(\beta d)} F$ as a function of the rescaled relative-time coordinate $V^{-z/d} \Delta t$ for fixed values of the rescaled central-time coordinate $V^{-1/(\beta d)} \tau$. We employ $\alpha/(\beta d) = 1.0$, $1/(\beta d) = 0.57$, and $z/d = 0.61$ for two different volumes with $\{256^3, 512^3\}$ lattice points. The inset shows the original function F without rescaling. The “width” of F_V as it decays with growing $|V^{-z/d} \Delta t|$ gives rise to the characteristic correlation time $\Delta t_*(V)$.

remarkably well on top of each other; in particular, since there is a large factor of more than 10^3 between the smallest and the largest volume.

To quantify the values of the exponents and their errors we make use of the fit routine explained in App. B. This yields

$$\frac{\alpha}{\beta d} = 1.00 \pm 0.02, \quad (4.13)$$

$$\frac{1}{\beta d} = 0.57 \pm 0.03, \quad (4.14)$$

where the error bars are due to statistical averaging and fitting errors. We emphasize again that all our numerical values are obtained from simulations in $d = 3$ spatial dimensions. Nevertheless, we keep here the parameter d in the notation to reflect the fact that from the scaling ansatz (4.5) only the combination βd of the scaling exponent for central time (β) and for volume (d) enters.

We are now going to extract the value of z/d from (4.7) for $\Delta t \neq 0$. For visualization purposes, we plot in Fig. 4.3 the rescaled correlation function F_V as a function of $V^{-z/d} \Delta t$ for different values of $V^{-1/(\beta d)} \tau$. To establish the scaling behavior requires the comparison of the correlation function for different volumes V_i at different times τ_i , when plotted versus Δt . In particular, the times chosen need to fulfil $\tau_i/\tau_j = (V_i/V_j)^{1/(\beta d)}$. In doing so, one needs to make sure that the times τ_i lie within the regime where scaling is valid, which lasts longer for larger volumes according to (4.10) and (4.11). For instance, we find that for 256^3 lattice sites the scaling regime is approximately given by the range of times $t, t' \in [200, 3000]$ and for 512^3 it is

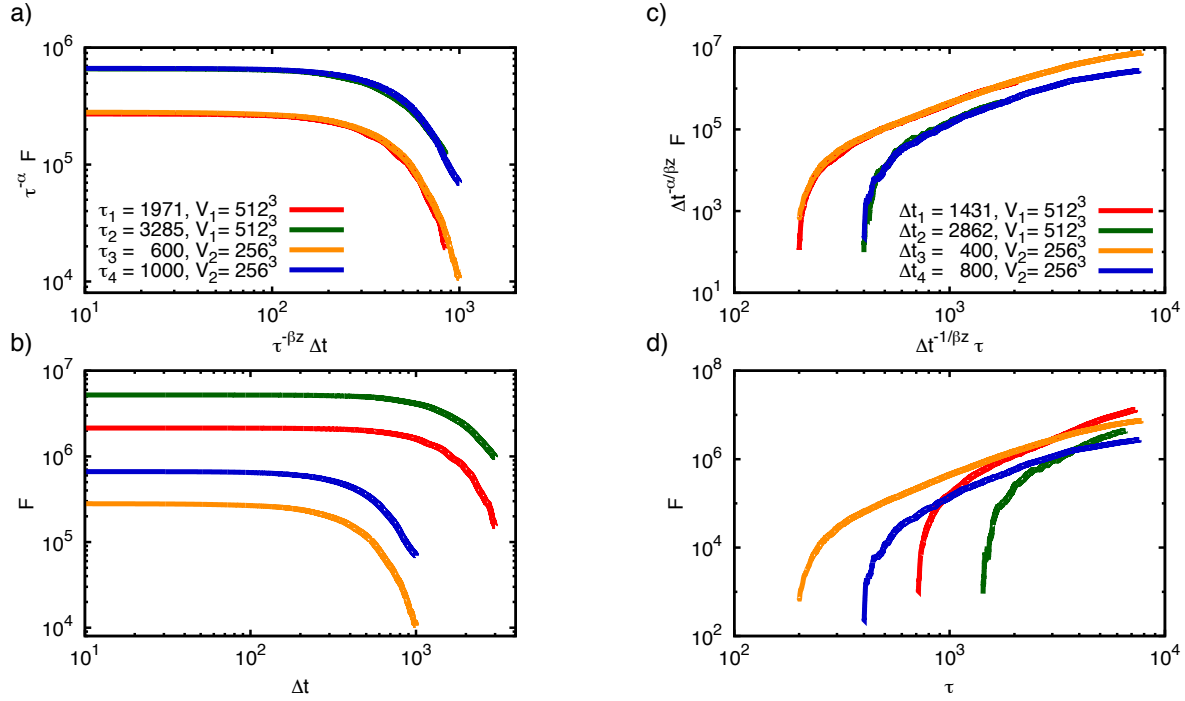


FIGURE 4.4: a) $F_\tau = \tau^{-\alpha} F$ as a function of the rescaled relative time $\tau^{-\beta z} \Delta t$ for two sets of values of $\tau^{-\beta d} V$ employing the exponents $\alpha = 1.74$ and $\beta z = 1.07$. b) Unrescaled function $F(\tau, \Delta t, V)$ for given values of τ as a function of Δt . c) $F_{\Delta t} = \Delta t^{-\alpha/\beta z} F$ as a function of the rescaled central-time $\Delta t^{-1/\beta z} \tau$ for given sets of $\Delta t^{-d/z} V$ with the same exponents. d) Unrescaled function $F(\tau, \Delta t, V)$ as a function of τ for given values of Δt .

$t, t' \in [200, 7000]$. Therefore, we plot in all figures values of τ and Δt which lie approximately within these intervals.

One observes from Fig. 4.3 that the rescaled curves lie pairwise on top of each other to remarkable accuracy. This is a clear demonstration of scaling dynamics in unequal-time correlation functions close to the nonthermal fixed point. Although we show only a couple of different times, we note that the agreement is valid for the whole scaling regime. In order to extract the exponents, we use our previous result (4.14) and employ the fit routine to obtain

$$\frac{z}{d} = 0.61 \pm 0.05. \quad (4.15)$$

As a consistency check, we find that the result for z/d does not depend much on whether we fix both $\alpha/(\beta d)$ and $1/(\beta d)$ by (4.13) and (4.14) or only one of them when applying the fit routine to extract exponents.

We can do the same type of analysis using the scaling forms (4.8) or (4.9), which leads to a determination of the same exponents, however, in different combinations. Fig. 4.4a shows the correlation function $F_\tau = \tau^{-\alpha} F$ as a function of $\tau^{-\beta z} \Delta t$ for two sets of values of $\tau^{-\beta d} V$ with the volumes 256^3 and 512^3 . The original function F without rescalings is given in Fig. 4.4b for comparison. The rescaled curves lie again well on top of each other. With the value of βd

given by (4.14) one obtains from the fit routine

$$\alpha = 1.74 \pm 0.03, \quad (4.16)$$

$$\beta z = 1.07 \pm 0.06, \quad (4.17)$$

which are consistent with the previous results within errors.

Fig. 4.4c shows $F_{\Delta t} = \Delta t^{-\alpha/\beta z} F$ as a function of the rescaled central-time $\Delta t^{-1/\beta z} \tau$ for given sets of $\Delta t^{-d/z} V$ with the exponents found above. For comparison, Fig. 4.4d displays the correlation function $F(\tau, \Delta t, V)$ for given values of Δt versus the central-time coordinate τ without rescalings. The curves corresponding to different volumes V_i and fulfilling $(\Delta t_i/\Delta t_j)^{d/z} = V_i/V_j$ lie pairwise well on top of each other. We checked that the results one obtains for exponents are consistent with the ones presented above within errors. For the plots one needs to fix the value for the dynamical scaling exponent z in order to determine the values of fixed Δt in different volumes. Furthermore, in Figs. 4.3 and 4.4 we only use the largest volumes with 256^3 and 512^3 lattice points since the smaller available volumes are not in the scaling regime for relevant times. Nevertheless, we checked that comparing with data for 128^3 and 256^3 lattices one gets similar results, although they are less reliable due to the short duration of the scaling regime.

The above values for the universal scaling exponents along with the scaling functions displayed represent the central results of this chapter. We first note that the scaling relation $\alpha = \beta d$ expected for particle transport, as shown in Chap. 3, is fulfilled to good accuracy according to (4.13). Furthermore, using $d = 3$ in (4.14) one obtains $\beta = 0.58 \pm 0.03$ and from (4.16) one has $\alpha = 1.74 \pm 0.03$. Comparison to the results (3.14) obtained from the scaling analysis of the (equal-time) distribution function in Chap. 3 indicates consistency within error bars. It is worth noting though, that the relatively large error for α obtained in the equal-time analysis is a result of the rather weak dependence of the distribution function at low momenta, and thus somewhat less accurate than (4.16) (c.f. App. B). In comparison, the value for β obtained in Chap. 3.1 has relatively small statistical errors and comes out directly from the fit procedure, i.e., without involving products such as βz or βd .

Most importantly, from the result (4.15) one may determine the scaling exponent z for this nonthermal fixed point. Setting $d = 3$ we obtain

$$z = 1.84 \pm 0.15. \quad (4.18)$$

This value seems to exclude a ‘‘linear dispersion’’ ($z \rightarrow 1$) in this scaling regime and for the statistical propagator F considered, but appears marginally consistent with a quadratic one ($z \rightarrow 2$). As a consistency check, we note that practically the same value for z is also obtained from (4.17) and (4.14) with $d = 3$. Alternatively, plugging the equal-time result for β , Eq. (3.14), into (4.17), or even into (4.14) with (4.15) treating the d from the scaling ansatz (4.5) as an independent parameter,⁶ would lead to $z \rightarrow 1.94 \pm 0.11$. While this is still fully consistent with our above result for z , its somewhat higher central value might be viewed as

⁶ Such a procedure would lead, for instance, from (4.14) and (3.14) to the value

$$d \rightarrow 3.18 \pm 0.13, \quad (4.19)$$

for the scaling parameter d in (4.5). The deviation from the spatial dimension three, for the statistical and fit error given, may point to a moderate additional systematic error.

an indication for a possible quadratic dispersion. In addition, (4.17) conveys the important information that the value obtained for z is rather accurately determined by $1/\beta$, even though the result for the errors stated indicates a small deviation. The agreement of z and $1/\beta$ is, e.g., assumed in related studies of equal-time correlators in Refs. [64, 146].

4.4 Conclusions

In this chapter, we have presented results on universal scaling for unequal-time correlation functions describing nonthermal fixed points in a nonrelativistic Bose gas. From a finite-size scaling analysis we were able to quantify the scaling of the characteristic time scales τ_* for condensation and of the correlation time Δt_* with volume. In particular, we found both characteristic quantities to scale in the same way with the volume.

From the finite size scaling analysis of the zero-momentum mode of the statistical correlator F we have obtained a value for the dynamical exponent $z = 1.84 \pm 0.15$ [Eq. (4.18)] rather close to a quadratic dispersion ($z \approx 2$). This result implies that to rather good accuracy one has $\beta = 1/z$, where β is related to scaling in the center-time coordinate. Since such a relation is often assumed in related studies of dynamical scaling [64, 146], it would be interesting to investigate under which conditions such a relation must hold.

The close to quadratic z obtained in this chapter seems to justify at first sight the case of a free dispersion $\omega_p \sim p^2$ in the vertex-resummed kinetic theory of Sec. 3.4. However, it must be noted that in the derivation of the kinetic theory, one assumes a specific form and scaling behavior for the spectral function ρ [Eq. (2.16)] as well. While F and ρ are related in equilibrium through the fluctuation-dissipation relation, Eq. (2.18), out of equilibrium this must not be the case. In particular, the conclusions reached in this chapter for F must not necessarily apply to ρ as well. To clarify this issue, we investigate in the next chapter the properties of the spectral function close to the nonthermal fixed point.

Chapter 5

Spectral Function and Anomalous Dimension

In the previous two chapters a consistent picture of the infrared dynamics of the nonrelativistic Bose gas (2.4) and the relativistic scalar field theory (2.1) near the nonthermal fixed point has emerged. We have demonstrated the self-similar scaling evolution of both equal-time and unequal-time correlation functions and have computed the associated scaling exponents and scaling functions. The far-from-equilibrium universality class defined by these universal quantities turns out to encompass both relativistic and nonrelativistic theories. Furthermore, the exponents obtained confirmed the existence of an inverse particle cascade transporting particles from higher to lower momenta, which leads to the formation of a condensate out of equilibrium.

However, a number of questions remain unsettled. The dynamical exponent z , which relates characteristic frequencies and momenta, was computed in the previous chapter from a finite size scaling analysis of the statistical correlator F . However, it is not clear whether the same exponent governs the behavior of the spectral function ρ and whether it can be related to a dispersion relation of propagating modes. Furthermore, the results obtained from the vertex-resummed kinetic theory in the relevant nonrelativistic limit (Chap. 3) do not shed light on this issue since they turned out to be independent of the value of z .

Another open question concerns the validity of the vertex-resummed kinetic theory and the associated quasiparticle picture presented in Sec. 3.4. While the remarkable agreement between the analytical results based on the $1/N$ expansion of the 2PI effective action to next-to-leading order and the classical-statistical simulations is encouraging, the existence of quasiparticles in the highly nonperturbative infrared regime is far from trivial and has not been definitely proven yet.

In this chapter, we address these two issues by computing numerically the spectral function of the nonrelativistic Bose gas close to the nonthermal fixed point. This quantity contains important information about the relevant excitations of the system together with their associated dispersion relation. We present evidence that justifies the description in terms of quasiparticles and extract the dynamical exponent z associated to the scaling of the dispersion at low-momenta. The comparison to the statistical function shows that the two quantities are

governed by different dynamical exponents and implies a breaking of the fluctuation-dissipation relation. Furthermore, we study the self-similar scaling behavior of the spectral function, which allows us to estimate the value of the anomalous dimension η .

5.1 Spectral function from linear response

We consider again a nonrelativistic scalar theory for a one-component complex field ψ with action (2.4). The spectral function $\rho = i\tilde{\rho}$ is defined in the complex basis in Eq. (3.66). We denote its two independent diagonal and off-diagonal components as

$$\rho_{\text{diag}}(t, t', \mathbf{x}, \mathbf{x}') \equiv \rho_{11}(t, t', \mathbf{x}, \mathbf{x}') = \langle i[\hat{\psi}(t, \mathbf{x}), \hat{\psi}^\dagger(t', \mathbf{x}')]\rangle, \quad (5.1)$$

$$\rho_{\text{ano}}(t, t', \mathbf{x}, \mathbf{x}') \equiv \rho_{12}(t, t', \mathbf{x}, \mathbf{x}') = \langle i[\hat{\psi}(t, \mathbf{x}), \hat{\psi}(t', \mathbf{x}')]\rangle. \quad (5.2)$$

Note that these quantities have in general a real and imaginary part. For a spatially homogeneous system we will consider the spatial Fourier transform

$$\begin{aligned} \rho(t, t', \mathbf{p}) &= \int d^d x e^{-i\mathbf{p}\mathbf{s}} \rho\left(t, t', \mathbf{X} + \frac{\mathbf{s}}{2}, \mathbf{X} - \frac{\mathbf{s}}{2}\right) \\ &= \frac{1}{V} \int d^d X \int d^d s e^{-i\mathbf{p}\mathbf{s}} \rho\left(t, t', \mathbf{X} + \frac{\mathbf{s}}{2}, \mathbf{X} - \frac{\mathbf{s}}{2}\right), \end{aligned} \quad (5.3)$$

where $\mathbf{X} = (\mathbf{x} + \mathbf{x}')/2$, $\mathbf{s} = \mathbf{x} - \mathbf{x}'$, and the integrals run over the finite volume V . At equal times one has $\rho_{\text{diag}}(t, t, \mathbf{p}) = i$ and $\rho_{\text{ano}}(t, t, \mathbf{p}) = 0$.

To compute the spectral function, we use a method inspired in linear response theory which we apply here to a nonequilibrium situation. Similar methods are routinely employed in condensed matter experiments [147] as well as in both theoretical and experimental studies of ageing dynamics [132, 148, 149]. In fact, one of the powers of this method is that it can be applied to both theory as well as experimental platforms, as will become apparent in what follows.

5.1.1 Uniform perturbation field

We consider the system in the functional integral representation introduced in Chap. 2 and work in the Wigner rotated basis of the fields [see Eq. (2.65)]. To avoid possible notational ambivalence we define the rotated fields in this chapter as

$$\psi_{\text{cl}} = \frac{\psi^+ + \psi^-}{2}, \quad \psi_{\text{q}} = \psi^+ - \psi^-, \quad (5.4)$$

where the subscripts refer to ‘classical’ and ‘quantum’, respectively. In this basis the retarded part of the spectral function is obtained up to a prefactor of i as [c.f. Eq. (2.69)]

$$\langle \psi_{\text{cl}}(t, \mathbf{x}) \psi_{\text{q}}(t', \mathbf{x}') \rangle = \theta(t - t') \langle [\hat{\psi}(t, \mathbf{x}), \hat{\psi}(t', \mathbf{x}')]\rangle, \quad (5.5)$$

where brackets $\langle \cdot \rangle$ around the fields ψ_{cl} and ψ_{q} imply an average with the functional integral of Sec. 2.2.

The method to compute ρ is inspired by the fact that, according to Eq. (2.69), the two-point function of Eq. (5.5) can be written as the derivative of the macroscopic field with respect to an external source, i.e. omitting indices $\langle \psi_{\text{cl}} \psi_{\text{q}} \rangle = \delta \langle \psi_{\text{cl}} \rangle / \delta (iJ_{\text{cl}})|_{J=0}$, where $J_{\text{cl}} = (J^+ + J^-)/2$ and J^\pm was defined in Sec. 2.2. Based on this we add to the action (2.4) the physical perturbation field term¹

$$S_h[\psi] = \frac{1}{2} \int_{t,\mathbf{x}} [h(t, \mathbf{x}) \psi_{\text{q}}^*(t, \mathbf{x}) + h^*(t, \mathbf{x}) \psi_{\text{q}}(t, \mathbf{x})], \quad (5.6)$$

where

$$h(t, \mathbf{x}) = h \delta(t - t_w) \delta(\mathbf{x} - \mathbf{y}). \quad (5.7)$$

Here, $|h| \ll 1$ is assumed to be small, \mathbf{y} is some given point in space and we call t_w the ‘waiting time’. We separate the field in real and imaginary parts as $h = h_R + ih_I$. Note that this external field is analogous to the source field J used in Sec. 2.2.

In the following we denote expectation values with respect to the combined action $S + S_h$ as $\langle \cdot \rangle_h$ and use $\langle \cdot \rangle_0$ for those with respect to the original action, i.e. for $h = 0$. We consider the expectation value of the field, $\langle \psi_{\text{cl}} \rangle_h = \langle \hat{\psi} \rangle_h$, and expand to linear order in h as

$$\begin{aligned} \langle \psi_{\text{cl}}(t, \mathbf{x}) \rangle_h &= \langle \psi_{\text{cl}}(t, \mathbf{x}) \rangle_0 + \left. \frac{\delta \langle \psi_{\text{cl}}(t, \mathbf{x}) \rangle_h}{\delta h_R} \right|_{h=0} h_R + \left. \frac{\delta \langle \psi_{\text{cl}}(t, \mathbf{x}) \rangle_h}{\delta h_I} \right|_{h=0} h_I + O(h^2) \\ &= \langle \psi_{\text{cl}}(t, \mathbf{x}) \rangle_0 + \frac{h_R}{2} \langle i \psi_{\text{cl}}(t, \mathbf{x}) (\psi_{\text{q}}^*(t_w, \mathbf{y}) + \psi_{\text{q}}(t_w, \mathbf{y})) \rangle_0 \\ &\quad + \frac{ih_I}{2} \langle i \psi_{\text{cl}}(t, \mathbf{x}) (\psi_{\text{q}}^*(t_w, \mathbf{y}) - \psi_{\text{q}}(t_w, \mathbf{y})) \rangle_0 + O(h^2) \\ &= \langle \hat{\psi}(t, \mathbf{x}) \rangle_0 + \theta(t - t_w) \frac{h_R}{2} \langle i [\hat{\psi}(t, \mathbf{x}), \hat{\psi}^\dagger(t_w, \mathbf{y}) + \hat{\psi}(t_w, \mathbf{y})] \rangle_0 \\ &\quad + \theta(t - t_w) \frac{ih_I}{2} \langle i [\hat{\psi}(t, \mathbf{x}), \hat{\psi}^\dagger(t_w, \mathbf{y}) - \hat{\psi}(t_w, \mathbf{y})] \rangle_0 + O(h^2). \end{aligned} \quad (5.8)$$

Thus, denoting by $\langle \cdot \rangle_{h_R(h_I)}$ the expectation value with $h = h_R$ ($h = ih_I$) we get

$$\begin{aligned} \theta(t - t_w) \rho_{\text{diag}}(t, t_w, \mathbf{x}, \mathbf{y}) &= \frac{\langle \hat{\psi}(t, \mathbf{x}) \rangle_{h_R} - \langle \hat{\psi}(t, \mathbf{x}) \rangle_0}{h_R} + \frac{\langle \hat{\psi}(t, \mathbf{x}) \rangle_{h_I} - \langle \hat{\psi}(t, \mathbf{x}) \rangle_0}{ih_I} + O(h), \quad (5.9) \\ \theta(t - t_w) \rho_{\text{ano}}(t, t_w, \mathbf{x}, \mathbf{y}) &= \frac{\langle \hat{\psi}(t, \mathbf{x}) \rangle_{h_R} - \langle \hat{\psi}(t, \mathbf{x}) \rangle_0}{h_R} - \frac{\langle \hat{\psi}(t, \mathbf{x}) \rangle_{h_I} - \langle \hat{\psi}(t, \mathbf{x}) \rangle_0}{ih_I} + O(h). \end{aligned} \quad (5.10)$$

Hence, the commutator between two fields can be obtained from suitable combinations of the macroscopic field by comparing the evolution of this quantity with and without external field, provided the external field can be assumed to be a small perturbation to the original action. While the above procedure only gives us access to the retarded part ($t > t_w$) of the spectral function, the advanced part ($t < t_w$) can be obtained straightforwardly using the (anti)symmetry properties of ρ .

¹This is ‘physical’ in the sense that one may write down a term in the original Hamiltonian which will lead to such a linear term in the action. On the time contour the action would be given by $S_h[\psi] = \frac{1}{2} \int_{t,\mathbf{x},\mathcal{C}} [h(t, \mathbf{x}) \psi^*(t, \mathbf{x}) + h^*(t, \mathbf{x}) \psi(t, \mathbf{x})]$. In this way, the dynamics remains unitary and the perturbation field $h(t, \mathbf{x})$ can be seen as an actual external field, accessible in experiments.

5.1.2 Random perturbation field

In order to obtain the momentum dependence of ρ one could in principle Fourier transform (5.9) and (5.10) using (5.3). However, for problems where one is only interested in specific momentum regions or integrals over momentum space, convergence of the above procedure can be improved.² For this we consider a random field³

$$h(t, \mathbf{x}) = h(\mathbf{x}) \delta(t - t_w) \quad (5.11)$$

with

$$\begin{aligned} \overline{h(\mathbf{x})} &= \overline{h_R(\mathbf{x})h_I(\mathbf{y})} = 0, \\ \overline{h_R(\mathbf{x})h_R(\mathbf{y})} &= \overline{h_I(\mathbf{x})h_I(\mathbf{y})} = h^2\delta(\mathbf{x} - \mathbf{y}), \end{aligned} \quad (5.12)$$

where the overbar denotes averaging over different $h(\mathbf{x})$ configurations and now h is a real number. Introducing the Fourier transform

$$h_{R(I)}(\mathbf{p}) = \int d^d x e^{-i\mathbf{p}\mathbf{x}} h_{R(I)}(\mathbf{x}) \quad (5.13)$$

yields $\overline{h_R(\mathbf{p})h_R^*(\mathbf{q})} = \overline{h_I(\mathbf{p})h_I^*(\mathbf{q})} = h^2(2\pi)^d\delta(\mathbf{p} - \mathbf{q})$ and $\overline{h(\mathbf{p})} = \overline{h_R(\mathbf{p})h_I(\mathbf{q})} = 0$. In a finite-size system the δ -function gets replaced by $(2\pi)^d\delta(\mathbf{p} - \mathbf{q}) \rightarrow V\delta_{\mathbf{p},\mathbf{q}}$.

We consider again the macroscopic field and expand to linear order in h to get

$$\begin{aligned} \langle \psi_{\text{cl}}(t, \mathbf{p}) \rangle_h &= \langle \hat{\psi}(t, \mathbf{p}) \rangle_0 + \int d^d \mathbf{p}' \left\{ \frac{h_R(\mathbf{p}')}{2} \left\langle i \left[\hat{\psi}(t, \mathbf{p}), \hat{\psi}^\dagger(t_w, \mathbf{p}') + \hat{\psi}(t_w, -\mathbf{p}') \right] \right\rangle_0 \right. \\ &\quad \left. + \frac{ih_I(\mathbf{p}')}{2} \left\langle i \left[\hat{\psi}(t, \mathbf{p}), \hat{\psi}^\dagger(t_w, \mathbf{p}') - \hat{\psi}(t_w, -\mathbf{p}') \right] \right\rangle_0 \right\}. \end{aligned} \quad (5.14)$$

In order to disentangle the different momentum modes appearing in this expression we multiply with the random field and average over random field configurations. In this way we obtain

$$\theta(t - t_w) \rho_{\text{diag}}(t, t_w, \mathbf{p}) = \frac{1}{Vh^2} \overline{h_R^*(\mathbf{p}) \langle \hat{\psi}(t, \mathbf{p}) \rangle_h} + \frac{1}{iVh^2} \overline{h_I^*(\mathbf{p}) \langle \hat{\psi}(t, \mathbf{p}) \rangle_h}, \quad (5.15)$$

$$\theta(t - t_w) \rho_{\text{ano}}(t, t_w, \mathbf{p}) = \frac{1}{Vh^2} \overline{h_R^*(\mathbf{p}) \langle \hat{\psi}(t, \mathbf{p}) \rangle_h} - \frac{1}{iVh^2} \overline{h_I^*(\mathbf{p}) \langle \hat{\psi}(t, \mathbf{p}) \rangle_h}. \quad (5.16)$$

5.2 Classical-statistical spectral function

Since we are interested in the dynamics close to the nonthermal fixed point involving high occupancies, we employ in this chapter again classical-statistical simulations. The method outlined above to compute the spectral function can be straightforwardly applied to classical-statistical dynamics and has the advantage that it requires, up to a multiplication with the external perturbation, the computation of only one-point functions of the fields. We outline in

²Note that the computation of the macroscopic field in classical-statistical simulations requires averaging over many different realizations. Aiming at specific observables by perturbing only the modes involved in their dynamics can reduce the noise and hence improve convergence. The same applies to any approximation or even experiment that requires averaging over realizations to obtain expectation values.

³This is similar to what is done in the literature of ageing phenomena [132, 148, 149].

the following the numerical implementation used and derive afterwards the classical statistical equation of motion fulfilled by the spectral function in this approximation.

5.2.1 Numerical implementation

Computation of the spectral function according to (5.15) and (5.16) requires the macroscopic fields $\langle \hat{\psi}(t, \mathbf{p}) \rangle_h$ and $\langle \hat{\psi}(t, \mathbf{p}) \rangle_0$. For our initial conditions the macroscopic field in the absence of an external field is zero. However, in order to reduce finite sampling errors as well as statistical errors coming from the average over a finite number of $h(\mathbf{x})$ configurations, we make in Eqs. (5.15) and (5.16) the substitution $h_R^*(\mathbf{p}) \langle \hat{\psi}(t, \mathbf{p}) \rangle_h \rightarrow h_R^*(\mathbf{p}) (\langle \hat{\psi}(t, \mathbf{p}) \rangle_{h_R} - \langle \hat{\psi}(t, \mathbf{p}) \rangle_0)$ and similarly for h_I .

The evolution equation of the classical-statistical field $\psi_h(t, \mathbf{x})$ with an external source h as defined in Eq. (5.6) is given by [c.f. Eq. (3.4)]

$$i\partial_t \psi_h(t, \mathbf{x}) = \left[-\frac{\nabla^2}{2m} + g|\psi_h(t, \mathbf{x})|^2 \right] \psi_h(t, \mathbf{x}) - \frac{h(t, \mathbf{x})}{2}. \quad (5.17)$$

We discretize the δ -function appearing in (5.11) as $\delta(t - t_w) \rightarrow \frac{1}{\Delta t} \delta_{t, t_w}$. To implement this, we first evolve the system with Eq. (5.17) for vanishing external field until the time $t = t_w$, which yields $\psi_{h=0}(t_w, \mathbf{x})$. At that time, we make two copies of the system and apply to each one a rotation as $\psi_h(t_w, \mathbf{x}) = \psi_{h=0}(t_w, \mathbf{x}) + i\frac{h(\mathbf{x})}{2}$ with $h(\mathbf{x}) = h_R(\mathbf{x})$ and $h(\mathbf{x}) = ih_I(\mathbf{x})$, respectively. For later times, we evolve the three systems in parallel with Eq. (5.17) for $h = 0$, and compute $\langle \psi(t, \mathbf{p}) \rangle_{h_R}$, $\langle \psi(t, \mathbf{p}) \rangle_{h_I}$, and $\langle \psi(t, \mathbf{p}) \rangle_0$ from ensemble averages over initial conditions.

In each realization, we sample the external field from a binomial distribution with $h(\mathbf{x}) = \pm h$ and $h = 0.01$. By repeating the simulations with different sizes of h we checked that the response of the system for the chosen value is linear. Since the system is isotropic, we further average over momenta with a similar modulus $|\mathbf{p}|$ to obtain a faster statistical convergence.

5.2.2 Equation of motion

It is instructive to derive the equation of motion fulfilled by the spectral function in the classical-statistical approximation. For this we consider again the external field to be given by $h(t, \mathbf{x}) = h \delta(t - t_w) \delta(\mathbf{x} - \mathbf{y})$ with $h = h_R + ih_I$ as in Eq. (5.7). Based on (5.9) and (5.10) we define the classical-statistical variables

$$\rho_{\text{diag}}^{\text{cl}}(t, t_w, \mathbf{x}, \mathbf{y}) \equiv \left(\frac{\delta \psi_h(t, \mathbf{x})}{\delta h_R} + \frac{\delta \psi_h(t, \mathbf{x})}{\delta i h_I} \right) \Big|_{h=0}, \quad (5.18)$$

$$\rho_{\text{ano}}^{\text{cl}}(t, t_w, \mathbf{x}, \mathbf{y}) \equiv \left(\frac{\delta \psi_h(t, \mathbf{x})}{\delta h_R} - \frac{\delta \psi_h(t, \mathbf{x})}{\delta i h_I} \right) \Big|_{h=0}, \quad (5.19)$$

where ψ_h denotes the classical field evolved with external field h . These definitions imply that for $t > t_w$

$$\rho_{\text{diag}} = \langle \rho_{\text{diag}}^{\text{cl}} \rangle, \quad \rho_{\text{ano}} = \langle \rho_{\text{ano}}^{\text{cl}} \rangle, \quad (5.20)$$

where $\langle \cdot \rangle$ stands here for an average over initial conditions. Using Eqs. (5.18) and (5.19) and taking the derivative of the equation of motion, Eq. (5.17), for $t > t_w$ one obtains

$$\left(i\partial_t + \frac{\nabla^2}{2m} - 2g|\psi(t, \mathbf{x})|^2 \right) \rho_{\text{diag}}^{\text{cl}}(t, t_w, \mathbf{x}, \mathbf{y}) - g\psi^2(t, \mathbf{x})(\rho_{\text{ano}}^{\text{cl}}(t, t_w, \mathbf{x}, \mathbf{y}))^* = 0, \quad (5.21)$$

$$\left(i\partial_t + \frac{\nabla^2}{2m} - 2g|\psi(t, \mathbf{x})|^2 \right) \rho_{\text{ano}}^{\text{cl}}(t, t_w, \mathbf{x}, \mathbf{y}) - g\psi^2(t, \mathbf{x})(\rho_{\text{diag}}^{\text{cl}}(t, t_w, \mathbf{x}, \mathbf{y}))^* = 0. \quad (5.22)$$

These equations are reminiscent of the full 2PI evolution equations for the spectral function, Eq. (2.31). In fact, Eqs. (5.21) and (5.22) can be obtained from the full 2PI equations by neglecting all self-energy terms and substituting $\rho \rightarrow \rho^{\text{cl}}$. This close relation between the classical-statistical and the quantum evolution equations will be further discussed in Chap. 8.

5.3 Nonequilibrium evolution

Similar to Chaps. 3 and 4 we study the dynamics close to the nonthermal fixed point starting from overoccupied initial conditions. Specifically, the distribution function, Eq. (3.11), at the initial time is given by $f_0(\mathbf{p}) = 25/(mgQ)$ for momenta $|\mathbf{p}| < Q$ and zero otherwise. In the following we plot dimensionless quantities obtained by $t \rightarrow tQ^2/(2m)$ and $\mathbf{p} \rightarrow \mathbf{p}/Q$.

Fig. 5.1 shows an overview of the evolution of the spectral function computed using Eqs. (5.15) and (5.16) for different momenta $|\mathbf{p}| \equiv p$. We only show results for the diagonal part ρ_{diag} , because the anomalous part ρ_{ano} turns out to be zero for all times considered.⁴ The results shown are averaged over 1000 iterations for a volume $V = 256^3$. We choose to show the dynamics of a representative set of momenta: $p = 0.2$ (Figs. 5.1a and 5.1b), $p = 0.5$ (Figs. 5.1c and 5.1d) and $p = 1.01$ (Figs. 5.1e and 5.1f).⁵ All these momenta lie approximately within the self-similar regime of the distribution function (c.f. Fig. 3.3) and slowly exit the scaling regime as time passes. Since the spectral function is a complex numbered function, we plot in Figs. 5.1a, 5.1c, and 5.1e (figures on the left) its real and imaginary parts and in Figs. 5.1b, 5.1d, and 5.1f (figures on the right) the absolute value. The figures on the left show the spectral function at fixed time $t_w = 800$, while the figures on the right show the evolution of the envelope with t_w , for $t_w = 400, 800$ and 1600 . These times are chosen to lie within the self-similar scaling regime (c.f. Fig. 3.3).

In general, the spectral function shows clear oscillations with Δt which get damped for large time differences. Comparing the different plots of Fig. 5.1, one sees that both frequency and damping rate increase with momentum p . The logarithmic-linear scale of Figs. 5.1b, 5.1d, and 5.1f further reveals that the damping is approximately exponential $\sim e^{-\gamma_p \Delta t}$ up to small oscillations of the envelope which damp out at longer times.⁶ We will show in the next section that these oscillations are the result of interference between two counter-propagating waves.

Figs. 5.1b, 5.1d, and 5.1f show that the damping rate $\gamma_p(t_w)$ depends on the time t_w . This damping is found to decrease at longer times for all momenta. The frequency of oscillation,

⁴This is not surprising, since the $U(1)$ symmetry of the system is not broken by the initial conditions.

⁵The smallest momentum in a lattice with $V = L^3$ is given by $p_{\text{min}} = 2\pi/L$ and the largest by $p_{\text{max}} = \sqrt{12}$. For reference, see the horizontal axis of Fig. 3.3.

⁶The noisy behavior observed between $\Delta t \approx 40$ and 50 is due to the finite size of the sampling.

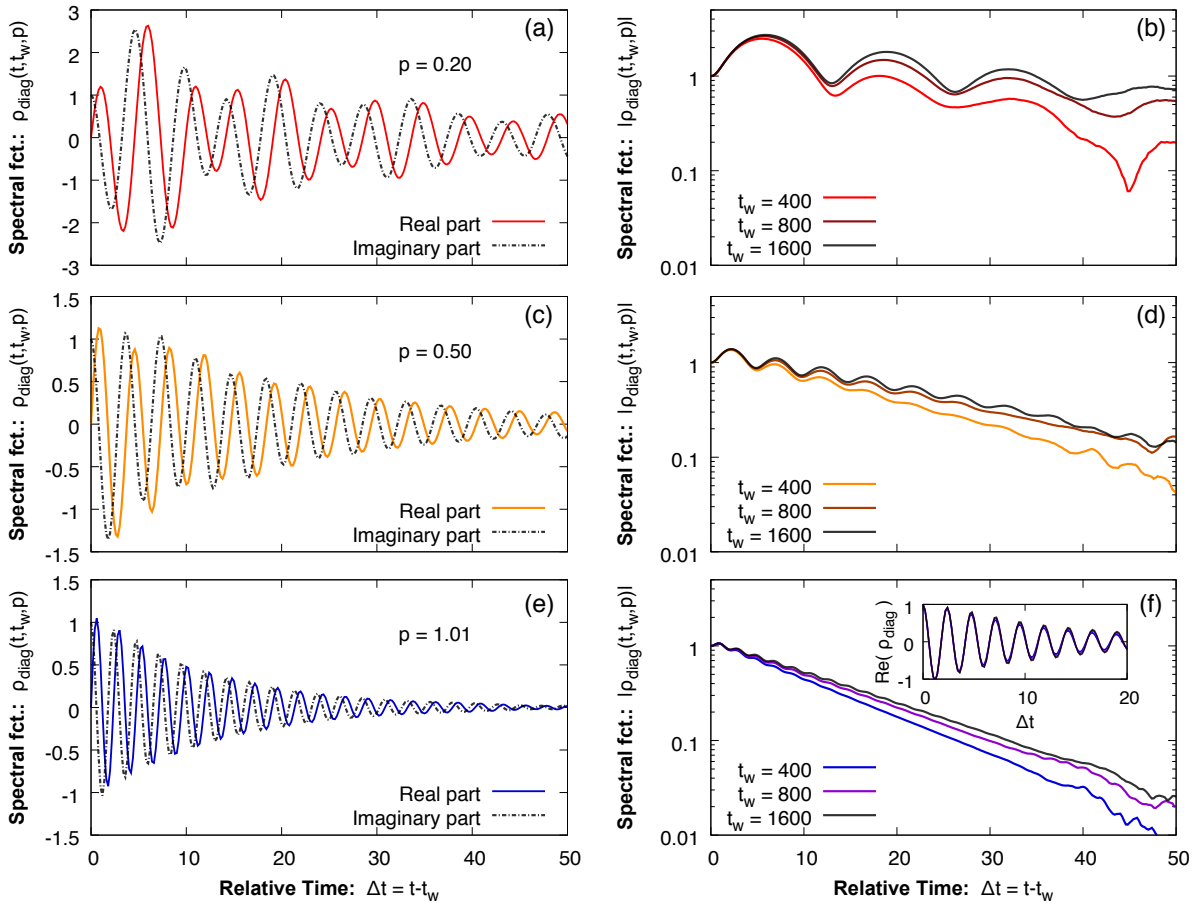


FIGURE 5.1: Spectral function $\rho_{\text{diag}}(t, t_w, \mathbf{p})$ computed as in Eq. (5.15) as a function of the relative time $\Delta t = t - t_w$ for different times t_w and momenta $|\mathbf{p}| \equiv p$. The figures on the left show the real and imaginary parts of the spectral function at $t_w = 800$, while the figures on the right show the absolute value for different times t_w . The momenta are given by: (a), (b) $p = 0.2$. (c), (d) $p = 0.5$. (e), (f) $p = 1.01$. The inset of (f) displays the real part for different t_w .

however, remains rather constant during the time interval considered. The inset of Fig. 5.1f provides evidence of this for $p = 1.01$ by displaying the real part of ρ_{diag} for different times t_w . This will be shown more conclusively in the next section when we analyse the Fourier transform of the spectral function. We anticipate as well that the interference oscillations observed in the envelope of ρ_{diag} tend to become more pronounced at later times. This can be best appreciated in Fig. 5.1d by comparing the amplitude and decay of the oscillations of $t_w = 1600$ to the earlier times shown.

5.4 Quasiparticle spectrum

In order to interpret the results of Fig. 5.1 and extract information about the excitations of the system, we analyse now the Fourier transform of the spectral function. For this we define again Wigner coordinates as [c.f. (4.4)]

$$\tau \equiv \frac{t + t_w}{2}, \quad \Delta t \equiv t - t_w, \quad (5.23)$$

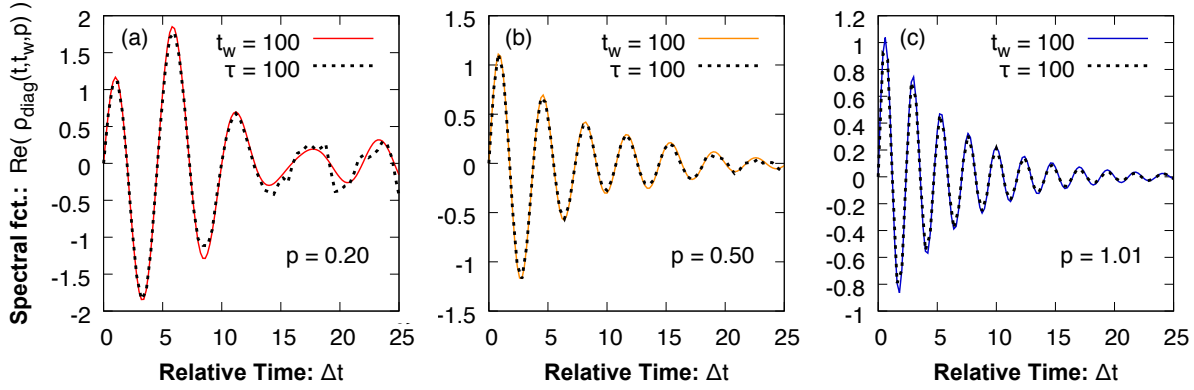


FIGURE 5.2: Comparison of the spectral function $\rho_{\text{diag}}(t, t_w, \mathbf{p})$ for constant $\tau \equiv (t + t_w)/2 = 100$ (black dashed line) and constant $t_w = 100$ (color line) plotted as a function of the relative time $\Delta t = t - t_w$ for three different momenta $|\mathbf{p}| \equiv p$. The momenta are given by: (a) $p = 0.2$. (b) $p = 0.5$. (d) $p = 1.01$.

and Fourier transform with respect to the relative time Δt as

$$\rho(\tau, \omega, \mathbf{p}) = \int d\Delta t e^{i\omega\Delta t} \rho(\tau, \Delta t, \mathbf{p}). \quad (5.24)$$

The Fourier transform has to be taken at constant τ . However, using the procedure outlined above [see Eq. (5.15)], each classical statistical simulation provides us instead with data for fixed and constant t_w . To obtain ρ at constant τ , one thus needs to compute the spectral function at many different values of t_w and then transform the data using (5.23).

Due to the large number of runs needed for convergence, this is, however, computationally rather costly. Instead, we argue in the following that within a given interval of Δt one can approximate $\rho(\tau, \Delta t, \mathbf{p}) \approx \rho(t = \Delta t + t_w, t_w = \tau, \mathbf{p})$, i.e. the spectral function is approximately the same for constant τ or constant t_w . Of course, this is exactly fulfilled in equilibrium, where the spectral function becomes time-translation invariant, i.e. $\rho(\tau, \Delta t, \mathbf{p}) \equiv \rho(\Delta t, \mathbf{p})$. During the dynamics this approximation can be justified, provided the change of ρ with t_w is slow. This can be fulfilled particularly well during self-similar scaling dynamics due to the algebraic nature of the corresponding evolution. In fact, we find an indication of slow dynamics already in Figs. 5.1b, 5.1d, and 5.1f. In particular, comparing the change in the spectral function between $t_w = 400$ and 800 to the change between $t_w = 800$ and 1600 indicates that the evolution becomes slower at later times.

To make this more precise, we compare in Fig. 5.2 the form of the spectral function at constant $\tau = 100$ and at constant $t_w = 100$ as a function of the relative time Δt .⁷ We show the same set of momenta as in Fig. 5.1, namely $p = 0.2$ (Fig. 5.2a), $p = 0.5$ (Fig. 5.2b), and $p = 1.01$ (Fig. 5.2c). The data for constant t_w has been averaged over 1000 realizations, whereas for constant τ we averaged over 20 realizations. Therefore, the long-time data for constant τ is rather noisy and we show only times up to $\Delta t = 25$.

Within the time range shown, the curves for constant τ and constant t_w lie remarkably well on top of each other. Small differences in the amplitude may be partly explained by statistical finite-sampling errors, especially for constant τ at low momenta and large Δt . Apart from

⁷The data for constant τ was obtained from combining the data of a large set of different t_w .

that, Fig. 5.2 shows that one can approximate $\rho(\tau, \Delta t, \mathbf{p}) \approx \rho(t = \Delta t + t_w, t_w = \tau, \mathbf{p})$ to rather good accuracy for short enough Δt . It should be emphasized that the comparison of Fig. 5.2 is done for relatively small t_w and τ , where the differences between constant τ and constant t_w are expected to be more pronounced. For later times, the evolution slows down, as we showed above. Therefore, the above approximation is justified to a greater extent at longer times, such as those within the self-similar scaling regime.⁸

5.4.1 Frequency spectrum

Using the approximation $\rho(\tau, \Delta t, \mathbf{p}) \approx \rho(t = \Delta t + t_w, t_w = \tau, \mathbf{p})$ we compute now the Fourier transform (5.24) for ρ_{diag} . Because of this approximation we will use in the following t_w and τ interchangeably. The spectral function has the symmetry property $\rho_{\text{diag}}(\tau, \Delta t, \mathbf{p}) = -(\rho_{\text{diag}}(\tau, -\Delta t, \mathbf{p}))^*$, which implies in Fourier space that $\rho_{\text{diag}}(\tau, \omega, \mathbf{p})$ is purely imaginary. Hence, we define the real-valued function $\tilde{\rho} \equiv -i\rho$. The equal-time commutation relations (2.7) imply the sum rule

$$\int \frac{d\omega}{2\pi} \tilde{\rho}(\tau, \omega, \mathbf{p}) = 1. \quad (5.25)$$

The quantities plotted in the following are normalized according to this.

Fig. 5.3 shows the Fourier transform of the spectral function of Fig. 5.1 as a function of the frequency ω . For this the integral over Δt in Eq. (5.24) is replaced by a finite integral $\int_{-T}^T d\Delta t$ with $T = 50$. Figs. 5.3a, 5.3c and 5.3e present the spectral function at $\tau = 800$ for different momenta divided in three intervals: $p \in [0, 0.22]$ (Fig. 5.3a), $p \in [0.22, 0.59]$ (Fig. 5.3c), and $p \in [0.59, 1.6]$ (Fig. 5.3e).⁹ At low momenta the Fourier transform of the spectral function shows a clear double-peak structure with one of the peaks having a negative amplitude. The two peaks are of similar height and the spectral function is approximately antisymmetric around the frequency $\omega = \mu$.¹⁰ The characteristic frequency μ can be seen as an effective chemical potential produced by medium effects and is related to the oscillation frequency of the zero-momentum mode.

As the momentum is increased, the position of the positive peak shifts to larger frequencies, while the negative peak moves to smaller ones. The peak positions remain for all momenta symmetric with respect to μ , as we will show more precisely further below. Most importantly, the amplitudes of the two peaks decrease monotonically with momentum, but each in a different manner.¹¹ While the positive peak remains visible at all momenta, the negative peak shrinks to practically zero at large momenta. Furthermore, both peaks tend to become wider with increasing momentum, which is consistent with the faster decay at large momenta observed in Fig. 5.1.

The slow evolution of the spectral function observed in Fig. 5.1 is also reflected in frequency space. Figs. 5.3b, 5.3d, and 5.3f show the spectral function at times $\tau = 400$ (colored line) and $\tau = 1600$ (black line) for fixed momenta as given in the plots. As anticipated above, the position of the peak, i.e. the frequency of oscillation, does not change, while the amplitude

⁸In particular, the approximation will be valid for larger time differences Δt .

⁹Momenta larger than $p = 1.6$ do not show any new features.

¹⁰The spectral function $\tilde{\rho}_{\text{diag}}(\tau, \omega, \mathbf{p})$ can not be exactly antisymmetric, since otherwise the integral over frequency space would yield zero, thus violating the sum rule (5.25).

¹¹Note the different scale in the y -axis of Figs. 5.3a, 5.3c and 5.3e

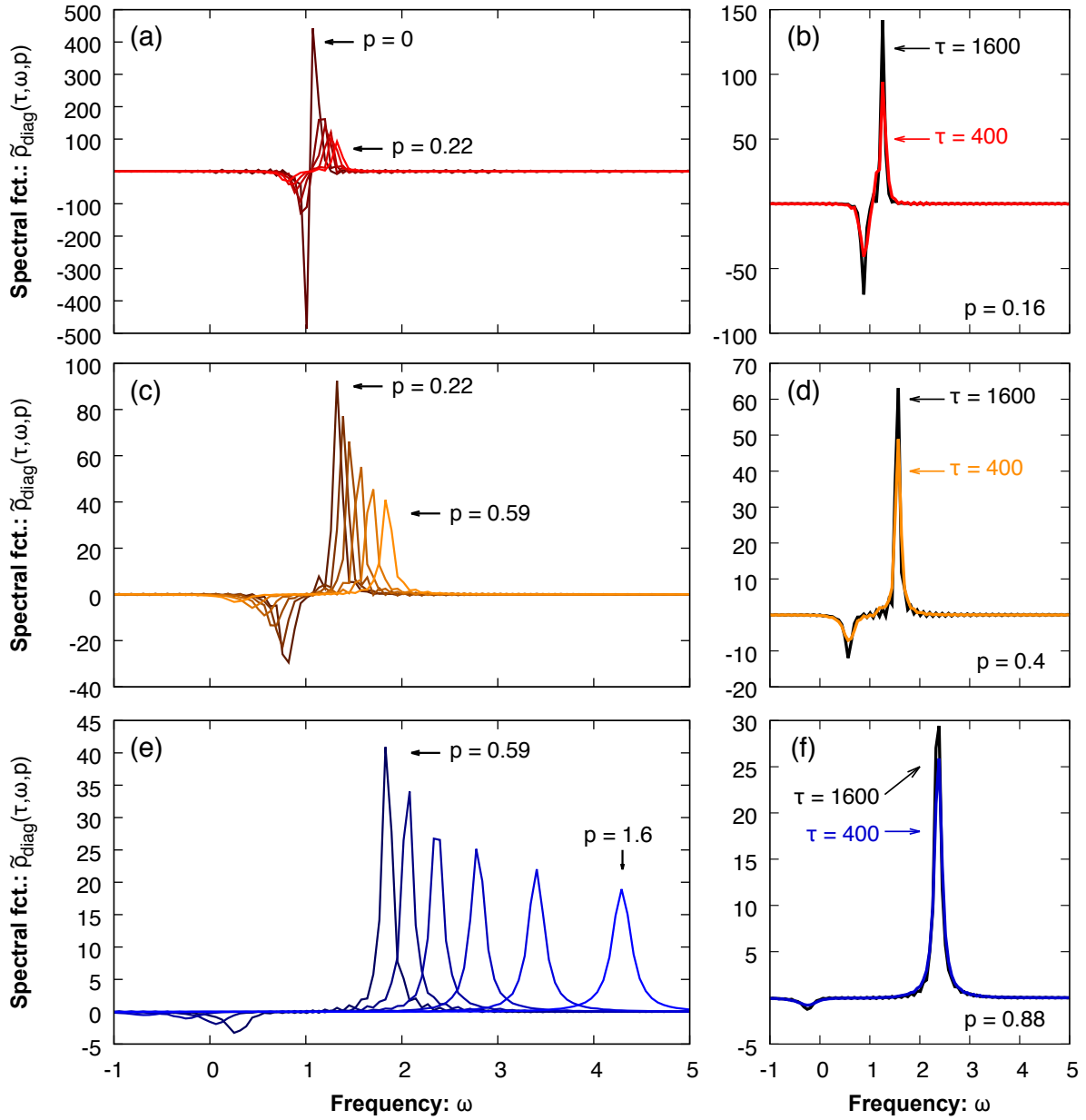


FIGURE 5.3: (a), (c), and (e): Spectral function $\tilde{\rho}_{\text{diag}}(\tau, \omega, \mathbf{p})$ for approximately constant $\tau \approx 800$ as a function of the frequency ω for various momenta $|\mathbf{p}| \equiv p$. (a) $p \in [0, 0.22]$, (c) $p \in [0.22, 0.59]$, and (e) $p \in [0.59, 1.6]$. As the momentum increases, the positive (negative) peak moves to the right (left) and its amplitude decreases. (b), (d), and (f): Spectral function $\rho_{\text{diag}}(\tau, \omega, \mathbf{p})$ for fixed momentum at two different times $\tau = 400$ (color line) and $\tau = 1600$ (black line). The amplitude of the peaks slightly increases with time.

of the peak maximum, which is related to the inverse decay rate $1/\gamma(p)$, seems to slightly increase with time.

5.4.2 Quasiparticles and dispersion relation

The peaks observed in Fig. 5.3 suggest the existence of two quasiparticles with finite lifetime. Since the decay was shown in Fig. 5.1 to be of exponential nature, the peaks are expected to

have a Lorentzian shape. Using this we make the following ansatz for the quasiparticle spectral function ($|\mathbf{p}| \equiv p$):

$$\tilde{\rho}(\tau, \omega, \mathbf{p}) = \frac{2 A_+(p) \gamma_+(\tau, p)}{(\omega - \mu - \omega(p))^2 + \gamma_+(\tau, p)^2} - \frac{2 A_-(p) \gamma_-(\tau, p)}{(\omega - \mu + \omega(p))^2 + \gamma_-(\tau, p)^2}. \quad (5.26)$$

Here, μ is the chemical potential, $\omega(p)$ is the dispersion relation of the quasiparticles, $\gamma_{\pm}(\tau, p)$ the decay rate (or width of the peak) and $A_{\pm}(p)$ the amplitude of the peak. In principle, μ , $\omega(p)$, and $A_{\pm}(p)$ could depend on the time τ as well. This is, however, not the case during the scaling regime considered, as we will see shortly. The normalization condition (5.25) implies for (5.26) that

$$A_+(p) - A_-(p) = 1 \quad (5.27)$$

for all momenta. Fourier transforming (5.26) back into the time regime yields a superposition of two counterpropagating damped waves as

$$\rho(\tau, \Delta t, \mathbf{p}) = i e^{-i\mu\Delta t} \left[A_+(p) e^{-\gamma_+(\tau, p)|\Delta t|} e^{-i\omega(p)\Delta t} - A_-(p) e^{-\gamma_-(\tau, p)|\Delta t|} e^{i\omega(p)\Delta t} \right]. \quad (5.28)$$

This form explains the oscillations of the envelope of ρ observed in Fig. 5.1. Taking the absolute value of (5.28) yields an oscillating interference term that decays with $e^{-(\gamma_+ + \gamma_-)|\Delta t|}$.

To study the nature of the quasiparticles, we fit the data using (5.26) and (5.28) and extract from it the values of μ , $\omega(p)$, $A_{\pm}(p)$ and $\gamma_{\pm}(\tau, p)$.¹² Fig. 5.4 shows some examples of the fit results for $\tau = 800$ and various momenta. In all cases shown the agreement between the fit function and the raw data is remarkable. The comparison between (5.26) and the Fourier transformed data (Figs. 5.4a-5.4c) shows some small deviations, especially at low momenta. However, these are caused to a large extent by the finite time interval used for the Fourier transform. In fact, Fourier transforming (5.28) over a finite interval $\int_{-T}^T d\Delta t$ leads to peaks with a Lorentz shape [Eq. (5.26)] up to an oscillating term that decays as $e^{-\gamma T}$ with the corresponding decay rate γ . Hence, this effect is enhanced at low momenta where γ becomes small. To avoid this we extract the values of the quasiparticle parameters at low momenta ($p \lesssim 1$) by fitting (5.28) in the time regime (Figs. 5.4d-5.4f). However, this fit method turns out to be worse at large momenta because of the smallness of the signal of the negative quasiparticle peak. Therefore, we preferably use at large momenta ($p \gtrsim 1$) the fit function (5.26) in the frequency domain.

Fig. 5.5 shows the dispersion relation $\omega(p)$ extracted in this way as a function of the momentum p in a double-logarithmic scale. Red circles of increasing size and opacity show the results obtained at different times $\tau = 400, 800$ and 1600 . As anticipated above, the dispersion $\omega(p)$ appears to be to a good approximation time-independent during the whole regime considered. Furthermore, we show in the inset that the chemical potential μ obtained from the fit is, up to small fluctuations on the order of 1–3%, constant for all momenta. This provides evidence of the momentum independence of μ assumed in (5.26).

The form of the dispersion relation exhibits two distinct momentum regimes. At low momenta ($p \lesssim 1$) it depends to a good approximation linearly on p , see blue dotted line $\sim p$. At large momenta ($p \gtrsim 1$) the dispersion tends to become quadratic, as revealed by comparison

¹²For this we use a non-linear square fit algorithm provided by the GSL library. For each fixed time and momentum we used as fit parameters ω_{\pm} , \tilde{A}_{\pm} , and $\tilde{\gamma}_{\pm}$, where we defined $\gamma_{\pm} \equiv \tilde{\gamma}_{\pm}^2$ and $A_{\pm} \equiv \tilde{A}_{\pm}^2$ to ensure positivity of these quantities as well as $\mu \equiv (\omega_+ + \omega_-)/2$, and $\omega(p) \equiv (\omega_+ - \omega_-)/2$.

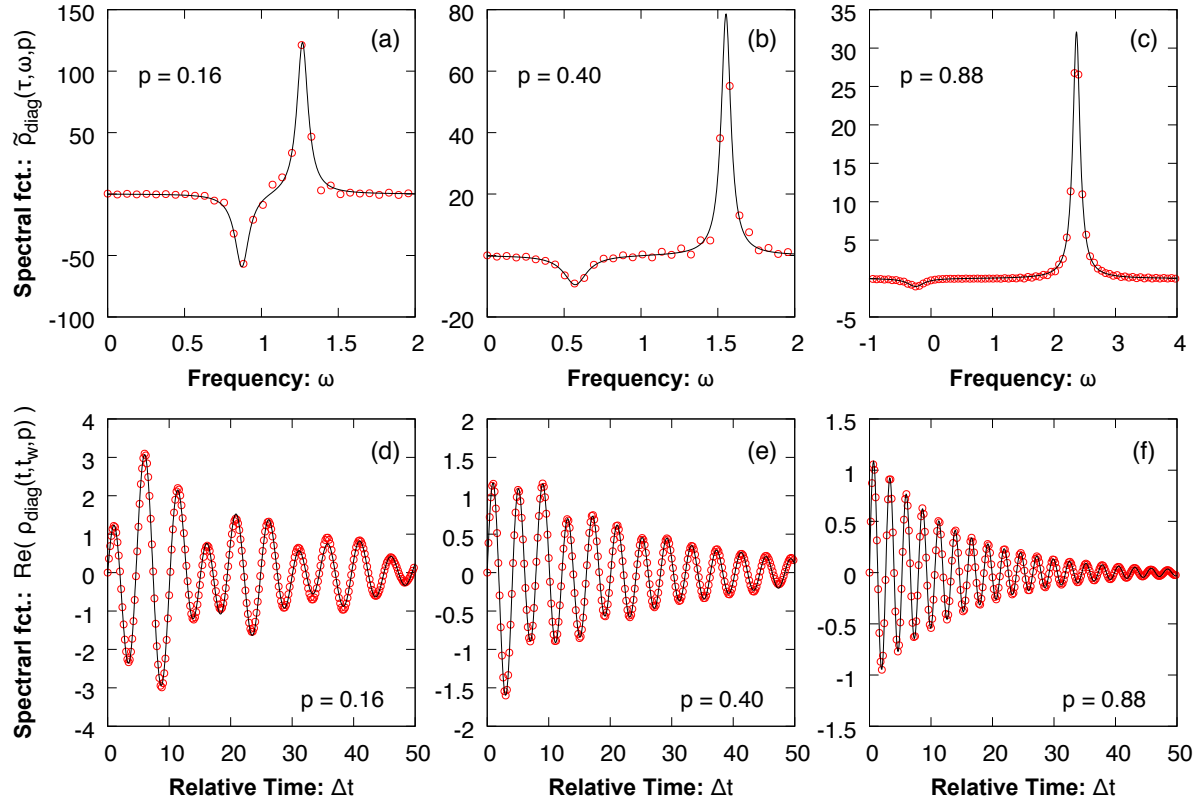


FIGURE 5.4: (a), (b), and (c): Fit function (5.26) (black line) compared to $\tilde{\rho}_{\text{diag}}(\tau, \omega, \mathbf{p})$ (red circles) for approximately constant $\tau \approx 800$ as a function of the frequency ω for different momenta $|\mathbf{p}| \equiv p$. (d), (e), and (f): Fit function (5.28) (black line) compared to the real part of $\rho_{\text{diag}}(t, t_w, \mathbf{p})$ (red circles) for $t_w = 800$ as a function of $\Delta t = t - t_w$ for different momenta p .

with the light-pink line $\sim p^2$. This structure is reminiscent of the Bogoliubov dispersion relation [142, 150]

$$\omega_{\text{bog}}(p) = \sqrt{\frac{p^2}{2m} \left(\frac{p^2}{2m} + 2gn_0 \right)}, \quad (5.29)$$

which can be obtained from a mean-field type approximation. Here, $n_0 \equiv N_0/V$ represents the condensate density with N_0 the number of condensed particles. It is related to the condensate fraction N_0/N_{total} and the total density n via $n_0 = n N_0/N_{\text{total}}$, where N_{total} is the total number of particles in the system. For the parameters used here, the evolution of the condensate fraction is shown in Fig. 3.5 of Chap. 3 (see also Fig. 4.2 of Chap. 4). Using the value reached asymptotically by this quantity as $t \rightarrow \infty$, together with the density, one obtains $n_0 \approx 0.72$. The black line of Fig. 5.5 shows the Bogoliubov dispersion (5.29) obtained with this value of n_0 . The agreement between the data and this analytic form is astonishing, especially taking into account that the system is still far from equilibrium and the condensate fraction at the times considered is far from its asymptotic value at long times.¹³

¹³A possible explanation is that the sum over the lowest-lying momentum modes may be acting as an effective condensate at intermediate times.

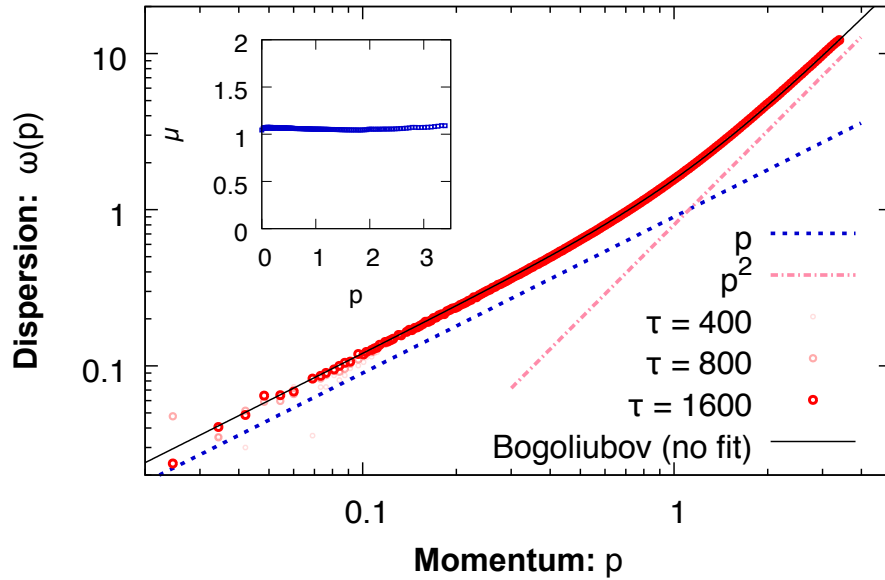


FIGURE 5.5: Oscillation frequency $\omega(p)$ of the spectral function ρ_{diag} as a function of the momentum $p \equiv |\mathbf{p}|$ at different times τ . The dispersion relation is to a good approximation time-independent within the regime shown. The values at low momenta ($p < 1$) are obtained from a fit in the time domain with Eq. (5.28) and for large momenta ($p > 1$) from a fit in frequency space with Eq. (5.26). The black line corresponds to a Bogoliubov dispersion, Eq. (5.29), with $n_0 = 0.72$. A linear (blue dashed line) and quadratic (pink dash-dotted line) dispersion are shown for comparison. The inset shows the result obtained for the chemical potential μ .

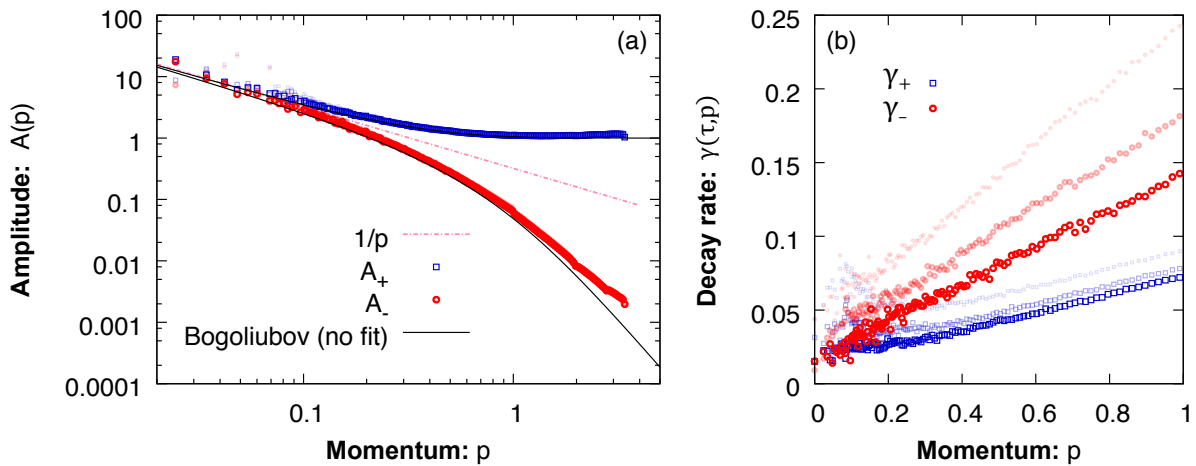


FIGURE 5.6: (a): Amplitude $A_{\pm}(p)$ extracted from a fit with (5.28) at low momenta ($p < 1$) and a fit with (5.26) at large momenta ($p > 1$). $A_{+(-)}$ is shown in blue squares (red circles) for three different times ($\tau = 400, 800$ and 1600) with symbols increasing with time in size and opacity. The black line corresponds to the Bogoliubov result, Eq. (5.31), with $n_0 = 0.72$. (b) Decay rate $\gamma_{\pm}(\tau, p)$ extracted from a fit with (5.28) at low momenta ($p < 0.7$) and a fit with (5.26) at large momenta ($p > 0.7$). $\gamma_{+(-)}$ is shown in blue squares (red circles) for three different times ($\tau = 400, 800$ and 1600) with symbols increasing with time in size and opacity.

The relation to the Bogoliubov dispersion can be further analyzed by considering the limit of the spectral function (5.26) as the decay rates vanish ($\gamma_{\pm} \rightarrow 0$), which is given by

$$\tilde{\rho}(\tau, \omega, \mathbf{p}) \xrightarrow{\gamma \rightarrow 0} 2\pi \left[A_+(p) \delta(\omega - \mu - \omega(p)) - A_-(p) \delta(\omega - \mu + \omega(p)) \right]. \quad (5.30)$$

In the Bogoliubov approximation one obtains the same form for the spectral function with the dispersion $\omega(p) \rightarrow \omega_{\text{bog}}(p)$ and the amplitude functions [150]

$$A_+^{\text{bog}}(p) = \frac{p^2/2m + gn_0 + \omega_{\text{bog}}(p)}{2\omega_{\text{bog}}(p)}, \quad A_-^{\text{bog}}(p) = \frac{p^2/2m + gn_0 - \omega_{\text{bog}}(p)}{2\omega_{\text{bog}}(p)}. \quad (5.31)$$

For low momenta $A_+^{\text{bog}} \sim A_-^{\text{bog}} \sim 1/p$, whereas at large momenta $A_+^{\text{bog}} \rightarrow 1$ and $A_-^{\text{bog}} \rightarrow 0$.

Fig. 5.6a shows the fit results obtained for the amplitude function A_+ (blue squares) and A_- (red circles) as a function of the momentum. We show different times with the same symbols in increasing size and opacity: $\tau = 400$ (smallest and more transparent symbols), $\tau = 800$ and $\tau = 1600$ (largest and more opaque symbols). As expected, at large momenta the amplitude A_- of the negative peak tends to zero, while A_+ tends to 1 as required by (5.25). As the momentum decreases, the amplitudes of both quasiparticles approach each other and follow approximately $\sim 1/p$ (c.f. light-pink line). This behavior is the same as predicted by the Bogoliubov approximation (5.31). A direct comparison is provided by the black line, which is obtained by using (5.31) with $n_0 = 0.72$. In general, the agreement over the whole momentum regime is rather good. The small deviations seen at large and small momenta could be caused by fit uncertainties, especially since those regimes are most sensitive to the discrete time step and the finite time interval used.

So far the Bogoliubov prediction agrees remarkably well, up to small corrections with our results for the nonequilibrium spectral function. An important difference comes, however, from the finite lifetime of the quasiparticles exhibited by the finite width of the peaks. Such a decay is caused by scattering effects beyond mean-field and is hence systematically neglected in the Bogoliubov approximation, which predicts a δ -peaked spectral function.

Fig. 5.6b shows the value of γ_+ (blue squares) and γ_- (red circles) extracted from the fits as a function of momentum. We only show results up to $p = 1$, since errors coming from the average procedure over momenta render the results for γ_{\pm} at higher momenta unreliable.¹⁴ We plot different times ($\tau = 400, 800$ and 1600) corresponding to the same peak (γ_{\pm}) using the same symbols, whose size and opacity increase with τ . Contrary to all other parameters of the spectral function, the decay rate shows a clear evolution in time. In general, both γ_+ and γ_- evolve to lower values, as expected from Fig. 5.1. In this sense, the spectral function gets closer to the Bogoliubov approximation at later times. For the momenta shown, both decay rates depend approximately linearly on p and tend to a nonzero constant $\gamma_{\pm,0}(\tau)$ as $p \rightarrow 0$. As time passes both the slope and $\gamma_{\pm,0}(\tau)$ tend to decrease. Whether this evolution can be understood as self-similar scaling will be discussed in the next section.

¹⁴The main error source comes from the fact that each momentum displayed represents in reality a momentum bin, for which the results of all momenta belonging to that bin have been averaged in order to obtain better statistics. Averaging over nearby momenta implies that the signal will decay due to dephasing of the oscillation frequencies, even in the absence of interactions. The decay produced by this binning at large momenta is not completely negligible and leads to inaccurate results for the decay rate γ_{\pm} . However, since we use a logarithmically spaced binning in order to better access the low-momentum regime, the decay produced by this averaging can be neglected at low momenta for the times Δt considered.

5.5 Self-similar scaling of the spectral function

We investigate in the following the infrared scaling behavior of the spectral function close to the nonthermal fixed point. To gain insight it is useful, as a first approach, to neglect the decay rate, i.e. let $\gamma \rightarrow 0$. In this case, the spectral function can be approximated by a sum of δ -peaks, Eq. (5.30), as we showed in the previous section. Since μ is nonzero, this prevents the function from scaling by simple rescaling of frequency and momenta. However, the chemical potential μ may be reabsorbed in a redefinition of the fields, similar to what was argued in Chap. 4. This amounts to measuring frequencies with respect to μ .

Figs. 5.5 and 5.6 show that at sufficiently low momenta the dispersion relation scales as $\omega(p) \sim p$ and the amplitude as $A_{\pm}(p) \sim 1/p$. Since both ω_p and $A_{\pm}(p)$ were shown to be constant for the times considered, the spectral function in the infrared would scale in this approximation as¹⁵

$$\begin{aligned}\tilde{\rho}_{\text{diag}}(\omega - \mu, p) &= s^{2-\eta} \tilde{\rho}_{\text{diag}}(s^z(\omega - \mu), sp) \\ &= \frac{1}{p^{2-\eta}} \tilde{\rho}_S(p^{-z}(\omega - \mu)),\end{aligned}\quad (5.32)$$

with $\tilde{\rho}_S(p^{-z}(\omega - \mu)) \equiv \tilde{\rho}(p^{-z}(\omega - \mu), 1)$, and the dynamical exponent z and anomalous dimension η given approximately by

$$z = 1, \quad (5.33)$$

$$\eta = 0. \quad (5.34)$$

This scaling behavior gets modified at large momenta, where one recovers instead the dispersion relation of free particles with $z = 2$ (c.f. Fig. 5.5).

The stationary scaling ansatz (5.32) neglects, however, important dynamical information. As we have shown above, the spectral function obtained from the classical-statistical simulations has a nonvanishing decay rate γ which evolves in time. Allowing for a self-similar scaling of the spectral function with time hence leads to the more general scaling ansatz

$$\begin{aligned}\tilde{\rho}_{\text{diag}}(\tau, \omega - \mu, p) &= s^{2-\eta} \tilde{\rho}_{\text{diag}}(s^{-1/\beta} \tau, s^z(\omega - \mu), sp) \\ &= \tau^{\beta(2-\eta)} \tilde{\rho}_S(\tau^{\beta z}(\omega - \mu), \tau^{\beta} p),\end{aligned}\quad (5.35)$$

where $\tilde{\rho}_S(\tau^{\beta z}(\omega - \mu), \tau^{\beta} p) \equiv \tilde{\rho}(\tau^{\beta z}(\omega - \mu), \tau^{\beta} p, 1)$. Note that while we are using the same exponents as in the scaling ansatz of the statistical function F [c.f. Eq. (4.5)], in principle the exponents z and β defined here need not be the same. This will be further discussed in the next section.

In order to establish whether the spectral function presented above behaves as in (5.32) or (5.35), we compare in Fig. 5.7 the results for $\tilde{\rho}_{\text{diag}}$ at different times and momenta to each other. Figures 5.5 and 5.6 have revealed that the dispersion relation and the amplitude only become a power-law at rather low momenta. Accordingly, we restrict the analysis to momenta $p \lesssim 0.3$. Figures 5.7a-5.7c show the original spectral function $\tilde{\rho}_{\text{diag}}$ without rescaling as a function of the shifted frequency $\omega - \mu$ for different times ($\tau_1 = 400$, $\tau_2 = 800$, and $\tau_3 = 1600$)

¹⁵We assume in the following that all quantities have been made dimensionless.

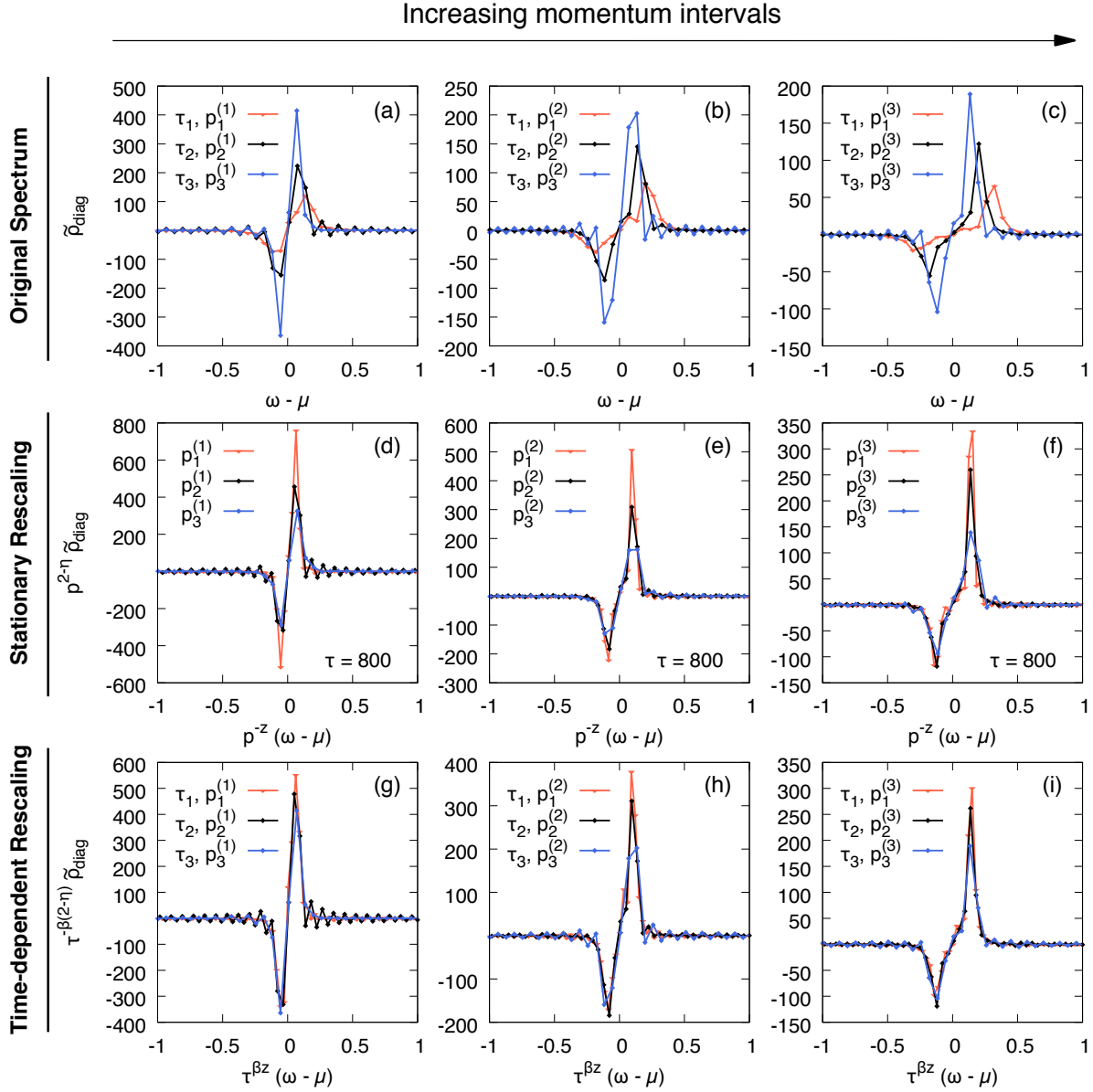


FIGURE 5.7: (a)-(c): Fourier transform of the spectral function $\tilde{\rho}_{\text{diag}}(\tau, \omega, \mathbf{p})$ without rescaling as a function of the shifted frequency $\omega - \mu$ with $\mu = 1.06$. This quantity is shown at the times $\tau_1 = 400$, $\tau_2 = 800$, and $\tau_3 = 1600$ for various infrared momenta given below. (d)-(f): Rescaled spectral function $p^{2-\eta} \tilde{\rho}_{\text{diag}}$ as a function of $p^{-z}(\omega - \mu)$ at fixed time $\tau = 800$ for different infrared momenta. (g)-(i): Rescaled spectral function $\tau^{-\beta(2-\eta)} \tilde{\rho}_{\text{diag}}$ as a function of $\tau^{-\beta z}(\omega - \mu)$ for different momenta chosen as to satisfy $p_i^{(n)}/p_{i-1}^{(n)} = (\tau_{i-1}/\tau_i)^\beta$ ($n \in \{1, 2, 3\}$, $i \in \{2, 3\}$). The momenta chosen for this plot are given by $p_1^{(1)} = 0.103$, $p_2^{(1)} = 0.069$, $p_3^{(1)} = 0.0482$, $p_1^{(2)} = 0.172$, $p_2^{(2)} = 0.118$, $p_3^{(2)} = 0.0809$, $p_1^{(3)} = 0.241$, $p_2^{(3)} = 0.165$, and $p_3^{(3)} = 0.113$. The exponents used for the rescalings are $\beta = 0.55$, $\eta = 0$, and $z = 1$.

and momenta within the scaling regime. For this we use the value $\mu = 1.06$ extracted from the data of the inset of Fig. 5.5 and note that the results presented are qualitatively insensitive to small variations in the choice of μ . The specific momenta chosen are given in the caption of Fig. 5.7.

To check the stationary scaling ansatz (5.32), Figs. 5.7d-5.7f show the rescaled spectral function $p^{2-\eta}\tilde{\rho}_{\text{diag}}$ as a function of the rescaled variable $p^{-z}(\omega - \mu)$ at time $\tau = 800$ for different momenta.¹⁶ For this we used the exponents z and η given in (5.34). If $\tilde{\rho}_{\text{diag}}$ obeys (5.32), all curves should collapse onto one single curve. The positions of the peaks, which are related to the time-independent dispersion relation ω_p , fall indeed respectively on top of each other to good accuracy after rescaling. However, the amplitudes of the rescaled peaks show a rather poor agreement.

To find out if the disagreement is related to the time evolution, we show in Figs. 5.7g-5.7i the rescaled spectral function $\tau^{-\beta(2-\eta)}\tilde{\rho}_{\text{diag}}$ against the rescaled variable $\tau^{\beta z}(\omega - \mu)$ [see Eq. (5.35)].¹⁷ The different times and momenta shown are chosen such that $p_i^{(n)}/p_{i-1}^{(n)} = (\tau_{i-1}/\tau_i)^\beta$, where $n \in \{1, 2, 3\}$ labels the columns of Fig. 5.7 and $i \in \{2, 3\}$.¹⁸ For this we use again the values (5.34) for η and z together with the value $\beta = 0.55$ obtained in Chap. 3 [Eq. (3.14)] from the self-similar analysis of the distribution function. Remarkably, we find that the curves corresponding to different times and momenta fall on top of each other considerably better than using the stationary approximation. While small deviations are still visible, this constitutes strong evidence for the self-similar scaling behavior (5.35) of the spectral function close to the nonthermal fixed point with exponents $\beta = 0.55$, $z = 1$ and $\eta = 0$.

The discrepancies from self-similarity observed in Figs. 5.7g-5.7i may be caused by small corrections to the scaling exponents used.¹⁹ However, because of the relatively small time interval chosen for the Fourier transformation, the resolution of the data is not optimal and a more quantitative analysis becomes hard. The finite time interval also induces small oscillations which lead to deviations from the actual form of the spectral function. Furthermore, we saw in Fig. 5.6 that the scaling regime is restricted to rather low momenta. This suggests that better agreement with the scaling form (5.35) may be observed deeper in the infrared, which can be accessed using larger volumes.

5.6 Breaking of fluctuation-dissipation relation

The value for the dynamical exponent $z \approx 1$ obtained from the scaling of the spectral function $\tilde{\rho}$ above is in sharp contrast to the result $z \approx 2$ obtained from the finite-size scaling analysis of the statistical function F in Chap. 4. To clarify this apparent contradiction we reanalyse in this section the properties of the statistical function, whose diagonal part is defined as

$$F_{\text{diag}}(t, t_w, \mathbf{x} - \mathbf{y}) = \frac{1}{2} \langle \{ \hat{\psi}(t, \mathbf{x}), \hat{\psi}^\dagger(t_w, \mathbf{y}) \} \rangle, \quad (5.36)$$

where we use the notation of this chapter with t_w . This quantity can be computed in classical-statistical simulations directly from $\langle \psi(t, \mathbf{x})\psi(t_w, \mathbf{y}) \rangle$, where $\langle \cdot \rangle$ stands for an ensemble average

¹⁶The rescaling with p is always done with respect to a reference momentum p_{ref} , e.g. $(p/p_{\text{ref}})^{2-\eta}\tilde{\rho}_{\text{diag}}$. As p_{ref} we choose in each of the Figs. 5.7d-f the smallest momentum shown, respectively.

¹⁷The rescaling with τ is also done with respect to a reference time τ_{ref} , e.g. $(\tau/\tau_{\text{ref}})^{-\beta(2-\eta)}\tilde{\rho}_{\text{diag}}$. As τ_{ref} we choose in Figs. 5.7g-i the latest time shown.

¹⁸Since in a finite volume the momenta form a discrete set, we choose momenta such that $p_i^{(n)}/p_{i-1}^{(n)} = (\tau_{i-1}/\tau_i)^\beta$ is fulfilled as well as possible.

¹⁹Slightly modified exponents still make the curves lie well on top of each other. In particular, the result $\beta = 1/(2 - \eta)$ with $\beta = 0.55$ obtained in Chap. 3 appears consistent with our results.

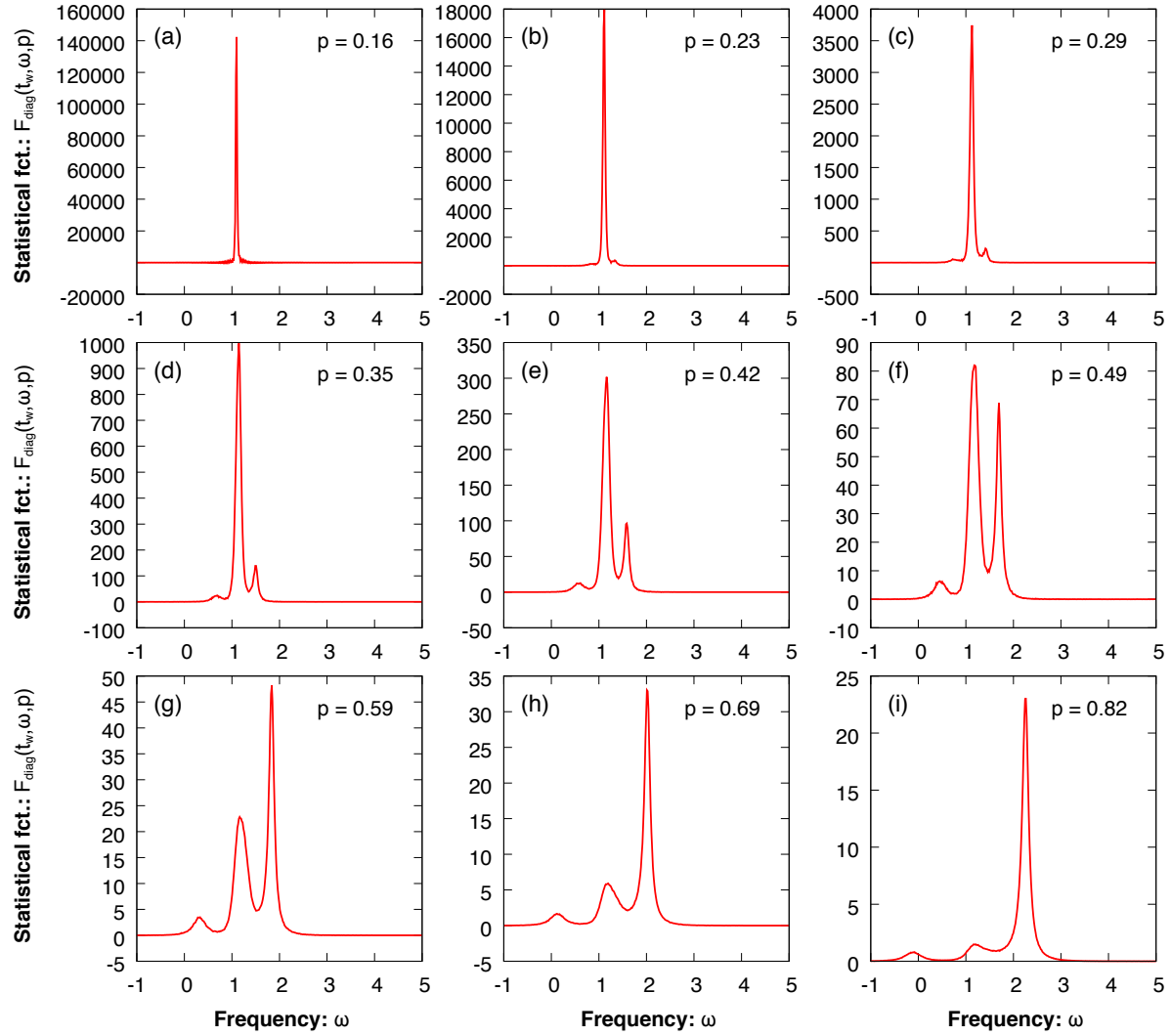


FIGURE 5.8: Fourier transform of the statistical function $F(t_w, \omega, \mathbf{p})$ as a function of the frequency ω for various momenta p (given in the plots) at time $t_w = 400$.

over initial conditions. Analog to the spectral function, we switch to center and relative coordinates, τ and Δt , and Fourier transform with respect to Δt and $\mathbf{x} - \mathbf{y}$ [c.f. Eqs. (5.3) and (5.24)]. During the self-similar scaling regime, F evolves as

$$F_{\text{diag}}(\tau, \omega, p) = s^{z+\alpha/\beta} F_{\text{diag}}(s^{-1/\beta}\tau, s^z\omega, sp). \quad (5.37)$$

Note that the finite size scaling presented in Eq. (4.6) can be recovered from this by setting $p \sim 1/L$ with $V = L^3$.

To shed light onto the discrepancy between the dynamical exponents z governing the dynamics of F and $\tilde{\rho}$, we study in Fig. 5.8 the statistical function F as a function of the frequency ω for various momenta.²⁰ The frequency Fourier transform has been computed again for fixed $t_w = 400$ instead of for fixed τ . This allows for better statistics and provides a faithful qualitative picture. However, compared to the spectral function, the statistical function varies

²⁰The data shown corresponds to a volume $V = 128^3$, slightly smaller than for the spectral function. However, for finite momentum the results are to a large extent independent of the volume, as opposed to the zero momentum mode of Chap. 4.

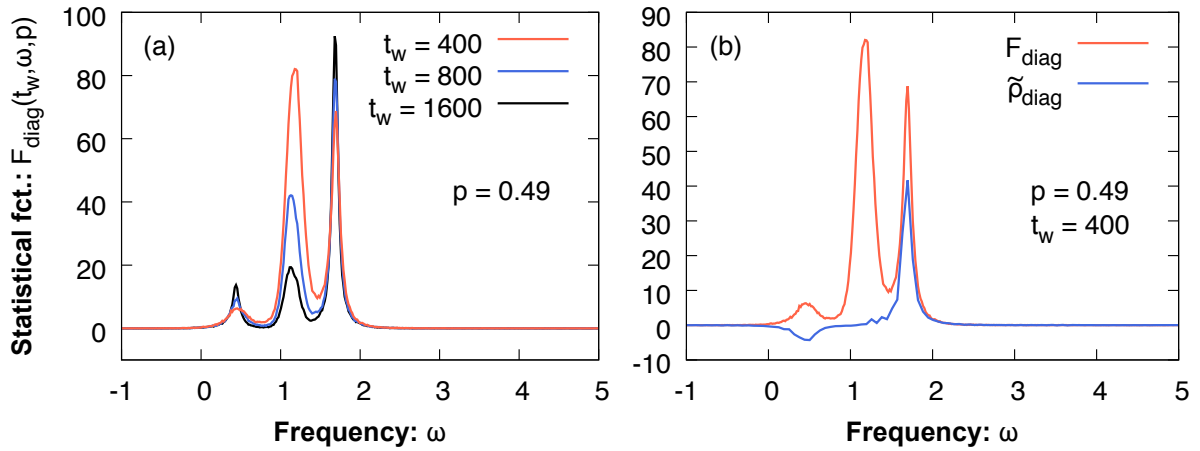


FIGURE 5.9: (a) Fourier transform of the statistical function $F(t_w, \omega, \mathbf{p})$ for momentum $p = 0.49$ at different times: $t_w = 400$, $t_w = 800$, and $t_w = 1600$. (b) Comparison of the Fourier transforms of the statistical function $F(t_w, \omega, \mathbf{p})$ and spectral function $\tilde{\rho}(t_w, \omega, \mathbf{p})$ for $p = 0.49$ at time $t_w = 400$.

more strongly with time and the identification $F(t_w, \omega, p) \approx F(\tau = t_w, \omega, p)$ is less accurate. Hence, quantitative statements need to be made with caution.

Figure 5.8 reveals an interesting peak structure of the statistical function. Note that the peaks in this case are all positive (c.f. Fig. 5.3) due to the different symmetry properties of F . At low momenta a single peak close to the chemical potential $\mu \approx 1.06$ dominates the spectrum. As the momentum is increased, two further peaks left and right from the previous peak become visible, while the amplitude of the middle one gets quickly suppressed (note the scale in the y -axis). At intermediate momenta $p \approx 0.5$ the center peak becomes comparable in size to the right peak. At yet larger momenta this trend continues and the spectrum becomes fully dominated by the right peak.

The left and right peaks observed in Fig. 5.8 can be identified with the Bogoliubov peaks of the spectral function. To illustrate this, we show in Fig. 5.9b a direct comparison of the statistical function $F(t_w, \omega, p)$ and spectral function $\tilde{\rho}(t_w, \omega, p)$ for $p = 0.49$ at $t_w = 400$ as a function of frequency. As it can be seen, the position and even shape of the left and right peaks is the same for both F and $\tilde{\rho}$, where we recall that the left peak of $\tilde{\rho}$ is negative due to the symmetry properties of the spectral function. The comparison of these functions for different momenta yields qualitatively the same result (c.f. Figs. 5.3 and 5.8), namely that the left and right peaks have the same shape and position for both F and $\tilde{\rho}$.²¹

Most importantly, the central peak is clearly a new feature of F which is completely absent in the spectral function. Furthermore, the form of this peak looks slightly different than the Bogoliubov peaks.²² These results clearly imply that the fluctuation-dissipation relation between F and ρ is broken at low momenta. Of course, this relation does not need to hold out of equilibrium. In this case though, the qualitative difference in peak structure observed between F and ρ is striking. Because of it, the scaling behavior of these two quantities is

²¹For the momenta where the Bogoliubov peaks of F do not overlap significantly with the center peak, a fit to the right peak results in the same dispersion relation as in Fig. 5.5.

²²While for extremely small momenta the central peak appears to have a Gaussian shape, its analytic form is in general unclear.

not guaranteed to be related and scaling exponents, such as the dynamical exponent z , can be different. The results presented for F indicate that the low-momentum scaling behavior of F , which was analyzed in Chap. 4, is dominated by the central peak. In contrast, the low-momentum scaling behavior of ρ is dominated by the Bogoliubov peaks. This explains the different results for z obtained in Chaps. 4 and 5.

At long times, the system slowly approaches equilibrium and hence the fluctuation dissipation relation should be restored. For this to happen, the central peak should tend to zero at long times. To check this tendency, we show in Fig. 5.9a the evolution of the Fourier transformed statistical function for fixed momentum $p = 0.49$. As expected, the central peak becomes suppressed as time passes, while the Bogoliubov peaks remain and even increase slightly with time.

5.7 A challenge for kinetic theory

The above findings have important implications for the (resummed) kinetic theory presented in Chap. 3. To understand this, it is useful to recall that the definition of the distribution function $f(t, p)$ is related to the equal-time statistical function and hence is given (for $p \neq 0$) by [c.f. Eq. (3.11)]

$$f(t, p) + \frac{1}{2} = \int \frac{d\omega}{2\pi} F_{\text{diag}}(t, \omega, p). \quad (5.38)$$

We have shown in Fig. 5.8 that at low momenta $F_{\text{diag}}(t, \omega, p)$ is clearly dominated by the central peak, whereas at large momenta the Bogoliubov peaks take over. Comparing the approximate momenta at which this transition happens with the distribution function of Fig. 3.3 reveals that the infrared dynamics of $f(t, p)$ close to the nonthermal fixed point are dominated by the central peak. Reversely, this shows that the change in amplitude of the central peak with time is at low momenta related to the self-similar evolution of $f(t, p)$.

In Secs. 3.4 and 3.5 we extracted the exponents α , and β determining the evolution of the distribution function $f(t, p)$ from kinetic theory using a number of assumptions. Using first a free spectral function, Eq. (3.80), with quadratic dispersion $\omega_p = p^2/2m$ we obtained a value for $\beta = 1/2$ very close to the numerical results from classical-statistical simulations (see Sec. 3.4). As we have seen in this section though, this assumption is not correct at low momenta and instead a Bogoliubov spectral function such as (5.30) needs to be used, which has a linear dispersion $\omega_p \sim p$ at low momenta.

In deriving a kinetic equation for the distribution function we further used the form of the fluctuation-dissipation relation to define an (off-shell) nonequilibrium distribution via $F(t, \omega, p) = (f(t, \omega, p) + 1/2)\tilde{\rho}(t, \omega, p)$ [Eq. (3.81)]. However, such a procedure is ill-defined, especially in the infrared, as we have seen that F and ρ can not be related to each other by simple multiplication with a function $f(t, \omega, p)$ due to the absence of the central peak in the spectral function. In Sec. 3.5 we considered instead an off-shell kinetic equation with general spectral and statistical function without assuming such a relation. However, in order to obtain scaling relations for α and β we assumed that F and ρ scale with the same dynamical exponent z . As we have learnt from Chaps. 4 and 5 this assumption is not correct.

In view of this, a proper kinetic description of the nonthermal fixed point needs to take into account the insights obtained in this chapter. First of all, the statistical and spectral functions need to be treated as truly independent quantities. In particular, the scaling exponents, such as the dynamical exponent z , describing their scaling behavior can be generally different. As a first approximation, one may neglect the widths of the peaks appearing in both F and $\tilde{\rho}$. For $\tilde{\rho}$ one may use Eq. (5.30) with the Bogoliubov dispersion and amplitudes given in (5.29) and (5.31). Based on Fig. 5.8 one can make for F the ansatz

$$F(\tau, \omega, p) \approx 2\pi \left[D(\tau, p) \delta(\omega - \mu - \omega_D(p)) + B_+(\tau, p) \delta(\omega - \mu - \omega(p)) + B_-(\tau, p) \delta(\omega - \mu + \omega(p)) \right]. \quad (5.39)$$

Here, $\omega_D(p)$ is the dispersion of the central peak and $\omega(p)$ is the Bogoliubov dispersion of (5.29). Using (5.38) the amplitudes of the peaks are related to the distribution function as

$$f(t, p) + \frac{1}{2} = D(t, p) + B_+(t, p) + B_-(t, p), \quad (5.40)$$

Despite the difficulty introduced by the extra central peak, it is highly remarkable that a relatively simple description of F and ρ during the universal self-similar regime has emerged, especially in the nonperturbative infrared regime. The derivation of a resummed kinetic equation using (5.30) and (5.39) may shed light onto the processes behind the self-similar behavior of $f(t, p)$ from a new perspective. In particular, it will allow to reexamine the predictive power of the $1/N$ expansion in the infrared regime of the nonthermal fixed point.

5.8 Conclusions

This chapter has been mainly devoted to the computation and analysis of the spectral function of the nonrelativistic Bose gas close to the nonthermal fixed point. In order to compute this quantity using classical-statistical simulations, we have used a method based on small perturbations of the system with external fields. In this framework, the spectral function emerges as the linear order response to such a perturbation and can be computed from one-point functions alone.

The spectral function in frequency space obtained at low momenta exhibits a characteristic double-peak structure associated to the existence of Bogoliubov quasiparticles. As the momentum is increased, one of the peaks vanishes and the spectral function approaches the one of a free particle. The amplitude and dispersion relation of the peaks were found to be approximately constant in time and remarkably well reproduced by the Bogoliubov formulae over the whole momentum range without fitting parameters. In particular, the dispersion of the quasiparticles scales linearly at low momenta and becomes quadratic at large momenta. Due to scattering effects the quasiparticles have a nonvanishing decay rate, which is reflected in the width of the peaks. In contrast to the amplitude and dispersion, the decay rates were found to evolve with time.

We further analyzed the self-similar scaling behavior of the spectral function in the infrared. We demonstrated that the spectral function shows self-similar scaling behavior consistent

with the exponent $\beta = 0.55$ obtained in Chap. 3, an anomalous dimension $\eta = 0$ and the dynamical exponent $z = 1$ associated to the low-momentum scaling of the dispersion relation. We emphasize though that the current results do not rule out small deviations from these exponents, in particular a nonvanishing anomalous dimension.

Motivated by these results we analyzed the statistical function F in frequency space and discovered the existence of an extra peak which is absent in the spectral function. This peak implies the breaking of the fluctuation-dissipation relation and it appears to be the dominant contribution at low momenta. In this sense, it is directly associated to the infrared dynamics of the distribution function. Importantly, the absence of this peak in the spectral function explains why the statistical function scales with a dynamical exponent $z \approx 2$, as found in Chap. 4, while the spectral function computed here scales with $z = 1$.

These results provide a new perspective on the physics of the nonthermal fixed point in the nonrelativistic Bose gas. While the spectral function shows a linear Bogoliubov dispersion at low momenta, we have seen that the statistical function, and hence the distribution function too, is an independent quantity which at low momenta is dominated by different processes related to an extra peak in frequency space. This new information can in principle be used to derive a more accurate (resummed) kinetic theory for the nonthermal fixed point using the $1/N$ expansion. In particular, this may help elucidate the types of processes responsible for the transport of particles in the infrared. Finally, it has become both necessary and compelling to do a similar computation for the relativistic theory. In view of the universality reported in Chap. 3, this chapter poses the question of whether the extra peak, which appears to be insensitive to the underlying spectral function, is present in the relativistic theory as well and whether it may be related to the emergence of universality.

Part II

Rydberg Spin Dynamics

Chapter 6

Relaxation Dynamics in a Dipolar Spin System

This chapter is based on the preprint “*Relaxation of an isolated dipolar-interacting Rydberg quantum spin system*”, A. Piñeiro Orioli, A. Signoles, H. Wildhagen, G. Günter, J. Berges, S. Whitlock, M. Weidemüller, arXiv:1703.05957 [90]. Figures and parts of the text are taken from that reference. The experimental results presented were obtained by the group of S. Whitlock and M. Weidemüller.

A many-body quantum system initially prepared in an out-of-equilibrium state can produce beautifully complex dynamics as a consequence of interparticle interactions. Usually, these same interactions also imply coupling to uncontrolled environmental degrees of freedom, causing rapid relaxation of the system towards an equilibrium state [151]. Remarkably though, relaxation is not restricted to open quantum systems. As explained in Chap. 1, even when effectively isolated from any external environment, an effective loss of details about initial conditions can occur for relevant observables of the unitary quantum many-body dynamics [3, 6, 7].

An example of this loss of memory was provided in the last three chapters, where we showed that a system prepared in an overoccupied initial state (c.f. Sec. 3.2) may approach at intermediate times a nonthermal fixed point, where most of the details about the initial state are washed out and the dynamics becomes universal. For other types of systems and initial conditions, however, the mechanisms responsible for relaxation in a closed system may be different. The picture may especially change when quantum effects are expected to become relevant, such as for quantum spin-1/2 systems. To study such cases is the purpose of this chapter.

Ultracold atoms, ions and molecules offer unique platforms for addressing such questions due to their high degree of isolation from their environments and the possibility to realize prototypical models such as quantum spin models [89, 152, 153]. These systems have already been used to study nonequilibrium dynamics such as collective spin dynamics [91, 92, 154–156], spin squeezing [88, 157–160], propagation of correlations [86, 161–164] and relaxation or localization effects [165–170]. While the vast majority of these experiments have involved either low-dimensional geometries or contact interactions, spin models can also be realized in three dimensions with dipolar interactions (scaling with interparticle distance as r^{-3}) by

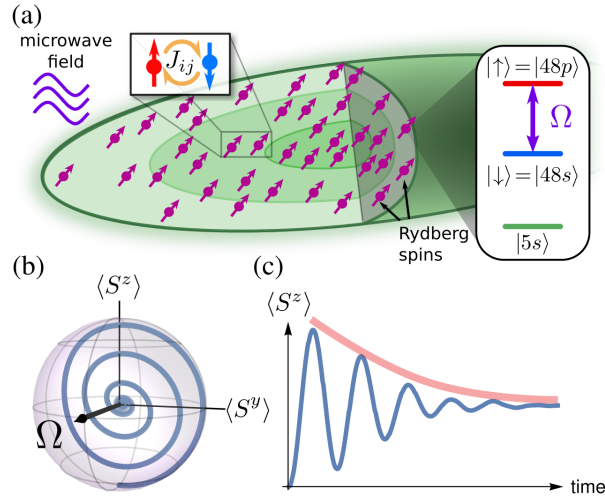


FIGURE 6.1: Sketch of a dipolar-interacting Rydberg spin system. (a) In an ultracold atomic gas Rydberg excitations are optically prepared in the initial state $|\downarrow\rangle$. Then a microwave field is turned on which resonantly couples the $|\downarrow\rangle$ and $|\uparrow\rangle$ states. (b) This drives coherent spin oscillations of each atom in the ensemble as seen in the Bloch sphere representation of a single embedded spin, based on the numerical solution of the 8 spin Schrödinger equation. (c) Strong dipolar exchange interactions between the spins J_{ij} compete with the driving field leading to relaxation of the spin oscillations.

using magnetic atoms [171, 172], polar molecules [82, 83] or highly excited Rydberg states of atoms [173]. This provides an interesting border case between long- and short-range physics and can dramatically influence the resulting phase structure [174], stability properties [175–177] and dynamics [178, 179].

In this chapter, we experimentally and theoretically investigate the relaxation dynamics of a quantum spin system and identify the role played by disorder and quantum fluctuations in this process. Experimentally, we consider a three-dimensional ensemble of ultracold Rydberg atoms (Fig. 6.1a) which can be mapped onto a dipolar XY quantum spin-1/2 Hamiltonian. Upon suddenly switching on an external microwave field we observe oscillatory dynamics and density-dependent relaxation of the many-body system to a practically unmagnetized state. We show that the many-body dynamics observed in the experiment can indeed be accurately described by unitary quantum dynamics of the dipolar spin-1/2 model without the need to invoke any external decoherence processes. Finally, we disentangle the different mechanisms leading to relaxation of the collective spin by employing a well-defined hierarchy of theoretical approximations.

6.1 Realization of a dipolar XY model

We start by introducing the experimental platform and presenting the mapping from Rydberg atoms to an effective spin-1/2 model.¹ The experiments are performed on a gas of ^{87}Rb atoms prepared in a cigar-shaped optical dipole trap (Fig. 6.1a). To realize the quantum spin system, a small fraction of atoms are first excited from the electronic ground state $|g\rangle =$

¹Further details on the experimental setup can be found in Refs. [90, 180].

$|5S_{1/2}, F = 2, m_F = +2\rangle$ to the Rydberg state $|\downarrow\rangle \equiv |48S_{1/2}, m_j = +1/2\rangle$ via the short-lived intermediate state $|e\rangle = |5P_{3/2}, F = 3, m_F = +3\rangle$. This is done by using a resonant two-photon laser excitation scheme involving narrow linewidth lasers, with wavelengths around 780 nm and 480 nm, both pulsed on for a duration of $0.8 \mu\text{s}$. The peak density of spins can be varied between $9 \times 10^7 \text{ cm}^{-3}$ and $9 \times 10^8 \text{ cm}^{-3}$ by tuning the ground-state density before the excitation pulse. In order to isolate and address a well-defined pair of Zeeman states a magnetic field of 6.4 G is applied to the system. To drive the spin dynamics we apply a microwave field of 35.1 GHz to resonantly couple the $|\downarrow\rangle$ and $|\uparrow\rangle \equiv |48P_{3/2}, m_j = +3/2\rangle$ states with Rabi frequency $\Omega/2\pi = (1.48 \pm 0.05) \text{ MHz}$.

The Rydberg states $|\uparrow\rangle$ and $|\downarrow\rangle$ of each atom constitute our spin-1/2 degree of freedom. Pairs of atoms involving different combinations of $|\uparrow\rangle, |\downarrow\rangle$ couple to each other via dipole-dipole interactions [181, 182] given by the operator

$$\hat{V}_{dd} = \frac{\hat{\mathbf{p}}_i \cdot \hat{\mathbf{p}}_j - 3(\mathbf{n} \cdot \hat{\mathbf{p}}_i)(\mathbf{n} \cdot \hat{\mathbf{p}}_j)}{R_{ij}^3}, \quad (6.1)$$

where $\hat{\mathbf{p}}_i$ and $\hat{\mathbf{p}}_j$ are the electric dipole moment operators of the two atoms i and j , $R_{ij} \equiv |\mathbf{R}_{ij}|$ is the relative distance between them and \mathbf{n} is a unit vector pointing along \mathbf{R}_{ij} . Starting from Eq. (6.1) one can derive a spin-1/2 Hamiltonian governing the dynamics of the effective spin system. For this we neglect the coupling to states outside the spin-1/2 manifold² and expand \hat{V}_{dd} in the $|\uparrow\rangle, |\downarrow\rangle$ basis. This involves calculating the matrix elements corresponding to all pair states involving combinations of $|\uparrow\rangle, |\downarrow\rangle$.

At first order, the only non-zero terms in the pair state basis are the *flip-flop* exchange terms that couple the states $|\downarrow\uparrow\rangle$ and $|\uparrow\downarrow\rangle$. In terms of the dipole raising and lowering operators $\hat{p}^\pm = \mp(\hat{p}^x \pm i\hat{p}^y)/\sqrt{2}$, Eq. (6.1) can be rewritten as $(\hat{\mathbf{p}}_i \cdot \hat{\mathbf{p}}_j) = -(\hat{p}_i^+ \hat{p}_j^- + \hat{p}_i^- \hat{p}_j^+)$ and $(\mathbf{n} \cdot \hat{\mathbf{p}}_i)(\mathbf{n} \cdot \hat{\mathbf{p}}_j) = -(1/2) \sin^2 \theta_{ij} (\hat{p}_i^+ \hat{p}_j^- + \hat{p}_i^- \hat{p}_j^+)$. Including the microwave coupling field we arrive at the dipolar XY Hamiltonian in an external field ($\hbar = 1$):

$$\hat{H} = \frac{1}{4} \sum_{i,j} J_{ij} (\hat{S}_i^+ \hat{S}_j^- + \hat{S}_i^- \hat{S}_j^+) + \Omega \sum_i \hat{S}_i^x, \quad (6.2)$$

where \hat{S}_i^α ($\alpha = \{x, y, z\}$) refers to the spin-1/2 angular momentum operator for spin i , $\hat{S}_i^\pm = (\hat{S}_i^x \pm i\hat{S}_i^y)$ are the spin raising and lowering operators and J_{ij} for $i \neq j$ is the matrix element of the dipole-dipole interaction

$$J_{ij} = \frac{C_3(1 - 3 \cos^2 \theta_{ij})}{R_{ij}^3}. \quad (6.3)$$

Here $C_3/2\pi = \langle \uparrow\downarrow | p^+ p^- | \downarrow\uparrow \rangle = -1.73 \text{ GHz } \mu\text{m}^3$ characterizes the strength of the exchange interaction³ and θ_{ij} is the angle between \mathbf{R}_{ij} and the quantization axis. Second order corrections to the interactions (van der Waals terms) scale as R_{ij}^{-6} and are approximately two orders of magnitude smaller than the direct dipole interaction, therefore they can be neglected. Of

²Assuming a laser linewidth of 1 MHz we estimate that unwanted population of Zeeman sublevels other than $|\downarrow\rangle$ is less than 2%, consistent with spectroscopic measurements.

³The dipole matrix elements are computed using a standard decomposition into radial and angular parts together with the Rydberg formulas for the energy shifts and wave-functions [181, 183–188] (see [189] for an outline of the procedure).

course, further corrections to the spin model (6.2) are in principle possible due to experimental imperfections. Possible sources of errors will be discussed further below.

6.2 Theoretical description of spin systems

For sufficiently small numbers of spins, the dynamics of (6.2) can be solved without further approximations by direct diagonalization. A corresponding numerical solution for a system of 8 spins is sketched in Fig. 6.1b, c. For larger systems one has to resort to additional approximations. In the following, we introduce the theoretical methods that will be used in this chapter to describe the dynamics of the Rydberg spin system (6.2).

6.2.1 Moving Average Cluster Expansion

The Moving Average Cluster Expansion (MACE) [84] consists in computing the exact quantum evolution of appropriately chosen small clusters of Rydberg atoms and then averaging over many clusters. Specifically, for each spin i one selects a cluster composed of the spins $\mathcal{C}_i \equiv \{i, i_1, \dots, i_{N_c-1}\}$ that lie closest to spin i , i.e. $|\mathbf{r}_i - \mathbf{r}_{i_n}| \leq |\mathbf{r}_i - \mathbf{r}_j|$ for all $j \notin \mathcal{C}_i$.⁴ This method is particularly well-suited for computing local observables such as one-point functions $\langle \hat{S}_i^\alpha \rangle$.

To compute the expectation value of the collective spin $\hat{S}^\alpha \equiv 1/N \sum_i \hat{S}_i^\alpha$, with $\alpha = \{x, y, z\}$, one makes the following approximation:

$$\langle \hat{S}^\alpha \rangle = \frac{1}{N} \sum_i \langle \hat{S}_i^\alpha \rangle \approx \frac{1}{N} \sum_i \langle \hat{S}_i^\alpha \rangle_{\mathcal{C}_i}, \quad (6.4)$$

where $\langle \cdot \rangle_{\mathcal{C}_i}$ is the expectation value calculated in the cluster \mathcal{C}_i . That is, for each cluster \mathcal{C}_i one calculates only the expectation value $\langle \hat{S}_i^\alpha \rangle_{\mathcal{C}_i}$ of spin i . Then, the results of all the clusters are added together to obtain the collective spin.

With a slight modification one may also estimate collective spin variances $\langle (\hat{S}^\alpha)^2 \rangle - \langle \hat{S}^\alpha \rangle^2$. This quantity involves in principle correlators of the form $\langle \hat{S}_i^\alpha \hat{S}_j^\alpha \rangle$ for arbitrary i and j . However, assuming that each spin is significantly correlated only with its closest neighbors we can neglect the contribution from the connected correlator $\langle \hat{S}_i^\alpha \hat{S}_j^\alpha \rangle - \langle \hat{S}_i^\alpha \rangle \langle \hat{S}_j^\alpha \rangle$ between far apart spins to the variance. In this way, one can compute the variance as follows:

$$\langle (\hat{S}^\alpha)^2 \rangle \approx \frac{1}{N^2} \sum_i \left(\langle \hat{S}_i^\alpha \hat{\Sigma}_i^\alpha \rangle_{\mathcal{C}_i} - \langle \hat{S}_i^\alpha \rangle_{\mathcal{C}_i} \langle \hat{\Sigma}_i^\alpha \rangle_{\mathcal{C}_i} \right) + \langle \hat{S}^\alpha \rangle^2, \quad (6.5)$$

where we defined the collective spin operator for a given cluster as

$$\hat{\Sigma}_i^\alpha = \sum_{j \in \mathcal{C}_i} \hat{S}_j^\alpha. \quad (6.6)$$

⁴Alternatively, the clusters can be built out of the strongest neighbors of spin i , i.e. $|J_{i,i_n}| \geq |J_{i,j}|$ for all $j \notin \mathcal{C}_i$. If J_{ij} decreases monotonically with the distance, these two methods are equivalent. However, a small speed-up in convergence can be obtained in some cases by using the strongest neighbors. Whenever we use the latter method, we check that the same result is obtained as with closest neighbors.

For each cluster \mathcal{C}_i one calculates only the connected correlators $\langle \hat{S}_i^\alpha \hat{S}_j^\alpha \rangle_{\mathcal{C}_i} - \langle \hat{S}_i^\alpha \rangle_{\mathcal{C}_i} \langle \hat{S}_j^\alpha \rangle_{\mathcal{C}_i}$ between the center spin i and each of the other spins $j \in \mathcal{C}_i$, thus neglecting correlations to $j \notin \mathcal{C}_i$. This is repeated for each spin i , with cluster \mathcal{C}_i , and then all terms are summed up.⁵ The disconnected part $\langle \hat{S}^\alpha \rangle^2$ is computed as in Eq. (6.4). It is important to note that for a given atom configuration one can leave this last term out to obtain the variance. However, when averaging over different configurations of randomly chosen atom positions, it is essential that the full two-point function $\langle (\hat{S}^\alpha)^2 \rangle$ is averaged and not the connected part $\langle (\hat{S}^\alpha)^2 \rangle - \langle \hat{S}^\alpha \rangle^2$.

The accuracy of MACE can be checked by increasing the size of the clusters used. If the outcome does not change by increasing the number of spins per cluster, then the MACE is an accurate approximation to the dynamics of the many-spin quantum system. In general, it can be expected to yield accurate results for short enough times and as long as correlations do not grow significantly beyond the size of the clusters chosen.

6.2.2 Discrete TWA for spins

The classical statistical or truncated Wigner approximation (TWA) (Sec. 2.5) used in previous chapters can be applied to spin systems as well [100, 102, 103, 190]. While the regime of validity of this approximation for spin-1/2 systems is still not fully understood,⁶ it has shown in some cases to yield accurate results [102]. As we will see, it can also be used to shed light onto the physical processes responsible for the relaxation dynamics.

Adapting TWA to treat spin systems requires the definition of a suitable Wigner function and Weyl symbols, according to the method presented in Sec. 2.5.3. A common way to do so is to map the spins onto bosonic operators, e.g. using Schwinger bosons [100], and then employ the same framework as for bosons. However, when applied to spin-1/2 systems this often leads to rather involved Wigner functions, which need to be further approximated in order to be sampled.⁷ Recently, alternative schemes based on discrete Wigner functions have been proposed [102, 191], which do not require such a mapping and allow for a sampling of the initial state without further approximations. This method is named discrete TWA (dTWA).

In dTWA each spin is represented by a classical vector S_i^α with $\alpha \in \{x, y, z\}$. The classical spins fulfil classical equations of motion, which are obtained from the Heisenberg equations for operators by substituting each operator by a classical vector, after proper symmetrization [see Sec. 2.5 and Eq. (6.9)]. Most importantly, the spins are initialized with random numbers drawn from a discrete Wigner function $W(\mathbf{S}_{i,0})$. For the special case of the spin state $|\downarrow\rangle$ we have

$$W(\mathbf{S}_{i,0}) = \frac{1}{4} \delta(S_{i,0}^z + 1/2) \sum_{x_i, y_i = \pm 1/2} \delta(S_{i,0}^x - x_i) \delta(S_{i,0}^y - y_i), \quad (6.7)$$

⁵We note that this procedure to estimate the variance is not unique. For instance, one may choose instead for each pair (i, j) of spins an optimum cluster \mathcal{C}_{ij} in order to compute each correlator $\langle \hat{S}_i^\alpha \hat{S}_j^\beta \rangle$ more accurately. However, we checked that the results and conclusions presented in this work are qualitatively insensitive to this. A more detailed discussion is beyond the scope of this work.

⁶TWA is usually a good approximation for large spins [100]. For spin-1/2 the classicality condition (2.84) does not seem to hold a priori. If one maps the spins to Schwinger bosons [81, 100], the occupancies of the Schwinger bosons are restricted, because of the mapping, to values of order one. Nevertheless, this does not rule out the possibility that the dynamics be in some regimes effectively classical.

⁷For instance, using Schwinger bosons the Wigner function of typical states such as $|\uparrow\rangle$ is highly oscillatory and not positive definite [100].

i.e. the z -component is fixed at $-1/2$ and the transverse directions are sampled with $\pm 1/2$. For rotated initial conditions we refer to App. D.

6.3 Relaxation dynamics of a Rydberg spin system

We consider now the relaxation dynamics of the Rydberg spin system introduced above. The experiment starts with N atoms spin-polarized in the state $|\downarrow\rangle$ ($N_\uparrow = 0, N_\downarrow = N$). We then suddenly switch on the microwave field Ω which quenches the system far-from-equilibrium. After letting the system evolve for some time we measure the magnetization along the z direction $\langle \hat{S}^z \rangle = \langle N_\uparrow \rangle / \langle N \rangle - 1/2$. For vanishing spin density ($J_{ij} \rightarrow 0$), the dynamics of the magnetization exhibits coherent oscillations between $\pm 1/2$ at the frequency Ω (Figs. 6.1c and 6.2a). As the density is increased ($J_{ij} \sim \Omega$), dipole-dipole interactions compete with the coherent oscillations to produce more complex many-body dynamics. The effect of these interactions can cause different atoms in the ensemble to become correlated, ultimately leading to a decaying total magnetization as sketched in Fig. 6.1b, c. For all practical purposes the state with $\langle \hat{S}^z \rangle = 0$ is the equilibrium state, as for a many-body system the time scale associated with possible revivals grows rapidly with system size.

To experimentally measure the magnetization we optically de-pump the $|\downarrow\rangle$ state and then detect the remaining $|\uparrow\rangle$ population N_\uparrow by field-ionization which is then averaged over typically 10 realizations.⁸ The mean total number of spins $\langle N \rangle$ is inferred by assuming the system equilibrates to a balanced state ($\langle \hat{S}^z \rangle = 0$).

The blue points in Fig. 6.2 show the time evolution of the magnetization measured for different mean numbers of spins $\langle N \rangle$ within a fixed volume (corresponding to different spin densities). Over the full dataset the magnetization appears to oscillate at a single frequency and with a damping rate between 0.2 MHz and 5 MHz. In particular, the high contrast Rabi oscillations seen in the lowest density data (Fig. 6.2a) demonstrate the successful isolation of a two-level system within the Rydberg-state Zeeman manifolds. As the spin density is increased (Fig. 6.2 from a–e) we observe a transition to an overdamped regime with a damping time which is at least an order of magnitude faster than any single-spin decoherence processes.

To investigate whether the experimental results of Fig. 6.2 can be understood from unitary quantum dynamics of the spin model (6.2) we compare to theoretical calculations. For this we use the MACE method introduced above, which is particularly suitable for the calculation of average magnetizations, and it has been successfully used to model the nonequilibrium dynamics of similar models realized with polar molecules in optical lattices [82, 84]. From the random positions of the atoms (and hence the randomness of J_{ij}) one can expect a rather slow spread of correlations through space [11], which indicates that different clusters can be approximated to evolve at early times independently from each other. To check this, we increase the size of the clusters until the results become insensitive to their size. For the

⁸Since in our case the field ionization process is state-insensitive, we first depopulate the Rydberg $|\downarrow\rangle$ state, by applying a $0.8 \mu\text{s}$ light pulse that resonantly couples it to the rapidly-decaying intermediate state $|e\rangle$. The remaining Rydberg atoms in the $|\uparrow\rangle$ state are then field-ionized and the produced ions are counted with a multichannel plate detector. From the distribution of arrival times we can verify that no ions are spontaneously created in the gas, which is consistent with earlier experiments for the short time scales and low densities of the experiment [192].

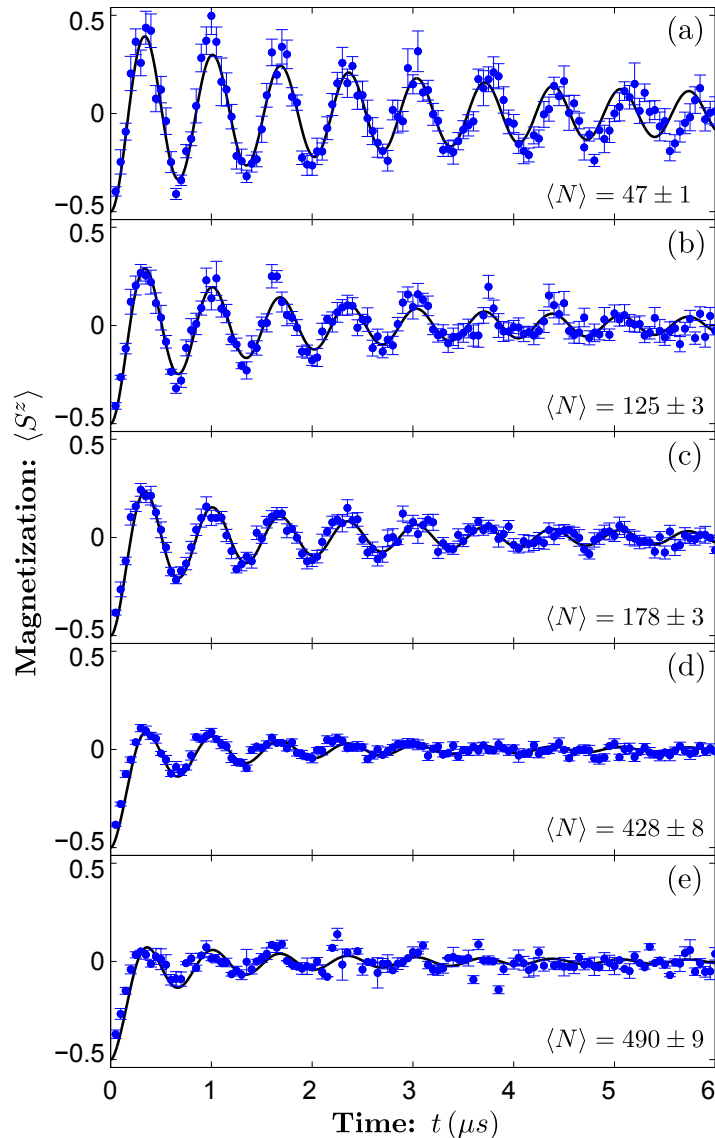


FIGURE 6.2: Non-equilibrium magnetization dynamics of a driven ensemble of spins for various mean numbers of spins N within a fixed volume. The experimental data (blue points) are compared to a MACE simulation (black solid line). The error bars represent the standard errors of the mean.

system considered here we found the results to approximately converge for clusters of about 10 spins.

In each experimental realization the position of the Rydberg atoms is random and can be assumed to be fixed, due to the fast timescales of the experiment ($\sim \mu s$). For the simulations, we model the distribution of spins in the experiment according to a three-dimensional Gaussian distribution. Further below we verify that our results do not depend much on the precise details of the distribution. A spatial configuration of spins is generated by sequentially choosing random coordinates from the Gaussian distribution and discarding cases which fall within a characteristic distance of $3.8 \mu m$ of another spin to account for the fact that during the preparation stage Rydberg atoms are created with a certain minimal distance from each other due to their van-der-Waals interactions (Rydberg blockade [193]). From the resulting

configuration we then compute the interaction coefficients J_{ij} according to Eq. (6.3). For the simulations we average the magnetization over different position realizations until the results converge.

To match the conditions of the experiment we choose the parameters of the Gaussian distribution to have the same aspect ratio as the atom trap. We adjust the overall effective volume of the spin distribution by taking the lowest-density experimental data and performing simulations assuming different Gaussian volumes V , while keeping the total number of spins fixed, until optimal agreement is found. The obtained volume $V = (2.7 \pm 0.4) \times 10^5 \mu\text{m}^3$ is kept fixed in all further simulations and different densities are simulated by changing the number of spins in accordance with the experiment. We note that the obtained effective volume is approximately 0.3 times the naive estimate based on the excitation laser beam waist and cloud size. This may be to partially compensate uncertainties in experimental parameters such as the ion detection efficiency.

In Fig. 6.2 we compare the MACE simulations with the experimental data. Remarkably, the simulated dynamics are in good agreement with the data for the full range of experimental parameters, including the density-dependent damping. A slight discrepancy of the oscillation frequency at long times is seen (e.g. in Fig. 6.2a). While the theoretical calculations predict a constant oscillation frequency, we find that the frequency of the measured data in Fig. 6.2a slowly drifts with time. This may be explained by transient power fluctuations of the microwave field after switching on the source. While we cannot rule out all possible sources of additional fluctuations in the experiment, the good agreement between the data and the MACE simulations points out that the observed relaxation can indeed be described in terms of unitary quantum evolution of the Hamiltonian (6.2) alone, without the need to invoke any external decoherence processes.

Possible sources of errors

Before we investigate the possible mechanisms responsible for the observed relaxation behavior, we study possible experimental imperfections and errors in the theoretical modeling of the experiment. We first quantify possible experimental deviations from the pure XY Hamiltonian (6.2) evolution, by analysing the contribution of a number of sources of noise to the experiment:

1. *Atomic motion.* The Rydberg atoms can move freely within the trap. The motion induced by the finite temperature $T = 40 \mu\text{K}$ of the gas during the $6 \mu\text{s}$ duration of the experiment leads to displacements of less than $1 \mu\text{m}$, more than one order of magnitude smaller than the typical interatomic distance. Electrostatic forces due to the Rydberg-Rydberg interactions cause displacements of less than $1 \mu\text{m}$ as well, even for the strongly interacting case (highest density). Additional corrections such as Doppler shifts of the microwave transition are on the order of ten hertz and are therefore also neglected.
2. *Rydberg state decay.* The radiative lifetimes (spontaneous emission) of the Rydberg states used are $120 \mu\text{s}$ and $240 \mu\text{s}$ for the $|\downarrow\rangle$ and $|\uparrow\rangle$ states, respectively [194]. Black-body redistribution to other Rydberg states also occurs with a time constant of $110 \mu\text{s}$ and $120 \mu\text{s}$, respectively. Thus the probability for decay within the $6 \mu\text{s}$ window of the experiment is $< 10\%$.

3. *Technical noise on the microwave source.* The relative frequency stability of the microwave source is approx $< 10^{-8}$, corresponding to sub-kilohertz uncertainty, and is thus not a contributing factor to the observed dynamics. However, we have found that the microwave power can fluctuate from shot-to-shot, leading to a fluctuating spin precession frequency. Since each data point is averaged over several repetitions of this experiment this would appear as an additional damping of the coherent spin dynamics. We estimate these fluctuations to be below 1%. This would lead to a maximal reduction of contrast of 15% at $\sim 6 \mu\text{s}$.

In summary, the sources of noise discussed may account for a maximum of about 15% of the magnetization decay. While this can not be fully neglected, it can not account for most of the magnetization decay observed. Furthermore, the deviations from the expected behavior would be on the order of the error bars of Fig. 6.2 and can thus not be resolved with the current experimental accuracy.

Next, we check that the agreement between theory and experiment does not rely on fitting details of the chosen distribution of Rydberg atoms. For this we compare the MACE simulations for three different spatial distributions, which we label “*Gauss*”, “*Mountains*” and “*Shell*”. The “*Gauss*” distribution is the one used for Fig. 6.2, while the two other distributions are generated as follows:

- *Mountains:* Each position coordinate is obtained by multiplying two random numbers η and ξ : η is a Gaussian random number with non-zero mean $\langle \eta \rangle$ and $\langle \eta \rangle / \sqrt{\langle \eta^2 \rangle - \langle \eta \rangle^2} = 1.7$, while ξ is drawn from a bimodal distribution with $\xi = \pm 1$ with probability 1/2.
- *Shell:* The position of each atom is obtained by first sampling one point from a uniform distribution on the surface of a unit sphere, and then multiplying the radius by $|\eta|$, where η is a Gaussian random number with $\langle \eta \rangle / \sqrt{\langle \eta^2 \rangle - \langle \eta \rangle^2} = 5$.

Both distributions are subsequently stretched to have the same aspect ratio as the Gaussian one. In all cases, the same short-distance cutoff due to Rydberg blockade is imposed. Figs. 6.3d-f show a two-dimensional projection of the three distributions. The blue points correspond to the atom positions of 20 different realizations with $N = 178$ superposed into one single graph.

In order to compare results from the above distributions we first adjust the effective volumes. For this we scale the *Mountains* and *Shell* distributions with an overall factor such that for intermediate density ($N = 178$) the results match those of the Gaussian profile as closely as possible. The scaling factor obtained in this way is kept fixed for the simulations at other densities. Figs. 6.3a-c show the results obtained from MACE with the three different distributions for the highest, the lowest and an intermediate density. The quantitative agreement between all distributions over the whole range of densities considered is remarkable and shows that the results and conclusions of this work are largely independent of details on the distribution of atom positions.

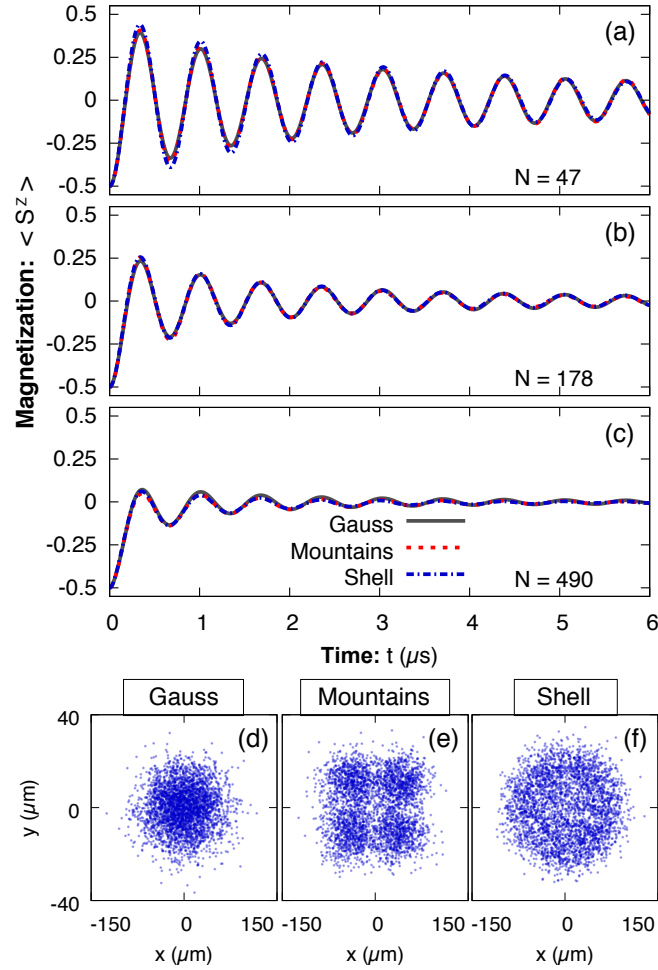


FIGURE 6.3: (a)-(c) Decay of the magnetization $\langle \hat{S}^z \rangle$ predicted by MACE for different N and for three different distributions of atom positions: Gaussian profile (“Gauss”, black line), multiple Gaussian peaks (“Mountains”, red dashed line), and the shell of a sphere (“Shell”, blue dash-dotted line). (d)-(f) Spatial two-dimensional projection of the distributions of atom positions used in the upper panels. The blue points correspond to 20 realizations of atom positions for $N = 178$ superposed into one single graph.

6.4 Role of quantum fluctuations

In the following we seek to identify the mechanisms responsible for the relaxation dynamics observed in Fig. 6.2. In general, the theoretical description of a non-equilibrium quantum many-body problem is based on two major ingredients: 1) the specification of an *initial state* at time $t = t_0$ and 2) the *dynamical laws* that evolve this state to later times $t > t_0$. The initial state considered here can be specified either by the full wavefunction $|\downarrow \dots \downarrow\rangle$ or, equivalently, in terms of a complete set of expectation values of spin operators, such as the means $\langle \hat{S}_i^\alpha(t_0) \rangle$ and variances $\Delta \hat{S}_i^\alpha(t_0) = \langle \hat{S}_i^\alpha(t_0)^2 \rangle - \langle \hat{S}_i^\alpha(t_0) \rangle^2$ for $\alpha = \{x, y, z\}$.⁹ At time $t = t_0$ the non-zero terms characterizing the pure state are

$$\langle \hat{S}_i^z(t_0) \rangle = -1/2, \quad \Delta \hat{S}_i^x(t_0) = \Delta \hat{S}_i^y(t_0) = 1/4. \quad (6.8)$$

⁹We note that the means and variances need to be supplemented by higher-order expectation values to form a complete set.

The full quantum Heisenberg equations of motion for the spin system with Hamiltonian (6.2) are given by

$$\frac{\partial}{\partial t} \begin{pmatrix} \hat{S}_i^x \\ \hat{S}_i^y \\ \hat{S}_i^z \end{pmatrix} = \begin{pmatrix} \Omega + \hat{K}_i^x \\ \hat{K}_i^y \\ 0 \end{pmatrix} \times \begin{pmatrix} \hat{S}_i^x \\ \hat{S}_i^y \\ \hat{S}_i^z \end{pmatrix} \quad (6.9)$$

where we define $\hat{K}_i^\alpha \equiv \sum_j J_{ij} \hat{S}_j^\alpha$.

The question of the origin of relaxation can be approached very efficiently from theory by treating separately the roles of quantum fluctuations in the initial state and in the dynamical laws that describe the non-equilibrium problem. We first consider a mean-field (MF) approximation where quantum fluctuations both in the initial conditions and in the time evolution equations are fully neglected. More precisely, in the MF approach quantum spins are replaced by classical spins S_i^α initialized to the quantum expectation values, $S_i^\alpha(t_0) = \langle \hat{S}_i^\alpha(t_0) \rangle$, with no fluctuations, i.e. $\Delta S_i^\alpha(t_0) = 0$. These classical spins are then evolved with the Heisenberg equations (6.9) with each spin operator replaced by the corresponding classical spin, $\hat{S}_i^\alpha \rightarrow S_i^\alpha$. With this approach the spin-spin interaction given in Eq. (6.2) is approximated by the interaction of each spin with the averaged field created by all the other spins and the fluctuations of this mean-field are neglected. Therefore, the Hamiltonian (6.2) leads to a closed set of classical evolution equations for the classical spins $S_i^\alpha(t)$ that are numerically solved using a Crank-Nicholson algorithm (see App. A). The mean-field computation is performed for the same spin configurations and couplings as for the MACE simulations.

Fig. 6.4a shows the MF prediction of the magnetization (dash-dotted green line) compared to the MACE simulation (solid black line) for an intermediate density corresponding to $\langle N \rangle = 178$. In the MF approximation relaxation arises as a consequence of dephasing: due to their random position in the atomic cloud, the spins experience different mean fields and precess at various frequencies, resulting in density-dependent relaxation of the collective spin observables. However, Fig. 6.4a shows that this dephasing distinctly underestimates the MACE simulation results, demonstrating that MF does not capture all the essential underlying processes and that quantum fluctuations cannot be fully neglected.

In a next step we include quantum fluctuations in the initial state while retaining the classical equations of motion to evolve the system to later times. Therefore, such an approximation takes into account only part of the quantum effects originating from the quantum initial state. This approach corresponds to the Truncated Wigner Approximation (TWA) introduced in Sec. 6.2.2, where the quantum initial state is modelled by an ensemble of classical spins with $\pm 1/2$ in the directions transversal to the mean $\langle \hat{S}_i^\alpha(t_0) \rangle$ that reproduces the quantum fluctuations at $t = t_0$ [102]. Each member of the ensemble is then evolved using the same classical equations of motion as in the MF approximation and the results are obtained from ensemble averages.

Remarkably, the dynamics of the total magnetization computed with TWA (dashed red line in Fig. 6.4a for $\langle N \rangle = 178$) and MACE (solid black line) are in rather close agreement. To quantify this agreement and to extend it to different interaction strengths, we consider the Fourier transform of the time-evolution of the magnetization (Fig. 6.4b). We see that apart from a small difference at $f = 0$, the TWA and MACE simulations closely agree, in particular

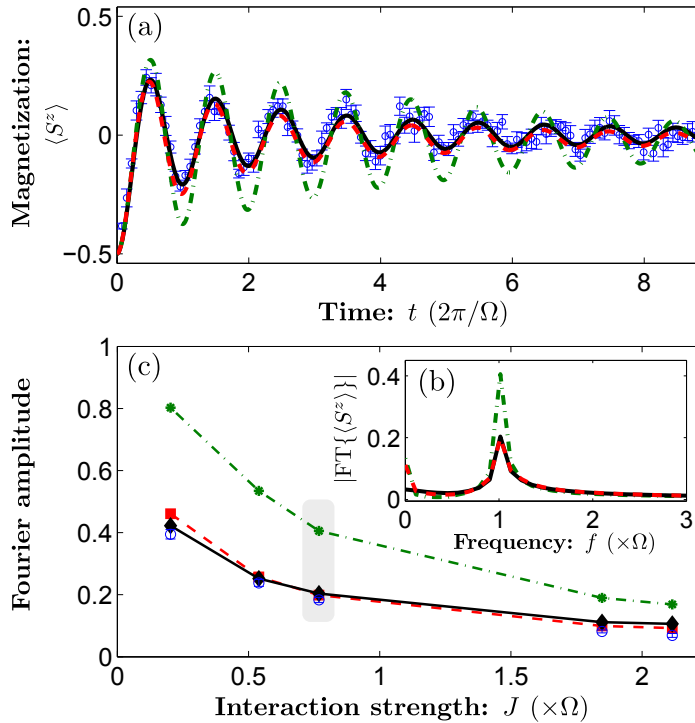


FIGURE 6.4: Relaxation dynamics computed by three theoretical methods: MACE (black solid lines), MF (green dash-dotted lines) and TWA (red dashed lines). Experimental data (blue dots) shown for comparison. (a) Magnetization as a function of time for $\langle N \rangle = 178$. (b) Amplitude of the Fourier transform of (a) normalized to the value expected for a full contrast oscillation. (c) Peak amplitude of the Fourier component $f = \Omega$ for different interaction strengths J . The grey box corresponds to the above parameter choice. Error bars on the experimental data correspond to the standard deviation of the sampling distributions estimated using the bootstrap method.

for $f \approx \Omega$. The narrow peak in the Fourier amplitude at $f = \Omega$ corresponds to the single-spin precession frequency and it provides a convenient measure for comparing the different theoretical results (Fig. 6.4c). The close agreement between TWA and MACE persists for different mean interaction strengths $J = C_3(N/V)^3$, corresponding to the whole range of densities considered in Fig. 6.2. In contrast, the MF simulations systematically exhibit about half the damping of the other methods.

We emphasize that the deviation of MF from the experimental results (blue points in Figs. 6.4a, c) is not a fitting artefact. In fact, one can find an effective volume to make MF lie on top of the experimental result for a given fixed density. However, extending the comparison to other densities with the same effective volume leads again to deviations from the experimental results. This seems to rule out MF as a valid description, whereas TWA and MACE both describe the data equally well (see Figs. 6.2 and 6.4a, c) including essential quantitative aspects such as the full density dependence.

This comparison sheds light onto the role of quantum fluctuations for the relaxation process. While neglecting all fluctuations (MF approximation) greatly underestimates the relaxation rate, the inclusion of just the initial quantum fluctuations of the spins via TWA manages to capture the essential quantitative features of the relaxation dynamics. Since TWA evolves the

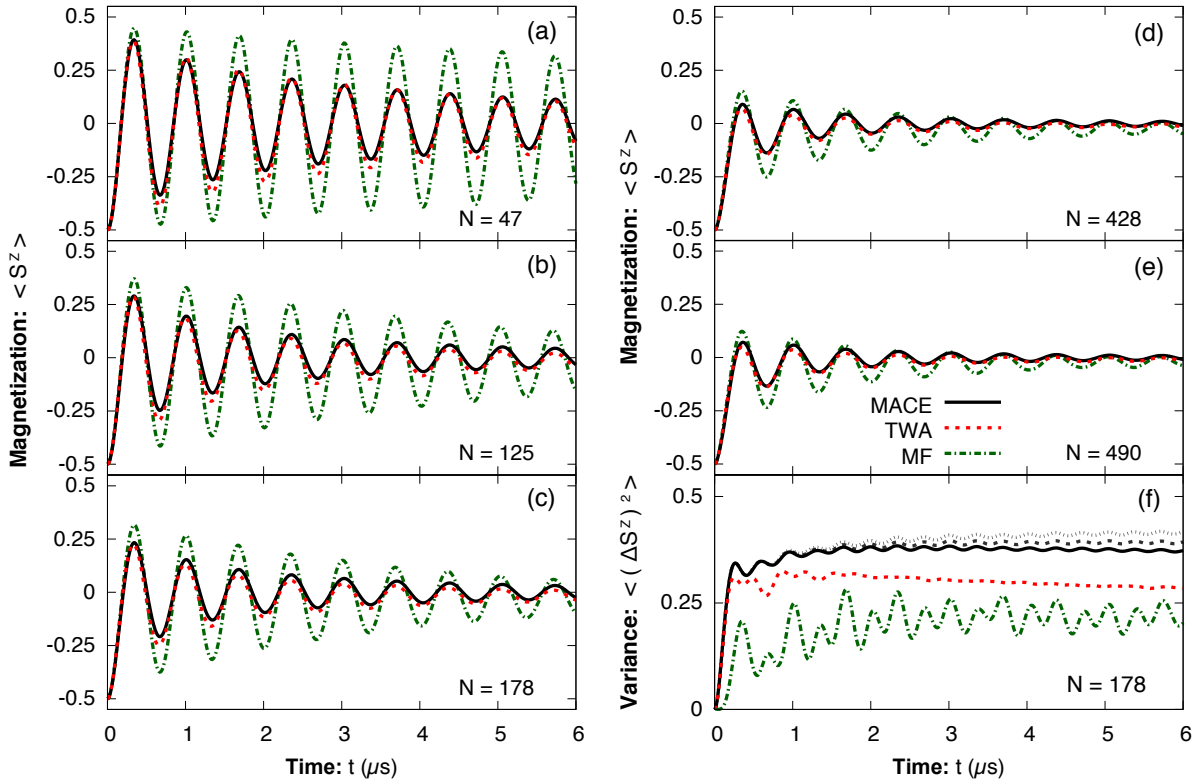


FIGURE 6.5: Relaxation dynamics computed by three theoretical methods: MACE (black solid lines), MF (green dash-dotted lines) and TWA (red dashed lines). (a)-(e): Magnetization $\langle \hat{S}^z \rangle$ computed for the same spin numbers as in Fig. 6.2 as a function of time. (f): Variance $\langle (\Delta \hat{S}^z)^2 \rangle \equiv N[\langle (\hat{S}^z)^2 \rangle - \langle \hat{S}^z \rangle^2]$ as a function of time for $N = 178$. We show MACE results for the cluster sizes $N_c = 8$ (dotted black line), $N_c = 10$ (dashed black line), and $N_c = 12$ (black line).

quantum initial conditions using purely classical dynamics, the similar success obtained with both TWA and MACE indicates that the dynamical fluctuations do not play an important role for the considered collective spin observable (magnetization). In turn, this shows that the dynamics of collective spin observables in Rydberg spin systems can probe the effects of primordial quantum fluctuations intrinsic to the spin-1/2 system.

Quantum fluctuations in dynamical laws

To resolve additional quantum corrections arising through the dynamical laws (which would be at least partially captured by MACE) would require a much higher level of experimental precision or measurements of different observables.

Figs. 6.5a-e show a direct comparison of the magnetization for the three different theoretical methods and the full range of densities considered in the experiment. Since the MACE algorithm has a well defined convergence criterion with cluster size, we use it as a reference (solid black lines). As demonstrated as well in Fig. 6.4 the MF approximation (dash-dotted green lines) systematically underestimates the damping for all densities. While the TWA (dashed red line) lies very close to the MACE result, small discrepancies can be observed, especially at lower densities. These differences are evidence of further quantum effects in the dynamical

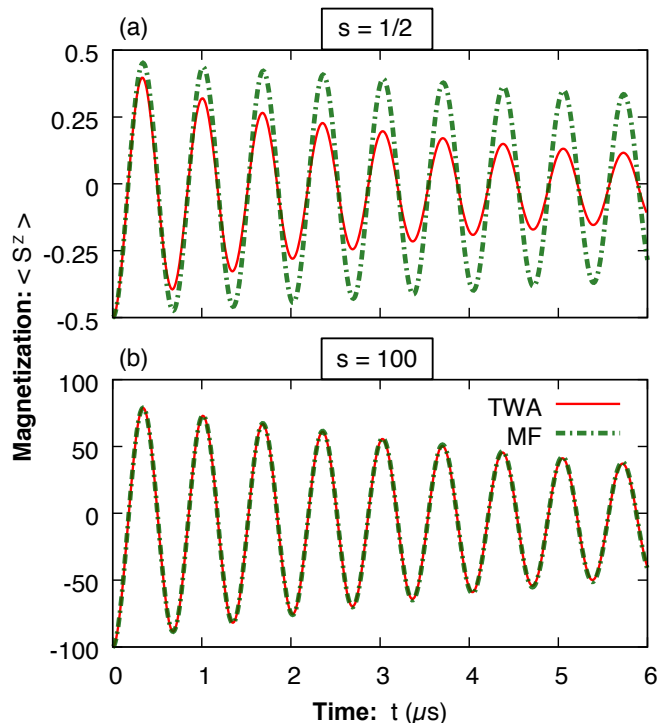


FIGURE 6.6: Decay of magnetization $\langle \hat{S}^z \rangle$ for $N = 47$ as obtained from MF (dashed green line) and TWA (red line) for different spin lengths s . (a): $s = 1/2$. (b): $s = 100$. The effect of the primordial quantum fluctuations present in the spin decreases as the length of the spin increases.

evolution, which are neglected in TWA. However, they are too small to be resolved with the current experimental precision.

Higher-order moments of the collective spin distribution may be used as well to distinguish MACE and TWA simulations. Figure 6.5 shows the time evolution of the variance $\langle (\Delta \hat{S}^z)^2 \rangle \equiv N[\langle (\hat{S}^z)^2 \rangle - \langle \hat{S}^z \rangle^2]$ for the same initial conditions and parameters as for the $N = 178$ data of Fig. 6.4a. For this observable we see significant deviations between all three theoretical methods. In this case though, the convergence of MACE is rather slow and hence can not be taken as reference.¹⁰ As it can be seen in Fig. 6.5f, the results for different cluster sizes have not converged yet: $N_c = 8$ (dotted black line), $N_c = 10$ (dashed black line), and $N_c = 12$ (black line). In spite of this, the clear deviation observed between MACE and TWA even at rather early times indicates that the dynamical quantum fluctuations neglected in TWA can play an important role in higher order functions such as the variance. This opens the possibility to probe such effects in future experiments.

Further insight into the role of quantum fluctuations can be gained by considering the classical limit $s \rightarrow \infty$ of the quantum spin system, where s is the spin length or spin quantum number. For an initial state with all spins pointing in the $-z$ direction, the initial variance $\langle \Delta \hat{S}_\perp^2 \rangle \equiv \langle \hat{S}_x^2 \rangle + \langle \hat{S}_y^2 \rangle$ in the transversal directions is proportional to s . This implies that $\langle \Delta \hat{S}_\perp^2 \rangle^{1/2} / |\langle \hat{\mathbf{S}} \rangle| \rightarrow 0$ as $s \rightarrow \infty$. Therefore, one expects the effect of primordial quantum

¹⁰In fact, for the cluster sizes considered the computation of the variance with MACE turns out to be rather sensitive to the way the clusters are built, even at early times (c.f. Sec. 6.2.1). This indicates that the results displayed in Fig. 6.5f for MACE can not be taken as exact results. Nevertheless, the conclusions drawn from the data are qualitatively the same, regardless of the clustering used.

fluctuations to vanish in this classical limit and, thus, MF and TWA to predict the same behavior.

To check this, we consider the lowest density with $N = 47$ and plot in Fig. 6.6 the evolution of the total magnetization for a spin system with $s = 1/2$ (Fig. 6.6a) and $s = 100$ (Fig. 6.6b) as predicted by these two methods. For $s = 100$ the interaction matrix has been rescaled as $J_{ij} \rightarrow J_{ij}/s$ and all other parameters are kept fixed. The $s = 1/2$ curves are the same as in Fig. 6.5a and show a large discrepancy in the damping. However, for $s = 100$ the MF and TWA simulations yield in this case practically indistinguishable results. This highlights once again the importance of quantum fluctuations in the Rydberg spin-1/2 system considered here.

6.5 Conclusions

We have experimentally and theoretically investigated many-body relaxation dynamics of a quantum spin system. Using Rydberg atoms as effective spin-1/2 variables, we have shown that the demagnetization dynamics following a quench to an out-of-equilibrium state can be understood in terms of unitary evolution of a dipolar XY spin model. While mean-field models often perform well for describing the general properties of systems with long-range interactions [195], here we have shown for three-dimensions and $1/r^3$ interactions that beyond mean-field effects coming from the dipolar exchange interaction play a substantial role in the relaxation dynamics. Specifically, our analysis has revealed the role of disorder and the importance of the initial quantum fluctuations on the relaxation process. In this sense, the dynamics observed can be understood in terms of an ensemble of classically evolving spins with an initial distribution reflecting the quantum nature of the spins-1/2.

The success of the dipolar XY model to capture the essential features of the experiment shows that Rydberg spin systems can serve as valuable testbeds for addressing fundamental questions about nonequilibrium quantum many-body dynamics, such as the role of quantum fluctuations. The study can be generalized to other observables and initial conditions, which could also be accessed in experiment (e.g., by full counting statistics [196, 197]). This would allow to study the influence of other processes on the relaxation dynamics, such as quantum fluctuations left out in TWA.

Finally, the role played by the initial quantum fluctuations in the relaxation process is to be contrasted to the nonthermal fixed point of the previous sections, which were dominated by classical fluctuations. In the latter scenario, quantum fluctuations are expected to become important at a later stage or for larger momenta, where occupancies become of order one. However, when that is the case, classical statistical approximations often lead to wrong results. The success of TWA in describing the dynamics of the Rydberg system for the specific initial conditions and observables considered hence poses the challenge of finding a natural condition for the validity of such classical approximations in spin-1/2 systems.

Part III

Quantum Corrections beyond TWA

Chapter 7

BBGKY Extension: Spin-Boson Dynamics

This chapter is based on the paper “*Nonequilibrium dynamics of spin-boson models from phase space methods*”, A. Piñeiro Orioli, A. Safavi-Naini, M. L. Wall, A. M. Rey, published in Phys. Rev. A **96**, 033607 (2017) [198]. Figures and parts of the text are taken from that reference. In the comparison of the TWA and BBGKY dynamics to exact results, I used for the latter a program written and modified by M. L. Wall and A. Safavi-Naini.

The classical statistical or truncated Wigner approximation (TWA) has been amply used in the last chapters to describe the nonequilibrium dynamics of both bosonic and spin systems. Within its range of validity this approximation is a powerful resource due to its simplicity and its potential to describe even highly nonperturbative systems. Because of this, it constitutes a firm basis for the development of improved methods, which take quantum corrections to TWA into account. This can have potential applications in fields ranging from heavy-ion collisions to cold quantum gases. The next two chapters are dedicated to the study of possible extensions of TWA.

In Chap. 2 we derived a classicality condition for the validity of TWA, which is fulfilled for highly-occupied systems. The infrared dynamics close to the nonthermal fixed point inspected in Chaps. 3, 4, and 5 involved unusually large occupancies at low momenta and hence could be described by TWA. However, once the regime of self-similar dynamics is over and the system starts to approach thermal equilibrium, typical occupancies become of order one and genuine quantum effects need to be taken into account, especially at large momenta. In this regime, the classical statistical approximation is known to yield wrong results due to Rayleigh-Jeans divergencies and the decay of the ‘quantum one-half’ [51, 79, 80]. The inclusion of quantum corrections to TWA may thus help shed light onto the dynamics after the nonthermal fixed point.

Another scenario where genuine quantum effects can become relevant concerns spin-1/2 systems. While in these systems condition (2.84) is apparently not fulfilled (see footnote 6 on page 101), TWA is often found to be a successful description beyond its apparent range of validity [102]. For instance, we showed in Chap. 6 for a dipolar spin model that at least

for certain initial conditions and observables the classical statistical approximation is capable of capturing essential aspects of the relaxation dynamics. Being able to compute next-order corrections to TWA becomes then an essential task in order to understand and extend its applicability to such systems.

In this chapter, we consider a system composed of both spin and bosonic degrees of freedom and generalize a method proposed in Ref. [110] to add corrections to TWA. In a first step, we adapt TWA to the spin-boson system, and make use of a discrete sampling for the spins [102] (see Sec. 6.2.2), thus differing from previous works on spin-boson systems [199]. Corrections are then added to TWA by using a larger set of classical variables with modified equations of motion. The extra variables are analog to n -point functions ($n \geq 2$) and their evolution will be described using a truncated Bogoliubov-Born-Green-Kirkwood-Yvon (BBGKY) hierarchy of equations. This method allows one in principle to add corrections order by order and hence estimate the error of the approximation. We benchmark the method by comparing to exact results for a wide range of system parameters in both one and two dimensions.

For the lack of a better name, we will refer in the following to TWA and its BBGKY extension generically as *phase-space methods*.

7.1 Introduction

Coupled spin and bosonic degrees of freedom appear in a variety of condensed matter and atomic, molecular, and optical (AMO) physics systems. As such, a detailed understanding of their nonequilibrium dynamics can have broad applications. While spin-boson models have been studied extensively in condensed matter physics [200], AMO systems offer a unique platform where the dynamics of both the spins and the bosons can be studied in a controlled manner. For example, many-body spin-boson models, where many spins couple to a single or many bosonic modes, can be engineered using cold atoms in cavities [201, 202] or trapped ions [85, 87, 203–205]. These realizations provide a great deal of flexibility, from the range of interactions to the dimensionality of the system.

Despite the ubiquity of spin-boson models in nature, efficient computational methods for studying the nonequilibrium dynamics are hard to develop. Theoretical approaches are applicable to specific situations. For instance, when the system features a large separation of scales between spins and bosons, the bosons may be adiabatically eliminated [204], resulting in an effective spin model. Alternatively, in the presence of permutational symmetry of the density matrix one may use computational methods which take advantage of the reduction of the complexity from exponential to polynomial [206]. However, for many physically relevant systems these idealized approximations are invalid.

Recently, methods based on Matrix Product States (MPSs) have been successfully applied to systems where the spins and bosons contribute on similar footing in the dynamics [207]. These include cases with non-uniform interactions, and could in principle also be applied to systems with additional non-commuting terms like a transverse field [208]. While MPSs can efficiently treat cases with many spins ($N_s \sim 100$) when coupled to only one mode, as soon as the number of relevant boson modes is higher only moderate sizes can be simulated ($N_s \sim N_b \sim 10$). Hence, alternative methods are required to handle large system sizes.

In the following we study the dynamics of a spin-boson system using TWA and an extension based on BBGKY equations. The computational cost of these phase-space methods scales with the number of equations to be solved. For TWA this depends linearly on the total number of spins and bosons. The extra computational cost introduced in BBGKY by solving the dynamics of n -point ($n \geq 2$) instead of single-particle terms translates to a larger number of equations to be solved. Nevertheless, this number still scales polynomially with the system size. As we show in this work, including $n = 2$ and a few relevant $n = 3$ terms, relatively large system sizes ($N \gtrsim 100$) are still within computational reach. Furthermore, unlike unbiased approaches where the dimensionality of the system is a fundamental limitation, here the dimensionality, at a given order of approximation, only enters the computational speed indirectly through the number of spins and bosons that are effectively coupled.

While these methods can in principle be applied to any system with spin and bosonic degrees of freedom, here we study an analytically solvable model relevant for trapped-ion experiments. Despite its integrability, this model exhibits non-trivial many-body phenomena such as spin-squeezing [88]. Moreover, it admits an effective description in terms of an Ising model with couplings that decay as $1/r^\alpha$ with interparticle distance r and tunable exponent $\alpha \in [0, 3)$, allowing one to investigate quantum magnetism. As such, it is an ideal model for benchmarking the current experimental realizations of spin-boson simulators [86, 87], as well as approximate computational methods such as those discussed in this chapter.

7.2 Spin boson model

We consider a system of trapped ions in one or two spatial dimensions where the two internal states of the ions, modeled as an effective spin-1/2, are coupled to the phonon modes of the ion crystal [85, 87]. The ion crystal is formed due to the interplay of the Coulomb repulsion between the ions and the external electromagnetic trapping potentials, and supports a set of normal modes. The spin-phonon coupling is generated by lasers in a Raman scheme used to impart net momentum k_R along the direction perpendicular to the crystal structure [209]. Following a frame transformation on the spins, the Hamiltonian can be expanded to the lowest order in the Lamb-Dicke parameter $\eta_\mu = k_R \sqrt{1/2M\omega_\mu}$, where M is the mass of an ion, $\{\omega_\mu\}$ are the phonon normal mode frequencies, and $\hbar = k_B = 1$ unless otherwise specified. The Hamiltonian takes the form

$$\hat{H} = \sum_{\mu=1}^{N_b} \omega_\mu \hat{n}_\mu - F \cos(\omega_R t) \sum_{i=1}^{N_s} \sum_{\mu=1}^{N_b} b_{i\mu} \frac{\eta_\mu}{k_R} (\hat{a}_\mu + \hat{a}_\mu^\dagger) \hat{\sigma}_i^z. \quad (7.1)$$

Here, $\hat{n}_\mu = \hat{a}_\mu^\dagger \hat{a}_\mu$, $\hat{a}^{(\dagger)}$ are bosonic annihilation (creation) operators with $[\hat{a}_\mu, \hat{a}_\mu^\dagger] = 1$, $\hat{\sigma}_i^\alpha$ with $\alpha = \{x, y, z\}$ are Pauli matrices, ω_R is the Raman beatnote frequency of the beams which create a spin dependent force with magnitude F , and $b_{i\mu}$ is the amplitude of the vibrational mode μ at site i in units of the normal mode oscillator length.

If $\omega_R \approx \omega_\mu$, for some mode μ , one can perform the Rotating Wave Approximation (RWA), following which we obtain the spin-boson Hamiltonian that will be used throughout this chapter,

namely

$$\hat{H}_{\text{RWA}} = -\frac{1}{2} \sum_{i,\mu} \Omega_{i\mu} \left(\hat{a}_\mu e^{i\delta_\mu t} + \hat{a}_\mu^\dagger e^{-i\delta_\mu t} \right) \hat{\sigma}_i^z. \quad (7.2)$$

Here, $\Omega_{i\mu} \equiv \Omega_\mu b_{i\mu} = F b_{i\mu} \eta_\mu / k_R$ and $\delta_\mu = \omega_R - \omega_\mu$ is the detuning from the near phonon mode. For small $\Omega_{i\mu} / \delta_\mu$ or alternatively at stroboscopic times given by $t = 2\pi n / \delta_\mu$ ($n \in \mathbb{Z}$) the dynamics of the spins effectively decouples from the bosons and is described by an effective Ising model given by

$$\hat{H}_{\text{Ising}} = \sum_{i < j} J_{ij} \hat{\sigma}_i^z \hat{\sigma}_j^z, \quad (7.3)$$

where $J_{ij} = 1/2 \sum_\mu \Omega_{i\mu} \Omega_{j\mu} / \delta_\mu$ [85]. For positive detunings the spin-spin coupling is well approximated by $J_{ij} \sim 1/r_{ij}^\alpha$, where r_{ij} is the distance between ions i and j , and $\alpha \in [0, 3)$ can be tuned by ω_R . Even outside its strict validity range this mapping to a spin-only Hamiltonian is useful to understand the dynamics of the full spin-boson model.

We use the model of Eq. (7.2) to benchmark the accuracy of our method by comparing the dynamics of different observables to their exact forms. For most of the work we let the system start from an initial state $|\psi(t=0)\rangle = |\rightarrow\rangle^{\otimes N_s} \otimes |0\rangle^{\otimes N_b}$, where $|\rightarrow\rangle$ denotes a spin pointing along the $+\hat{x}$ direction and $|0\rangle$ is the vacuum state of the phonons. However, we will consider as well more general initial conditions, such as rotated states $(\cos(\theta/2)|\uparrow\rangle + \sin(\theta/2)|\downarrow\rangle)^{\otimes N_s}$ with $\theta \neq \pi/2$ for the spins (see Section 7.4.3). Since trapped ion experiments operate at finite temperatures we consider as well the more general case of a thermal initial state for the phonons given by $\hat{\rho}_{th} \equiv \bigotimes_\mu e^{-\beta_\mu \hat{H}_{b,\mu}} / \text{Tr}(e^{-\beta_\mu \hat{H}_{b,\mu}})$ with $\hat{H}_{b,\mu} = \omega_\mu \hat{n}_\mu$ and a mode-dependent inverse temperature $\beta_\mu = 1/T_\mu$ (see Section 7.4.4).

We compute the ab-initio dynamics of three sets of observables: the collective spin $\langle \hat{S}_x \rangle \equiv \sum_i \langle \hat{\sigma}_i^x \rangle / N_s$, spin-spin two-point correlators $\langle \hat{\sigma}_i^\alpha \hat{\sigma}_j^\beta \rangle_c \equiv \langle \hat{\sigma}_i^\alpha \hat{\sigma}_j^\beta \rangle - \langle \hat{\sigma}_i^\alpha \rangle \langle \hat{\sigma}_j^\beta \rangle$ and spin-phonon correlators of the form $\langle \hat{a}_\mu \hat{\sigma}_i^\alpha \rangle_c \equiv \langle \hat{a}_\mu \hat{\sigma}_i^\alpha \rangle - \langle \hat{a}_\mu \rangle \langle \hat{\sigma}_i^\alpha \rangle$. For later comparison with the proposed method we give the exact formulas for the evolution of these observables under the Hamiltonian \hat{H}_{RWA} for initial states with the spins pointing in $+\hat{x}$ and the phonons thermally occupied. We begin by measuring the site-resolved magnetization $\langle \hat{\sigma}_i^x \rangle$ given by [210]

$$\langle \hat{\sigma}_i^x \rangle = e^{-\Gamma_i(t)} \prod_{k \neq i} \cos(\varphi_{ik}(t)), \quad (7.4)$$

where

$$\Gamma_i(t) \equiv 4 \sum_\mu \left(\bar{n}_\mu + \frac{1}{2} \right) \frac{\Omega_{i\mu}^2}{\delta_\mu^2} \sin^2(\delta_\mu t / 2), \quad (7.5)$$

$$\varphi_{ij}(t) \equiv \sum_\mu \frac{\Omega_{i\mu} \Omega_{j\mu}}{\delta_\mu} \left(t - \frac{\sin(\delta_\mu t)}{\delta_\mu} \right), \quad (7.6)$$

and

$$\bar{n}_\mu \equiv \langle \hat{n}_\mu \rangle(t=0) = \frac{1}{e^{-\beta_\mu \omega_\mu} - 1}. \quad (7.7)$$

The product of cosine functions in Eq. (7.4) describes the depolarization of the collective spin, while the factor $e^{-\Gamma_i(t)}$ adds oscillations on top of it. This dynamics can also be understood if

one studies the effective spin model (7.3), where the coherent depolarization of the collective spin length is caused by the Ising coupling. In this case, one obtains the same evolution as in (7.4) but with $\Gamma_i \equiv 0$ and $\varphi_{ij}(t) \rightarrow 2J_{ij}t$. In fact, the latter substitution becomes exact in the long time limit, as it can be seen from the full expression (7.6) for $\varphi_{ij}(t)$.

The interactions between the spins lead as well to the buildup of spin-spin correlations, which evolve as

$$\langle \hat{\sigma}_i^x \hat{\sigma}_j^x \rangle = \frac{e^{-\Gamma_{ij}^-}}{2} \prod_{k \neq i, j} \cos(\varphi_{ik} - \varphi_{jk}) + \frac{e^{-\Gamma_{ij}^+}}{2} \prod_{k \neq i, j} \cos(\varphi_{ik} + \varphi_{jk}), \quad (7.8)$$

where

$$\Gamma_{ij}^\pm \equiv 4 \sum_{\mu} \left(\bar{n}_{\mu} + \frac{1}{2} \right) \frac{(\Omega_{i\mu} \pm \Omega_{j\mu})^2}{\delta_{\mu}^2} \sin^2(\delta_{\mu}t/2). \quad (7.9)$$

The evolution of the yy -component shows a similar behavior to (7.8) and therefore we restrict the discussion to the xx -component. At the same time, the spin-dependent displacement of the phonon modes leads to the growth of spin-phonon correlations as characterized by

$$\langle \hat{a}_{\mu} \hat{\sigma}_i^y \rangle = \frac{i}{2\delta_{\mu}} \left(1 - e^{-i\delta_{\mu}t} \right) e^{-\Gamma_i(t)} \prod_{k \neq i} \cos(\varphi_{ik}) \left[2 \left(\bar{n}_{\mu} + \frac{1}{2} \right) \Omega_{i\mu} - i \sum_{m \neq i} \Omega_{m\mu} \tan(\varphi_{im}) \right], \quad (7.10)$$

where we note that for our particular initial state $\langle \hat{a}_{\mu} \hat{\sigma}_i^x \rangle = 0$. The spin-phonon correlations oscillate rapidly with δ_{μ} and are responsible for the $e^{-\Gamma_i}$ and $e^{-\Gamma_i^\pm}$, which imprint oscillations on top of the general trend of the collective spin and the spin-spin correlators, respectively. Additionally we see that Eq. (7.10) is proportional to Eq. (7.4) and hence the decay of the magnetization runs parallel to that of the spin-phonon correlator. Further insight into the evolution of these observables will be given in the next sections by numerically evaluating the above expressions.

For the most part of the remainder of this chapter we consider a system of ions in a linear 1D trap but emphasize that our conclusions are largely independent of the dimensionality of the system and give a 2D example in Section 7.4.4.

7.3 Nonequilibrium dynamics from phase-space methods

In this section, we first review the truncated Wigner approximation (TWA) (see Sec. 2.5 for further details) and adapt it to treat the spin-boson system considered, Eq. (7.2). For this we use the Wigner representation in the Heisenberg picture and follow the same procedure as in Sec. 2.5.3. Within this framework, the extension of TWA using BBGKY equations follows naturally from its construction. As it will be shown, the extra variables in the BBGKY method correspond to Weyl symbols, whose equations of motion are straightforwardly obtained from the Heisenberg equations for operators.

7.3.1 TWA for spins and bosons

For simplicity, we consider first a single spin $\hat{\boldsymbol{\sigma}} = (\hat{\sigma}^x, \hat{\sigma}^y, \hat{\sigma}^z)$ coupled to a single mode \hat{a} . To adapt TWA to a system of spins and bosons, we start with the Wigner-Weyl representation, which maps operators to classical functions. For the spin part we use the discrete Wigner representation introduced in Sec. 6.2.2. For bosons in the basis of \hat{a} and \hat{a}^\dagger one defines [c.f. Eq. (2.86)]

$$O_W(A) = \int d^2\eta \langle A - \eta/2 | \hat{O} | A + \eta/2 \rangle e^{(\eta^* A - \eta A^*)/2}, \quad (7.11)$$

where $|\eta\rangle$, $\eta \in \mathbb{C}$, is a coherent state and $d^2\eta = d\text{Re}\eta d\text{Im}\eta/\pi$. Here and in the following we suppress the dependence on A^* . Weyl symbols for the combined spin-boson system are then defined as the direct product between the spin and the boson parts, and are functions of the classical vector $\mathbf{S} = (S^x, S^y, S^z)^T$ and the complex numbers A and A^* .

The Weyl symbol of the density matrix $\hat{\rho}$ is the Wigner function $W(\mathbf{S}, A)$. As usual, this quantity plays the role of a (quasi) probability distribution, in the sense that expectation values of observables are obtained via $\langle \hat{O} \rangle = \int d^2A d\mathbf{S} W(\mathbf{S}, A) O_W(\mathbf{S}, A)$ [c.f. Eq. (2.89)], where $d\mathbf{S} = dS^x dS^y dS^z$. For later purposes, we work in the Heisenberg picture, where the time-dependence is in the operators and hence in the Weyl symbols. As explained in Secs. 2.5.3 and App. D the Weyl symbol at $t = 0$ of symmetrically ordered operators can be obtained by substituting $\hat{\boldsymbol{\sigma}} \rightarrow \mathbf{S}$, $\hat{a} \rightarrow A$, and $\hat{a}^\dagger \rightarrow A^*$.

To compute observables at times $t > 0$ one needs to evolve the Weyl symbols in time. As explained in Sec. 2.5.3, the TWA is obtained by splitting Weyl symbols of products of operators into products of the one-point Weyl symbols, in this case $(\hat{\sigma}^\alpha(t))_W \equiv \mathbf{S}(t)$, $(\hat{a}(t))_W \equiv A(t)$, and $(\hat{a}^\dagger(t))_W \equiv A^*(t)$. In this way one obtains

$$\langle \hat{O}(t; \hat{\boldsymbol{\sigma}}, \hat{a}) \rangle \approx \int d\mathbf{S}_0 d^2A_0 W(\mathbf{S}_0, A_0) O_W(\mathbf{S}_{\text{cl}}(t), A_{\text{cl}}(t)) \equiv \langle O_W(t; \mathbf{S}, A) \rangle_{\text{cl}}, \quad (7.12)$$

where $A_0 \equiv A(0)$, $\mathbf{S}_0 \equiv \mathbf{S}(0)$, and $\mathbf{S}_{\text{cl}}(t) \equiv \mathbf{S}_{\text{cl}}(t; \mathbf{S}_0, A_0)$ and $A_{\text{cl}}(t) \equiv A_{\text{cl}}(t; \mathbf{S}_0, A_0)$ fulfil the classical equations of motion. The latter can be obtained from the mean-field equations for the expectation values $\langle \hat{\boldsymbol{\sigma}} \rangle$ and $\langle \hat{a} \rangle$ by replacing $\langle \hat{\boldsymbol{\sigma}} \rangle \rightarrow \mathbf{S}$ and $\langle \hat{a} \rangle \rightarrow A$, assuming all products of operators have been previously symmetrized. Numerically, this expression can be evaluated in a three-step process: Monte Carlo sampling of the initial conditions with the Wigner distribution, evolution with the classical equations of motion and averaging.

In this work we are interested in modelling the dynamics of many spins \mathbf{S}_i and many bosons A_μ . To accomplish that we consider only initial states where all the bosons and the spins are uncorrelated. Hence, the Wigner function factorizes as $W(\{\mathbf{S}_i\}, \{A_\mu\}) = \prod_i W_s(\mathbf{S}_i) \prod_\mu W_b(A_\mu)$ and spins and bosons can be sampled independently from each other. For bosons, we will consider vacuum and free thermal states. In this case, the Wigner function is just given by a Gaussian distribution

$$W_b(A_{\mu,0}) = \frac{1}{2\pi\sigma_\mu^2} \exp(-|A_{\mu,0}|^2/(2\sigma_\mu^2)), \quad (7.13)$$

where $\sigma_\mu^2 = (\bar{n}_\mu + 1/2)/2$ and $\bar{n}_\mu = 0$ for vacuum. For spins we use again the discrete sampling introduced in Sec. 6.2.2 [102, 191]. For instance, for the $|\uparrow\rangle$ state the Wigner distribution is

given by

$$W_s(\mathbf{S}_{i,0}) = \frac{1}{4} \delta(S_{i,0}^z - 1) \sum_{x_i, y_i = \pm 1} \delta(S_{i,0}^x - x_i) \delta(S_{i,0}^y - y_i), \quad (7.14)$$

i.e. the z -component is fixed at $+1$ and the transverse directions are sampled with ± 1 .¹ Based on this, one can also construct the Wigner distribution for rotated initial conditions, see App. D.

The classical equations that govern the evolution of the classical variables $\{A_\mu\}$ and $\{\mathbf{S}_i\}$ can be derived in the following way. First, one derives the Heisenberg equations of motion for the operators \hat{a}_μ and $\hat{\sigma}_i$. After that, all products of operators need to be totally symmetrized using the corresponding equal-time commutation relations. In particular, products like $(\hat{\sigma}_i^x)^2$ need to be simplified to $\mathbb{1}$. Finally, one simply substitutes $\hat{a}_\mu \rightarrow A_\mu$ and $\hat{\sigma}_i \rightarrow \mathbf{S}_i$. Following this recipe one obtains for the Hamiltonian (7.2) the classical equations of motion

$$\begin{aligned} \dot{A}_\mu &= \frac{i}{2} e^{-i\delta_\mu t} \sum_i \Omega_{i\mu} S_i^z, \\ \dot{S}_i^x &= 2 \sum_\mu \Omega_{i\mu} \operatorname{Re} \left[(S_i^y A_\mu) e^{i\delta_\mu t} \right], \\ \dot{S}_i^y &= -2 \sum_\mu \Omega_{i\mu} \operatorname{Re} \left[(S_i^x A_\mu) e^{i\delta_\mu t} \right], \\ \dot{S}_i^z &= 0. \end{aligned} \quad (7.15)$$

To solve these equations we use a Crank-Nicolson algorithm (App. A).

7.3.2 BBGKY extension

In order to add corrections to TWA we generalize the method proposed in Ref. [110] to our spin-boson system. For this it is useful to go back to the Wigner-Weyl representation introduced above. In the Heisenberg picture, the time evolution is dictated by the evolution equations for the Weyl symbols. These can be obtained by first deriving the Heisenberg equations of motion for the corresponding operators and then applying the Weyl transformation to both sides. In this way, one obtains an infinite hierarchy of coupled equations for the Weyl symbols, analogous to the BBGKY hierarchy of equations for correlation functions. For instance, for the system considered here the evolution of $(\hat{\sigma}_i^x)_W$ will depend on $(\hat{a}_\mu \hat{\sigma}_i^y)_W$, which in turn depends on $(\hat{a}_\mu \hat{a}_\nu \hat{\sigma}_i^x)_W$ and so on. In order to truncate this infinite hierarchy of equations one may define connected Weyl symbols analogous to connected correlation functions, e.g. $(\hat{a}_\mu \hat{\sigma}_i^y)_W \equiv (\hat{a}_\mu \hat{\sigma}_i^y)_{W,c} + (\hat{a}_\mu)_W (\hat{\sigma}_i^y)_W$. Setting all connected parts to zero one recovers the TWA. A natural extension of TWA is hence to avoid this splitting and take the evolution of the connected parts into account. In the following we elaborate in more depth on this idea.

¹The factor $1/2$ difference in the δ -functions between Eqs. (6.7) and (7.14) stems from the different definition of the classical variable \mathbf{S}_i .

To simplify the notation we define Weyl symbols of products of operators as

$$\begin{aligned}
S_i^\alpha &\equiv (\hat{\sigma}_i^\alpha)_W, & A_\mu &\equiv (\hat{a}_\mu)_W, & M_{i\mu}^\alpha &\equiv (\hat{\sigma}_i^\alpha \hat{a}_\mu)_W, \\
S_{ij}^{\alpha\beta} &\equiv (\hat{\sigma}_i^\alpha \hat{\sigma}_j^\beta)_W, & A_{\mu\nu}^{00} &\equiv (\hat{a}_\mu \hat{a}_\nu)_W, & M_{ij\mu}^{\alpha\beta} &\equiv (\hat{\sigma}_i^\alpha \hat{\sigma}_j^\beta \hat{a}_\mu)_W, \\
S_{ijk}^{\alpha\beta\gamma} &\equiv (\hat{\sigma}_i^\alpha \hat{\sigma}_j^\beta \hat{\sigma}_k^\gamma)_W, & A_{\mu\nu}^{10} &\equiv \frac{1}{2}(\{\hat{a}_\mu^\dagger, \hat{a}_\nu\})_W, & M_{i\mu\nu}^{\alpha 10} &\equiv \frac{1}{2}(\hat{\sigma}_i^\alpha \{\hat{a}_\mu^\dagger, \hat{a}_\nu\})_W,
\end{aligned} \tag{7.16}$$

where $i \neq j \neq k \neq i$, all products of operators are symmetrized, and in this notation ‘0(1)’ stands for $\hat{a}^{(\dagger)}$. Note that products of operators are automatically symmetrized when the operators act on different sites or modes. We define connected Weyl symbols (calligraphy letters) in the same way one would do it for expectation values, e.g.

$$\begin{aligned}
S_{ij}^{\alpha\beta} &= \mathcal{S}_{ij}^{\alpha\beta} + S_i^\alpha S_j^\beta, \\
A_{\mu\nu}^{10} &= \mathcal{A}_{\mu\nu}^{10} + A_\mu^* A_\nu, \\
M_{i\mu}^\alpha &= \mathcal{M}_{i\mu}^\alpha + S_i^\alpha A_\mu,
\end{aligned} \tag{7.17}$$

and analogously for higher order products. The equations of motion for the connected Weyl symbols \mathcal{S} , \mathcal{A} and \mathcal{M} can be obtained by combining the equations for the full Weyl symbols S , A and M . As explained above, the latter follow directly from the Heisenberg equations of motion for the corresponding operators. For instance, for the one-point Weyl symbols one obtains

$$\begin{aligned}
\dot{A}_\mu &= \frac{i}{2} e^{-i\delta_\mu t} \sum_i \Omega_{i\mu} S_i^z, \\
\dot{S}_i^x &= 2 \sum_\mu \Omega_{i\mu} \operatorname{Re} \left[(\mathcal{M}_{i\mu}^y + S_i^y A_\mu) e^{i\delta_\mu t} \right], \\
\dot{S}_i^y &= -2 \sum_\mu \Omega_{i\mu} \operatorname{Re} \left[(\mathcal{M}_{i\mu}^x + S_i^x A_\mu) e^{i\delta_\mu t} \right], \\
\dot{S}_i^z &= 0.
\end{aligned} \tag{7.18}$$

Note that setting $\mathcal{M} \rightarrow 0$ one recovers the classical equations of motion (7.15). To go beyond TWA we keep the mixed spin-boson connected Weyl symbols $\mathcal{M} \neq 0$, whose evolution couples to yet higher-order Weyl symbols. To truncate the hierarchy one needs to discard connected Weyl symbols higher than some given order. In this work, we take all two-point functions into account and neglect all third and higher order functions with one exception: the spin-spin-boson symbol $\mathcal{M}_{ij\mu}^{\alpha\beta}$. The reason for this is that these terms turn out to be relevant in the evolution of spin-spin correlators. The full set of equations obtained in this way is provided in App. C. To solve them we use a Crank-Nicolson algorithm (App. A).

The success of the BBGKY hierarchy depends on the correct initialization of \mathcal{S} , \mathcal{A} and \mathcal{M} . To this end, consider the classical average of a product of classical variables, i.e. of one-point Weyl symbols, at $t = 0$. According to the Wigner-Weyl framework, this gives precisely the expectation value of the corresponding symmetrized product of operators, e.g. $\langle \hat{\sigma}_i^x \hat{\sigma}_j^x \rangle = \int d\mathbf{S}_0 W(\mathbf{S}_0) S_i^x S_j^x$, as long as one is using the correct Wigner function. Therefore, all connected Weyl symbols are exactly zero at the beginning. This is in particular true regardless of whether one has correlated or uncorrelated initial conditions.

To obtain expectation values within the BBGKY framework, one uses the relation between

Weyl symbols and expectation values presented in Secs. 2.5 and 7.3.1, which is symbolically given by $\langle O \rangle = \int O_W W$. It is important to note that two-point connected Weyl symbols are not in one-to-one correspondence with connected correlators. To see this consider

$$\begin{aligned} \langle \hat{\sigma}_i^\alpha \hat{\sigma}_j^\beta \rangle_c &= \langle \hat{\sigma}_i^\alpha \hat{\sigma}_j^\beta \rangle - \langle \hat{\sigma}_i^\alpha \rangle \langle \hat{\sigma}_j^\beta \rangle \\ &= \int \mathcal{D}\mathbf{S}_0 \left[\mathcal{S}_{ij}^{\alpha\beta} + S_i^\alpha S_j^\beta \right] - \int \mathcal{D}\mathbf{S}_0 S_i^\alpha \int \mathcal{D}\mathbf{S}_0 S_j^\beta \\ &\neq \int \mathcal{D}\mathbf{S}_0 \mathcal{S}_{ij}^{\alpha\beta}, \end{aligned} \quad (7.19)$$

where $\mathcal{D}\mathbf{S}_0 = \prod_k d\mathbf{S}_{k,0} W(\mathbf{S}_{k,0})$. This implies that sampling $\mathcal{S}_{ij}^{\alpha\beta}$ alone does not yield the connected part $\langle \hat{\sigma}_i^\alpha \hat{\sigma}_j^\beta \rangle_c$. At the same time, neglecting $\mathcal{S}_{ij}^{\alpha\beta}$, as done in the usual TWA, does not necessarily make connected correlators vanish.

7.4 Benchmark of TWA and BBGKY

In the following we compare the dynamics predicted by the spin-boson TWA and its BBGKY extension to exact results for the model of Eq. (7.2). We examine a variety of different scenarios including several initial conditions for both bosons and spins, as well as coupling to different number of bosonic modes. While in Secs. 7.4.1, 7.4.2, and 7.4.3 we look into a rather small ($N \sim 10$) one-dimensional system, we demonstrate as well the applicability of the method to considerable system sizes ($N \sim 100$) in two dimensions in Sec. 7.4.4.

7.4.1 Single mode

We start by applying the TWA to the regime where $\delta_\mu \gg \Omega_\mu$ for all modes except for the center of mass mode (COM) where $\delta_{\text{COM}} \gtrsim \Omega_{\text{COM}}$. In this regime the dynamics of the system is dominated by the COM mode and the homogeneity of this mode generates an effective Ising model with uniform, all-to-all interactions (see Figs. 7.1a-b).

Throughout this work we express frequencies in units of 2π and define for convenience $\delta \equiv \delta_{\text{COM}}$, $\Omega \equiv \Omega_{\text{COM}}$ and $\omega \equiv \omega_{\text{COM}}$. We consider a chain of $N_s = 10$ atoms with parameters $\delta = 1$ kHz and $\Omega = 0.65$ kHz. To show that for this choice of parameters the influence of the other modes is suppressed we first note that the detuning with respect to other modes can be expressed in terms of the COM frequency as $\delta_\mu = \delta + \Delta\omega_\mu$ where $\Delta\omega_\mu = \omega - \omega_\mu$. The frequency difference with respect to the COM mode ($\mu \neq \text{COM}$) is $\Delta\omega_\mu \geq 80$ kHz (c.f. Fig. 7.1a). Similarly one can write $\Omega_\mu = \Omega \sqrt{\omega/\omega_\mu}$. As a result of this we have $\Omega/\delta = 0.65$ and $\Omega_\mu/\delta_\mu \leq 0.008 \ll \Omega/\delta$ for the remaining modes.

We let the system start in a product state of both bosons and spins. The bosons start in the vacuum state $|0\rangle^{\otimes N_b}$ with $N_b = 1$ and the spins begin in a product state $|\rightarrow\rangle^{\otimes N_s}$ pointing in the $+x$ direction. Fig. 7.2a shows the results obtained with TWA for the total magnetization $\langle \hat{S}_x \rangle \equiv \sum_i \langle \hat{\sigma}_i^x \rangle / N_s$ compared to the exact solution. We find a remarkable agreement with the exact solution except for a small deviation. As anticipated, the total magnetization decays to zero due to the phonon-mediated spin-spin interactions while the coupling to the phonons induces oscillations on top at a frequency δ .

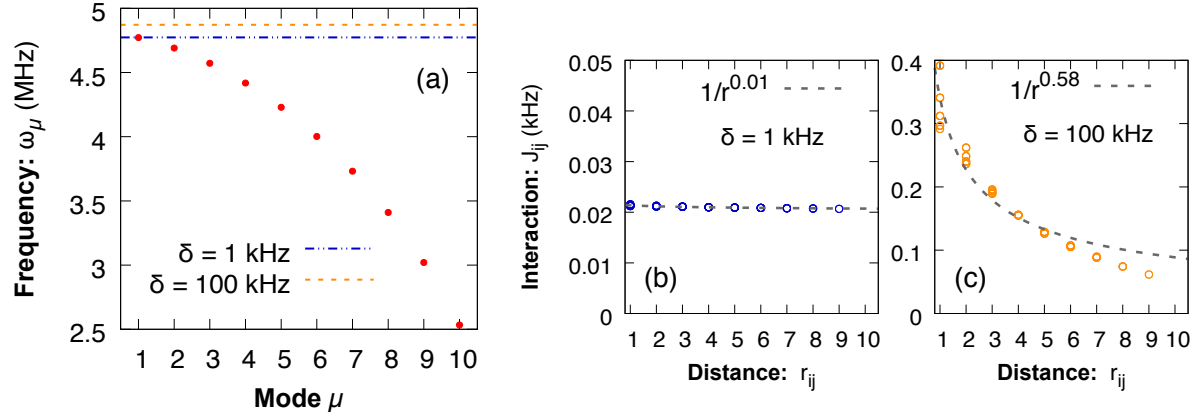


FIGURE 7.1: (a) Phonon frequencies for 1D. The dashed lines correspond to the position of the beatnote frequency ω_R for the different detunings δ used in Secs. 7.4.1 and 7.4.2. (b), (c) Effective spin-spin interaction J_{ij} as a function of the interparticle distance $r_{ij} \equiv |i - j|$ (dimensionless) for the two different detunings. The grey dashed lines show the result of a fit to $1/r_{ij}^\alpha$.

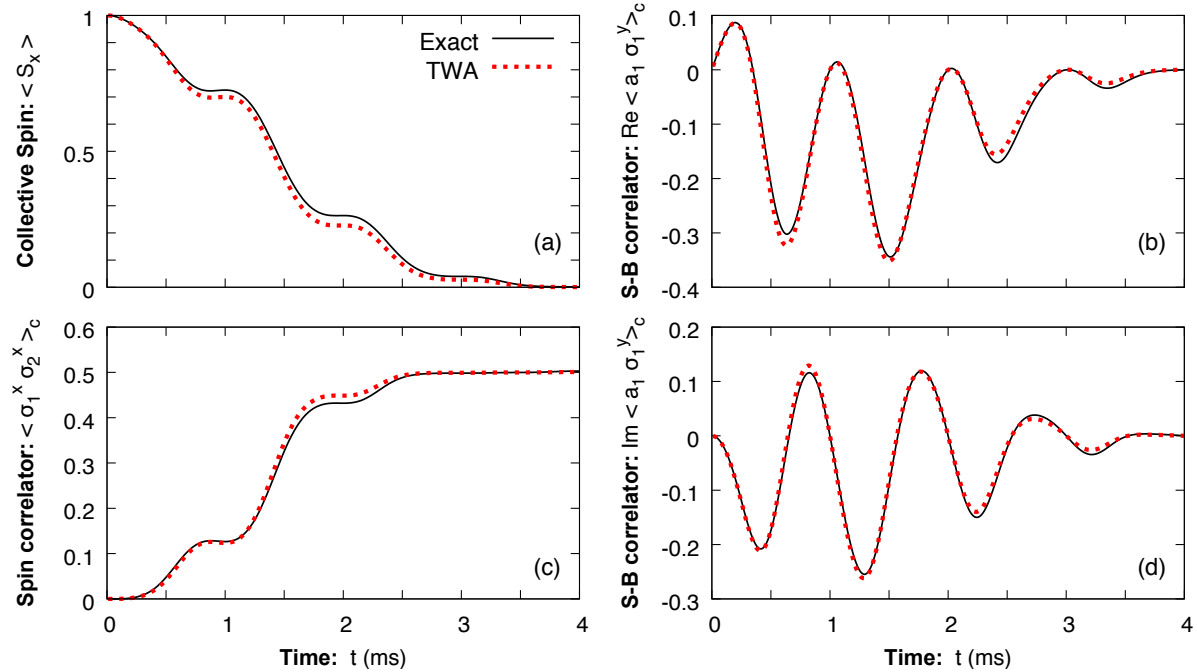


FIGURE 7.2: Comparison of different observables using TWA and the exact solution for the single mode case in 1D and for $N_s = 10$ spins, $\delta = 1$ kHz and $\Omega = 0.65$ kHz. Panels (a) and (c) show the total magnetization and a spin-spin correlator, whereas panels (b) and (d) show the real and imaginary parts of the two-point correlator between a single spin and the bosonic mode, respectively. The deviation of the TWA solution from the exact behavior is due to the self-interaction terms.

The spin-spin interactions create correlations between BBG spins at arbitrary distances. This is quantified by the spin-spin connected two-point correlators $\langle \hat{\sigma}_i^\alpha \hat{\sigma}_j^\beta \rangle_c$. As Fig. 7.2c shows for $i = 1$ and $j = 2$, correlations are built up between spins during the time that the total magnetization decreases. In fact, due to the uniformity of the interactions all spin-spin correlators ($i \neq j$) show exactly the same behavior as Fig. 7.2c. The correlations between phonon and spins are also the same for all spins. Figs. 7.2b and 7.2d show the real and imaginary parts

of the connected spin-phonon correlator $\langle \hat{a}_1 \hat{\sigma}_1^y \rangle_c$. This quantity oscillates with the frequency δ , while its envelope first grows and then decays to zero as the total magnetization vanishes. Except for small deviations the agreement between TWA and the exact solution is remarkable for both spin-spin and spin-phonon correlation functions.

To understand the origin of the small discrepancies observed in Fig. 7.2 we solve the classical equations of motion (7.15) and perform the TWA sampling analytically. This yields [198]

$$\langle S_i^x \rangle_{\text{cl}} = e^{-\Gamma_i(t)} \prod_k \cos(\varphi_{ik}(t)) , \quad (7.20)$$

$$\langle S_i^x S_j^x \rangle_{\text{cl}} = \frac{e^{-\Gamma_{ij}^-}}{2} \prod_k \cos(\varphi_{ik} - \varphi_{jk}) + \frac{e^{-\Gamma_{ij}^+}}{2} \prod_k \cos(\varphi_{ik} + \varphi_{jk}) , \quad (7.21)$$

$$\langle A_\mu S_i^y \rangle_{\text{cl}} = \frac{i}{2\delta_\mu} \left(1 - e^{-i\delta_\mu t}\right) e^{-\Gamma_i(t)} \prod_k \cos(\varphi_{ik}) \left[2 \left(\bar{n}_\mu + \frac{1}{2} \right) \Omega_{i\mu} - i \sum_m \Omega_{m\mu} \tan(\varphi_{im}) \right] . \quad (7.22)$$

These expressions look identical to the exact quantum solutions, Eqs. (7.4), (7.8) and (7.10), except that the indices i and j are excluded in the sums and products of the quantum solution. This stems from a kind of ‘self-interaction’ that is an artefact of the TWA solution. To see this we compare Eq. (7.20) to the expression we obtain by instead integrating out the bosons exactly and then doing TWA. For this we first solve the Heisenberg equation of motion for \hat{a}_μ at the quantum level and then insert it into the equations for $\hat{\sigma}_i^x$ and $\hat{\sigma}_i^y$. The $k = i$ in the sum automatically drops out after symmetrization, due to the anti-commutativity of the spin matrices. After symmetrization we substitute operators by classical variables. Due to the excluded $k = i$ term the result of TWA becomes exact, $\langle S^x \rangle_{\text{cl}} = \langle \hat{S}^x \rangle$, for the initial conditions considered here. Similar self-interaction terms in higher order products are also responsible for the differences observed in the two-point correlators, but identifying them becomes more involved.

For a single mode, this self-interaction term leads only to a small discrepancy which, in fact, becomes negligible as the number of spins N_s is increased, see also the results of Section 7.4.4. However, the situation can be different when many modes contribute to the dynamics. To illustrate this we use $\varphi_{ij} \sim \sum_\mu b_{i\mu} b_{j\mu} / (\omega_\mu \delta_\mu)$, valid at times $t \gg 1/\delta_\mu$, and the fact that the vibrational eigenvectors $b_{i\mu}$ form an orthonormal set, i.e. $\sum_\mu b_{i\mu} b_{j\mu} = \delta_{ij}$. When, for instance, the COM mode dominates the dynamics, all $\mu \neq \text{COM}$ summands in φ_{ij} are suppressed by $1/\delta_\mu$ and only the $\mu = \text{COM}$ survives. Thus $\varphi_{ij} \equiv \varphi$ becomes independent of i and j and the difference between the TWA and exact solutions is simply one power of $\cos(\varphi)$. A similar reasoning applies when the detuning is tuned close to a different mode. However, consider the limit of a large enough detuning δ_μ such that it is approximately μ -independent.² In this limit, $\varphi_{ij} \sim \sum_\mu b_{i\mu} b_{j\mu} / \omega_\mu$. If the frequencies ω_μ are all of the same order of magnitude we have that φ_{ii} is a sum of positive terms, whereas $\varphi_{i \neq j}$ is a sum of positive and negative terms that tend to cancel each other due to the orthonormality of $b_{i\mu}$. Therefore, for large detuning the TWA solution, $\langle S_i^x \rangle_{\text{cl}} = \cos(\varphi_{ii}) \langle \hat{\sigma}_i^x \rangle$, acquires an extra cosine factor with an argument $\varphi_{ii} \gg \varphi_{i \neq j}$ oscillating much faster than typical time scales. This makes the TWA prediction deviate significantly from the quantum solution already at early times. In the next section,

²Strictly speaking one needs to go beyond the RWA in the limit $\delta \rightarrow \infty$. However, we emphasize that the arguments that follow are valid as well without the RWA.

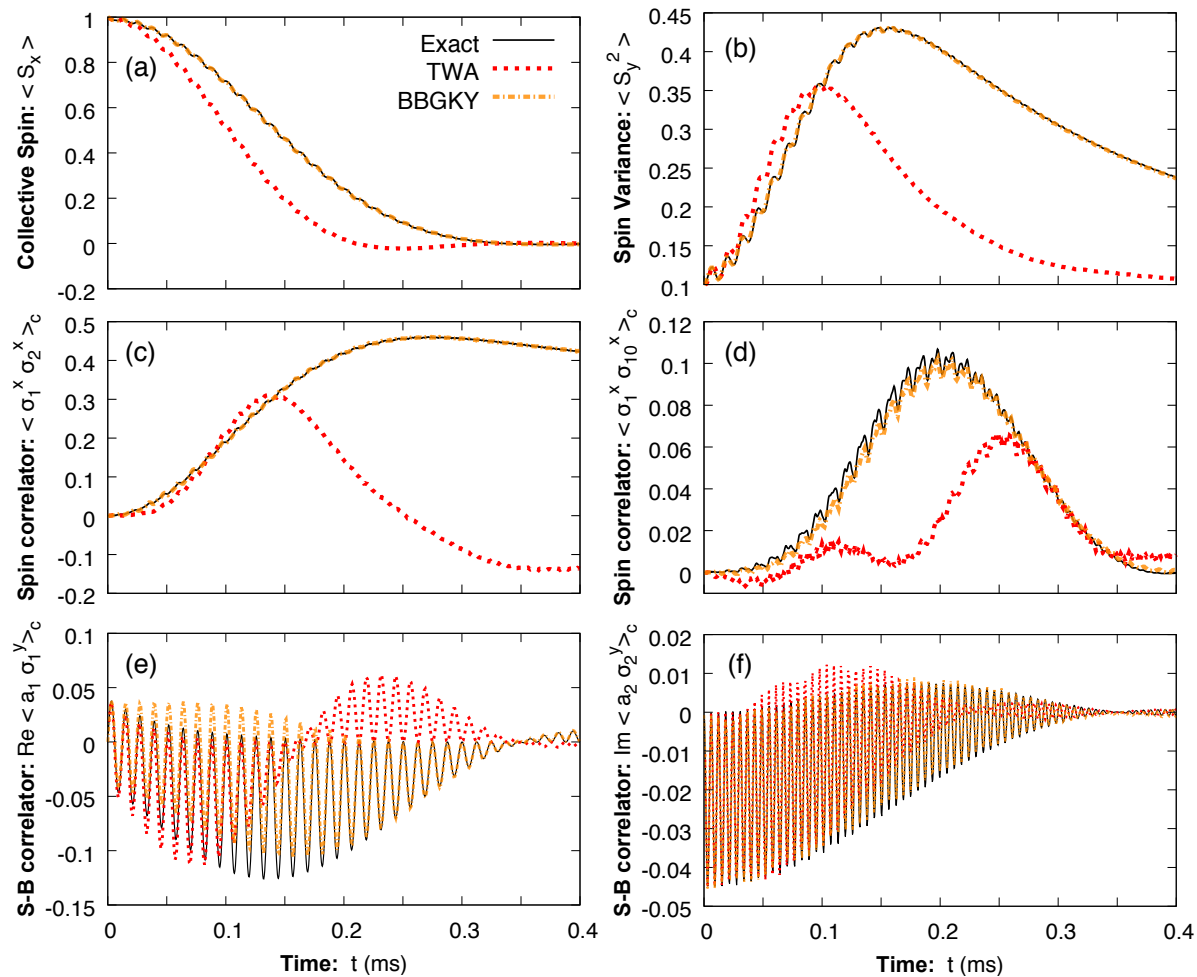


FIGURE 7.3: Comparison of collective, single spin, and mixed spin-boson observables using TWA, BBGKY and the exact solution for the many-mode case with $N_s = N_b = 10$, $\delta = 80$ kHz and $\Omega = 19.42$ kHz. In the above panels we demonstrate how using the BBGKY extension allows one to greatly improve on the TWA in capturing the dynamics of (a) collective spin length and (b) variance, (c) and (d) spin-spin correlators, as well as (e) and (f) spin-phonon correlators.

we show how the use of the BBGKY extension can cure this and yield accurate results even in the many-mode case.

7.4.2 Many modes

In this section we apply the BBGKY method to the same system as in Sec 7.4.1 but operate in a regime where many phonon modes contribute to the dynamics. We choose the experimentally relevant parameters [86] $\delta = 80$ kHz and $\Omega = 19.42$ kHz and perform the simulation using $N_b = 10$ modes. This is the other regime of interest in current trapped-ion simulators and can be accessed if $\delta_\mu \gg \Omega_\mu$ for all modes of the crystal. In this regime the spin-spin interactions mediated by the phonons decay approximately as $1/r^\alpha$ with the interparticle distance r , where α increases monotonically with the detuning. For the above parameters the range of the interaction is approximately given by $\alpha \approx 0.58$ (see Figs. 7.1a and 7.1c).

Figs. 7.3a-f show the evolution of a representative selection of observables: the collective spin $\langle \hat{S}_x \rangle$, the spin variance in the orthogonal direction $\langle \hat{S}_y^2 \rangle$, spin-spin correlators $\langle \hat{\sigma}_1^x \hat{\sigma}_j^x \rangle_c$ for $j = 2, 10$ and the spin-phonon correlator $\langle \hat{a}_\mu \hat{\sigma}_i^y \rangle_c$ for $\mu = 1, 2$ and $i = 1, 2$, respectively. As compared to the single mode case of Fig. 7.2 the dynamics happen at a shorter time scale due to the larger value chosen for the coupling Ω . The larger detuning leads however to the spin-phonon coupling being effectively weaker and hence the oscillations caused by the rotation of the phonons are not only faster but their amplitude is also smaller. Because of this, the spin-spin and spin-phonon correlations built up are weaker as for the single mode case and partly decay at long times, see Figs. 7.3c-f. For spin-spin correlations one finds, as expected, that the larger the distance between the spins the smaller the correlations are (c.f. Figs. 7.3c and 7.3d). Similarly, for phonons that are further away from resonance the spin-phonon entanglement created is smaller (c.f. Figs. 7.3e and 7.3f).

The results obtained with TWA (red) and with its BBGKY extension (orange) are shown in Fig. 7.3 for comparison with the exact solution (black). As anticipated above, the TWA solution deviates from the exact one at relatively short times. The reason for this is that the effect of self-interactions becomes increasingly important as the detuning δ_μ becomes larger (see end of Section 7.4.1). Remarkably, the corrections introduced by the BBGKY extension explained above lead to a large improvement, as seen by the close agreement between the BBGKY and the exact dynamics. While some small deviations still persist (see e.g. Fig. 7.3e), the error of the approximation can be further reduced by extending the hierarchy to include higher order terms, e.g. $\mathcal{M}_{i\mu\nu}^\alpha$. In fact, the inclusion of the third order terms $\mathcal{M}_{ij\mu}^{\alpha\beta}$ proved to be crucial for obtaining a good agreement between the spin-spin correlators computed with BBGKY and the exact result, see Figs. 7.3c and 7.3d.

7.4.3 Role of sampling in BBGKY

The BBGKY equations derived in Sec. 7.3.2 for the connected Weyl symbols have exactly the same form as for the corresponding correlation functions. Given the success shown by the BBGKY method (see Fig. 7.3) one may wonder how relevant the sampling over initial conditions is as compared to just solving the higher-order BBGKY equations for the correlation functions directly. In the ideal case in which one would be able to solve the full hierarchy of equations without approximation, the sampling would not be needed since one could solve for the correlation functions directly.³ However, in realistic situations a truncation of the full hierarchy of equations is needed. As we show in the following, in this case the sampling over initial conditions can lead to significant improvements as compared to using the same equations to evolve correlation functions.

Solving the BBGKY equations without sampling means to initialize each correlation function to its value at initial time. For the initial condition $|\rightarrow\rangle^{\otimes N_s} \otimes |0\rangle^{\otimes N_b}$, the only nonzero one-point function is given by $\langle \hat{\sigma}_i^x \rangle = 1$. Since the initial state is uncorrelated, all two- and three-point connected correlation functions that we take into account are initially zero except $\langle \frac{1}{2} \{ \hat{a}_\mu, \hat{a}_\mu^\dagger \} \rangle_c = 1/2$ (the ‘quantum one-half’). Using these initial conditions we solve the BBGKY equations for the same parameters as in Fig. 7.3. Figure 7.4a shows the evolution of the collective spin obtained from this prescription (blue line) against TWA, BBGKY with

³One may check this in a system with a small number of N spins where the hierarchy closes at order N .

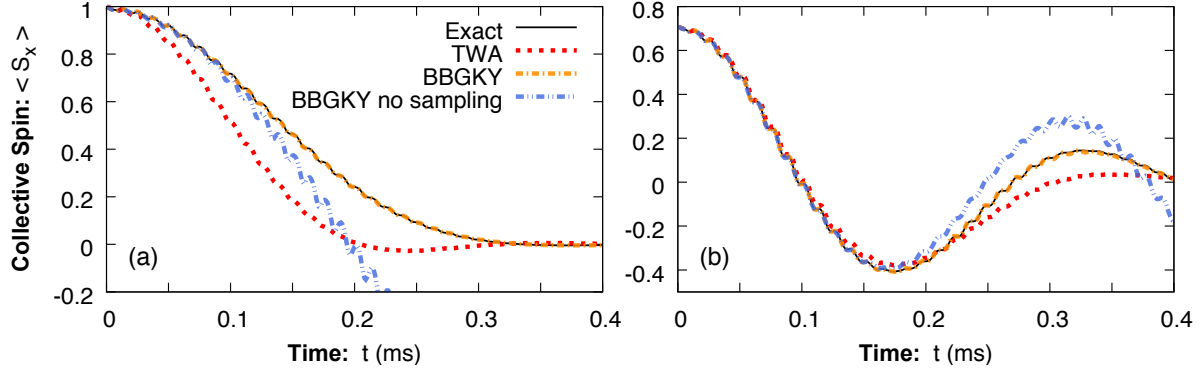


FIGURE 7.4: Evolution of the collective spin $\langle S_x \rangle$ as obtained from BBGKY with and without sampling, TWA, and the exact solution for the many-mode case with $N_s = N_b = 10$. Initial conditions: the bosons start in the vacuum and the spins along $(\cos(\theta/2)|\uparrow\rangle + \sin(\theta/2)|\downarrow\rangle)^{\otimes N_s}$ with (a) $\theta = \pi/2$ and (b) $\theta = \pi/4$.

sampling and the exact solution. Although the BBGKY without sampling correctly predicts the evolution at early times, it clearly differs from the exact solution for times $t \gtrsim 0.1$ ms.

To extend the analysis to other scenarios we consider in Fig. 7.4b the state $(\cos(\pi/8)|\uparrow\rangle + \sin(\pi/8)|\downarrow\rangle)^{\otimes N_s}$, for which the mean value of the spins is initially given by $\langle \hat{\sigma}_i \rangle = (1/\sqrt{2}, 0, 1/\sqrt{2})^T$. At early times all methods agree with the full solution. The BBGKY with sampling is however the only method that lies perfectly well on top of the exact solution over the whole time range shown. In contrast, TWA and the BBGKY without sampling show significant deviations from the exact solution for times $t \gtrsim 0.2$ ms. These two examples clearly show that when using BBGKY equations, sampling over initial conditions as prescribed in Sec. 7.3.2 can lead to a large improvement as compared to just solving the equations for correlation functions directly.

7.4.4 Large system sizes

In the previous sections we have shown that the spin-boson TWA together with a systematic BBGKY expansion reproduces the dynamics of the spin-boson model (7.2) for both the single-mode and the many-mode case. While so far we have considered small systems in one dimension, here we show that the method can easily be applied to larger systems in higher dimensions and with realistic initial conditions for the phonons.

To this end we consider a system composed of $N_s = 100$ spins and $N_b = 100$ phonon modes in two dimensions in a setting similar to the experiment of Ref. [87]. We initialize the spins in the fully magnetized $|\rightarrow\rangle$ state. To mimic realistic experimental conditions we let each phonon mode μ start in a thermal equilibrium state $\hat{\rho}_{th} \equiv \bigotimes_{\mu} e^{-\beta_{\mu} \hat{H}_{b,\mu}} / \text{Tr}(e^{-\beta_{\mu} \hat{H}_{b,\mu}})$ with $\hat{H}_{b,\mu} = \omega_{\mu} \hat{n}_{\mu}$. We assign to each phonon initially a fixed but random mean occupancy of $\bar{n}_{\mu} = 5 + \eta_{\mu}$ where η_{μ} is a gaussian random number with $\langle \eta_{\mu} \rangle = 0$ and $\sqrt{\langle \eta_{\mu}^2 \rangle} = 2$. This sets the inverse temperature $\beta_{\mu} = 1/T_{\mu}$ using (7.7).

Figures 7.5a-d show the evolution of the total magnetization $\langle \hat{S}_x \rangle$ for a range of different detunings $\delta = \{100, 1, -26, -250\}$ kHz, where the force is respectively given by $\Omega = \{12, 1, 5, 2\}$ kHz. As the detuning is changed, the coupling strength of the spins to the different modes μ varies

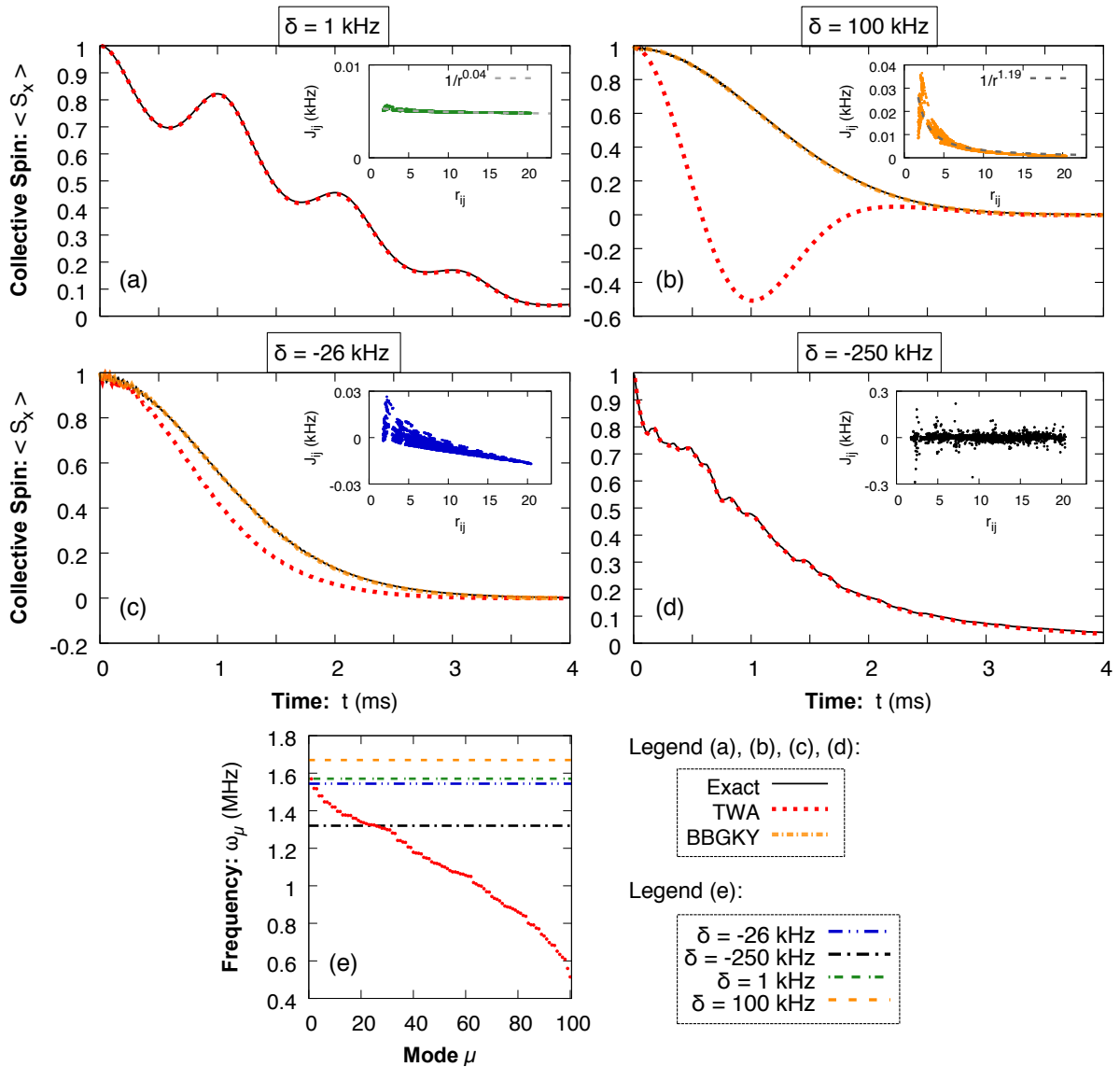


FIGURE 7.5: (a)-(d) Comparison of the collective spin $\langle S_x \rangle$ using TWA and BBGKY for thermal initial conditions in two spatial dimensions. The different plots correspond to the following values $\{\delta, \Omega\}$ of detuning and force: (a) $\{1, 1\}$ kHz, (b) $\{100, 12\}$ kHz, (c) $\{-26, 5\}$ kHz and (d) $\{-250, 2\}$ kHz. The insets show the corresponding values of J_{ij} as a function of the interparticle distance $r_{ij} \equiv |r_i - r_j|/\ell_0$ in units of $\ell_0 = (2e^2/(4\pi\epsilon_0 M\omega))^{1/3}$. (e) Phonon frequencies for 2D. The dashed lines correspond to the position of the beatnote frequency ω_R for the different detunings used.

depending on how close the beatnote frequency, $\omega_R = \omega + \delta$, is to the corresponding mode frequency ω_μ . In Fig. 7.5e we show for reference the values of the different ω_R as compared to the mode frequencies. Because of this, the nature of the effective phonon-mediated Ising interaction J_{ij} changes as well. In the inset of Figs. 7.5a-d we show J_{ij} for the corresponding detuning as a function of the interparticle distance r_{ij} .

For $\delta = 1$ kHz the spins couple predominantly to the COM mode and the Ising interaction is practically uniform ($\alpha \approx 0.04$), analogous to Sec. 7.4.1. This can be observed in the slow single-frequency oscillations on top of the decay of the magnetization in Fig. 7.5a. The amplitude of these oscillations is however comparably larger due to the initial thermal occupation of the

phonons. As compared to the results presented in Fig. 7.2, Fig. 7.5a shows that TWA (red) agrees even better with and in fact lies almost perfectly on top of the exact solution (black). The reason behind this is that, in the single mode case, the self-interaction term responsible for the deviation becomes negligible in the limit $N_s \rightarrow \infty$, as argued in Sec. 7.4.1.

For $\delta = 100$ kHz we have a situation similar to Sec. 7.4.2, where many weakly coupled modes contribute to the evolution. The Ising interaction is characterized in this case by a power-law with $\alpha \approx 1.19$. Due to the large detuning the coupling to the phonon modes is weaker and hence the amplitude of the oscillations is practically negligible, as shown in Fig. 7.5b. Analogous to the results presented in Sec. 7.4.2, we see here that the TWA again fails to accurately describe the dynamics of the systems, whereas the BBGKY method (orange) adds the necessary corrections to make the result lie remarkably well on top of the exact solution.

To explore other parameter regimes we consider as well negative detunings. Compared to positive detunings the landscape of Ising interactions is less trivial and can not be captured by a simple power-law [211] (see insets of Figs. 7.5c-d). For $\delta = -250$ kHz the beatnote frequency ω_R lies within a dense region of mode-frequencies (see Fig. 7.5e) and hence the spins couple strongly to a handful of modes. As shown in Fig. 7.5d this leads to superposed oscillations of different frequencies, whose amplitude is additionally enhanced by the initial thermal occupation of the phonons. Once again, we find that the TWA result lies almost perfectly on top of the exact solution and no BBGKY is needed. This is consistent with the argument presented in Section 7.4.1 that the effect of the self-interaction term in TWA is ameliorated when δ_μ varies strongly with μ .

Lastly, we consider $\delta = -26$ kHz, which makes ω_R lie approximately equidistant from the COM and the next two phonon modes (see Fig. 7.5e). Because the detuning from the nearest modes is relatively large, the amplitude of the oscillations remains small as seen in Fig. 7.5c. This choice of detuning implies as well that the coupling of the spins to the modes does not vary strongly enough with μ to make the self-interaction term negligible. Therefore, TWA shows a considerable deviation from the exact solution, which is, however, cured again using the BBGKY method.

In summary, we have shown that TWA and BBGKY can be efficiently used for large system sizes, higher dimensions and thermal initial conditions. TWA accurately describes the spin-boson dynamics when a handful of modes are dominant, whereas the BBGKY method adds the necessary corrections whenever this is not the case. Although for large system sizes the number of equations to be solved grows rapidly, we note that for the initial conditions considered in this section and for computing just the collective spin, the set of equations to be solved can be significantly reduced without further approximations, see App. C.

7.5 Conclusions

In this chapter we have studied the dynamics of a spin-boson model using the truncated Wigner Approximation (TWA) and a promising method to add corrections to this approximation. We began by adapting the TWA to spins and bosons, making use of recently developed discrete sampling methods for the spins. We then improved the TWA by introducing more classical variables and equations in a fashion similar to a BBGKY hierarchy, where the extra variables

are associated to Weyl symbols of the Wigner representation. From this point of view, TWA emerges as the lowest order approximation in the BBGKY hierarchy.

We tested the convergence of the various approximations extensively by comparing to exact dynamics of a system of spins coupled to one or many bosonic modes, where the system parameters require one to treat the spins and the bosons on equal footing. Such models are particularly relevant to experimental AMO systems, such as those realized by a 1D chain or a 2D array of trapped-ions used for quantum simulation of a variety of spin Hamiltonians. We found excellent agreement for various one- and two-point functions for a large range of parameters. Specifically, if a handful of bosonic modes dominates the dynamics, the TWA was found to give accurate results while in all remaining cases the BBGKY extension added the necessary corrections allowing the results to converge to the exact ones. Most importantly, we demonstrated the applicability of the method to large systems ($N \sim 100$) in higher dimensions (2D) with a thermal occupation of the bosonic modes, a case relevant to current experiments. We emphasize that the fact that the accuracy of TWA was found to depend on the number of relevant bosonic modes does not necessarily generalize to other models.

Of course better convergence always comes with a cost. The inclusion of each subsequent order of classical variables increases the computational time by an order $\sim N$ thus limiting the size of the systems which can be simulated efficiently. However, it is worth pointing out that depending on the observable of interest one may need to go to different orders in the BBGKY approximation, which can reduce the computational complexity.

While in this work we concentrated on an exactly solvable model, the TWA and BBGKY methods can also be applied to more generic problems that do not admit an exact solution. In this case, however, two challenges need to be addressed. First, because of the lack of an exact solution to compare with, a systematic evaluation of the parameter regime of validity will be necessary. To this end, computing higher orders in the BBGKY expansion or comparing to exact numerical results in small systems can help estimate the error of a given order of approximation. Second, the truncation of the BBGKY hierarchy can lead to numerically unstable equations and hence stable truncation schemes need to be developed. An alternative approach to overcome this using a different set of equations will be the topic of Chap. 8.

Chapter 8

2PI Extension: Anharmonic Oscillator and φ^4 -theory

In the previous chapter we have demonstrated that important quantum corrections to the classical statistical approximation can be added by enlarging the set of classical variables and equations to be solved. The extra variables are associated to Weyl symbols, which in the Wigner representation are the counterpart of Heisenberg operators. Using a truncated hierarchy of BBGKY-type equations for these Weyl symbols, we showed for an exactly solvable spin-boson model that this procedure can lead to large improvements. However, while the method could be successfully implemented for the specific model considered (see also [110]), it is known that the truncation of such BBGKY equations can lead in general to secularities and instabilities in time [212]. In this chapter, we provide an alternative route to add corrections to TWA by combining this idea with the 2PI framework introduced in Chap. 2.

An important take home message of Chap. 7 is the fact that Weyl symbols and correlation functions fulfil the same equations of motion. This was explicitly seen in the derivation of the BBGKY equations for the Weyl symbols of the previous chapter. While such equations describe the evolution of *equal-time* quantities, nothing prevents one from applying the same principle to *unequal-time* functions. The evolution of such quantities can be described by the 2PI equations derived in Chap. 2. This naturally leads to the possibility of employing such equations to evolve Weyl symbols, combined with a sampling over initial conditions. In this chapter we investigate such a method, which will be referred to as *Sampled 2PI* (S2PI).

Similar approaches have been studied in the past using, e.g., a Hartree-Fock approximation to the evolution equations [213]. For the success of such a method, it is, however, essential to use the correct sampling scheme for the initial conditions. This point is clarified in the derivation of our method. Furthermore, our approach allows for a systematic inclusion of higher orders based on an expansion of the self-energy. This differs from the BBGKY approach, where truncations are made instead by neglecting higher-order connected Weyl symbols.¹

As a proof of principle, we first apply the Sampled 2PI method to an anharmonic oscillator, which can be solved numerically. Using a loop expansion of the self-energy to the next nontrivial order we show the potential of the method to add corrections to TWA. Following that, we

¹Neglecting contributions to the self-energy also implies neglecting contributions from higher-order processes. However, at a technical level, this truncation is different from the one done in BBGKY.

show how the method can be straightforwardly applied to a (relativistic) scalar field theory. In this context, we pose the question of whether the Sampled 2PI method can remedy well-known flaws of the classical-statistical approximation such as the Rayleigh-Jeans divergence and the decay of the quantum 1/2 [51, 79, 80].

8.1 Anharmonic Oscillator

To illustrate the method we consider the dynamics of a 0 + 1 dimensional φ^4 theory, i.e. of the quantum mechanical anharmonic oscillator. The Hamiltonian of the anharmonic oscillator is given by [c.f. Eq. (2.85)]

$$\hat{H} = \frac{\hat{\pi}^2}{2} + \frac{m^2}{2}\hat{\varphi}^2 + \frac{\lambda}{4!}\hat{\varphi}^4, \quad (8.1)$$

where the operator $\hat{\varphi}$ and its conjugate momentum $\hat{\pi}$ fulfil $[\hat{\varphi}, \hat{\pi}] = i$ (c.f. Sec. 2.1). The Hamiltonian formulation of the problem will later be useful to compute the dynamics of the anharmonic oscillator numerically, by solving the Schrödinger equation $i\partial_t |\psi\rangle = \hat{H} |\psi\rangle$ for the state $|\psi\rangle$. For later purposes, it is useful to introduce the creation and annihilation operators

$$\hat{a} = \sqrt{\frac{m}{2}} \left(\hat{\varphi} + \frac{i}{m} \hat{\pi} \right), \quad \hat{a}^\dagger = \sqrt{\frac{m}{2}} \left(\hat{\varphi} - \frac{i}{m} \hat{\pi} \right), \quad (8.2)$$

which diagonalize (8.1) for $\lambda = 0$. We will further denote by $|n\rangle$ the eigenstate of $\hat{n} \equiv \hat{a}^\dagger \hat{a}$ with eigenvalue n .

In order to employ the 2PI techniques introduced in Chap. 2 on this system we consider the functional integral representation of (8.1). This leads to the closed-time path action [c.f. Eq. (2.1)]

$$S[\varphi] = \int_{t, \mathcal{C}} \left\{ \frac{1}{2} \partial_t \varphi \partial_t \varphi - \frac{m^2}{2} \varphi^2 - \frac{\lambda}{4!} \varphi^4 \right\}, \quad (8.3)$$

where the scalar φ depends on the time t along the time contour \mathcal{C} of Fig. 2.1. The anharmonic oscillator in the 2PI formalism is described in terms of the one- and two-point functions (c.f. see Sec. 2.2.2)

$$\phi(t) \equiv \langle \hat{\varphi}(t) \rangle, \quad (8.4)$$

$$F(t, t') \equiv \frac{1}{2} \langle \{ \hat{\varphi}(t), \hat{\varphi}(t') \} \rangle_c, \quad (8.5)$$

$$\rho(t, t') \equiv i \langle [\hat{\varphi}(t), \hat{\varphi}(t')] \rangle. \quad (8.6)$$

The evolution of these quantities is given by the 2PI equations (2.29), (2.30), and (2.31). For the anharmonic oscillator they can be simplified to

$$\left[\partial_t^2 + m^2 + \frac{\lambda}{6} \phi^2(t) + \frac{\lambda}{2} F(t, t) \right] \phi(t) = \frac{\delta \Gamma_2}{\delta \phi(t)}, \quad (8.7)$$

$$\begin{aligned} \left[\partial_t^2 + m^2 + \frac{\lambda}{2} \phi^2(t) + \Sigma^{(0)}(t) \right] F(t, t') &= - \int_0^t dt'' \Sigma^p(t, t'') F(t'', t') \\ &+ \int_0^{t'} dt'' \Sigma^F(t, t'') \rho(t'', t'), \end{aligned} \quad (8.8)$$

$$\left[\partial_t^2 + m^2 + \frac{\lambda}{2} \phi^2(t) + \Sigma^{(0)}(t) \right] \rho(t, t') = - \int_{t'}^t dt'' \Sigma^\rho(t, t'') \rho(t'', t'), \quad (8.9)$$

where the self-energies $\Sigma^{(0)}$, Σ^F , and Σ^ρ are defined in (2.28), and Γ_2 is the sum of two-particle-irreducible diagrams of Eq. (2.25). In this chapter we will consider a coupling expansion of the 2PI effective action to order λ^2 . The diagrams contributing at this order are given in Eqs. (2.37) and (2.38). To this order the self-energies are given by [see Eq. (2.27)]

$$\Sigma^{(0)}(t) = \frac{\lambda}{2} F(t, t), \quad (8.10)$$

and

$$\Sigma^F(t, t') = - \frac{\lambda^2}{6} \left[3\phi(t)\phi(t') \left(F^2(t, t') - \frac{1}{4}\rho^2(t, t') \right) + F(t, t') \left(F^2(t, t') - \frac{3}{4}\rho^2(t, t') \right) \right], \quad (8.11)$$

$$\Sigma^\rho(t, t') = - \frac{\lambda^2}{2} \left[2\phi(t)\phi(t')F(t, t')\rho(t, t') + \rho(t, t') \left(F^2(t, t') - \frac{1}{12}\rho^2(t, t') \right) \right]. \quad (8.12)$$

This approximation leads as well to

$$\frac{\delta\Gamma_2}{\delta\phi(t)} = \frac{\lambda^2}{2} \int_0^t dt' \rho(t, t') \left[F^2(t, t') - \frac{1}{12}\rho^2(t, t') \right] \phi(t'), \quad (8.13)$$

which appears on the right hand side of (8.7).

The above evolution equations need to be supplemented by appropriate initial conditions. In the following, we will consider different types of gaussian initial conditions in the symmetric phase, i.e. for vanishing initial macroscopic fields.² In this case, they can be parametrized by [214]

$$\begin{aligned} \phi(0) = 0, & & F(0, 0) = \xi^2, & & \rho(0, 0) = 0, \\ \partial_t \phi(t)|_{t=0} = 0, & & \partial_t F(t, 0)|_{t=0} = \xi \eta, & & \partial_t \rho(t, 0)|_{t=0} = 1, \\ & & \partial_t \partial_{t'} F(t, t')|_{t=t'=0} = \eta^2 + \sigma^2/4\xi^2, & & \partial_t \partial_{t'} \rho(t, t')|_{t=t'=0} = 0. \end{aligned} \quad (8.14)$$

where σ , ξ and η are real numbers. Note that the initial conditions for the spectral function ρ are fixed by the equal-time commutation relations between $\hat{\varphi}$ and $\hat{\pi}$. In the case of (free) *vacuum* initial conditions, i.e. $|\psi(t=0)\rangle = |0\rangle$ with $\hat{a}(0)|0\rangle = 0$, we have

$$\xi_{\text{vac}}^2 = \frac{1}{2m}, \quad \eta_{\text{vac}} = 0, \quad \sigma_{\text{vac}} = 1. \quad (8.15)$$

For comparison, we mention that for *thermal* initial conditions given by the density matrix

$$\rho(t=0) = \frac{1}{Z} \sum_n e^{-\beta m(n+1/2)} |n\rangle \langle n|, \quad (8.16)$$

²We emphasize though that the S2PI method can be applied equally well to the case of initially nonvanishing $\phi(0)$ and $\partial_t \phi(t)|_{t=0}$.

where $\beta = 1/T$ and $Z = \sum_n e^{-\beta m(n+1/2)}$ one has

$$\xi_{\text{th}}^2 = \frac{1}{m} \left(\frac{1}{2} + n_{\text{BE}} \right), \quad \eta_{\text{th}} = 0, \quad \sigma_{\text{th}} = 1 + 2n_{\text{BE}}, \quad (8.17)$$

where $n_{\text{BE}} = (e^{\beta m} - 1)^{-1}$.

8.2 Sampled 2PI

To derive the Sampled 2PI (S2PI) method it is convenient to start with the Wigner representation introduced in Sec. 2.5.3. We recall that in this framework expectation values of observables $\hat{O}(\hat{\varphi}, \hat{\pi})$ are obtained via

$$\langle \hat{O}(\hat{\varphi}, \hat{\pi}) \rangle = \int \frac{d\varphi d\pi}{2\pi} W(\varphi, \pi) O_W(\varphi, \pi), \quad (8.18)$$

where the Weyl symbol $O_W(\varphi, \pi)$ and Wigner function $W(\varphi, \pi)$ are defined in Eqs. (2.86) and (2.87), respectively. In the Heisenberg picture, the time-dependence is in the operators and hence in the Weyl symbols. At time $t = 0$ they can be computed using the fact that Weyl symbols of symmetrically ordered operators follow from substituting $\hat{\varphi} \rightarrow \varphi$ and $\hat{\pi} \rightarrow \pi$, as discussed in Sec. 2.5.3.

The expectation value of operators at later times $t > 0$ can be obtained by sampling over the Wigner function³ and evolving the Weyl symbols in time. The equations of motion for the Weyl symbols can be directly derived from the Heisenberg operator equations, as explained in Chap. 7. For example, from the equation for the operator $\hat{\varphi}$ one obtains

$$\left[\partial_t^2 + m^2 + \frac{\lambda}{6} \hat{\varphi}^2(t) \right] \hat{\varphi}(t) = 0 \quad (8.19)$$

$$\implies \left[\partial_t^2 + m^2 \right] (\hat{\varphi}(t))_W + \frac{\lambda}{6} (\hat{\varphi}^3(t))_W = 0. \quad (8.20)$$

If one compares this to the equation fulfilled by the corresponding expectation values

$$\left[\partial_t^2 + m^2 \right] \langle \hat{\varphi}(t) \rangle + \frac{\lambda}{6} \langle \hat{\varphi}^3(t) \rangle = 0, \quad (8.21)$$

one notices both equations can be mapped onto each other by substituting $(\hat{\varphi}(t))_W \leftrightarrow \langle \hat{\varphi}(t) \rangle$ and $(\hat{\varphi}^3(t))_W \leftrightarrow \langle \hat{\varphi}^3(t) \rangle$. This correspondence between Weyl symbols and expectation values can be generalized to higher orders, including both equal-time and unequal-time quantities. The fact that both Weyl symbols and expectation values fulfil the same equations of motion follows directly from the fact that both can in principle be obtained from the operator equations by just applying $(\cdot)_W$ or $\langle \cdot \rangle$ to both sides. Nevertheless, there are important differences between these two types of objects. While the initial conditions of the expectation values are fixed, those of the Weyl symbols need to be sampled according to the Wigner function. Furthermore, Weyl symbols need to be averaged over initial conditions as expressed by (8.18) in order to obtain quantum expectation values.

³Assuming a positive definite Wigner function.

This correspondence between Weyl symbols and expectation values implies that the 2PI equations for ϕ , F , and ρ , Eqs. (8.7), (8.8), and (8.9), can in principle be used as well to evolve Weyl symbols. For this one needs to substitute

$$\phi(t) \longleftrightarrow \phi_w(t) \equiv (\hat{\varphi}(t))_W, \quad (8.22)$$

$$F(t, t') \longleftrightarrow F_w(t, t') \equiv \frac{1}{2}(\{\hat{\varphi}(t), \hat{\varphi}(t')\})_W - \phi_w(t)\phi_w(t'), \quad (8.23)$$

$$\rho(t, t') \longleftrightarrow \rho_w(t, t') \equiv i([\hat{\varphi}(t), \hat{\varphi}(t')])_W. \quad (8.24)$$

where we defined the Weyl variables ϕ_w , F_w , and ρ_w .⁴ This leads to

$$\left[\partial_t^2 + m^2 + \frac{\lambda}{6}\phi_w^2(t) + \frac{\lambda}{2}F_w(t, t) \right] \phi_w(t) = \frac{\delta\Gamma_{2,w}}{\delta\phi_w(t)}, \quad (8.25)$$

$$\begin{aligned} \left[\partial_t^2 + m^2 + \frac{\lambda}{2}\phi_w^2(t) + \Sigma_w^{(0)}(t) \right] F_w(t, t') &= - \int_0^t dt'' \Sigma_w^\rho(t, t'') F_w(t'', t') \\ &\quad + \int_0^{t'} dt'' \Sigma_w^F(t, t'') \rho_w(t'', t'), \end{aligned} \quad (8.26)$$

$$\left[\partial_t^2 + m^2 + \frac{\lambda}{2}\phi_w^2(t) + \Sigma_w^{(0)}(t) \right] \rho_w(t, t') = - \int_{t'}^t dt'' \Sigma_w^\rho(t, t'') \rho_w(t'', t'), \quad (8.27)$$

where the Weyl quantities Σ_w and $\Gamma_{2,w}$ are obtained respectively from Σ and Γ_2 by substituting $\phi \leftrightarrow \phi_w$, $F \leftrightarrow F_w$ and $\rho \leftrightarrow \rho_w$.

The initial conditions for ϕ_w , F_w and ρ_w follow directly from (8.18) and the fact that at $t = 0$ averages over products of $\phi_w(0)$ and $\pi_w(0) \equiv (\hat{\pi}(0))_W$ give expectation values of symmetrically ordered operators.⁵ This implies that the classical fields ϕ_w and π_w have to be sampled in the same way as in TWA, which is consistent with the fact that TWA and S2PI have to agree in the limit $t \rightarrow 0$. Because of this one further has that $\frac{1}{2}(\{\hat{\varphi}(0), \hat{\varphi}(0)\})_W = (\varphi(0))_W(\varphi(0))_W = \phi_w^2(0)$ and hence all F_w and derivatives vanish identically at the initial time [see Eq. (8.23)]. The initial conditions for ρ_w are the same as for ρ , as follows from inserting the equal-time commutation relations into (2.86) using (8.24). Thus, for the gaussian initial conditions (8.14) one obtains

$$\begin{aligned} \phi_w(0) &= \xi r_1, & F_w(0, 0) &= 0, & \rho_w(0, 0) &= 0, \\ \partial_t \phi_w(t)|_{t=0} &= \eta r_1 + \frac{\sigma}{2\xi} r_2, & \partial_t F_w(t, 0)|_{t=0} &= 0, & \partial_t \rho_w(t, 0)|_{t=0} &= 1, \\ \partial_t \partial_{t'} F_w(t, t')|_{t=t'=0} &= 0, & \partial_t \partial_{t'} \rho_w(t, t')|_{t=t'=0} &= 0, \end{aligned} \quad (8.28)$$

where r_1 and r_2 are gaussian random numbers with⁶

$$\begin{aligned} \langle r_1 \rangle &= \langle r_2 \rangle = \langle r_1 r_2 \rangle = 0, \\ \langle r_1^2 \rangle &= \langle r_2^2 \rangle = 1. \end{aligned} \quad (8.29)$$

⁴In a sense, the Sampled 2PI method can be seen (similar to the Wigner representation) as a classical-statistical or ensemble reformulation of the quantum problem, in which the Weyl or ‘classical’ variables ϕ_w , F_w , and ρ_w are evolved with 2PI equations of motion with statistically distributed initial conditions defined by the Wigner function.

⁵At $t = 0$ the one-point Weyl symbols $\phi_w(0)$ and $\pi_w(0)$ are equal to the classical variables φ and π .

⁶A nonvanishing macroscopic field at initial time would be reflected in nonvanishing values for $\langle r_1 \rangle$ and $\langle r_2 \rangle$.

According to the above, expectation values of observables in Sampled 2PI are hence obtained by sampling over initial conditions with (8.28), evolving with the 2PI equations (8.25)-(8.27) and finally averaging over all trajectories as in (8.18). As discussed in Chap. 7 (Sec. 7.3.2), one needs to take into account that averaging over connected Weyl symbols does not result in connected correlators. For the statistical function one has for instance

$$F(t, t') = \int \frac{d\phi_w^0 d\pi_w^0}{2\pi} W(\phi_w^0, \pi_w^0) \left(\frac{1}{2} \{ \hat{\varphi}(t), \hat{\varphi}(t') \} \right)_W (\phi_w^0, \pi_w^0) - \phi(t)\phi(t') \quad (8.30)$$

where we defined $\phi_w^0 \equiv \phi_w(0)$ and $\pi_w^0 \equiv \pi_w(0)$ and used that one can identify $\varphi \leftrightarrow \phi_w^0$ and $\pi \leftrightarrow \pi_w^0$. Using (8.23) it then follows that

$$\begin{aligned} \phi(t) &= \langle \phi_w(t) \rangle, \\ F(t, t') &= \langle \phi_w(t)\phi_w(t') + F_w(t, t') \rangle - \langle \phi_w(t) \rangle \langle \phi_w(t') \rangle, \\ \rho(t, t') &= \langle \rho_w(t, t') \rangle, \end{aligned} \quad (8.31)$$

where $\langle \cdot \rangle$ applied to a Weyl variable stands for an ensemble average over initial conditions with the Wigner function [c.f. Eq. (8.18)].

It is instructive to rederive the classical statistical approximation or TWA from the Sampled 2PI framework. This is done by setting Σ_w and $\Gamma_{2,w}$ to zero which leads to

$$\left[\partial_t^2 + m^2 + \frac{\lambda}{6} \phi_w^2(t) + \frac{\lambda}{2} F_w(t, t) \right] \phi_w(t) = 0, \quad (8.32)$$

$$\left[\partial_t^2 + m^2 + \frac{\lambda}{2} \phi_w^2(t) \right] F_w(t, t') = 0, \quad (8.33)$$

$$\left[\partial_t^2 + m^2 + \frac{\lambda}{2} \phi_w^2(t) \right] \rho_w(t, t') = 0. \quad (8.34)$$

Because of the initial conditions of F_w and Eq. (8.33), this quantity remains zero in this order of approximation. Hence, the evolution for ϕ_w decouples from the rest and is given by the classical equation of motion as in TWA. Furthermore, it can be shown that the evolution equation (8.34) for ρ_w is the same as would be obtained for the classical-statistical spectral function defined in Chap. 5 from linear response. The derivation follows along the same lines as shown in Sec. 5.2 for the nonrelativistic theory.

8.3 Quantum corrections to TWA

In view of the Sampled 2PI (S2PI) framework presented above, a natural way of adding corrections to the classical statistical approximation (TWA) is by not setting all 2PI diagrams to zero. To go beyond TWA, we consider here a coupling expansion in powers of λ . The lowest-order term is the Hartree term (8.10), i.e.

$$\Sigma_w^{(0)}(t) = \frac{\lambda}{2} F_w(t, t), \quad (8.35)$$

which appears as a mass correction on the left hand side of the 2PI equations (8.26) and (8.27). However, including only this term does not lead to any correction to TWA since F_w

still remains zero during the whole dynamics. Hence, the evolution of ϕ_w is still given by the classical equation of motion.

In order to make F_w depart from zero we need to add at least one correction term to (8.26) which is not proportional to F_w itself. This is achieved in the next order in λ , where according to Eqs. (8.11), (8.12), and (8.13) one has

$$\Sigma_w^F(t, t') = -\frac{\lambda^2}{6} \left[3\phi_w(t)\phi_w(t') \left(F_w^2(t, t') - \frac{1}{4}\rho_w^2(t, t') \right) + F_w(t, t') \left(F_w^2(t, t') - \frac{3}{4}\rho_w^2(t, t') \right) \right], \quad (8.36)$$

$$\Sigma_w^\rho(t, t') = -\frac{\lambda^2}{2} \left[2\phi_w(t)\phi_w(t')F(t, t')\rho_w(t, t') + \rho_w(t, t') \left(F_w^2(t, t') - \frac{1}{12}\rho_w^2(t, t') \right) \right], \quad (8.37)$$

and

$$\frac{\delta\Gamma_{2,w}}{\delta\phi_w(t)} = \frac{\lambda^2}{2} \int_0^t dt' \rho_w(t, t') \left[F_w^2(t, t') - \frac{1}{12}\rho_w^2(t, t') \right] \phi_w(t'). \quad (8.38)$$

Inserting this into (8.26) one sees that the term $\sim \phi^2\rho^3$ appearing in the product $\Sigma^F\rho$ is not necessarily zero at all times and hence can trigger a nontrivial evolution of F_w .

As explained above, TWA is recovered by setting all self-energies to zero and hence can be seen as the leading-order (LO) expansion in S2PI. Further we have in the TWA that $F_w = 0$, whereas the fluctuations of the field are encapsulated in ϕ_w^2 . Therefore, in regimes where the dynamics is well-approximated by TWA we postulate that the condition

$$\phi_w^2 \gg F_w \quad (\text{TWA}) \quad (8.39)$$

will hold. This is certainly fulfilled at early enough times where $F_w \approx 0$ due to the initial conditions (8.28). As we will see later, for small deviations from TWA Eq. (8.39) is also fulfilled and the self-energies (8.36) and (8.37) are dominated by the terms proportional to ϕ_w^2 coming from the ϕ -dependent diagram in (2.38). The corrections implemented by Eqs. (8.35)-(8.38) can thus be seen as the next-to-leading order (NLO) correction in S2PI.

In the following we examine the performance of the S2PI method to NLO, which will sometimes be referred to as simply S2PI for simplicity. We will compare it to TWA (i.e. S2PI to LO) as well as to the evolution obtained from the 2PI equations for expectation values [Eqs. (8.7)-(8.9)] using (8.14) and the NLO self-energies, Eqs. (8.10)-(8.13). The latter method we will denote simply by 2PI. The numerical methods used for solving the respective equations are outlined in App. A. For TWA and S2PI we average over typically $10^5 - 10^6$ iterations, such that the results show approximate convergence. To test the accuracy of these approximations we compare these methods to the numerical solution of the quantum anharmonic oscillator [214, 215]. For this we solve the Schrödinger equation in the position representation (see App. A), where $\hat{\varphi} \rightarrow x$, $\hat{\pi} \rightarrow -i\partial_x$, and $|\psi\rangle \rightarrow \psi(x) = \langle x|\psi\rangle$. For the gaussian initial conditions given in (8.14) the wave function is initially given by [214]

$$\psi_0(x) = \frac{1}{(2\pi\xi^2)^{1/4}} \exp \left[-\left(\frac{1}{4\xi^2} - i\frac{\eta}{2\xi} \right) x^2 \right], \quad (8.40)$$

where we consider only pure states by setting $\sigma = 1$.

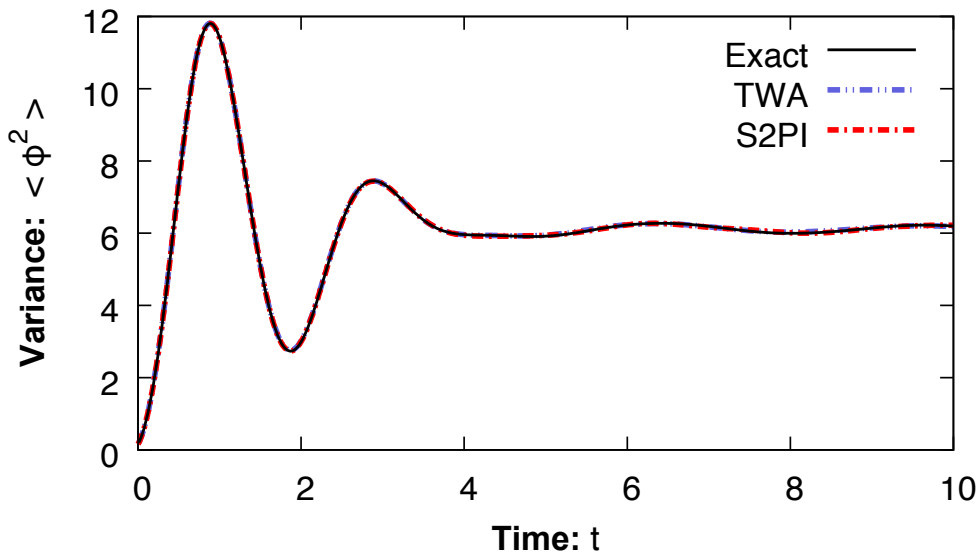


FIGURE 8.1: Evolution of the variance $\langle \hat{\varphi}^2(t) \rangle = F(t, t)$ as predicted by TWA and S2PI to NLO compared to the numerically exact solution for $\lambda = 1$ and gaussian initial conditions with $\xi = 0.4$, $\eta = 5$, $\sigma = 1$.

As a consistency check we consider first initial conditions for which TWA yields accurate results. Figure 8.1 shows the evolution of the variance $\langle \hat{\varphi}^2(t) \rangle = F(t, t)$ for $\lambda = 0.5$ and gaussian initial conditions with $\xi = 0.4$ and $\eta = 5$.⁷ While initially small, the variance rapidly grows and after few oscillations it approximately relaxes. The evolution predicted by TWA (blue dash-dot-dotted line) perfectly follows the exact solution (black line) including the more detailed features. Because of this agreement the NLO of S2PI should not make any significant difference. This is indeed confirmed in Fig. 8.1 where S2PI (red dash-dotted line) lies practically on top of both the TWA and exact solutions. We emphasize that the fact that solving the S2PI equations with or without memory integrals yields in this case the same result is far from trivial.

Next, we consider in Fig. 8.2 initial conditions with $\xi = 0.4$ and $\eta = 1$, for which the variance grows to smaller values and consequently the TWA starts to deviate from the exact solution. We show in Fig. 8.2a results for TWA, S2PI and 2PI. At early times, all methods agree with the exact solution. However, the solution of 2PI (grey dashed line) clearly starts deviating from the exact solution after the first oscillation. The TWA manages to stay close to the exact solution for a longer time, but the amplitude of the oscillation increasingly deviates from the real behavior as well. Remarkably, these small deviations are overcome by the S2PI to NLO, which lies on top of the exact solution up to about $t \approx 10$. For later times, this method starts deviating as well, although the amplitude of oscillation still stays closer to the exact solution than TWA. These results demonstrate that the S2PI method is capable of adding relevant quantum corrections to TWA even with a low-order coupling expansion of the self-energies⁸. This is particularly striking since the same evolution equations used for expectation values instead clearly fail to capture the dynamics.

⁷We set $m = 1$ throughout and hence quantities are given in units of m .

⁸Note that the coupling $\lambda = 0.5$ used is not small enough to rule out the contribution of higher-order diagrams. These would lead to further corrections at later times.

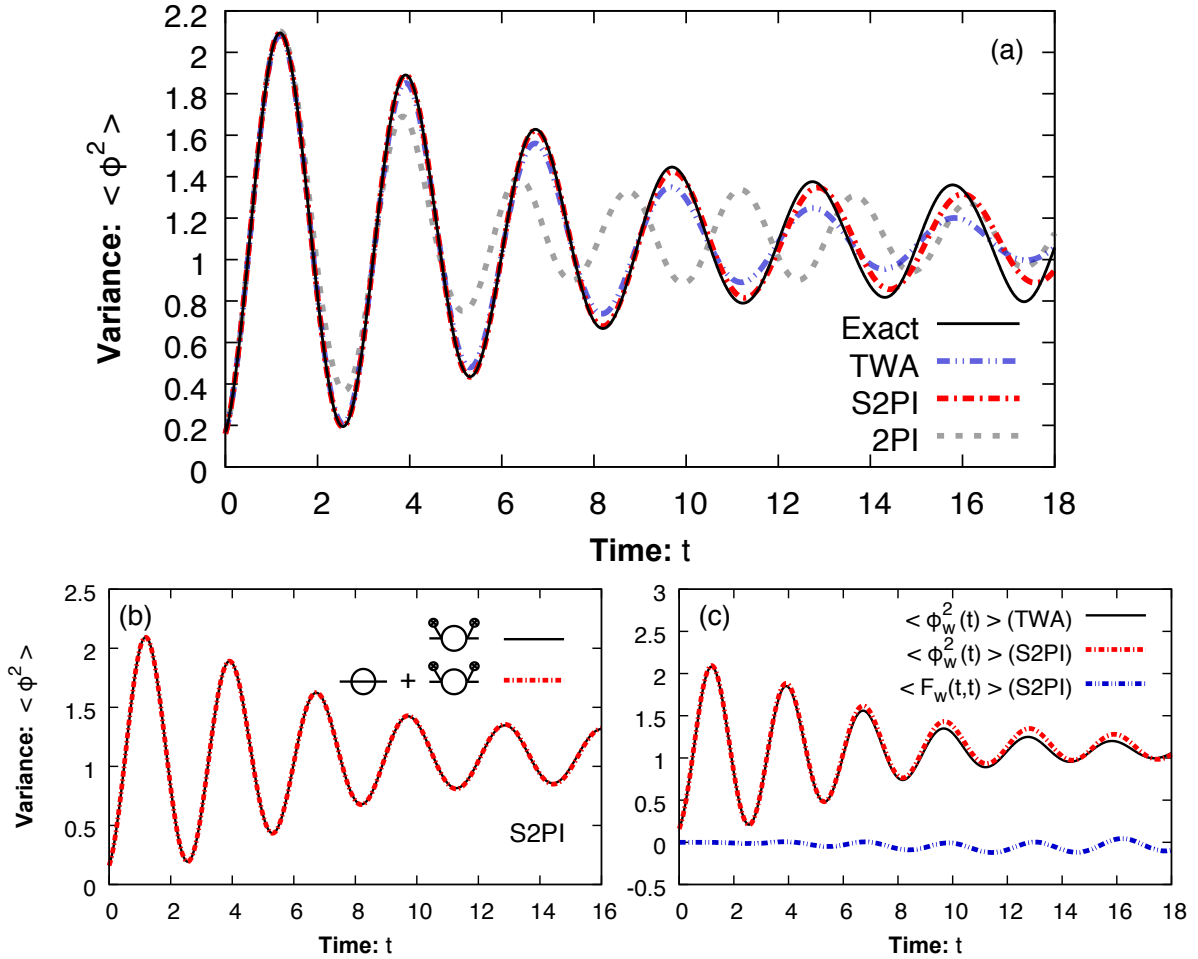


FIGURE 8.2: (a) Evolution of the variance $\langle \hat{\varphi}^2(t) \rangle = F(t, t)$ as predicted by TWA, S2PI to NLO and 2PI compared to the numerically exact solution for $\lambda = 0.5$ and gaussian initial conditions with $\xi = 0.4$, $\eta = 1$, $\sigma = 1$. (b) Comparison between S2PI with and without the sunset diagram. (c) Evolution of the different contributions to the variance $\langle \hat{\varphi}^2(t) \rangle = \langle \phi_w^2(t) \rangle + \langle F_w(t, t) \rangle$.

Since the deviations of TWA from the exact solution are small at early times, we should expect (8.39) to hold. Figure 8.2c shows a comparison of $\langle \phi_w^2(t) \rangle$ (red dash-dotted line) to $\langle F_w(t, t) \rangle$ (blue dash-dot-dotted line) for S2PI. Indeed, we find that $F_w(t, t)$ is very close to zero at early times and practically negligible compared to $\phi_w^2(t)$. At those times the evolution of $\phi_w^2(t)$ is furthermore indistinguishable from the corresponding evolution in TWA (black line). However, as time passes, $F_w(t, t)$ grows larger and the S2PI result for $\phi_w^2(t)$ starts deviating from the TWA prediction. Nevertheless, even at late times the leading contribution seems to come from $\phi_w^2(t)$. This is further supported by Fig. 8.2b, where we show the variance as obtained from S2PI to NLO with and without the sunset diagram contribution [second term in Eqs. (8.36) and (8.37)]. Remarkably, both results lie on top of each other, which shows that in this case the self-energies (8.36) and (8.37) are dominated by the first term, which is proportional to ϕ_w^2 .

In order to capture the longer time behavior in Fig. 8.2 further corrections beyond NLO in S2PI would be needed. Alternatively, one may suppress such contributions by choosing a smaller coupling. Fig. 8.3 shows the results obtained for $\lambda = 0.1$ and initial conditions with $\xi = 0.4$

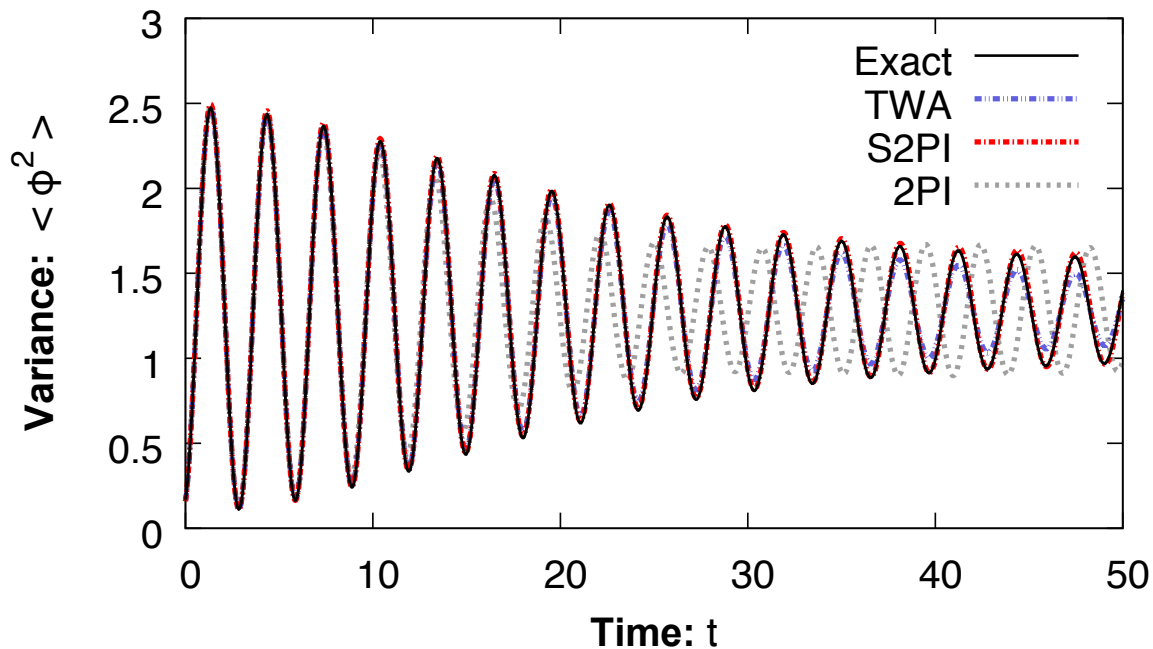


FIGURE 8.3: Evolution of the variance $\langle \hat{\varphi}^2(t) \rangle = F(t, t)$ as predicted by TWA and S2PI to NLO compared to the numerically exact solution for $\lambda = 0.1$ and gaussian initial conditions with $\xi = 0.4$, $\eta = 1$, $\sigma = 1$.

and $\eta = 1$. Due to the weaker interaction, the decay of the oscillations is much slower than in Fig. 8.2. While at early times all methods agree with the exact solution, we find again that the result of 2PI quickly leads to wrong results, in particular it overestimates the oscillation frequency. The TWA manages to capture both frequency and amplitude of oscillations for a longer time, but slowly deviates from the exact solution as time passes. Remarkably, S2PI to NLO introduces the relevant corrections that make it lie on top of the exact result for the whole time window shown.

It should be noted that the results obtained from S2PI to NLO in Fig. 8.2a show numerical instabilities at times longer than the ones shown.⁹ While the origin of these instabilities is unclear, we note that the equations tend to become more stable for smaller λ . An example of this is the result of Fig. 8.3, which could be simulated to longer times with no unstable behavior. This is, of course, consistent with the fact that we employed a coupling expansion for the self-energies, which is justified at small enough coupling.

8.4 Scalar field theory

While the anharmonic oscillator constitutes a useful system to test our S2PI method against exact solutions, the final aim is to apply it to field theory. Therefore, we consider next a

⁹In fact, for the times shown a couple of iterations show instabilities as well. When averaging over iterations, we neglected the few that showed such instabilities.

relativistic scalar field theory specified by the action

$$S[\varphi] = \int_{x,c} \left[\frac{1}{2} \partial^\mu \varphi(x) \partial_\mu \varphi(x) - \frac{m^2}{2} \varphi^2(x) - \frac{\lambda}{24} \varphi^4(x) \right]. \quad (8.41)$$

This is identical to the relativistic action used in Chap. 3 for $N = 1$ components [c.f. Eq. (2.1)]. The 2PI equations for this action are given in Chap. 2, Eqs. (2.29)-(2.31). The self-energies expanded to the same order as for the anharmonic oscillator can be obtained from Eqs. (8.35), (8.36), (8.37), and (8.38) by adding a spatial dependence to the correlators. For Eq. (8.38) one further needs to integrate over space. In the following, we assume spatial homogeneity.

Similar to Chaps. 3-5, we investigate the evolution of the distribution function $f(t, \mathbf{p})$. In the following we assume spatial homogeneity and write $F(t, t', \mathbf{x} - \mathbf{x}') \equiv F(t, t', \mathbf{x}, \mathbf{x}')$. For the relativistic system we define¹⁰ [c.f. Eq. (3.23)]

$$f(t, \mathbf{p}) + \frac{1}{2} = \sqrt{F(t, t', \mathbf{p}) \partial_t \partial_{t'} F(t, t', \mathbf{p})} \Big|_{t=t'}, \quad (8.42)$$

where \mathbf{p} is the Fourier momentum with respect to the $\mathbf{x} - \mathbf{x}'$ variable [see Eq. (3.18)]. We consider ‘box’-type initial conditions for the distribution function with

$$f(0, \mathbf{p}) = A \theta(p - Q). \quad (8.43)$$

In contrast to Chaps. 3-5, we will consider here values of A and Q for which TWA is not necessarily valid. The initial condition for $f(0, \mathbf{p})$ needs to be translated into initial values for the one- and two-point correlators. The macroscopic field $\phi(t, \mathbf{x})$ and its derivative $\partial_t \phi(t, \mathbf{x})|_{t=0}$ will be set to zero. The spectral function ρ is fixed by the equal-time commutation relations as $\rho(0, 0, \mathbf{x} - \mathbf{y}) = 0$, $\partial_t \rho(t, 0, \mathbf{x} - \mathbf{y})|_{t=0} = \delta(\mathbf{x} - \mathbf{y})$, and $\partial_t \partial_{t'} \rho(t, t', \mathbf{x} - \mathbf{y})|_{t=t'=0} = 0$. Using (8.42) and (3.24) the statistical function is given at the initial time by

$$\begin{aligned} F(0, 0, \mathbf{p}) &= \frac{1}{\omega_p} \left(f(0, \mathbf{p}) + \frac{1}{2} \right), \\ \partial_t F(t, 0, \mathbf{p})|_{t=0} &= 0, \\ \partial_t \partial_{t'} F(t, t', \mathbf{p})|_{t=t'=0} &= \omega_p \left(f(0, \mathbf{p}) + \frac{1}{2} \right), \end{aligned} \quad (8.44)$$

where $\omega_p = \sqrt{\mathbf{p}^2 + m^2}$.

In S2PI the definition of the distribution function follows from (8.42) and the relation (8.31) and is given by

$$f(t, \mathbf{p}) + \frac{1}{2} = \sqrt{\left\langle \frac{1}{V} |\phi_w(t, \mathbf{p})|^2 + F_w(t, t, \mathbf{p}) \right\rangle \left\langle \frac{1}{V} |\partial_t \phi_w(t, \mathbf{p})|^2 + \partial_t \partial_{t'} F_w(t, t', \mathbf{p}) \right\rangle} \Big|_{t=t'}. \quad (8.45)$$

We note that in S2PI single realizations are inhomogeneous and only averaged quantities become homogeneous. For each single realization we define $F_w(t, t', \mathbf{p}) = \frac{1}{V} \int d^d x d^d y e^{i\mathbf{p}(\mathbf{y}-\mathbf{x})} F_w(t, t', \mathbf{x}, \mathbf{y})$. Given these definitions and the discussion of the previous sections we can write

¹⁰The form of this definition is related to the definition of the creation and annihilation operators in the free theory [c.f. Eq. (8.2)]. For a more detailed explanation see Sec. 3.3.

down the corresponding initial conditions for S2PI. In contrast to (8.44), in S2PI F_w and its derivatives are zero at the initial time. However, the spectral function ρ_w is initially fixed by the equal-time commutation relations, in the same way as ρ . The initial distribution function is reflected in the initial conditions for the field, which are given by

$$\phi_w(0, \mathbf{p}) = \xi_{\mathbf{p}}^R + i\xi_{\mathbf{p}}^I, \quad (8.46)$$

$$\partial_t \phi_w(0, \mathbf{p}) = \eta_{\mathbf{p}}^R + i\eta_{\mathbf{p}}^I, \quad (8.47)$$

with real independent gaussian random numbers $\xi_{\mathbf{p}}^{R,I}$ and $\eta_{\mathbf{p}}^{R,I}$ with variance

$$\langle (\xi_{\mathbf{p}}^R)^2 \rangle = \langle (\xi_{\mathbf{p}}^I)^2 \rangle = \frac{1}{2\omega_p} \left(f(0, \mathbf{p}) + \frac{1}{2} \right) V, \quad (8.48)$$

$$\langle (\eta_{\mathbf{p}}^R)^2 \rangle = \langle (\eta_{\mathbf{p}}^I)^2 \rangle = \frac{\omega_p}{2} \left(f(0, \mathbf{p}) + \frac{1}{2} \right) V. \quad (8.49)$$

Since $\phi_w(t, \mathbf{x})$ is a real field one further needs to ensure that $\phi_w(0, \mathbf{p}) = \phi_w^*(0, -\mathbf{p})$.¹¹ As one can see, 2PI and S2PI encode the information on the initial distribution function in a different way. For 2PI it is in the two-point function F , while for S2PI it is in the one-point ϕ_w . This sheds light on why the two methods can lead to considerably different results, despite using the same form for the evolution equations.

8.5 On thermalization and the quantum 1/2

In Chap. 3 we studied the evolution of the distribution function $f(t, \mathbf{p})$ starting from far-from-equilibrium initial conditions. While the classical-statistical approximation or TWA accurately describes the highly-occupied low-momentum regime ($f(\mathbf{p}) \gg 1$), this approach is not justified in the large momentum regime where occupancies become of order one, $f(\mathbf{p}) \sim 1$. In particular, it is known that TWA fails to capture the late time equilibration of the quantum system in the low-occupied regime [51, 79, 80].

To understand this, consider the case of a free theory. Classical equipartition implies that the equilibrium distribution in the classical statistical approach will be given by $f_{\text{RJ}}(\mathbf{p}) + 1/2 = T/(\omega_p - \mu)$, where T is the temperature and μ is the chemical potential. This distribution leads to the famous Rayleigh-Jeans divergence of the energy density at large momenta. In the quantum problem, the equilibrium distribution is given instead by the Bose-Einstein distribution $f_{\text{BE}}(\mathbf{p}) = 1/(e^{(\omega_p - \mu)/T} - 1)$, which, up to a vacuum renormalization, has a finite energy density. The classical equilibrium distribution agrees with the quantum one in the (low-momentum) regime where $(\omega_p - \mu)/T \ll 1$, but fails to reproduce the (high-momentum) regime where $(\omega_p - \mu)/T \gg 1$. In particular, at large enough momenta the classical distribution will fall below the quantum bound of 1/2, i.e. $f_{\text{RJ}}(\mathbf{p}) + 1/2 < 1/2$, which implies that $f_{\text{RJ}}(\mathbf{p})$ becomes negative in this regime. In the interacting theory, the same qualitative picture emerges, up to corrections coming from the interactions [80].

¹¹Special care needs to be taken with the frequencies 0 and $N/2$, since in these cases the field in Fourier space must be real.

For a weakly-coupled system, the low-occupied regime may in principle be described with 2PI using a low-order loop/perturbative expansion. Indeed, this approximation captures scattering effects and equilibrates to the right Bose-Einstein distribution [5, 104].¹² However, a perturbative approximation is doomed to fail as soon as the occupancies become of the order $f(\mathbf{p}) \sim 1/\lambda$, as is the case in the infrared of the nonthermal fixed point of Chap. 3. Hence, while TWA and perturbative expansions manage to capture the low- and highly-occupied regimes separately (assuming a small coupling), neither can be used over the full momentum regime.

In some sense, the S2PI method to NLO combines both approaches: at LO it corresponds to the classical-statistical approximation, whereas the NLO includes the same form for the self-energy corrections as in 2PI to NLO, although S2PI does it at the level of the Weyl function Σ_w instead of Σ . This poses the question of whether the S2PI method to NLO can describe quantum thermalization over the entire momentum regime.

Describing thermalization requires evolving the system to extremely late times. With the S2PI method this is very costly because of the inhomogeneity of the Weyl functions, the memory integrals and the additional sampling involved. Therefore, we concentrate here on some aspects of thermalization. While the exact form of the classical Rayleigh-Jeans distribution will only be achieved asymptotically in time in TWA, the quantum $1/2$ may start to decay already at relatively early times, as will be shown below. In the following, we investigate numerically whether S2PI to NLO respects the quantum bound of $1/2$, which is an important ingredient to describe quantum thermalization.

We consider a (2+1)-dimensional relativistic scalar field theory (8.41) on a two-dimensional lattice with $L^2 = 10 \times 10$ lattice points. In order to speed up the dynamics of the system, we consider a relatively large coupling $\lambda = 6$ ($m = 1$) [65].¹³ In this case, the validity of a perturbative expansion of Σ_w is not guaranteed and hence quantitatively precise predictions are not expected. To study the evolution of the low-occupied regime, we consider box initial conditions (8.43) with $A = 10$ and $Q = 0.8$. Details on the numerical method used to solve the 2PI equations can be found in App. A.

Figures 8.4a and 8.4b show the evolution of the distribution function $f(t, \mathbf{p})$ obtained from TWA and S2PI to NLO, respectively. Qualitatively, both approximations predict a quick redistribution of modes towards intermediate momenta $p \approx 1 - 2$ followed by slower dynamics. An important difference between them can be observed at the highest momenta. In TWA the distribution function clearly falls below the quantum $1/2$, even at the relatively early times considered. Remarkably though, the S2PI result stays above the quantum $1/2$ over the whole time interval shown. This can be better appreciated in Fig. 8.4c, which shows a comparison of the distribution at $t = 10$ for TWA and S2PI. Apart from the deviation at large momenta, Fig. 8.4c also shows that TWA and S2PI differ over the whole momentum regime, especially at intermediate momenta $p \approx 1 - 2$.

Of course, the times considered are relatively small and it is not guaranteed that the quantum $1/2$ will remain stable at later times. Nevertheless, these results are encouraging and show

¹²This can be seen from the kinetic equation derived in Chap. 3. Using a perturbative expansion one obtains $\partial_t f(t, \mathbf{p}) = C[f](t, \mathbf{p})$ with the collision integral (3.40). A fixed point of this equation is given by the Bose-Einstein distribution, i.e. $C[f_{\text{BE}}](t, \mathbf{p}) = 0$.

¹³Quantities are given in units of the lattice spacing.

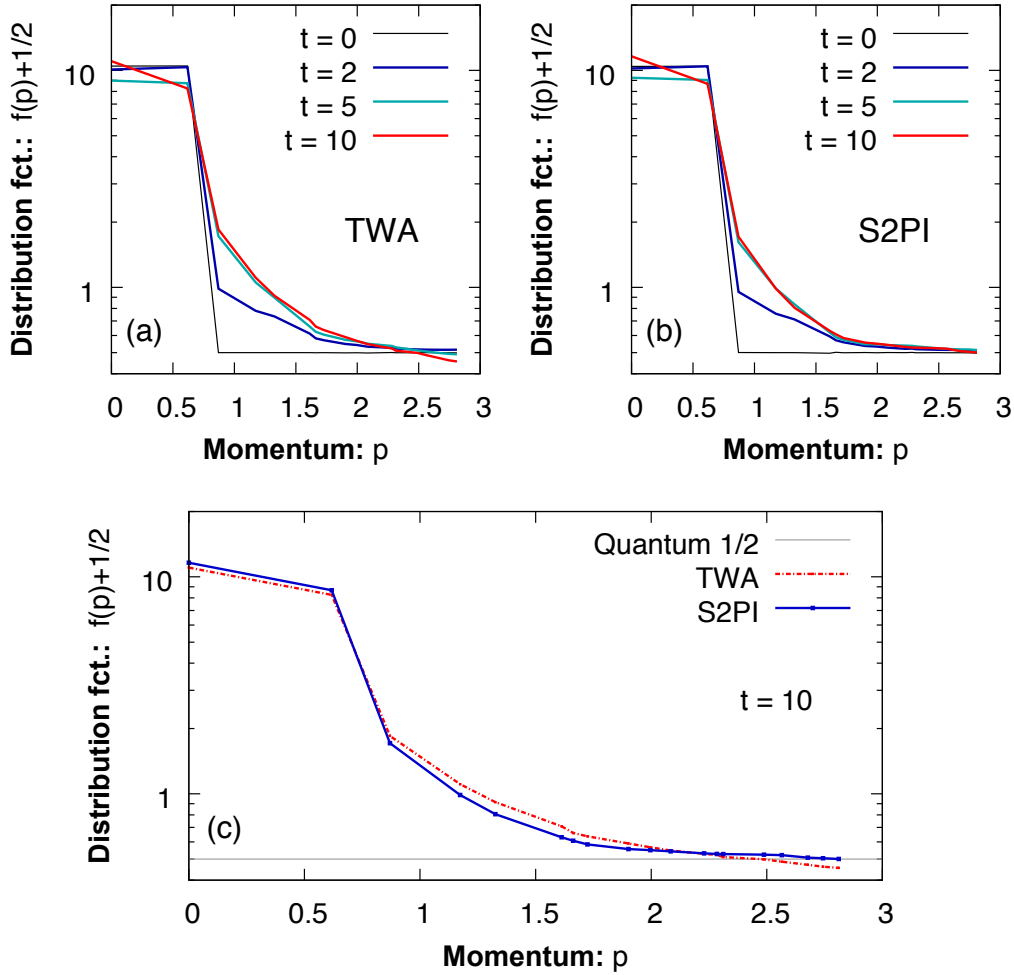


FIGURE 8.4: (a), (b) Evolution of the distribution function $f(t, \mathbf{p}) + 1/2$ computed with (a) TWA and (b) S2PI to NLO. (c) Comparison of the distribution function at $t = 10$ from TWA and S2PI to NLO against the quantum 1/2. The simulation was done on a 10×10 square lattice with $\lambda = 6$, $m = 1$ for box initial conditions with $A = 10$, $Q = 0.8$.

the potential of the S2PI method to NLO to add important quantum corrections to TWA that are needed to describe the quantum thermalization of a relativistic scalar field theory. Moreover, we should emphasize that these promising results were obtained for a relatively large coupling constant. The application of S2PI to NLO to weakly coupled systems should hence yield more accurate results. It should be noted again though, that the results of S2PI for the parameters used in Fig. 8.4 become numerically unstable for longer times. As for the anharmonic oscillator, we expect a weaker coupling to make the equations more stable.¹⁴

We close the section by reminding that S2PI to NLO is trivially also applicable to highly-occupied regimes, where the difference between TWA and S2PI to NLO should vanish. To check this, we show in Fig. 8.5 results for initial conditions with a higher initial box. Specifically, we chose $A = 60$ and $\lambda = 1$, thus keeping the product λA constant with respect to

¹⁴In fact, we find similar instabilities at strong coupling already in the solution of the 2PI equations with quantum initial conditions.

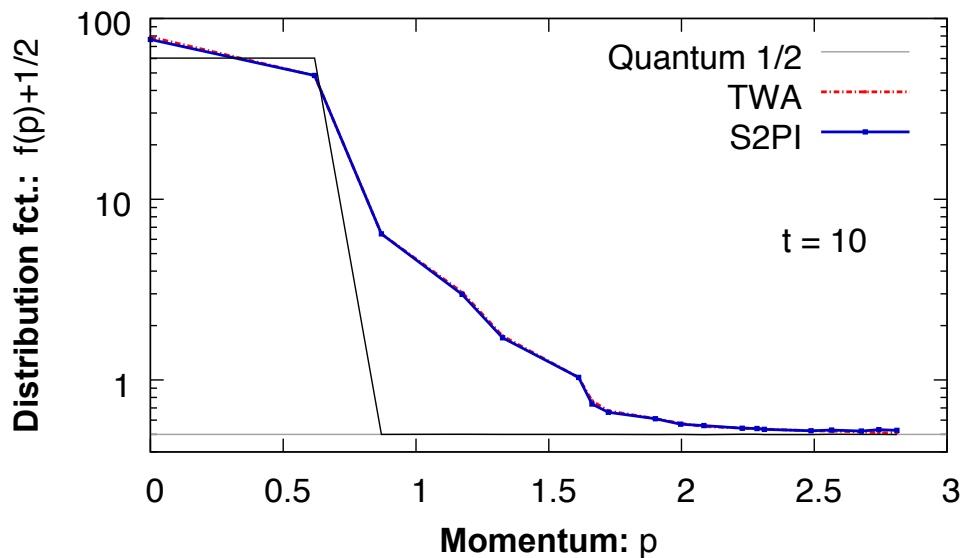


FIGURE 8.5: Comparison of the distribution function $f(t, \mathbf{p})$ at $t = 10$ from TWA and S2PI to NLO against the quantum 1/2 with a higher initial box amplitude (black line). The simulation was done on a 10×10 square lattice with $\lambda = 1$, $m = 1$ for box initial conditions with $A = 60$, $Q = 0.8$.

Fig. 8.4.¹⁵ As expected, the TWA (red line) and S2PI (blue line) results at $t = 10$ lie much closer to each other than in Fig. 8.4. For the parameters chosen, discrepancies between TWA and S2PI are likely to appear at longer times. However, these tend to zero in the limit $\lambda \rightarrow 0$ with $\lambda A = \text{const}$.

8.6 Conclusions

In this chapter we have demonstrated the power of the Sampled 2PI (S2PI) method to add relevant quantum corrections to TWA. The method is based on solving 2PI equations (instead of the BBGKY hierarchy of Chap. 7) and sampling over initial conditions. The leading order (LO) is given by the usual TWA and is obtained by setting all self-energies Σ_w to zero. Here, we have shown that using a coupling expansion of the effective action Γ_w to next-to-leading order (NLO) is enough to introduce important corrections to TWA.

We first tested the method against numerically exact results of an anharmonic oscillator. In regimes where the exact dynamics was captured already with TWA, both TWA and S2PI to NLO lied on top of each other. In regimes where this was not the case, the S2PI result was found to agree with the exact solution for a longer time than TWA. The accuracy of S2PI to NLO was further improved by choosing a smaller coupling. Interestingly, we showed that using the 2PI equations to evolve expectation values instead leads to comparably worse results.

In a next step, we applied the S2PI method to a (2+1)-dimensional relativistic scalar field theory. We studied the evolution towards equilibrium of the distribution function $f(t, \mathbf{p})$

¹⁵In the limit $\lambda \rightarrow 0$ with $A\lambda = \text{const}$ the effect of the modes occupied initially with the quantum 1/2 is negligible [51] and hence the classical-statistical approximation should be valid for sufficiently small λ .

with both TWA and S2PI to NLO. The TWA is known to equilibrate to the Rayleigh-Jeans distribution at long times and to hence violate the quantum bound $f(t, \mathbf{p}) + 1/2 \geq 1/2$. We considered initial conditions for which the quantum $1/2$ in TWA decays at relatively early times. Remarkably, we showed that for the times considered this unphysical decay is corrected at S2PI to NLO. While the behavior at longer times still needs to be studied, this opens the exciting possibility to study quantum thermalization using the S2PI method to NLO.

The power of S2PI lies in its potential to capture both the highly-occupied classical-statistical regime as well as the low-occupied region where quantum effects play an important role. For scalar theories, this may be achieved as well using the nonperturbative $1/N$ resummation techniques introduced in Chap. 2 (see [65]). However, such nonperturbative expansions are not possible or have not been accomplished yet in other systems such as gauge theories. The application of the S2PI method to such systems may thus enable the description of phenomena which currently can not be described with other state-of-the-art methods.

Chapter 9

Conclusions and Outlook

In this thesis, we have explored the nonequilibrium dynamics of various many-body systems and have developed theoretical tools to treat them. In the following, we summarize the main conclusions, discuss open questions and possible future directions, and highlight the interconnections between all the topics considered.

Nonthermal fixed points

Chapters 3, 4, and 5 have extensively contributed towards the understanding of universal self-similar dynamics emerging far from equilibrium in both relativistic and nonrelativistic scalar field theories. Starting from initial states with overoccupied characteristic modes, the system is quickly attracted towards a nonthermal fixed point, characterized by slow self-similar dynamics and transport of conserved quantities. During this regime, the distribution function of modes, $f(t, \mathbf{p})$, exhibits a characteristic dual cascade in which energy is transported to higher momenta and particle number to lower momenta. The latter leads to the formation of a Bose condensate out of equilibrium.

The transport of conserved quantities through momentum space is linked to the self-similar evolution of the distribution function. In Chap. 3 we demonstrated the self-similar dynamics of $f(t, \mathbf{p})$ in the nonperturbative infrared regime, thus extending previous works that concentrated on the higher-momentum regime or stationary properties of the infrared [40, 41, 43, 55–57]. Using classical-statistical simulations we computed the universal scaling exponents (α , β) and scaling functions (f_S) characterizing the self-similar evolution, $f(t, \mathbf{p}) = t^\alpha f_S(t^\beta \mathbf{p})$. Remarkably, we found both relativistic and nonrelativistic scalar theories to be described by approximately the same set of universal exponents in the infrared, $\alpha = \beta d$ and $\beta \approx 0.5$, [c.f. Eqs. (3.14), (3.27), and (3.28)] and to even share the same universal scaling function (Fig. 3.2). Since the relation $\alpha = \beta d$ is linked to particle conservation, the positive sign of β confirms the existence of the inverse particle cascade towards low momenta, with a condensate growing as $\sim t^\alpha$.

To gain analytic understanding, we analyzed the problem from the point of view of kinetic theory. Perturbative techniques, useful in the description of the energy cascade at higher momenta [40], become invalid in the infrared, where occupancies become parametrically of

the order of the inverse (small) coupling or diluteness parameter. In particular, perturbative approaches applied to the infrared predict the wrong sign and values of the exponents, which would imply a particle transport in the wrong direction. To remedy this we derived a resummed kinetic theory based on a $1/N$ expansion of the 2PI effective action to next-to-leading order (NLO) [41, 43, 108]. As we showed, this nonperturbative approximation captures essential aspects of the self-similar dynamics in the infrared. Using a simplified approach, we derived exponents with the correct sign, $\alpha, \beta > 0$, and with values in close agreement with the numerical simulation results.

Further insight into the physics of the nonthermal fixed point was gained by extending the above analysis, which is based on the equal-time distribution function, to correlation functions that depend on two times. In particular, this allows to extract the dynamical exponent z , which relates characteristic frequencies and momenta. In Chaps. 4 and 5 we investigated the behavior of the statistical function $F(t, t', \mathbf{p})$ and spectral function $\rho(t, t', \mathbf{p})$ for the nonrelativistic theory. While in equilibrium these two quantities are related by the fluctuation-dissipation relation, we strikingly found that during the self-similar regime this relation is broken, especially in the infrared.

In frequency space, the spectral function exhibits clear quasiparticle peaks, even in the strongly correlated infrared regime. The dispersion relation and amplitude of the peaks are approximately time-independent during the self-similar regime and agree impressively well with the predictions from Bogoliubov theory without fitting parameters. The dispersion in the infrared regime studied in Chap. 3 turns out to be linear and becomes quadratic at larger momenta. These Bogoliubov peaks were also found in the frequency dependence of the statistical function. Additionally though, this function exhibits an extra peak, which dominates in the infrared over the Bogoliubov peaks, and is absent in the spectral function. Since $f(t, \mathbf{p})$ is related to the equal-time F , this means that the infrared scaling of $f(t, \mathbf{p})$ is dominated by this extra peak.

This striking breaking of the fluctuation-dissipation theorem at low momenta has important implications for the scaling behavior of these quantities close to the nonthermal fixed point. From a finite-size scaling analysis of the zero-momentum mode we showed in Chap. 4 that F evolves in a self-similar fashion with dynamical exponent $z \approx 1/\beta \approx 2$ [c.f. Eq. (4.18)]. However, the spectral function exhibits at low-momenta self-similar scaling with small anomalous dimension $\eta \approx 0$ and a different dynamical exponent, $z = 1$, related to the linear part of the Bogoliubov dispersion relation.

The results presented leave a number of open questions. In Chap. 3 we pointed to the emergence of a dynamically generated mass in the relativistic theory as the reason for the universality observed in the exponents α and β for both relativistic and nonrelativistic theories. The corresponding dispersion relation for the relativistic theory was roughly of the form $\sqrt{p^2 + m^2}$, which in the nonrelativistic limit becomes $m + p^2/2m$, and was obtained from time derivatives of F . However, the nonrelativistic results have shown that F can have a more complex structure with different peaks contributing in different momentum ranges and hence different dispersion relations. In this context, it would be interesting to see whether an extra peak appears in the relativistic F , since this may be connected to the universality observed between relativistic and nonrelativistic theories. Moreover, given the breaking of the fluctuation-dissipation relation in the nonrelativistic theory, especially at low momenta, it is not clear whether or in which way the form of the spectral function affects the universality

of α and β . Computation of the relativistic spectral function can shed light onto this issue and help elucidate whether the universality found concerns only the equal-time distribution function or also unequal-time quantities, in particular the dynamical exponent(s) z .

Characterization of the extra peak found in F , such as its frequency dependence and time evolution, has become of capital importance to deepen our understanding on the physics behind the nonthermal fixed point. In particular, since the infrared dynamics of the distribution function appears to be strongly influenced by the extra peak, it would be of interest to study the relation of this peak to the transport of particles. Similarly, it may help elucidating the role of topological defects in the dynamics [56, 67] as well as the relation of nonthermal fixed points to turbulence and coarsening. Moreover, a better understanding of the peak properties can help developing a more precise kinetic theory for the self-similar regime. While the results obtained from the $1/N$ resummation are already encouraging, a more accurate description requires the use of a different scaling behavior for F and ρ , as we found out numerically.

These results have revealed the importance of studying the dynamics of unequal-time quantities such as the statistical and spectral function in order to understand the behavior of many-body systems far-from equilibrium. In particular, such an analysis can help elucidate the structure of other nonthermal fixed points appearing in different theories or for different initial conditions [12, 48, 50, 62–64]. In this regard, a particularly interesting development concerns the calculation of spectral functions out of equilibrium. The generality of the method employed, which is based on linear responses to external perturbations [131, 132], allows its straightforward implementation also in different systems, including experimental platforms. Experiments with ultracold gases constitute an ideal testbed for such endeavors (for a related example see e.g. [216]), since the apparatus needed for the implementation of the necessary rotations is already commonly used for similar purposes in many experiments. In turn, based on universality, these experiments can help understanding important aspects of other systems such as the early-universe dynamics after the inflationary era [73]. Recent experiments show that the study of dynamical scaling properties in nonrelativistic Bose gases is indeed within reach [217–219].

Rydberg spin dynamics

An example of the potential of experiments with ultracold quantum gases to understand nonequilibrium processes in many-body quantum systems was given in Chap. 6. Using an ensemble of Rydberg atoms we demonstrated in a combined effort of theory and experiment that important aspects of the relaxation dynamics of quantum spin systems can be investigated. Specifically, using two different Rydberg states to encode a spin-1/2 degree of freedom, the system considered realizes an XY model with long-range dipolar interactions in an external field. Starting from a fully magnetized initial state we observed the relaxation dynamics to an unmagnetized state after a quench of the external field. Compared to other platforms for realizing quantum spin models such as polar molecules [82–84] or trapped ions [85–88], one of the advantages of Rydberg systems is that the dynamics happens faster than typical decoherence processes and hence the system can be well isolated from the environment for considerably long times in units of the typical interaction energies [220, 221]. Comparison of the measured evolution to theoretical calculations showed that the observed dynamics is

indeed well-reproduced by unitary dynamics alone without the need to invoke any decoherence processes.

As compared to the scaling physics close to the nonthermal fixed point of Chaps. 3-5, which is dominated by classical fluctuations, quantum effects can play an important role in quantum spin-1/2 systems. Interestingly, for the case and observables considered, the Rydberg spin system could still be reproduced by classical-statistical dynamics (TWA). However, the ‘quantumness’ of the spin is not washed out. Using a well-defined hierarchy of theoretical approximations, we found out that the dynamics observed is strongly influenced by the disorder and the initial quantum fluctuations of the spin-1/2. The latter determine the variance of the initial classical ensemble for TWA and were shown to become less important for longer spin lengths.

While quantum corrections on the dynamical laws, which are neglected in TWA, did not play an important role in the dynamics of the magnetization, theoretical predictions suggest that higher-order correlation functions, such as variances, can be sensitive to this. Hence, computation of such correlators appears as an attractive prospect for future experiments aiming at deciphering the role of quantum fluctuations in the relaxation dynamics of spin systems. In particular, spatial resolution [91, 92, 222] combined with measurements of unequal-time functions, e.g. using the method of Chap. 5 to compute spectral functions, can shed new light on the thermalization process. These quantities would allow, for instance, to investigate the nonequilibrium breaking of the fluctuation-dissipation relation, as well as its restoration at long times, where quantum effects can not be neglected, as discussed in Chap. 8.

In view of the power of TWA to capture some important aspects of quantum spin systems, a study of its range of validity for these systems appears essential. Furthermore, since the nonthermal fixed point of Chaps. 3-5 is dominated by classical fluctuations, this issue is closely related to the quest for universal self-similar dynamics in isolated spin systems. Since close to thermal phase transitions spin systems and scalar theories can be related to each other through universality [38], a similar connection may be true in isolated systems out of equilibrium. In this case, Rydberg atoms would offer the possibility to study the influence of long-range interactions on the universality class, which in equilibrium is known to be sensitive to it [223–226]. Recent works [168, 227–231] suggest that Rydberg atoms can indeed become a powerful platform for the study of scaling phenomena in quantum spin systems out of equilibrium.

Quantum corrections to TWA

Despite the success of the classical statistical approximation, or TWA, in describing several nonequilibrium phenomena throughout Chaps. 3-6, certain regimes are not well reproduced by this approximation. These include higher-order observables in the Rydberg spin system, as well as the high-momentum region of scalar theories, especially at long times, where occupancies become of order one. In Chaps. 7 and 8 we studied methods to add quantum corrections to TWA by enlarging the set of variables and equations to be solved. It is based on the Wigner representation of quantum theory, where operators are mapped onto phase-space functions called Weyl symbols. The additional variables in the extension of TWA are related to Weyl symbols of n -point operators ($n \geq 2$), while $n = 1$ Weyl symbols correspond to the classical

variables of TWA. The equations of motion fulfilled by the Weyl symbols follow directly from the Heisenberg equations for operators and are hence analogous to the ones fulfilled by the corresponding expectation values, but with different initial conditions. To obtain expectation values, one needs to average Weyl symbols over an ensemble of initial conditions, similar to TWA. In this framework, the lowest-order approximation corresponds to TWA.

In this work, we considered two different extensions of TWA: one based on BBGKY equations for equal-time quantities and the other one based on 2PI equations for unequal-time functions. The BBGKY approach was tested in Chap. 7 against exact solutions for a spin-boson model relevant in the description of trapped-ion experiments. The method used is an adaptation of [110] to the spin-boson model, combined with recent discrete sampling techniques for the spins [102]. The extra variables are in this case Weyl symbols of n -point equal-time operators, evolving through an infinite hierarchy of coupled equations. Approximations beyond TWA are made by keeping at least second-order terms and neglecting higher-order Weyl symbols, thus truncating the hierarchy. To benchmark TWA and the BBGKY extension we compared the dynamics of various one- and two-point observables against exact solutions. In general, we found excellent agreement for a large range of parameters, including coupling to single or multiple bosonic modes, and different interaction structures in one and two dimensions. Specifically, we found TWA to yield accurate results when a handful of modes dominates the dynamics, whereas in all other cases the BBGKY extension introduced the necessary corrections to make the result lie almost perfectly well on top of the exact result for the times considered.

Based on the correspondence between the equations for Weyl symbols and for correlation functions, we employed in Chap. 8 2PI equations instead to evolve unequal-time Weyl symbols. In the so-named Sampled 2PI (S2PI) method, the variables are the Weyl symbols ϕ_w , F_w and ρ_w analog to the one- and two-point correlators in the 2PI framework. Approximations in this framework are made at the level of the ‘Weyl’ self-energy Σ_w or 2PI action $\Gamma_{2,w}$. We considered a coupling expansion to order $\sim \lambda^2$ and demonstrated the capability of the S2PI method to improve the prediction of TWA, especially at small coupling, by comparing to exact numerical results of an anharmonic oscillator. We further applied S2PI to a relativistic scalar field theory, where we considered initial conditions for which TWA leads to an unphysical decay of the quantum 1/2, or zero-point motion. Remarkably, we found that, for the times considered, S2PI stabilizes this decay and respects the quantum bound. Since this is an important ingredient for describing quantum thermalization, the results offer exciting prospects for the application of S2PI to thermalization problems.

An important observation of Chaps. 7 and 8 is the fact that both the BBGKY and 2PI equations lead to considerably less accurate results when used to evolve correlation functions as compared to sampling over initial conditions and using these equations to instead evolve Weyl symbols. This suggests that the sampling introduces corrections well beyond the apparent approximation order of the equations of motion. Of course, this is well-known in TWA, where the sampling of classical, or mean-field type, equations generates corrections of arbitrary order in fluctuations around mean-field. Careful inspection of these corrections leads to the classicality condition presented in Chap. 2. Similarly, understanding the nature of the corrections in the BBGKY extension and S2PI is essential to establish their range of validity. One possibility may be to proceed as in TWA by constructing a path integral and comparing the diagrammatic expansion to the full quantum theory.

The quantum corrections to TWA added in the BBGKY and S2PI extensions come naturally at a cost. The introduction of inhomogeneous¹ two- or higher-point variables increases the memory requirements considerably, especially in the 2PI approach due to the memory integrals. Furthermore, one needs to sample over initial conditions, which means that the equations need to be solved in general many times. All this reduces the size of the systems and the times that can be simulated efficiently. Possible improvements may be accomplished by neglecting variables that do not contribute significantly to the dynamics. This was done, for instance, in Chap. 7 for BBGKY, where only a subset of all the three-point functions was used. In S2PI, one may impose memory cuts to the memory integrals thus reducing the amount of memory needed. In both cases, further approximations to the equations of motion, such as gradient expansions, may allow the simulation of larger systems to longer times. Apart from this, it should be mentioned that care with possible numerical instabilities needs to be taken, especially in the BBGKY expansion [212].

Despite these difficulties, the results presented are encouraging and show that the BBGKY and S2PI extensions of TWA can lead to important quantum corrections in the dynamics. In principle, these methods can be applied to generic spin and boson systems (and perhaps also fermions [232]) and have potentially wide ranging applications from ultracold quantum gases to heavy-ion collisions. In the case of the Rydberg spin system studied in Chap. 6, quantum corrections such as those introduced in these methods will be needed for the description of higher-order observables or other initial conditions. Regarding the nonthermal fixed point of the scalar field theories investigated in Chaps. 3-5, the S2PI method may potentially be able to capture both the highly-occupied classical regime as well as the low-occupied quantum regime at weak couplings. While in these theories $1/N$ resummation techniques can interpolate between these two regimes as well [65], such nonperturbative approximations are not easily implemented in other systems, such as gauge theories. Thus, weakly-coupled non-Abelian plasmas far from equilibrium constitute an interesting candidate for the application of the S2PI method.

Final word

The topics covered in this thesis have shown to interconnect different disciplines and to have implications for numerous fields covering a large spectrum of physical systems and energy scales - the previous paragraph is just one example of this. Some of the unifying elements for all these fields are the methods used in the description of many-body quantum systems, as well as the questions posed about their nonequilibrium dynamics. Strong, even quantitative, connections are established also by the emergence of universal behavior. From the experimental point of view, the explosive progress in ultracold quantum gases has undoubtedly contributed towards bringing together vastly different fields [20, 233], owing to the possibility of realizing a myriad of physical models which can be investigated with an unprecedented degree of control. This results in a rich melting-pot of different views and ideas, from which this thesis and I have greatly benefited.

¹The inhomogeneity of the variables may not constitute an additional complication in problems that are intrinsically inhomogeneous, such as in studies of many-body localization [11].

Acknowledgements

If there is one thing I have learned about science over the course of my PhD, it is the importance of the people who make it. I would like to dedicate the next lines to thank all those people which in one way or another have had an influence on this thesis.

First and foremost, I would like to express my sincerest gratitude to my supervisor, Jürgen Berges. Not only has he provided me with the opportunity of delving into the research world in a very stimulating field and environment, but he has been a constant source of inspiration. He has both given me (almost too much) freedom to follow my way, as well as words of encouragement when needed.

I am also deeply grateful to Ana María Rey, who, despite hardly knowing me, welcomed me with open arms in her group at JILA (Boulder, USA). I have learned a lot from her and I have collected many interesting international experiences thanks to her.

At this point, I would also like to acknowledge funding from the German Academic Exchange Service (DAAD) under the grant Kurzstipendien für Doktoranden (57044996), which supported my research stay in the group of Ana María Rey at JILA (Boulder, USA).

The work presented here would not have been possible without my collaborators, which I honestly want to thank (omitting the already mentioned): Adrien Signoles, Shannon Whitlock, Matthias Weidemüller, Hannah Wildhagen, Georg Günter, Arghavan Safavi-Naini, Michael Wall, Kirill Boguslavski, and Andreas Schachner. Not only have I learned a lot from all of them, but they have showed me how fun it is to do physics with other people.

I am also indebted to the following people for insightful discussions and/or collaborations on related work: Thomas Gasenzer, Isara Chantesana, Andreas Elben, Torsten Zache, Alexander Schuckert, Ignacio Aliaga Sirvent, Valentin Kasper, Johannes Schachenmayer, Martin Gärtner, Stephan Helmrich, Titus Franz, Alexander Rothkopf, Roland Walz, and Oscar García Montero.

I would like to express my deepest appreciation to the whole Berges group for creating such a relaxed and warm atmosphere. Without their support it would not have been the same. I would also like to thank the whole Rydberg experimental group for their patience and for enriching discussions as well as the entire Rey group in Boulder for their hospitality.

I would like to thank Kirill B., Torsten Z., Martin G., Andreas S., and Alexander S. for proof-reading parts of this thesis. All remaining errors are on my account.

Finally, I would like to thank from my heart my family and my friends for their unconditional love and support. And, of course, an ineffable thank you goes to the person that has been closest to me over the last years and breathes life into me every day, my ‘half-orange’², Emmanuela.

²Spanish saying.

Appendix A

Numerical Methods

In this section, we fill in some details about the numerical methods used in Chaps. 3-8 that were left out of the main text.

A.1 Space and Time Discretization

In Chaps. 3-5 we performed classical-statistical simulations for both relativistic and nonrelativistic scalar theories in $d = 3$ dimensions. In Chap. 5 we also performed simulations using both classical-statistical methods as well as 2PI equations for the relativistic theory in $d = 2$ dimensions.

The simulations run on a rectangular lattice with periodic boundary conditions and volume $V = (aN)^d$, where N is the number of grid points per lattice side and a is the lattice spacing. Positions on the lattice are discrete points given by $\mathbf{r} = (r_1a, \dots, r_da)$ with $r_i \in \{0, \dots, N-1\}$. The Fourier momenta on the lattice are given by $\mathbf{p}_{\text{lat}} = (p_1, \dots, p_d)$, where $p_i = 2\pi n_i/aN$ with $n_i \in \{0, \dots, N-1\}$. The corresponding physical momenta are defined, up to a sign, as the eigenvalues of the discretized version of the Laplace operator¹ and are given by

$$\mathbf{p}^2 = \sum_{i=1}^d \frac{4}{a^2} \sin^2\left(\frac{ap_i}{2}\right). \quad (\text{A.1})$$

The momenta shown in the plots of the main text correspond to this definition of momentum. From this one obtains the infrared and ultraviolet cutoffs

$$\Lambda_{IR} = \frac{2\pi}{aN}, \quad (\text{A.2})$$

$$\Lambda_{UV} = \frac{\sqrt{4d}}{a}. \quad (\text{A.3})$$

As we can see, increasing the number of lattice points allows us to access a larger portion of the infrared.

¹In 1 dimension one would have: $\partial_x^2 e^{-ipx} \mapsto e^{-ipx} [e^{ipa} + e^{-ipa} - 2]/a^2 = -e^{-ipx} 4 \sin^2(pa/2)/a^2$.

To solve the corresponding differential equations on a lattice, we discretize as well time in N_t steps with Δt time step, such that $t \rightarrow n\Delta t$ with $n \in \mathbb{N}$. For second order derivatives we use the symmetric forms

$$\frac{\partial^2}{\partial t^2} f(t, \mathbf{x}) \longrightarrow \frac{1}{\Delta t^2} [f(t + \Delta t, \mathbf{x}) - 2f(t, \mathbf{x}) + f(t - \Delta t, \mathbf{x})], \quad (\text{A.4})$$

$$\nabla_x^2 f(t, \mathbf{x}) \longrightarrow \frac{1}{a^2} \sum_{i=1}^d [f(t, \mathbf{x} + a\mathbf{e}_i) - 2f(t, \mathbf{x}) + f(t, \mathbf{x} - a\mathbf{e}_i)], \quad (\text{A.5})$$

where $f(t, \mathbf{x})$ represents here a generic function and \mathbf{e}_i is a unit vector pointing in the direction of the i -th dimension. The time and spatial integrals appearing in the 2PI equations of motion of Chap. 8 are calculated using the trapezoid rule as

$$\int_0^t dt' f(t', \mathbf{x}) \longrightarrow \frac{\Delta t}{2} [f(0, \mathbf{x}) + f(t, \mathbf{x})] + \Delta t \sum_{l=1}^{n-1} f(l\Delta t, \mathbf{x}), \quad (\text{A.6})$$

$$\int d^d x f(t, \mathbf{x}) \longrightarrow a \sum_{i=1}^{N^d} f(t, \mathbf{x}_i). \quad (\text{A.7})$$

As mentioned in the main text, the classical-statistical equation of motion (3.4) for the non-relativistic theory is solved using a split-step method [56, 57], whereas the relativistic classical equation (3.16) is solved with a leapfrog algorithm [41, 51]. The algorithm employed for solving the 2PI equations of motion is outlined in the next section.

A.2 2PI equations

We specify in the following the algorithm used in Chap. 8 for solving the 2PI equations of the relativistic scalar field theory, which can be straightforwardly applied as well to the anharmonic oscillator. It is based on Ref. [234] and partly on Ref. [70].

Time and space are discretized as given in the previous section. Because of the memory integrals, one needs to store the whole one-point function $\phi(t, \mathbf{x})$ and two-point functions $F(t, t', \mathbf{x}, \mathbf{y})$ and $\rho(t, t', \mathbf{x}, \mathbf{y})$. However, due to symmetry, it is enough to just save the $t \geq t'$ part of the two-point functions. Thus, ϕ is an array with $N_t \times N$ points and F and ρ are $N_t^2 \times N(N+1)/2$ -sized arrays. For simplicity, we suppress in the following the space dependence and write just $\phi(i)$, $F(i, j)$, and $\rho(i, j)$ with $i, j \in \{0, \dots, N_t - 1\}$.

To initialize the dynamics, we need to assign values to $\phi(0)$, $\phi(1)$, $F(0, 0)$, $F(1, 0)$, $F(1, 1)$, $\rho(0, 0)$, $\rho(1, 0)$, and $\rho(1, 1)$. The initial conditions for the correlators specified in Chap. 8 can be translated into initial values for these quantities by using single Euler forward steps for the derivatives ∂_t and $\partial_{t'}$, e.g. $\partial_t \phi(t)|_{t=0} = (\phi(1) - \phi(0))/\Delta t$. Furthermore, one needs to substitute $\delta(\mathbf{x} - \mathbf{y}) \rightarrow \delta_{\mathbf{x}, \mathbf{y}}/a^d$.

In the 2PI equations for F and ρ given in the main text [see Eqs. (2.30), (2.31), (8.8), and (8.9)], the time derivatives are applied to the first argument of the two-point functions. However, using the symmetries of F and ρ they can be transformed into equations of motion for the second argument. For the relativistic (one-component) field theory one obtains from

Eqs. (2.30) and (2.31)

$$\left[\square_y + M^{(\text{rel})}(y) \right] F(x, y) = \int_0^{y_0} dz F(x, z) \Sigma^\rho(z, y) - \int_0^{x_0} dz \rho(x, z) \Sigma^F(z, y), \quad (\text{A.8})$$

$$\left[\square_y + M^{(\text{rel})}(y) \right] \rho(x, y) = - \int_{y_0}^{x_0} dz \rho(x, z) \Sigma^\rho(z, y), \quad (\text{A.9})$$

where the mass function $M^{(\text{rel})}(y)$ is defined in (2.32).

We now outline the algorithm used to advance forward in time. We assume that we know the functions $\phi(l)$, $F(l, m)$ and $\rho(l, m)$ as well as the self-energies $\Sigma^F(l, m)$ and $\Sigma^\rho(l, m)$ for all $0 \leq l \leq i$ and $m \leq l$. To advance one step forward in time, $i \rightarrow i + 1$, we proceed as follows:

1. With the equation of motion for ϕ , Eq. (2.29), and the values of $\phi(i)$ and $\phi(i - 1)$, we compute $\phi(i + 1)$ for all points in space.
2. Using the equal-time commutation relations we fix the values of $\rho(i + 1, i + 1)$ and $\rho(i + 1, i)$. Following that we use the equation for the second time argument, Eq. (A.9), to evolve backwards in time and obtain $\rho(i + 1, j)$ starting from $j = i - 1$ all the way down to $j = 0$. Note that in each step, all points in space need to be computed.
3. Using the equations for the first time argument of F , Eq. (2.30), we compute from $F(i, l)$ and $F(i - 1, l)$ the value $F(i + 1, l)$ for $l = 0$ and $l = 1$, respectively.
4. Starting from the values obtained in the previous step, $F(i + 1, 0)$ and $F(i + 1, 1)$, we evolve forwards in time with (A.8) to compute $F(i + 1, j)$ from $j = 2$ to $j = i + 1$. Again, the full space dependence of F is needed at each time step, before progressing to the next step.
5. We compute the self-energies $\Sigma^F(i + 1, l)$ and $\Sigma^\rho(i + 1, l)$ for $0 \leq l \leq i + 1$ from the results of the previous points as preparation for the next time step.

A.3 Crank-Nicolson

The TWA equations of motion for the Rydberg spin system of Chap. 6 and the TWA and BBGKY equations for the spin-boson system of Chap. 7 were solved using a Crank-Nicolson algorithm [235]. With this method, equations (or systems of equations) of the form

$$\frac{\partial}{\partial t} u = F(u). \quad (\text{A.10})$$

can be solved. Time is discretized as $t \rightarrow n\Delta t$, $u(t) \rightarrow u_n$, with $n \in \mathbb{N}$. Combining a forward and backward Euler step, one writes the equation as

$$\frac{u_{n+1} - u_n}{\Delta t} = \frac{1}{2} (F(u_n) + F(u_{n+1})). \quad (\text{A.11})$$

This approximation is stable, preserves unitarity and is second-order accurate. To move forward in time, this implicit equation needs to be solved. However, using the fact that the

method is accurate to second-order, one may solve it iteratively by following these steps:

$$\tilde{u}_1 = u_n + \frac{\Delta t}{2} F(u_n), \quad (\text{A.12})$$

$$\tilde{u}_2 = u_n + \frac{\Delta t}{2} F(\tilde{u}_1), \quad (\text{A.13})$$

$$u_{n+1} = 2\tilde{u}_2 - u_n. \quad (\text{A.14})$$

One can check by expanding in powers of Δt that the expression obtained for u_{n+1} out of this procedure agrees with (A.11) up to order Δt^2 . The generalization of this method to systems of equations with N variables is straightforward by replacing $u \rightarrow \mathbf{u} \equiv (u_1, \dots, u_N)$.

A.4 Anharmonic Oscillator

In Chap. 8 we presented exact numerical results for the quantum anharmonic oscillator for initial conditions starting in a pure state. For this we solve the Schrödinger equation in the position representation

$$i \frac{\partial}{\partial t} \psi(t, x) = H \psi(t, x). \quad (\text{A.15})$$

Using $\hat{\varphi} \rightarrow x$ and $\hat{\pi} \rightarrow -i\partial_x$, the Hamiltonian (8.1) is given by

$$H = -\frac{1}{2} \frac{\partial}{\partial x} + \frac{1}{2} m^2 x^2 + \frac{\lambda}{4!} x^4. \quad (\text{A.16})$$

The initial wave function reads (c.f. Eq. (8.40))

$$\psi_0(x) = \frac{1}{(2\pi \xi^2)^{1/4}} \exp \left[- \left(\frac{1}{4\xi^2} - i \frac{\eta}{2\xi} \right) x^2 \right], \quad (\text{A.17})$$

where the parameters are chosen to agree with (8.14) for $\sigma = 1$. To solve this equation we discretize space into N points with lattice spacing a . We increase N and the total length $L \equiv Na$ until convergence is reached and check that the results are insensitive to the boundary conditions used. For the derivative we use the symmetric discretized form $\partial_x^2 f(x) = (f(x+1) - 2f(x) + f(x-1))/a^2$. The equation (A.15) is then solved by matrix exponentiation and the variance is computed by

$$\langle \hat{\varphi}^2(t) \rangle = \int dx x^2 |\psi(t, x)|^2. \quad (\text{A.18})$$

We checked that the integration method preserves to good accuracy the norm of the state $\int dx |\psi(t, x)|^2 = 1$.

Appendix B

Self-similarity fit procedure

This appendix is based on “*Universal self-similar dynamics of relativistic and nonrelativistic field theories near nonthermal fixed points*”, A. Piñeiro Orioli, K. Boguslavski and J. Berges, published in Phys. Rev. D **92**, 025041 (2015) [66], as well as on “*Universal scaling of unequal-time correlation functions in ultracold Bose gases far from equilibrium*”, A. Schachner, A. Piñeiro Orioli and J. Berges, published in Phys. Rev. A **95**, 053605 (2017) [145]. Parts of the text are taken from these references.

In this section, we describe the fit routine used in Chaps. 3 and 4 to extract the scaling exponents of the self-similar evolution, as well as the errors of the mean. The method is based on [50]. For simplicity, we discuss first the fit routine applied to the self-similar dynamics of the distribution function $f(t, \mathbf{p})$ given in (3.1) and comment on how to adapt it to the unequal-time case afterwards.

In order to quantify the deviation from the self-similar behavior we need to compare rescaled curves to each other. For this, we take the distribution at a fixed time t_{ref} as reference and define for given exponents α , and β the rescaled function ($|\mathbf{p}| \equiv p$)

$$f_{\text{resc}}(t, p) = (t/t_{\text{ref}})^{-\alpha} f(t, (t/t_{\text{ref}})^{-\beta} p). \quad (\text{B.1})$$

A perfectly self-similar evolution (3.1) implies $\Delta f(t, p) \equiv f_{\text{resc}}(t, p) - f(t_{\text{ref}}, p) = 0$ for all t within the scaling regime.

Deviations from perfect scaling behavior as well as statistical uncertainties will be reflected in a nonvanishing Δf . Minimizing the deviations yields the best fit for the scaling exponents α and β , while the errors of the fit may be estimated from the distribution of the deviations as a function of the exponents. Specifically, we select a set of times t_k , $k \in \{1, \dots, N_{\text{com}}\}$, spanning the whole self-similar regime and quantify the total deviations by

$$\chi^2(\alpha, \beta) = \frac{1}{N_{\text{com}}} \sum_{k=1}^{N_{\text{com}}} \frac{\int d(\log(p)) (\Delta f(t_k, p)/f(t_{\text{ref}}, p))^2}{\int d(\log(p))}. \quad (\text{B.2})$$

We use integration over $d(\log(\bar{p}))$ to increase the sensitivity at low momenta. The upper limit of integration is given by the highest momentum included in the inverse particle cascade, see

e.g. knick point in Fig. 3.3. Since the momenta in a finite volume form a discrete set,¹ the integrals translate to sums over momenta $\int d(\log(p)) \rightarrow \sum_{i=1}^{n_k-1} \log(p_{i+1}/p_i)$, where $p_{i+1} > p_i$ are the discrete momenta of each $f(t_k, p)$, and n_k is the number of momenta in the scaling regime. To compute the difference $\Delta f(t_k, p_i)$, we linearly interpolate between momenta of the reference distribution to coincide with the discrete momenta of the rescaled distribution.

We define the best fit exponents $\bar{\alpha}$ and $\bar{\beta}$ as those that minimize the function $\chi^2(\alpha, \beta)$. To estimate the errors we further define, in analogy to Ref. [50], the likelihood function

$$W(\alpha, \beta) = \frac{1}{\mathcal{N}} \exp \left[-\frac{\chi^2(\alpha, \beta)}{2 \chi^2(\bar{\alpha}, \bar{\beta})} \right], \quad (\text{B.3})$$

where \mathcal{N} is a normalization constant such that $\int d\alpha d\beta W = 1$. Integrating $W(\alpha, \beta)$ over one of the exponents provides a marginal likelihood function for the other one, e.g. $W(\alpha) = \int d\beta W(\alpha, \beta)$. Approximating the marginal likelihood functions with Gaussian distributions, we obtain an estimate for the standard deviations σ_α and σ_β , while the means are still given by $\bar{\alpha}$ and $\bar{\beta}$. The final scaling exponents that we provide in the main text [Eqs. (3.14), (3.27), and (3.28)] are, thus, written in the form

$$\alpha = \bar{\alpha} \pm \sigma_\alpha, \quad \beta = \bar{\beta} \pm \sigma_\beta. \quad (\text{B.4})$$

With small adaptations, the same procedure was used to obtain the values of the exponents given in Chap. 4 from a finite size scaling analysis. To illustrate the modifications needed in this case we discuss it shortly for the scaling form (4.7). In this case, there are three variables that need to be rescaled, τ , Δt , and V , and hence three combinations of exponents that can be varied, namely $\alpha/\beta d$, $1/\beta d$, and z/d . Similarly to the distribution function, we consider in this case a reference volume V_{ref} and define for given exponents the rescaled function

$$F_{\text{resc}}(\tau, \Delta t, V) \equiv (V/V_{\text{ref}})^{-\alpha/(\beta d)} F \left((V/V_{\text{ref}})^{1/(\beta d)} \tau, (V/V_{\text{ref}})^{z/d} \Delta t, V \right). \quad (\text{B.5})$$

Deviations from a perfect self-similar evolution with (4.7) can be quantified by $\Delta F(\tau, \Delta t, V) \equiv F_{\text{resc}}(\tau, \Delta t, V) - F(\tau, \Delta t, V_{\text{ref}})$.

To estimate the values of the exponents and their errors, we need to define again a χ^2 -function. Because of the larger number of exponents though, we divide the analysis into two steps. First we set $\Delta t = 0$ and estimate $\alpha/\beta d$, $1/\beta d$. For this, we consider a set of volumes V_k , $k \in \{1, \dots, N_V\}$ and quantify the deviations by

$$\chi^2 \left(\frac{\alpha}{\beta d}, \frac{1}{\beta d} \right) \equiv \frac{1}{N_V} \sum_{k=1}^{N_V} \int \left(\frac{\Delta F(\tau, 0, V_k)}{F(\tau, 0, V_{\text{ref}})} \right)^2 \frac{d(\log(\tau))}{\int d(\log(\tau))}, \quad (\text{B.6})$$

where the integration limits are chosen within the self-similar regime (see Chap. 4) and $\tau > 0$. Again, the logarithmic integral enhances the sensitivity to small times τ , where the density of points is smaller. For this first fit scheme we considered the set of volumes $\{32^3, 64^3, 128^3, 256^3, 512^3\}$ and chose V_{ref} to be 128^3 . We checked that choosing a different V_{ref} within the scaling regime does not change the outcome significantly. Using this χ^2 -function

¹We note that our data is binned logarithmically in momentum space over nearly lying momenta.

and proceeding as explained above for the distribution function yields the exponents and errors given in Eqs. (4.13) and (4.14).

In a second step, we proceed similarly for $\Delta t \neq 0$. To apply the fit routine, we consider slices of constant V and τ as a function of Δt . The set of volumes we use is $\{128^3, 256^3, 512^3\}$ with $V_{\text{ref}} = 256^3$. Due to the rescaling of (B.5), the central times τ of the different volumes V have to fulfil

$$\frac{\tau}{\tau_{\text{ref}}} = \left(\frac{V}{V_{\text{ref}}} \right)^{1/(\beta d)}, \quad (\text{B.7})$$

where τ_{ref} corresponds to V_{ref} . It is important to note that both τ and τ_{ref} have to lie within the scaling regime. For V_{ref} we choose $\tau_{\text{ref}} \in [600, 2000]$. To solve for τ in (B.7) we use the exponent $1/(\beta d)$ that was determined by the first fit, see Eq. (4.14). Hence, only $\alpha/(\beta d)$ and z/d remain as fitting parameters. Using this we define again a χ^2 function to be minimized for fixed V , V_{ref} , τ and τ_{ref} by

$$\chi^2 \left(\frac{\alpha}{\beta d}, \frac{z}{d} \right) \equiv \int \left(\frac{\Delta F(\tau, \Delta t, V)}{F(\tau_{\text{ref}}, \Delta t, V_{\text{ref}})} \right)^2 \frac{d(\log(\Delta t))}{\int d(\log(\Delta t))}. \quad (\text{B.8})$$

The central values and statistical errors of the exponents $\alpha/(\beta d)$ and z/d are obtained from χ^2 in the same way as presented above. To obtain more accurate results, we have considered around 30 different τ_{ref} within the scaling regime and averaged the final result over all fits. As explained in the main text, we can only compare two different volumes with each other because of the condition (B.7) and the requirement that all times lie inside the scaling regime. Therefore, the results given in (4.15) and used in Fig. 4.3 correspond to the largest volumes 256^3 and 512^3 .

An important point concerns the error of the exponent $1/(\beta d)$ which propagates into the chosen values of τ by means of (B.7). To quantify this additional source of error, we first use (B.7) to define the times τ^\pm lying at the edges of the error interval by

$$\frac{\tau^\pm}{\tau_{\text{ref}}} = \left(\frac{V}{V_{\text{ref}}} \right)^{\frac{1}{\beta d} \pm \Delta \left(\frac{1}{\beta d} \right)}, \quad (\text{B.9})$$

where $\Delta(1/\beta d)$ denotes the error of the exponent $1/(\beta d)$. Repeating the fit routine with the values τ^\pm yields slightly different central values for the exponents $\alpha/(\beta d)$ and z/d . We interpret the deviation from our main result, calculated with τ from (B.7), as the error propagated from $\Delta(1/\beta d)$. Adding this extra error quadratically to the statistical error obtained before from the width of the χ^2 -distribution, we obtain the final result given by (4.15) and $\alpha/(\beta d) = 1.0 \pm 0.07$, which is consistent with (4.13).

The application of the fit routine to the scaling forms (4.8), and (4.9) follows along the same lines. The main difference comes from defining a different rescaled function. For (4.8) we use

$$F_{\text{resc}}(\tau, \Delta t, V) \equiv (\tau/\tau_{\text{ref}})^{-\alpha} F(\tau, (\tau/\tau_{\text{ref}})^{\beta z} \Delta t, (\tau/\tau_{\text{ref}})^{\beta d} V). \quad (\text{B.10})$$

The χ^2 -function can be defined similarly to (B.8). Volumes and central times have to be chosen again such that (B.7) is fulfilled. We choose $V_{\text{ref}} = 256^3$ with $\tau_{\text{ref}} \in [600, 2000]$ and compare to $V = 512^3$ with τ from (B.7), as a function of Δt . Proceeding as before yields the fit results (4.16) and (4.17) where the error in τ coming from (B.9) was taken into account as

above. In an analogous way, one can check the consistency of our results by making use of the scaling relation (4.9).

Appendix C

BBGKY Equations

This appendix is based on “Nonequilibrium dynamics of spin-boson models from phase space methods”, A. Piñeiro Orioli, A. Safavi-Naini, M. L. Wall, A. M. Rey, published in Phys. Rev. A **96**, 033607 (2017) [198]. Parts of the text are taken from that reference.

In the following we list the BBGKY equations of motion used in Chap. 7, which can be obtained as explained in Section 7.3.2. The equations for the one-point functions are given by

$$\begin{aligned}
 \dot{A}_\mu &= \frac{i}{2} e^{-i\delta_\mu t} \sum_i \Omega_{i\mu} S_i^z, \\
 \dot{S}_i^x &= 2 \sum_\mu \Omega_{i\mu} \operatorname{Re} \left[(\mathcal{M}_{i\mu}^y + S_i^y A_\mu) e^{i\delta_\mu t} \right], \\
 \dot{S}_i^y &= -2 \sum_\mu \Omega_{i\mu} \operatorname{Re} \left[(\mathcal{M}_{i\mu}^x + S_i^x A_\mu) e^{i\delta_\mu t} \right],
 \end{aligned} \tag{C.1}$$

where $\dot{S}_i^z = 0$. Note that setting $\mathcal{M} \rightarrow 0$ one recovers the classical equations of motion (7.15). Keeping the mixed spin-boson connected Weyl symbols $\mathcal{M} \neq 0$ one needs to supplement these equations by

$$\begin{aligned}
 \dot{\mathcal{M}}_{i\mu}^x &= \sum_\nu \Omega_{i\nu} \left\{ 2 \mathcal{M}_{i\mu}^y \operatorname{Re} \left(A_\nu e^{i\delta_\nu t} \right) + S_i^y \left(\mathcal{A}_{\nu\mu}^{00} e^{i\delta_\nu t} + \mathcal{A}_{\nu\mu}^{10} e^{-i\delta_\nu t} \right) \right\} \\
 &\quad + \frac{i}{2} e^{-i\delta_\mu t} \left\{ \sum_{k \neq i} \Omega_{k\mu} \mathcal{S}_{ik}^{xz} - \Omega_{i\mu} S_i^z S_i^x \right\}, \\
 \dot{\mathcal{M}}_{i\mu}^y &= - \sum_\nu \Omega_{i\nu} \left\{ 2 \mathcal{M}_{i\mu}^x \operatorname{Re} \left(A_\nu e^{i\delta_\nu t} \right) + S_i^x \left(\mathcal{A}_{\nu\mu}^{00} e^{i\delta_\nu t} + \mathcal{A}_{\nu\mu}^{10} e^{-i\delta_\nu t} \right) \right\} \\
 &\quad + \frac{i}{2} e^{-i\delta_\mu t} \left\{ \sum_{k \neq i} \Omega_{k\mu} \mathcal{S}_{ik}^{yz} - \Omega_{i\mu} S_i^z S_i^y \right\}, \\
 \dot{\mathcal{M}}_{i\mu}^z &= \frac{i}{2} e^{-i\delta_\mu t} \Omega_{i\mu} (1 - S_i^z S_i^z),
 \end{aligned} \tag{C.2}$$

where we neglected three-point Weyl symbols of the form $\mathcal{M}_{i\mu\nu}^\alpha$. These equations couple as well to the two-point Weyl symbols $\mathcal{A}_{\mu\nu}$ and $\mathcal{S}_{ij}^{\alpha\beta}$. Their evolution is given by

$$\begin{aligned}\dot{\mathcal{A}}_{\mu\nu}^{00} &= \frac{i}{2} \sum_j \left[\Omega_{j\mu} \mathcal{M}_{j\nu}^z e^{-i\delta_\mu t} + (\mu \leftrightarrow \nu) \right], \\ \dot{\mathcal{A}}_{\mu\nu}^{10} &= -\frac{i}{2} \sum_j \left[\Omega_{j\mu} \mathcal{M}_{j\nu}^z e^{i\delta_\mu t} - (\mu \leftrightarrow \nu, \text{c.c.}) \right],\end{aligned}\tag{C.3}$$

and

$$\begin{aligned}\dot{\mathcal{S}}_{ij}^{xx} &= 2 \sum_\mu \left\{ \Omega_{i\mu} \text{Re} \left[\left(\mathcal{M}_{ij\mu}^{yx} + \mathcal{S}_{ij}^{yx} A_\mu + \mathcal{M}_{j\mu}^x S_i^y \right) e^{i\delta_\mu t} \right] + (i \leftrightarrow j) \right\}, \\ \dot{\mathcal{S}}_{ij}^{xy} &= 2 \sum_\mu \left\{ \Omega_{i\mu} \text{Re} \left[\left(\mathcal{M}_{ij\mu}^{yy} + \mathcal{S}_{ij}^{yy} A_\mu + \mathcal{M}_{j\mu}^y S_i^y \right) e^{i\delta_\mu t} \right] - (i \leftrightarrow j, x \leftrightarrow y) \right\}, \\ \dot{\mathcal{S}}_{ij}^{xz} &= 2 \sum_\mu \Omega_{i\mu} \text{Re} \left[\left(\mathcal{M}_{ij\mu}^{yz} + \mathcal{S}_{ij}^{yz} A_\mu + \mathcal{M}_{j\mu}^z S_i^y \right) e^{i\delta_\mu t} \right], \\ \dot{\mathcal{S}}_{ij}^{yy} &= -2 \sum_\mu \left\{ \Omega_{i\mu} \text{Re} \left[\left(\mathcal{M}_{ij\mu}^{xy} + \mathcal{S}_{ij}^{xy} A_\mu + \mathcal{M}_{j\mu}^y S_i^x \right) e^{i\delta_\mu t} \right] + (i \leftrightarrow j) \right\}, \\ \dot{\mathcal{S}}_{ij}^{yz} &= -2 \sum_\mu \Omega_{i\mu} \text{Re} \left[\left(\mathcal{M}_{ij\mu}^{xz} + \mathcal{S}_{ij}^{xz} A_\mu + \mathcal{M}_{j\mu}^z S_i^x \right) e^{i\delta_\mu t} \right].\end{aligned}\tag{C.4}$$

where $\dot{\mathcal{S}}_{ij}^{zz} = 0$, ‘‘c.c.’’ stands for complex conjugate and expressions like $(i \leftrightarrow j)$ are shorthand notation for the whole expression appearing on its left, within the same level of parenthesis, after applying the indicated substitution. The latter equations couple to the spin-spin-boson Weyl symbols $\mathcal{M}_{ij\mu}^{\alpha\beta}$, which one may approximately neglect to close the hierarchy. However, for the particular problem considered in this work we found these variables to be relevant in the dynamics of correlators such as $\langle \hat{\sigma}_i^\alpha \hat{\sigma}_j^\beta \rangle$. Therefore, we take into account the evolution equations of these spin-spin-boson variables, which are given by

$$\begin{aligned}\dot{\mathcal{M}}_{ij\mu}^{xx} &= 2 \sum_\nu \left\{ \Omega_{i\nu} \left[\mathcal{M}_{ij\mu}^{yx} \text{Re} \left(A_\nu e^{i\delta_\nu t} \right) + \mathcal{M}_{i\mu}^y \text{Re} \left(\mathcal{M}_{j\nu}^x e^{i\delta_\nu t} \right) \right] + (i \leftrightarrow j) \right\} \\ &\quad + \sum_\nu \left\{ \Omega_{i\nu} \mathcal{S}_{ij}^{yx} \left(\mathcal{A}_{\mu\nu}^{00} e^{i\delta_\nu t} + \mathcal{A}_{\mu\nu}^{01} e^{-i\delta_\nu t} \right) + (i \leftrightarrow j) \right\} \\ &\quad - \frac{i}{2} e^{-i\delta_\mu t} \left\{ \mathcal{S}_{ij}^{xx} \left(\Omega_{i\mu} S_i^z + \Omega_{j\mu} S_j^z \right) + \left(\Omega_{j\mu} \mathcal{S}_{ij}^{xz} S_j^x + (i \leftrightarrow j) \right) \right\}, \\ \dot{\mathcal{M}}_{ij\mu}^{xy} &= 2 \sum_\nu \left\{ \Omega_{i\nu} \left[\mathcal{M}_{ij\mu}^{yy} \text{Re} \left(A_\nu e^{i\delta_\nu t} \right) + \mathcal{M}_{i\mu}^y \text{Re} \left(\mathcal{M}_{j\nu}^y e^{i\delta_\nu t} \right) \right] - (i \leftrightarrow j, x \leftrightarrow y) \right\} \\ &\quad + \sum_\nu \left\{ \Omega_{i\nu} \mathcal{S}_{ij}^{yy} \left(\mathcal{A}_{\mu\nu}^{00} e^{i\delta_\nu t} + \mathcal{A}_{\mu\nu}^{01} e^{-i\delta_\nu t} \right) - (i \leftrightarrow j, x \leftrightarrow y) \right\} \\ &\quad - \frac{i}{2} e^{-i\delta_\mu t} \left\{ \mathcal{S}_{ij}^{xy} \left(\Omega_{i\mu} S_i^z + \Omega_{j\mu} S_j^z \right) + \left(\Omega_{j\mu} \mathcal{S}_{ij}^{xz} S_j^y + (i \leftrightarrow j, x \leftrightarrow y) \right) \right\}, \\ \dot{\mathcal{M}}_{ij\mu}^{xz} &= 2 \sum_\nu \Omega_{i\nu} \left[\mathcal{M}_{ij\mu}^{yz} \text{Re} \left(A_\nu e^{i\delta_\nu t} \right) + \mathcal{M}_{i\mu}^y \text{Re} \left(\mathcal{M}_{j\nu}^z e^{i\delta_\nu t} \right) \right] \\ &\quad + \sum_\nu \Omega_{i\nu} \mathcal{S}_{ij}^{yz} \left(\mathcal{A}_{\mu\nu}^{00} e^{i\delta_\nu t} + \mathcal{A}_{\mu\nu}^{01} e^{-i\delta_\nu t} \right) \\ &\quad - \frac{i}{2} e^{-i\delta_\mu t} \left\{ \mathcal{S}_{ij}^{xz} \left(\Omega_{i\mu} S_i^z + \Omega_{j\mu} S_j^z \right) + \Omega_{j\mu} \mathcal{S}_{ij}^{xz} S_j^z \right\},\end{aligned}\tag{C.5}$$

$$\begin{aligned}
\dot{\mathcal{M}}_{ij\mu}^{yy} &= -2 \sum_{\nu} \left\{ \Omega_{i\nu} \left[\mathcal{M}_{ij\mu}^{xy} \operatorname{Re} \left(A_{\nu} e^{i\delta_{\nu}t} \right) + \mathcal{M}_{i\mu}^x \operatorname{Re} \left(\mathcal{M}_{j\nu}^y e^{i\delta_{\nu}t} \right) \right] + (i \leftrightarrow j) \right\} \\
&\quad - \sum_{\nu} \left\{ \Omega_{i\nu} \mathcal{S}_{ij}^{xy} \left(\mathcal{A}_{\mu\nu}^{00} e^{i\delta_{\nu}t} + \mathcal{A}_{\mu\nu}^{01} e^{-i\delta_{\nu}t} \right) + (i \leftrightarrow j) \right\} \\
&\quad - \frac{i}{2} e^{-i\delta_{\mu}t} \left\{ \mathcal{S}_{ij}^{yy} \left(\Omega_{i\mu} S_i^z + \Omega_{j\mu} S_j^z \right) + \left(\Omega_{j\mu} \mathcal{S}_{ij}^{yz} S_j^y + (i \leftrightarrow j) \right) \right\}, \\
\dot{\mathcal{M}}_{ij\mu}^{yz} &= -2 \sum_{\nu} \Omega_{i\nu} \left[\mathcal{M}_{ij\mu}^{xz} \operatorname{Re} \left(A_{\nu} e^{i\delta_{\nu}t} \right) + \mathcal{M}_{i\mu}^x \operatorname{Re} \left(\mathcal{M}_{j\nu}^z e^{i\delta_{\nu}t} \right) \right] \\
&\quad - \sum_{\nu} \Omega_{i\nu} \mathcal{S}_{ij}^{xz} \left(\mathcal{A}_{\mu\nu}^{00} e^{i\delta_{\nu}t} + \mathcal{A}_{\mu\nu}^{01} e^{-i\delta_{\nu}t} \right) \\
&\quad - \frac{i}{2} e^{-i\delta_{\mu}t} \left\{ \mathcal{S}_{ij}^{yz} \left(\Omega_{i\mu} S_i^z + \Omega_{j\mu} S_j^z \right) + \Omega_{j\mu} \mathcal{S}_{ij}^{yz} S_j^z \right\}.
\end{aligned}$$

Here, $\dot{\mathcal{M}}_{ij\mu}^{zz} = 0$ and we neglected higher order terms in order to close the hierarchy.

This set of equations becomes less involved when the spins start in the state $|\rightarrow\rangle^{\otimes N}$. In this case, $S_i^z(t) = \pm 1$ and it follows from Eq. (C.2) that $\mathcal{M}_{i\mu}^z \equiv 0$. This in turn implies together with Eq. (C.3) that $\mathcal{A}_{\mu\nu} \equiv 0$. Using this in Eqs. (C.4) and (C.5) we further obtain that $\mathcal{S}_{ij}^{xz} \equiv 0$, $\mathcal{S}_{ij}^{yz} \equiv 0$, $\mathcal{M}_{ij\mu}^{xz} \equiv 0$ and $\mathcal{M}_{ij\mu}^{yz} \equiv 0$. With these simplifications one is left with a reduced number of equations and variables which take computationally less effort to solve. We made use of this in the results presented in Sections 7.4.1 and 7.4.2.

The system of equations can be further reduced if one is only interested in computing one-point functions $\langle \hat{\sigma}_i^{\alpha} \rangle$ or spin-boson correlators $\langle \hat{a}_{\mu} \hat{\sigma}_i^{\alpha} \rangle$. In such a case one may use the fact that Eqs. (C.1) and (C.2) constitute for the initial condition $|\rightarrow\rangle^{\otimes N}$ a closed set of equations and thus neglect all other equations. The results presented in Section 7.4.4 were computed using this reduced set of equations.

Despite all these simplifications, we emphasize that for general initial conditions, such as those considered in Section 7.4.3, the full set of equations has to be solved, at this order of approximation.

Appendix D

Discrete sampling

This appendix is based on “Nonequilibrium dynamics of spin-boson models from phase space methods”, A. Piñeiro Orioli, A. Safavi-Naini, M. L. Wall, A. M. Rey, published in Phys. Rev. A **96**, 033607 (2017) [198]. Parts of the text are taken from that reference.

In this appendix we fill some details about the discrete sampling scheme used for the application of TWA to spins in Chaps. 6 and 7. In particular, we discuss how to sample rotated spin initial conditions, i.e. initial states that are not aligned along x , y or z . To simplify the discussion we consider a system composed of just a single spin-1/2, $\hat{\boldsymbol{\sigma}} = (\hat{\sigma}^x, \hat{\sigma}^y, \hat{\sigma}^z)^T$. The following procedure is nevertheless also applicable to systems of many spins starting in a product state.

We start by recalling the sampling used for a spin initially in the state $|\uparrow\rangle$, namely:

$$W_{|\uparrow\rangle}(\mathbf{S}_0) = \frac{1}{4} \delta(S_0^z - 1) \sum_{x,y=\pm 1} \delta(S_0^x - x) \delta(S_0^y - y). \quad (\text{D.1})$$

This sampling can be shown to fulfil

$$\begin{aligned} \langle (\hat{\sigma}^\alpha)^n \rangle &= \int d\mathbf{S}_0 W(\mathbf{S}_0) (S^\alpha)^n, \\ \langle \{(\hat{\sigma}^\alpha)^m, (\hat{\sigma}^\beta)^n\}_S \rangle &= \int d\mathbf{S}_0 W(\mathbf{S}_0) (S^\alpha)^m (S^\beta)^n, \\ \langle \{(\hat{\sigma}^x)^m, (\hat{\sigma}^y)^n, (\hat{\sigma}^z)^l\}_S \rangle &= \int d\mathbf{S}_0 W(\mathbf{S}_0) (S^x)^m (S^y)^n (S^z)^l, \end{aligned} \quad (\text{D.2})$$

where $d\mathbf{S}_0 \equiv dS_0^x dS_0^y dS_0^z$ and we defined the symmetric product of two and three operators as

$$\{A, B\}_S \equiv \frac{1}{2} (AB + BA), \quad (\text{D.3})$$

$$\{A, B, C\}_S \equiv \frac{1}{6} (ABC + ACB + BAC + BCA + CAB + CBA). \quad (\text{D.4})$$

Importantly, Eq. (D.2) shows that the discrete sampling used captures the values of the expectation values of the spin (after appropriate symmetrization) to arbitrary order. This is a remarkable improvement as compared to other (continuous) sampling techniques based on gaussian approximations [100, 103].

Using this we will show in the following that rotated initial states of the form

$$|\uparrow_R\rangle \equiv e^{-i\phi/2} \cos(\theta/2) |\uparrow\rangle + e^{i\phi/2} \sin(\theta/2) |\downarrow\rangle \quad (\text{D.5})$$

can be sampled using the Wigner function

$$W_{|\uparrow_R\rangle}(\mathbf{S}_0) = \frac{1}{4} \delta(S_{R,0}^z - 1) \sum_{x,y=\pm 1} \delta(S_{R,0}^x - x) \delta(S_{R,0}^y - y). \quad (\text{D.6})$$

Here, the subscript ‘ R ’ denotes the rotated spin variables $\mathbf{S} = R^T \mathbf{S}_R$ and R is a rotation matrix given by

$$R = \begin{pmatrix} \cos(\phi) \cos(\theta) & \sin(\phi) \cos(\theta) & -\sin(\theta) \\ -\sin(\phi) & \cos(\phi) & 0 \\ \cos(\phi) \sin(\theta) & \sin(\phi) \sin(\theta) & \cos(\theta) \end{pmatrix} \quad (\text{D.7})$$

with $R^T R = \mathbf{1}$.

To show the accuracy of the sampling (D.6) the strategy consists in rotating the whole system to make the initial state lie along the z -direction, sample the initial conditions in the rotated basis and then rotate back. We write the initial state as

$$|\uparrow_R\rangle \equiv \hat{U}_R(\phi, \theta) |\uparrow\rangle, \quad (\text{D.8})$$

where we defined the rotation operator $\hat{U}_R(\phi, \theta) = e^{-i(\phi/2)\hat{\sigma}_z} e^{-i(\theta/2)\hat{\sigma}_y}$. Using this we define the rotated spin operators $\hat{\sigma}_R^\mu \equiv \hat{U}_R \hat{\sigma}^\mu \hat{U}_R^\dagger$, which can also be written as $\hat{\sigma}_R = R \hat{\sigma}$.

We define rotated classical spin variables $\mathbf{S}_R = R \mathbf{S} = (x_R, y_R, z_R)^T$, which are the Weyl symbols of the rotated spin matrices, $(\hat{\sigma}_R^\alpha)_W = S_R^\alpha$. In the rotated basis, the spin points in the (rotated) z -direction. Therefore, if we sample the rotated spins according to (D.6), i.e. $x_{R,0} = \pm 1$, $y_{R,0} = \pm 1$, $z_{R,0} = 1$, then (D.2) will be fulfilled for $\hat{\sigma} \rightarrow \hat{\sigma}_R$ and $S \rightarrow S_R$. This justifies the sampling given in (D.6).

The equations of motion for the rotated spin \mathbf{S}_R can be obtained from the Heisenberg equations for $\hat{\sigma}_R$ after all products of operators have been symmetrized and simplified as explained in the main text. For the spin-1/2 case considered here, they can be obtained as well by rotating the equations for \mathbf{S} as

$$\dot{\mathbf{S}}_R = R \dot{\mathbf{S}}(R^T \mathbf{S}_R). \quad (\text{D.9})$$

Again, it is essential that in deriving the equations for \mathbf{S} all products of spin matrices have been symmetrized and simplified as, e.g., $(\hat{\sigma}^x)^3 = \hat{\sigma}^x$.

Given (D.6) and (D.9) one could in principle work in the rotated basis. However, it is usually convenient to reexpress everything in terms of the original basis. To this end, one can use Eq. (D.6) to initialize the rotated spins and then rotate back to the original basis. Rotating back (D.9) one can then evolve the spins using the original equations for \mathbf{S} . In order to compute expectation values of the original spin matrices, one needs to first express the observable in terms of the rotated spin operators. Then all products have to be symmetrized and simplified. After that one substitutes $\hat{\sigma}_R^\alpha \rightarrow S_R^\alpha = \sum_\lambda R_{\alpha\lambda} S^\lambda$ and the resulting function of classical spin variables is the one to be averaged. The expectation value of, for instance, $\hat{\sigma}$, would thus be

given by

$$\langle \hat{\boldsymbol{\sigma}} \rangle = R^T \langle \hat{\boldsymbol{\sigma}}_R \rangle \approx R^T \langle \mathbf{S}_R \rangle_{\text{cl}} = \langle \mathbf{S} \rangle_{\text{cl}}. \quad (\text{D.10})$$

Here $\langle \cdot \rangle_{\text{cl}}$ has to be understood as an average by sampling the rotated spins as mentioned above.

Based on the previous equality one could in principle skip the back and forth rotation and directly associate $\sigma^\alpha \leftrightarrow S^\alpha$. However, this procedure works generally only when computing observables that have been symmetrized and reduced to their simplest form. For example, if one chooses to compute $\langle (\hat{\sigma}^x)^3 \rangle$ as $\langle (S^x)^3 \rangle_{\text{cl}}$ instead of using $(\hat{\sigma}^x)^3 = \hat{\sigma}^x$ to compute it as $\langle S^x \rangle_{\text{cl}}$ one may not obtain the correct result. The reason for this is that in general

$$\begin{aligned} \langle (\hat{\sigma}^\lambda)^3 \rangle &= \sum_{\alpha, \beta, \gamma} R_{\lambda\alpha}^T R_{\lambda\beta}^T R_{\lambda\gamma}^T \langle \hat{\sigma}_R^\alpha \hat{\sigma}_R^\beta \hat{\sigma}_R^\gamma \rangle \\ &\stackrel{i.g.}{\neq} \sum_{\alpha, \beta, \gamma} R_{\lambda\alpha}^T R_{\lambda\beta}^T R_{\lambda\gamma}^T \langle S_R^\alpha S_R^\beta S_R^\gamma \rangle_{\text{cl}} = \langle (S^\lambda)^3 \rangle_{\text{cl}}, \end{aligned} \quad (\text{D.11})$$

unless the product $\hat{\sigma}_R^\alpha \hat{\sigma}_R^\beta \hat{\sigma}_R^\gamma$ happens to be automatically symmetrized. In other words, given a symmetrically ordered operator $f(\hat{\boldsymbol{\sigma}})$, we have that $(f(\hat{\boldsymbol{\sigma}}_R))_W = f(\mathbf{S}_R)$, but in general $(f(\hat{\boldsymbol{\sigma}}))_W = (f(R^T \hat{\boldsymbol{\sigma}}_R))_W \neq f(R^T \mathbf{S}_R) = f(\mathbf{S})$, since $f(R^T \hat{\boldsymbol{\sigma}}_R)$ is not necessarily symmetric.

Bibliography

- [1] R. Pathria and P. Beale, *Statistical Mechanics (Third Edition)*, third edition ed. (Academic Press, Boston, 2011).
- [2] J. M. Deutsch, *Phys. Rev. A* **43**, 2046 (1991).
- [3] M. Rigol, V. Dunjko, and M. Olshanii, *Nature* **452**, 854 (2008).
- [4] M. Srednicki, *Phys. Rev. E* **50**, 888 (1994).
- [5] J. Berges and J. Cox, *Physics Letters B* **517**, 369 (2001).
- [6] A. Polkovnikov, K. Sengupta, A. Silva, and M. Vengalattore, *Rev. Mod. Phys.* **83**, 863 (2011).
- [7] J. Eisert, M. Friesdorf, and C. Gogolin, *Nature Phys.* **11**, 124 (2015).
- [8] E. T. Jaynes, *Phys. Rev.* **106**, 620 (1957).
- [9] M. Rigol, V. Dunjko, V. Yurovsky, and M. Olshanii, *Phys. Rev. Lett.* **98**, 050405 (2007).
- [10] T. Kinoshita, T. Wenger, and D. S. Weiss, *Nature* **440**, 900 (2006).
- [11] R. Nandkishore and D. A. Huse, *Annual Review of Condensed Matter Physics* **6**, 15 (2015).
- [12] J. Berges, K. Boguslavski, S. Schlichting, and R. Venugopalan, *Phys. Rev. Lett.* **114**, 061601 (2015).
- [13] M. H. Anderson, J. R. Ensher, M. R. Matthews, C. E. Wieman, and E. A. Cornell, *Science* **269**, 198 (1995).
- [14] K. B. Davis, M. O. Mewes, M. R. Andrews, N. J. van Druten, D. S. Durfee, D. M. Kurn, and W. Ketterle, *Phys. Rev. Lett.* **75**, 3969 (1995).
- [15] C. C. Bradley, C. A. Sackett, J. J. Tollett, and R. G. Hulet, *Phys. Rev. Lett.* **75**, 1687 (1995).
- [16] A. Celi, A. Sanpera, V. Ahufinger, and M. Lewenstein, *Physica Scripta* **92**, 013003 (2017).
- [17] D. Bouwmeester, A. Ekert, and A. Zeilinger, *The Physics of Quantum Information: Quantum Cryptography, Quantum Teleportation, Quantum Computation*, Physics and astronomy online library (Springer Berlin Heidelberg, 2000).

- [18] P. Zoller, T. Beth, D. Binosi, R. Blatt, H. Briegel, D. Bruss, T. Calarco, J. I. Cirac, D. Deutsch, J. Eisert, A. Ekert, C. Fabre, N. Gisin, P. Grangiere, M. Grassl, S. Haroche, A. Imamoglu, A. Karlson, J. Kempe, L. Kouwenhoven, S. Kröll, G. Leuchs, M. Lewenstein, D. Loss, N. Lütkenhaus, S. Massar, J. E. Mooij, M. B. Plenio, E. Polzik, S. Popescu, G. Rempe, A. Sergienko, D. Suter, J. Twamley, G. Wendin, R. Werner, A. Winter, J. Wrachtrup, and A. Zeilinger, *The European Physical Journal D - Atomic, Molecular, Optical and Plasma Physics* **36**, 203 (2005).
- [19] M. Lewenstein, A. Sanpera, and V. Ahufinger, *Ultracold Atoms in Optical Lattices: Simulating quantum many-body systems* (OUP Oxford, 2012).
- [20] I. Bloch, J. Dalibard, and W. Zwerger, *Rev. Mod. Phys.* **80**, 885 (2008).
- [21] S. Giorgini, L. P. Pitaevskii, and S. Stringari, *Rev. Mod. Phys.* **80**, 1215 (2008).
- [22] R. P. Feynman, *International Journal of Theoretical Physics* **21**, 467 (1982).
- [23] S. Lloyd, *Science* **273**, 1073 (1996).
- [24] Y. Aoki, G. Endrodi, Z. Fodor, S. D. Katz, and K. K. Szabo, *Nature* **443**, 675 (2006).
- [25] S. Borsányi, Z. Fodor, C. Hoelbling, S. D. Katz, S. Krieg, C. Ratti, and K. K. Szabó, *Journal of High Energy Physics* **2010**, 73 (2010).
- [26] J. Adams *et al.* (STAR), *Nucl. Phys.* **A757**, 102 (2005).
- [27] K. Aamodt *et al.* (ALICE), *Phys. Rev. Lett.* **105**, 252302 (2010), 1011.3914 .
- [28] S. Chatrchyan *et al.* (CMS), *Phys. Lett.* **B724**, 213 (2013), 1305.0609 .
- [29] J. Berges, J.-P. Blaizot, and F. Gelis, *Journal of Physics G: Nuclear and Particle Physics* **39**, 085115 (2012).
- [30] A. H. Guth, *Phys. Rev. D* **23**, 347 (1981).
- [31] A. Linde, *Physics Letters B* **108**, 389 (1982).
- [32] A. A. Penzias and R. W. Wilson, *The Astrophysical Journal* **142**, 419 (1965).
- [33] B. Ryden, *Introduction to Cosmology* (Cambridge University Press, 2016).
- [34] A. D. Linde, *Contemp. Concepts Phys.* **5**, 1 (1990).
- [35] K. G. Wilson, *Phys. Rev. B* **4**, 3174 (1971).
- [36] K. G. Wilson, *Phys. Rev. B* **4**, 3184 (1971).
- [37] J. Cardy, *Scaling and Renormalization in Statistical Physics*, Cambridge Lecture Notes in Physics (Cambridge University Press, 1996).
- [38] J. Zinn-Justin, *Quantum Field Theory and Critical Phenomena*, International series of monographs on physics (Clarendon Press, 2002).
- [39] R. Micha and I. I. Tkachev, *Phys. Rev. Lett.* **90**, 121301 (2003).
- [40] R. Micha and I. I. Tkachev, *Phys. Rev. D* **70**, 043538 (2004).

- [41] J. Berges, A. Rothkopf, and J. Schmidt, *Phys.Rev.Lett.* **101**, 041603 (2008).
- [42] J. Berges, S. Scheffler, and D. Sexty, *Phys. Lett. B* **681**, 362 (2009).
- [43] J. Berges and D. Sexty, *Phys. Rev. D* **83**, 085004 (2011).
- [44] J. Berges, D. Gelfand, and J. Pruschke, *Phys. Rev. Lett.* **107**, 061301 (2011).
- [45] T. Gasenzer, B. Nowak, and D. Sexty, *Phys. Lett. B* **710**, 500 (2012).
- [46] S. Schlichting, *Phys. Rev. D* **86**, 065008 (2012).
- [47] A. Kurkela and G. D. Moore, *Phys. Rev. D* **86**, 056008 (2012).
- [48] J. Berges, K. Boguslavski, S. Schlichting, and R. Venugopalan, *Phys. Rev. D* **89**, 074011 (2014).
- [49] T. Gasenzer, L. McLerran, J. M. Pawlowski, and D. Sexty, *Nucl. Phys. A* (2014).
- [50] J. Berges, K. Boguslavski, S. Schlichting, and R. Venugopalan, *Phys. Rev. D* **89**, 114007 (2014).
- [51] J. Berges, K. Boguslavski, S. Schlichting, and R. Venugopalan, *JHEP* **1405**, 054 (2014).
- [52] J. Berges, D. Gelfand, and D. Sexty, *Phys. Rev. D* **89**, 025001 (2014).
- [53] M. C. A. York, A. Kurkela, E. Lu, and G. D. Moore, *Phys. Rev. D* **89**, 074036 (2014).
- [54] A. Kurkela and E. Lu, *Phys. Rev. Lett.* **113**, 182301 (2014).
- [55] B. Nowak, D. Sexty, and T. Gasenzer, *Phys. Rev. B* **84**, 020506 (2011).
- [56] B. Nowak, J. Schole, D. Sexty, and T. Gasenzer, *Phys. Rev. A* **85**, 043627 (2012).
- [57] J. Berges and D. Sexty, *Phys. Rev. Lett.* **108**, 161601 (2012).
- [58] J. Schole, B. Nowak, and T. Gasenzer, *Phys. Rev. A* **86**, 013624 (2012).
- [59] B. Nowak, J. Schole, and T. Gasenzer, *New Journal of Physics* **16**, 093052 (2014).
- [60] M. Karl, B. Nowak, and T. Gasenzer, *Phys. Rev. A* **88**, 063615 (2013).
- [61] J. Berges and J. Jaeckel, *Phys. Rev. D* **91**, 025020 (2015).
- [62] C. Ewerz, T. Gasenzer, M. Karl, and A. Samberg, *Journal of High Energy Physics* **2015**, 70 (2015).
- [63] S. Mathey, T. Gasenzer, and J. M. Pawlowski, *Phys. Rev. A* **92**, 023635 (2015).
- [64] M. Karl and T. Gasenzer, *New Journal of Physics* **19**, 093014 (2017).
- [65] J. Berges and B. Wallisch, *Phys. Rev. D* **95**, 036016 (2017).
- [66] A. Piñeiro Orioli, K. Boguslavski, and J. Berges, *Phys. Rev. D* **92**, 025041 (2015).
- [67] G. D. Moore, *Phys. Rev. D* **93**, 065043 (2016).
- [68] J. Berges and G. Hoffmeister, *Nucl. Phys. B* **813**, 383 (2009).

- [69] C. Scheppach, J. Berges, and T. Gasenzer, *Phys. Rev. A* **81**, 033611 (2010).
- [70] J. Berges, (2015), [arXiv:1503.02907](https://arxiv.org/abs/1503.02907) [hep-ph] .
- [71] T. V. Zache, V. Kasper, and J. Berges, *Phys. Rev. A* **95**, 063629 (2017).
- [72] M. J. Davis, T. M. Wright, T. Gasenzer, S. A. Gardiner, and N. P. Proukakis, “Formation of bose-einstein condensates,” in *Universal Themes of Bose-Einstein Condensation*, edited by N. P. Proukakis, D. W. Snoke, and P. B. Littlewood (Cambridge University Press, 2017) p. 117150.
- [73] J. Schmiedmayer and J. Berges, *Science* **341**, 1188 (2013).
- [74] P. B. Greene, L. Kofman, A. D. Linde, and A. A. Starobinsky, *Phys. Rev. D* **56**, 6175 (1997).
- [75] F. Gelis, E. Iancu, J. Jalilian-Marian, and R. Venugopalan, *Ann. Rev. Nucl. Part. Sci.* **60**, 463 (2010).
- [76] V. E. Zakharov, V. S. L’vov, and G. Falkovich, *Kolmogorov Spectra of Turbulence I: Wave Turbulence* (Springer-Verlag, Berlin, 1992).
- [77] S. Nazarenko, *Wave Turbulence* (Springer-Verlag, 2011).
- [78] A. Bray, *Advances in Physics* **43**, 357 (1994).
- [79] D. Boyanovsky, C. Destri, and H. J. de Vega, *Phys. Rev. D* **69**, 045003 (2004).
- [80] G. D. Moore, *Journal of High Energy Physics* **2001**, 021 (2001).
- [81] A. Auerbach, *Interacting Electrons and Quantum Magnetism*, Graduate Texts in Contemporary Physics (Springer New York, 1998).
- [82] B. Yan, S. A. Moses, B. Gadway, J. P. Covey, K. R. A. Hazzard, A. M. Rey, D. S. Jin, and J. Ye, *Nature* **501**, 521 (2013).
- [83] K. R. A. Hazzard, S. R. Manmana, M. Foss-Feig, and A. M. Rey, *Phys. Rev. Lett.* **110**, 075301 (2013).
- [84] K. R. A. Hazzard, B. Gadway, M. Foss-Feig, B. Yan, S. A. Moses, J. P. Covey, N. Y. Yao, M. D. Lukin, J. Ye, D. S. Jin, and A. M. Rey, *Phys. Rev. Lett.* **113**, 195302 (2014).
- [85] K. Kim, M.-S. Chang, R. Islam, S. Korenblit, L.-M. Duan, and C. Monroe, *Phys. Rev. Lett.* **103**, 120502 (2009).
- [86] P. Richerme, Z.-X. Gong, A. Lee, C. Senko, J. Smith, M. Foss-Feig, S. Michalakis, A. V. Gorshkov, and C. Monroe, *Nature* **511**, 198 (2014).
- [87] J. W. Britton, B. C. Sawyer, A. C. Keith, C. C. J. Wang, J. K. Freericks, H. Uys, M. J. Biercuk, and J. J. Bollinger, *Nature* **484**, 489 (2012).
- [88] J. G. Bohnet, B. C. Sawyer, J. W. Britton, M. L. Wall, A. M. Rey, M. Foss-Feig, and J. J. Bollinger, *Science* **352**, 1297 (2016).
- [89] R. Blatt and C. F. Roos, *Nature Phys.* **8**, 277 (2012).

- [90] A. Piñeiro Orioli, A. Signoles, H. Wildhagen, G. Günter, J. Berges, S. Whitlock, and M. Weidemüller, (2017), [arXiv:1703.05957 \[physics.atom-ph\]](#) .
- [91] D. Barredo, H. Labuhn, S. Ravets, T. Lahaye, A. Browaeys, and C. S. Adams, *Phys. Rev. Lett.* **114**, 113002 (2015).
- [92] H. Labuhn, D. Barredo, S. Ravets, S. de Léséleuc, T. Macrì, T. Lahaye, and A. Browaeys, *Nature* **534**, 667 (2016).
- [93] M. Nielsen and I. Chuang, *Quantum Computation and Quantum Information: 10th Anniversary Edition* (Cambridge University Press, 2010).
- [94] U. Schollwöck, *Annals of Physics* **326**, 96 (2011), january 2011 Special Issue.
- [95] S. Y. Khlebnikov and I. I. Tkachev, *Phys. Rev. Lett.* **77**, 219 (1996).
- [96] D. T. Son, (1996), [arXiv:hep-ph/9601377 \[hep-ph\]](#) .
- [97] G. Aarts and J. Berges, *Phys. Rev. Lett.* **88**, 041603 (2002).
- [98] A. Arrizabalaga, J. Smit, and A. Tranberg, *JHEP* **0410**, 017 (2004).
- [99] J. Berges and T. Gasenzer, *Phys. Rev. A* **76**, 033604 (2007).
- [100] A. Polkovnikov, *Annals of Physics* **325**, 1790 (2010).
- [101] P. Blakie, A. Bradley, M. Davis, R. Ballagh, and C. Gardiner, *Advances in Physics* **57**, 363 (2008).
- [102] J. Schachenmayer, A. Pikovski, and A. M. Rey, *Phys. Rev. X* **5**, 011022 (2015).
- [103] S. M. Davidson and A. Polkovnikov, *Phys. Rev. Lett.* **114**, 045701 (2015).
- [104] G. Aarts and J. Berges, *Phys. Rev. D* **64**, 105010 (2001).
- [105] P. B. Arnold, G. D. Moore, and L. G. Yaffe, *JHEP* **01**, 030 (2003).
- [106] A. Kurkela and Y. Zhu, *Phys. Rev. Lett.* **115**, 182301 (2015).
- [107] J. Berges, *Nucl.Phys.* **A699**, 847 (2002).
- [108] G. Aarts, D. Ahrensmeier, R. Baier, J. Berges, and J. Serreau, *Phys.Rev.* **D66**, 045008 (2002).
- [109] G. 't Hooft, “Large N ,” in *Phenomenology of Large N_c QCD* (World Scientific, 2012) pp. 3–18.
- [110] L. Pucci, A. Roy, and M. Kastner, *Phys. Rev. B* **93**, 174302 (2016).
- [111] A. Kamenev, *Field Theory of Non-Equilibrium Systems* (Cambridge University Press, 2011).
- [112] E. Calzetta and B. Hu, *Nonequilibrium Quantum Field Theory*, Cambridge Monographs on Mathem (Cambridge University Press, 2008).
- [113] T. Gasenzer, *The European Physical Journal Special Topics* **168**, 89 (2009).

- [114] J. Berges, *AIP Conf. Proc.* **739**, 3 (2005).
- [115] M. E. Peskin and D. V. Schroeder, *An Introduction to quantum field theory* (Addison-Wesley, Reading, USA, 1995).
- [116] J. Schwinger, *Journal of Mathematical Physics* **2**, 407 (1961).
- [117] L. V. Keldysh, *Zh. Eksp. Teor. Fiz.* **47**, 1515 (1964), [*Sov. Phys. JETP*20,1018(1965)].
- [118] L. Kadanoff, G. Baym, and D. Pines, *Quantum Statistical Mechanics*, Advanced Books Classics Series (Avalon Publishing, 1994).
- [119] J. M. Luttinger and J. C. Ward, *Phys. Rev.* **118**, 1417 (1960).
- [120] G. Baym, *Phys. Rev.* **127**, 1391 (1962).
- [121] J. M. Cornwall, R. Jackiw, and E. Tomboulis, *Phys.Rev.* **D10**, 2428 (1974).
- [122] J. Berges and J. Serreau, *Phys. Rev. Lett.* **91**, 111601 (2003).
- [123] J. Berges and S. Borsanyi, *Phys.Rev.* **D74**, 045022 (2006).
- [124] P. Romatschke and R. Venugopalan, *Phys. Rev. Lett.* **96**, 062302 (2006).
- [125] J. Berges, S. Scheffler, and D. Sexty, *Phys. Rev. D* **77**, 034504 (2008).
- [126] J. Berges, D. Gelfand, S. Scheffler, and D. Sexty, *Physics Letters B* **677**, 210 (2009).
- [127] J. Berges, K. Boguslavski, S. Schlichting, and R. Venugopalan, *Phys. Rev. D* **89**, 074011 (2014).
- [128] C. Gardiner and P. Zoller, *Quantum Noise: A Handbook of Markovian and Non-Markovian Quantum Stochastic Methods with Applications to Quantum Optics*, Springer Series in Synergetics (Springer, 2004).
- [129] D. F. Walls and G. J. Milburn, *Quantum Optics* (Springer-Verlag, Berlin, 1994).
- [130] M. Hillery, R. O’Connell, M. Scully, and E. Wigner, *Physics Reports* **106**, 121 (1984).
- [131] M. Henkel, H. Hinrichsen, and S. Lübeck, *Non-Equilibrium Phase Transitions: Volume 1: Absorbing Phase Transitions*, Theoretical and Mathematical Physics (Springer Netherlands, 2008).
- [132] M. Henkel and M. Pleimling, *Non-Equilibrium Phase Transitions: Volume 2: Ageing and Dynamical Scaling Far from Equilibrium*, Theoretical and Mathematical Physics (Springer Netherlands, 2011).
- [133] P. C. Hohenberg and B. I. Halperin, *Rev. Mod. Phys.* **49**, 435 (1977).
- [134] A. J. Bray, in *Soft and fragile matter*, edited by M. E. Cates and M. R. Evans (IOP Press, Bristol, 2000) Chap. 8, pp. 205–236.
- [135] U. Frisch and A. Kolmogorov, *Turbulence: The Legacy of A. N. Kolmogorov* (Cambridge University Press, 1995).
- [136] D. Semikoz and I. Tkachev, *Phys. Rev. Lett.* **74**, 3093 (1995).

- [137] D. Semikoz and I. Tkachev, *Phys. Rev. D* **55**, 489 (1997).
- [138] B. Svistunov, *J. Mosc. Phys. Soc.* **1**, 373 (1991).
- [139] Y. Kagan, B. Svistunov, and G. Shlyapnikov, *Sov. Phys. JETP* **74**, 279 (1992).
- [140] N. Berloff and B. Svistunov, *Phys. Rev. A* **66**, 013603 (2002).
- [141] J. Berges, S. Borsanyi, and C. Wetterich, *Phys. Rev. Lett.* **93**, 142002 (2004).
- [142] N. Bogoliubov, *J. Phys. (U.S.S.R.)* **11**, 23 (1947).
- [143] M. Alford, J. Berges, and J. M. Cheyne, *Phys. Rev. D* **70**, 125002 (2004).
- [144] A. Branschadel and T. Gasenzer, *J. Phys. B* **41**, 135302 (2008).
- [145] A. Schachner, A. Piñeiro Orioli, and J. Berges, *Phys. Rev. A* **95**, 053605 (2017).
- [146] K. Damle, S. N. Majumdar, and S. Sachdev, *Phys. Rev. A* **54**, 5037 (1996).
- [147] A. Altland and B. Simons, *Condensed Matter Field Theory*, Cambridge books online (Cambridge University Press, 2010).
- [148] A. Barrat, *Phys. Rev. E* **57**, 3629 (1998).
- [149] D. Hérisson and M. Ocio, *Phys. Rev. Lett.* **88**, 257202 (2002).
- [150] L. Pitaevskii and S. Stringari, *Bose-Einstein Condensation*, International Series of Monographs on Physics (Clarendon Press, 2003).
- [151] H.-P. Breuer and F. Petruccione, *The theory of open quantum systems* (Oxford University Press, 2002).
- [152] A. Micheli, G. K. Brennen, and P. Zoller, *Nature Phys.* **2**, 341 (2006).
- [153] I. Bloch, J. Dalibard, and S. Nascimbène, *Nature Phys.* **8**, 267 (2012).
- [154] B. P. Lanyon, C. Hempel, D. Nigg, M. Müller, R. Gerritsma, F. Zähringer, P. Schindler, J. T. Barreiro, M. Rambach, G. Kirchmair, M. Hennrich, P. Zoller, R. Blatt, and C. F. Roos, *Science* **334**, 57 (2011).
- [155] J. Simon, W. S. Bakr, R. Ma, M. E. Tai, P. M. Preiss, and M. Greiner, *Nature* **472**, 307 (2011).
- [156] M. J. Martin, M. Bishof, M. D. Swallows, X. Zhang, C. Benko, J. von Stecher, A. V. Gorshkov, A. M. Rey, and J. Ye, *Science* **341**, 632 (2013).
- [157] C. Gross, T. Zibold, E. Nicklas, J. Esteve, and M. K. Oberthaler, *Nature* **464**, 1165 (2010).
- [158] M. F. Riedel, P. Böhi, Y. Li, T. W. Hänsch, A. Sinatra, and P. Treutlein, *Nature* **464**, 1170 (2010).
- [159] C. D. Hamley, C. S. Gerving, T. M. Hoang, E. M. Bookjans, and M. S. Chapman, *Nature Phys.* **8**, 305 (2012).

- [160] W. Muessel, H. Strobel, D. Linnemann, D. B. Hume, and M. K. Oberthaler, *Phys. Rev. Lett.* **113**, 103004 (2014).
- [161] M. Cheneau, P. Barmettler, D. Poletti, M. Endres, P. Schauß, T. Fukuhara, C. Gross, I. Bloch, C. Kollath, and S. Kuhr, *Nature* **481**, 484 (2012).
- [162] T. Fukuhara, P. Schauß, M. Endres, S. Hild, M. Cheneau, I. Bloch, and C. Gross, *Nature* **502**, 76 (2013).
- [163] T. Langen, R. Geiger, M. Kuhnert, B. Rauer, and J. Schmiedmayer, *Nature Phys.* **9**, 640 (2013).
- [164] P. Jurcevic, B. P. Lanyon, P. Hauke, C. Hempel, P. Zoller, R. Blatt, and C. F. Roos, *Nature* **511**, 202 (2014).
- [165] S. Trotzky, Y.-A. Chen, A. Flesch, I. P. McCulloch, U. Schollwöck, J. Eisert, and I. Bloch, *Nature Phys.* **8**, 325 (2012).
- [166] S. Hild, T. Fukuhara, P. Schauß, J. Zeiher, M. Knap, E. Demler, I. Bloch, and C. Gross, *Phys. Rev. Lett.* **113**, 147205 (2014).
- [167] M. Schreiber, S. S. Hodgman, P. Bordia, H. P. Lüschen, M. H. Fischer, R. Vosk, E. Altman, U. Schneider, and I. Bloch, *Science* **349**, 842 (2015).
- [168] M. Marcuzzi, J. Miná, D. Barredo, S. de Léséleuc, H. Labuhn, T. Lahaye, A. Browaeys, E. Levi, and I. Lesanovsky, *Phys. Rev. Lett.* **118**, 063606 (2017).
- [169] J. Smith, A. Lee, P. Richerme, B. Neyenhuis, P. W. Hess, P. Hauke, M. Heyl, D. A. Huse, and C. Monroe, *Nature Phys.* **12**, 907 (2016).
- [170] J.-Y. Choi, S. Hild, J. Zeiher, P. Schauß, A. Rubio-Abadal, T. Yefsah, V. Khemani, D. A. Huse, I. Bloch, and C. Gross, *Science* **352**, 1547 (2016).
- [171] T. Lahaye, C. Menotti, L. Santos, M. Lewenstein, and T. Pfau, *Rep. Prog. Phys.* **71**, 126401 (2009).
- [172] A. De Paz, A. Sharma, A. Chotia, E. Maréchal, J. H. Huckans, P. Pedri, L. Santos, O. Gorceix, L. Vernac, and B. Laburthe-Tolra, *Phys. Rev. Lett.* **111**, 185305 (2013).
- [173] G. Günter, H. Schempp, M. Robert-de Saint-Vincent, V. Gavryusev, S. Helmrich, C. S. Hofmann, S. Whitlock, and M. Weidemüller, *Science* **342**, 954 (2013).
- [174] S. Yi, T. Li, and C. P. Sun, *Phys. Rev. Lett.* **98**, 260405 (2007).
- [175] T. Lahaye, T. Koch, B. Fröhlich, M. Fattori, J. Metz, A. Griesmaier, S. Giovanazzi, and T. Pfau, *Nature* **448**, 672 (2007).
- [176] S. Baier, M. J. Mark, D. Petter, K. Aikawa, L. Chomaz, Z. Cai, M. Baranov, P. Zoller, and F. Ferlaino, *Science* **352**, 201 (2016).
- [177] Y. Li, W. Pang, J. Xu, C. Lee, B. A. Malomed, and L. Santos, *New J. Phys.* **19**, 013030 (2017).
- [178] J. Eisert, M. van den Worm, S. R. Manmana, and M. Kastner, *Phys. Rev. Lett.* **111**, 260401 (2013).

- [179] N. Y. Yao, C. R. Laumann, S. Gopalakrishnan, M. Knap, M. Müller, E. A. Demler, and M. D. Lukin, *Phys. Rev. Lett.* **113**, 243002 (2014).
- [180] C. S. Hofmann, G. Günter, H. Schempp, N. L. M. Müller, A. Faber, H. Busche, M. Robert-de Saint-Vincent, S. Whitlock, and M. Weidemüller, *Frontiers of Physics* **9**, 571 (2014).
- [181] A. Reinhard, T. C. Liebisch, B. Knuffman, and G. Raithel, *Phys. Rev. A* **75**, 032712 (2007).
- [182] S. Ravets, H. Labuhn, D. Barredo, T. Lahaye, and A. Browaeys, *Phys. Rev. A* **92**, 020701 (2015).
- [183] T. F. Gallagher, *Rydberg Atoms*, Cambridge Monographs on Atomic, Molecular and Chemical Physics (Cambridge University Press, 1994).
- [184] J. Toennis and I. Sobelman, *Atomic Spectra and Radiative Transitions*, Springer Series on Atomic, Optical, and Plasma Physics (Springer Berlin Heidelberg, 1996).
- [185] M. Weissbluth, *Atoms and Molecules* (Elsevier Science, 2012).
- [186] M. L. Zimmerman, M. G. Littman, M. M. Kash, and D. Kleppner, *Phys. Rev. A* **20**, 2251 (1979).
- [187] M. Marinescu, H. R. Sadeghpour, and A. Dalgarno, *Phys. Rev. A* **49**, 982 (1994).
- [188] W. Li, I. Mourachko, M. W. Noel, and T. F. Gallagher, *Phys. Rev. A* **67**, 052502 (2003).
- [189] N. ibali, J. Pritchard, C. Adams, and K. Weatherill, *Computer Physics Communications* **220**, 319 (2017).
- [190] A. Altland, V. Gurarie, T. Kriecherbauer, and A. Polkovnikov, *Phys. Rev. A* **79**, 042703 (2009).
- [191] W. K. Wootters, *Annals of Physics* **176**, 1 (1987).
- [192] M. Robert-de Saint-Vincent, C. S. Hofmann, H. Schempp, G. Günter, S. Whitlock, and M. Weidemüller, *Phys. Rev. Lett.* **110**, 045004 (2013).
- [193] D. Comparat and P. Pillet, *J. Opt. Soc. Am. B* **27**, A208 (2010).
- [194] I. I. Beterov, I. I. Ryabtsev, D. B. Tretyakov, and V. M. Entin, *Phys. Rev. A* **79**, 052504 (2009).
- [195] T. Mori, *Phys. Rev. E* **82**, 060103 (2010).
- [196] H. Schempp, G. Günter, M. Robert-de Saint-Vincent, C. S. Hofmann, D. Breyel, A. Komnik, D. W. Schönleber, M. Gärttner, J. Evers, S. Whitlock, and M. Weidemüller, *Phys. Rev. Lett.* **112**, 013002 (2014).
- [197] N. Malossi, M. M. Valado, S. Scotto, P. Huillery, P. Pillet, D. Ciampini, E. Arimondo, and O. Morsch, *Phys. Rev. Lett.* **113**, 023006 (2014).
- [198] A. Piñeiro Orioli, A. Safavi-Naini, M. L. Wall, and A. M. Rey, *Phys. Rev. A* **96**, 033607 (2017).

- [199] A. Altland, V. Gurarie, T. Kriecherbauer, and A. Polkovnikov, *Phys. Rev. A* **79**, 042703 (2009).
- [200] A. Caldeira and A. Leggett, *Annals of Physics* **149**, 374 (1983).
- [201] I. D. Leroux, M. H. Schleier-Smith, and V. Vuletić, *Phys. Rev. Lett.* **104**, 073602 (2010).
- [202] H. Ritsch, P. Domokos, F. Brennecke, and T. Esslinger, *Rev. Mod. Phys.* **85**, 553 (2013).
- [203] A. Sørensen and K. Mølmer, *Phys. Rev. Lett.* **82**, 1971 (1999).
- [204] D. Porras and J. I. Cirac, *Phys. Rev. Lett.* **92**, 207901 (2004).
- [205] D. Porras, F. Marquardt, J. von Delft, and J. I. Cirac, *Phys. Rev. A* **78**, 010101 (2008).
- [206] M. Richter, M. Gegg, T. S. Theuerholz, and A. Knorr, *Phys. Rev. B* **91**, 035306 (2015).
- [207] M. L. Wall, A. Safavi-Naini, and A. M. Rey, *Phys. Rev. A* **94**, 053637 (2016).
- [208] M. L. Wall, A. Safavi-Naini, and A. M. Rey, *Phys. Rev. A* **95**, 013602 (2017).
- [209] D. Leibfried, B. DeMarco, V. Meyer, D. Lucas, M. Barrett, J. Britton, W. Itano, B. Jenlenković, C. Langer, T. Rosenband, *et al.*, *Nature* **422**, 412 (2003).
- [210] D. Dylewsky, J. K. Freericks, M. L. Wall, A. M. Rey, and M. Foss-Feig, *Phys. Rev. A* **93**, 013415 (2016).
- [211] T. Graß, D. Raventós, B. Juliá-Díaz, C. Gogolin, and M. Lewenstein, *Nature Communications* **7**, 11524 (2016).
- [212] R. Pakauskas and M. Kastner, *Journal of Statistical Mechanics: Theory and Experiment* **2012**, P02005 (2012).
- [213] M. Sallé, J. Smit, and J. C. Vink, *Phys. Rev. D* **64**, 025016 (2001).
- [214] G. Aarts and A. Tranberg, *Phys. Rev. D* **74**, 025004 (2006).
- [215] B. Mihaila, T. Athan, F. Cooper, J. Dawson, and S. Habib, *Phys. Rev. D* **62**, 125015 (2000).
- [216] M. Knap, A. Kantian, T. Giamarchi, I. Bloch, M. D. Lukin, and E. Demler, *Phys. Rev. Lett.* **111**, 147205 (2013).
- [217] N. Navon, A. L. Gaunt, R. P. Smith, and Z. Hadzibabic, *Nature* **539**, 72 (2016).
- [218] N. Navon, A. L. Gaunt, R. P. Smith, and Z. Hadzibabic, *Science* **347**, 167 (2015).
- [219] J. Beugnon and N. Navon, *Journal of Physics B: Atomic, Molecular and Optical Physics* **50**, 022002 (2017).
- [220] M. Saffman, T. G. Walker, and K. Mølmer, *Rev. Mod. Phys.* **82**, 2313 (2010).
- [221] M. Saffman, *Journal of Physics B: Atomic, Molecular and Optical Physics* **49**, 202001 (2016).
- [222] S. Whitlock, A. W. Glaetzle, and P. Hannaford, *Journal of Physics B: Atomic, Molecular and Optical Physics* **50**, 074001 (2017).

- [223] M. E. Fisher, S.-k. Ma, and B. G. Nickel, *Phys. Rev. Lett.* **29**, 917 (1972).
- [224] A. Dutta and J. K. Bhattacharjee, *Phys. Rev. B* **64**, 184106 (2001).
- [225] M. C. Angelini, G. Parisi, and F. Ricci-Tersenghi, *Phys. Rev. E* **89**, 062120 (2014).
- [226] N. Defenu, A. Trombettoni, and A. Codello, *Phys. Rev. E* **92**, 052113 (2015).
- [227] R. Gutiérrez, J. P. Garrahan, and I. Lesanovsky, *Phys. Rev. E* **92**, 062144 (2015).
- [228] R. Gutierrez, C. Simonelli, M. Archimi, F. Castellucci, E. Arimondo, D. Ciampini, M. Marcuzzi, I. Lesanovsky, and O. Morsch, ArXiv e-prints (2016), [arXiv:1611.03288](https://arxiv.org/abs/1611.03288) [cond-mat.stat-mech] .
- [229] M. Marcuzzi, M. Buchhold, S. Diehl, and I. Lesanovsky, *Phys. Rev. Lett.* **116**, 245701 (2016).
- [230] M. Buchhold, B. Everest, M. Marcuzzi, I. Lesanovsky, and S. Diehl, *Phys. Rev. B* **95**, 014308 (2017).
- [231] S. Helmrich, A. Arias, and S. Whitlock, ArXiv e-prints (2016), [arXiv:1605.08609](https://arxiv.org/abs/1605.08609) [physics.atom-ph] .
- [232] S. Davidson, D. Sels, and A. Polkovnikov, *Annals of Physics* **384**, 128 (2017).
- [233] M. Lewenstein, A. Sanpera, V. Ahufinger, B. Damski, A. Sen(De), and U. Sen, *Advances in Physics* **56**, 243 (2007).
- [234] A. Elben, *Nonequilibrium Dynamics and Thermalization of Inhomogeneous Quantum Fields*, Master's thesis, Heidelberg University, Germany (2016).
- [235] W. H. Press, S. A. Teukolsky, W. T. Vetterling, and B. P. Flannery, *Numerical Recipes 3rd Edition: The Art of Scientific Computing*, 3rd ed. (Cambridge University Press, New York, NY, USA, 2007).